SCATTERING AND DIFFRACTION OF ANTI-PLANE (SH) ELASTIC WAVES BY PARABOLIC SURFACE TOPOGRAPHIES

by

LiPing Lily Teng

A Dissertation Presented to the
FACULTY OF THE USC GRADUATE SCHOOL
UNIVERSITY OF SOUTHERN CALIFORNIA
In Partial Fulfillment of the
Requirements for the Degree
DOCTOR OF PHILOSOPHY
(CIVIL ENGINEERING)

August 2012

Acknowledgements

I would like to thank my parents for their mental and financial support of my university education throughout, their inspiration and encouragement.

I would also like to thank every member of my thesis defense committee, namely, Professor H. Wong, Professor C. Wang and Professor V. Lee for their attention, administration and guidance of the presentation and defense of my thesis. I would thank my thesis adviser and supervisor, Professor Vincent Lee, for his unlimited patience, constant guidance and planning, and infinite energy in orchestrating every word of the paragraph and page of every chapter of the thesis.

Finally, I would like to thank the Astani Civil and Environmental Engineering Department for its financial support during the earlier years, when I was given the teaching assistantship award, which enabled me to gain teaching experience, making it a simple matter for me, as General Manager, to give presentation to my general clients associates and customers at my work place at City of Los Angeles, Department of Building and Safety.

Table of Contents

List of Figures

Chapter I. Introduction

I.1 Previous Study of Diffraction of Anti-Plane (SH) Waves

It has long been known in earthquake engineering and strong-motion seismology that surface topographies and sub-surface irregularities can play a major role in the amplification and de-amplification of elastic waves at a given site. However, the stress-free boundaries often pose a much more difficult waveguide problem than those in acoustics, thus limiting the number of cases which can be solved exactly. The simplest type of problem in elastic wave scattering is that of 2-D SH-wave scattering. Its simplicity rests in the acoustic behavior of 2-D SH-waves, allowing it to be analyzed separately from the in-plane P- and SV-waves. Using an image method, exact series solutions for the diffraction of SH-waves in an elastic half-space exist for those problems which can be described by coordinate systems where the scalar wave equation is separable.

These problems have been studied by many investigators. Trifunac (1973) solved the 2-D scattering and diffraction of plane SH-waves by a semi-circular canyon. Wong & Trifunac (1974) solved a similar problem involving canyons of semi-elliptical shape. Lee (1977) solved the scattering of plane SH-waves by underground circular cavities. Lee & Trifunac (1979) studied the corresponding problem of underground circular tunnels. Approximate solutions have also been obtained for the diffraction of SH-waves from surface topography of arbitrary shape (Wong & Jennings 1975; Sabina & Willis 1975;

Sanchez-Sesma & Rosenblueth 1979; Moeen-Vaziri & Trifunac 1985). Analytic solutions for shallow circular canyons of various depth to width ratios were given by Cao & Lee (1989, 1990), Lee & Cao (1989) for both anti-plane SH and in-plane P and SV waves. Todorovska & Lee (1991a, b) extended their work to Rayleigh Waves and shallow alluvial valleys, Lee & Wu (1994a, b) using weighted residual methods, continued their work on the diffraction of 2D canyons of arbitrary shape by SH, P, SV and Rayleigh waves. Lee et al (1999) did SH diffraction of circular canyon above a circular underground cavity. Liang et al (2000), Liang, Yan & Lee (2001a, b, 2002, 2003a, b), Liang, Zhang et al (2003a, b) presented SH, P and SV waves diffraction by circular-arc canyon and layered alluvial valleys. Liang et al (2004a, b, c, d, 2005a, b) continued their work on underground single and twin cavities.

The above works are all half-space diffraction problems. One thing in common for all these previous solved problems is that, irrespective of whether they are surface or subsurface topographies, all diffraction problems and solutions are for topographies that are finite in dimensions. This thesis plans to expand these studies to a case of semi-infinite surface topographies.

The first such work on semi-infinite surface topography on a half space is the case of diffraction around a semi-parabolic canyon in an elastic half-space by anti-plane SH waves (Lee, 1990). The work of this thesis will start and continue on such a semi-parabolic canyon and extend the work to a semi-parabolic hill.

I.2 Waves in Parabolic Coordinates in an Elastic Full Space

The equation used to solve wave function numerically for parabolic coordinates in an elastic full space was first accomplished by Thau & Pao (1966). First, parabolic coordinates was defined and inverse transformations in terms of Cartesian and polar coordinates. Then, transfer the Helmholtz equation in parabolic cylinder coordinates will result with standard form of Weber's equation.

In the last century, due to the difficulty in matching the boundary conditions at the surface, the solution for diffraction of waves in elastic cylinder cannot be solved easily. Therefore, it was first solved with the analogous to the diffraction of light by a semi-infinite screen with zero focal length. The use of parabolic coordinates in studying wave diffraction problems dated as far back as the end of last century, when Sommerfeld (1896) found an exact solution to the diffraction of a plane wave by a perfectly conducting semi-infinite screen. Subsequently, Lamb (1907) showed that the same solution could be obtained by solving the wave equation in parabolic coordinates. Later, Epstein (1914), using the wave series functions in parabolic coordinates, solved the problem of diffraction of electromagnetic waves by a partially conducting parabolic cylinder. It was not until 1966 that the theory was applied to the study of diffraction of elastic waves by a parabolic cylinder, as reported in a dissertation by Thau (1966) and a series of papers by Thau & Pao (1966, 1967a, b).

In this paper, the problem of scattering and diffraction of plane SH-waves by a semi-parabolic canyon in an elastic half-space is first reviewed. It was first solved by Lee (1990). The SH-waves are assumed to be coming from the side of the half-space towards the front of the canyon. The purpose of this study is to add the exact series solution to the limited collection of exact solutions describing the effects of surface topography on wave propagation in an elastic half-space.

The results will also be useful for the approximate evaluation of the amplification effects near topographic features with portions near the surface that can be approximated as parabolic in shape. Furthermore, it is of value to different approximate techniques, since the model studied here can in future be used for comparison with the results obtained by approximate methods. It can in general serve as a guide to the behavior of arbitrarily shaped topographic features, as in the case of semi-circular cylindrical canyons (Trifunac 1973). However, unlike the circular canyon, which is symmetrical and has only one radius of curvature, a semi-parabolic canyon is asymmetrical and every point has a different radius of curvature. The solution for a semi-parabolic canyon in an elastic half-space will be similar, and yet different from that of a parabolic canyon in an elastic full-space. The difference comes from the fact that, in the present case, an additional stress-free boundary condition has to be satisfied on the surface of the half-space.

I.3 The case of Parabolic Waves in Half-Space (Lee, 1990)

The latest work regarding the scattering of plane SH-waves was studied by Lee in 1990. The problem solved was the scattering of plane SH-waves by a semi-parabolic canyon in an elastic half-space. The model is made up of a half-space in which a semi-infinite part of the surface is removed to form a canyon which is parabolic in shape. The half-space is assumed to be elastic, isotropic and homogeneous, with its material properties characterized by the rigidity μ and the shear wave velocity β. See Fig. 1.1a for the cross section of the model.

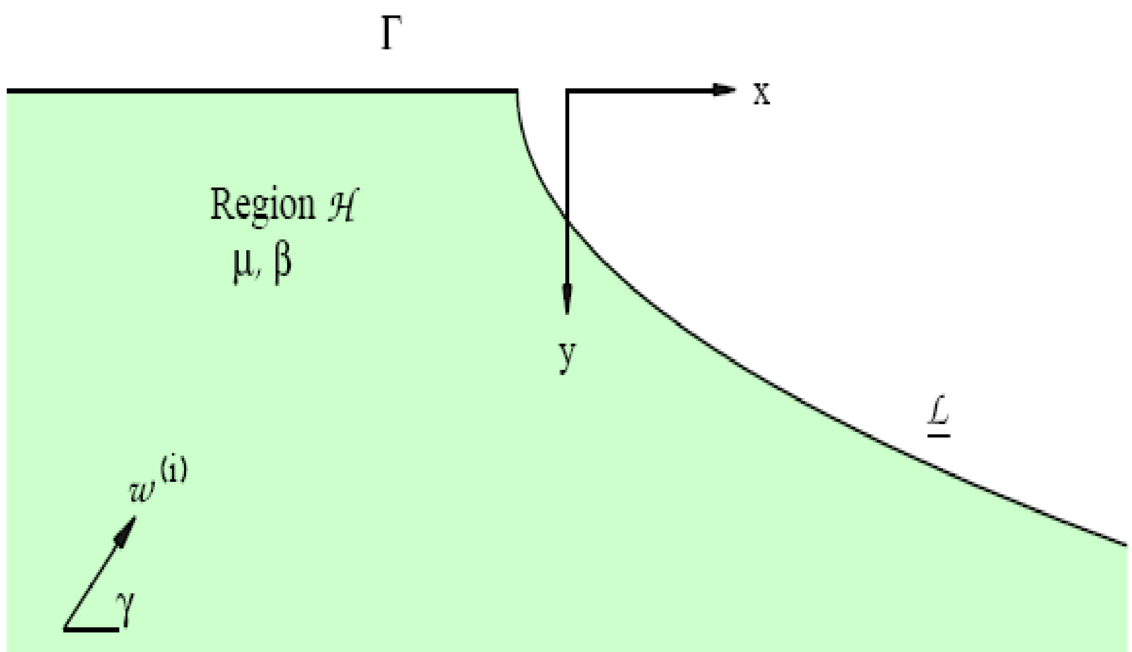

Fig. 1.1a The 2-D Model Representing a Half-space with a Semi-parabolic on the Right has Material Properties Characterized by Rigidity μ and Shear Wave Velocity β. The Incident Plane SH Wave from the Left makes an Angle γ with Horizontal.

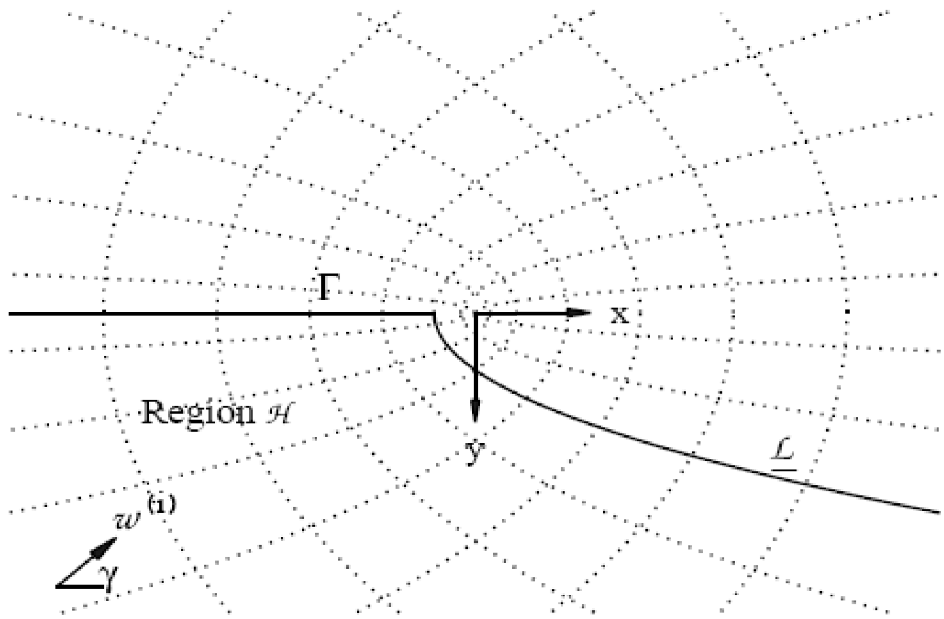

Fig. 1.1b The Parabolic, $\xi-\eta$ and Rectangular, x-y Coordinates both Their Origins on the Focal Point of the Parabolic Canyon. They are related by $\xi+i\eta=\left[2\left(x+iy\right)\right]^{1/2}$. The Half-space Surface is on $\xi=0$ and the Canyon is on the Lower Half of $\eta=1$.

Two coordinate systems are employed (Fig. 1.1b). The rectangular coordinate system is centered at the focus of the parabolic canyon with the y-axis pointing downwards. The parabolic coordinate system $\left(\xi,\eta\right)$ obtained by the transformation from the rectangular system (x, y), $\xi+i\eta=\left[2\left(x+iy\right)\right]^{1/2}$, will also be used. The coordinate curves $\eta=$ constant and $\xi=$constant in the half-space are shown in Fig. 1.1b. The surface of the parabolic canyon on the right is defined by the curve $\eta=\eta_0$ which, without loss of generality, is represented by the curve $\eta=1$ in the figure. The surface of the half-space on the left corresponds to $\xi = 0$. The distance from the focal point (origin) O to the apex, the corner point or tip of the canyon is $h = \eta_1^2/2$.

The two coordinate systems are related by

$$\begin{aligned}
x &= \frac{1}{2}\left(\xi^2 - \eta^2\right), -\infty < \xi < \infty \\
y &= \xi\eta, -\infty < \eta < \infty \\
\xi &= \pm\left[\left(x^2 + y^2\right)^{1/2} + x\right]^{1/2} \\
\eta &= \pm\left[\left(x^2 + y^2\right)^{1/2} - x\right]^{1/2}
\end{aligned} \tag{1}$$

I.3.1 Excitation: Incident SH Waves

The excitation of the half-space, W^i, to consists of an infinite train of plane SH-waves from the left with frequency ω, non-zero motion in the z-direction only, and having an angle of incidence γ with the positive x-axis (Fig. 1.1a):

$$W^i = \exp\left[-i\omega\left(t - \frac{x}{c_x} + \frac{y}{c_y}\right)\right] \tag{2}$$

Where c_x and c_y are respectively the phase velocities along the horizon x- and vertical y-directions, and are given by

$$\begin{aligned} c_x &= \frac{\beta}{\cos\gamma} \\ c_y &= \frac{\beta}{\sin\gamma} \end{aligned} \tag{3}$$

where β is the shear wave velocity.

It is assumed in equation (2) that W^i has unit amplitude of motion. The time factor $\exp(-i\omega t)$ will be understood and deleted from all subsequent equations. In terms of shear wave number $k = \omega / \beta$ equation (2) becomes

$$W^i = \exp\left[ik\left(x\cos\gamma - y\sin\gamma\right)\right] \tag{4}$$

Equation (4) is of the same form as that used by Thau & Pao (1966) to represent the incident SH-wave propagating in the positive x- and y-directions. The fact that the angle γ with the horizontal x-axis is used, rather than the angle with the vertical y-axis, to specify the direction of the incident SH-wave will become clear in the equations to follow, where the SH-wave will be expressed in terms of parabolic functions with terms involving the angle γ (Equation 7).

In the absence of the parabolic canyon, the incident SH-wave from the left would be reflected from the plane free surface ($y=0$). The reflected plane SH-wave W^r is given by

$$W^r = \exp\left[ik\left(x\cos\gamma + y\sin\gamma\right)\right] \tag{5}$$

The resultant motion in the free-field half-space, W^{ff} then becomes

$$W^{ff} = W^i + W^r = \exp\left(ikx\cos\gamma\right)\sin\left(y\sin\gamma\right) \tag{6}$$

of amplitude equals to 2.

In the presence of the parabolic canyon, it is appropriate to express the incident and reflected plane SH-waves as parabolic functions using parabolic coordinates. The expansions for W^i and W^r are (Morse & Feshbach 1953):

$$\begin{aligned} W^i &= \sec\left(\gamma/2\right)\sum_{n=0}^{\infty}\frac{\left(+i\right)^2}{n!}\tan^n\left(\gamma\!\!\diagup\!2\right)D_n\left(\bar{\lambda}\eta\right)D_n\left(\lambda\xi\right) \\ W^r &= \sec\left(\gamma/2\right)\sum_{n=0}^{\infty}\frac{\left(-i\right)^2}{n!}\tan^n\left(\gamma\!\!\diagup\!2\right)D_n\left(\bar{\lambda}\eta\right)D_n\left(\lambda\xi\right) \end{aligned} \tag{7}$$

with, $\lambda=\sqrt{-2ik}, \bar{\lambda}=\sqrt{2ik}$ and the $D_n\left(\bullet\right)$ functions are eth Weber (parabolic cylinder) functions of order n n and the sum of W^i and W^r is W^{ff}, the free-field waves

$$W^{ff} = 2\sec\left(\gamma\!\!\diagup\!2\right)\sum_{n=0}^{\infty}\frac{\left(-1\right)^n}{2n!}\tan^{2n}\left(\gamma\!\!\diagup\!2\right)D_{2n}\left(\bar{\lambda}\eta\right)D_{2n}\left(\lambda\xi\right) \tag{8}$$

I.3.2 Solution of the Problem

In the presence of the parabolic canyon, the incoming plane SH-wave, W^{ff} , are scattered and diffracted from the surface of the canyon $\eta = \eta_1$ resulting in additional scattered waves, W^s, diverging from the parabolic canyon. The resultant total displacement field W will then be the superposition of the incident and reflected plane waves, W^{ff} and the scattered waves, W^s. The resultant waves $W = W^{ff} + W^s$ must satisfy the Helmboltz equation in parabolic coordinates

$$\left(\nabla^2 + k^2\right)W = \frac{1}{J^2}\left(\frac{\partial^2 W}{\partial \xi^2} + \frac{\partial^2 W}{\partial \eta^2}\right) + k^2 W = 0 \tag{9}$$

with $J^2 = \xi^2 + \eta^2$. The boundary conditions for W are

$$\tau_{yz} = 0 \tag{10}$$

at the surface of the half-space ($y = 0$) to the left of the canyon, and at the surface of the parabolic canyon $\eta = \eta_1$

$$\tau_{\eta z}\Big|_{\eta=\eta_1} = \mu \frac{1}{J}\frac{\partial W}{\partial \eta}\Big|_{\eta=\eta_1} = 0 \tag{11}$$

The scattered wave W^s as an outgoing wave diverging from the parabola $\eta = \eta_1$ must, by itself, satisfy the differential equation (Equation 9). Since the incident and reflected plane SH-waves W^{ff} already satisfy the stress-free boundary condition (Equation (10)) at

$y = 0$, the scattered wave W^s itself must satisfy the same stress-free boundary condition. In terms of parabolic coordinates, Equation (10) takes the form (Pao & Mow 1971):

$$\tau_{\xi z} = \mu \frac{1}{J} \frac{\partial W}{\partial \xi} = 0 \text{ at } \xi = 0 \tag{12}$$

The waves W^s satisfying Equations (9) and (12) can be written as

$$W^s = 2\sec\left(\gamma/2\right) \sum_{n=0}^{\infty} B_n D_{-2n-1}(\lambda\eta) D_{2n}(\lambda\xi) \tag{13}$$

where for each n, the wave function $D_{-2n-1}(\lambda\eta) D_{2n}(\lambda\xi)$ represents a wave diverging from the parabolic canyon $\eta = \eta_1$. The zero-stress boundary condition at $y = 0(\xi = 0)$ to the left of the canyon is satisfied because

$$D'_{2n}(\lambda\xi)\Big|_{\xi=0} = 0 \tag{14}$$

The coefficient b_n can be determined from the boundary condition at the surface of the canyon (Equation 11). This gives, for $n = 0, 1, 2, \ldots,$

$$B_n = \frac{-i(-1)^n}{(2n)!} \tan^{2n}\left(\gamma/2\right) \frac{D'_{2n}(\lambda\eta_1)}{D'_{-2n-1}(\lambda\eta_1)} \tag{15}$$

Each term of the infinite series representing the solution is thus expressed in closed form, and the resultant wave, W, is given by:

$$W = W^{ff} + W^s =$$

$$2\sec\left(\gamma/2\right) \sum_{n=0}^{\infty} \frac{(-1)^n}{2n!} \tan^{2n}\left(\gamma/2\right) \left[D_{2n}(\bar{\lambda}\eta) - \frac{D'_{2n}(\lambda\eta_1)}{D'_{-2n-1}(\lambda\eta_1)} D_{-2n-1}(\lambda\eta) \right] D_{2n}(\lambda\xi) \tag{16}$$

I.3.3 Surface Displacements

The resulting motion at every point will be characterized here by the displacement amplitude and phase, $|W|$ and φ. The incident SH-wave W^i is assumed to have unit amplitude, so that the resulting free-field surface displacement amplitude corresponding to the plane waves W^{ff}, Equation (7), in the absence of the canyon will be 2. The resultant amplitude $|W|$ of the displacement in Equation (16) thus represents the amplification or de-amplification due to the presence of the canyon. Both the amplitude and phase will depend on the angle of incidence of the SH-wave, the frequency ω, shear wave velocity β and the parameter η_0, where $\eta = \eta_0$ defines the surface of the semi-parabolic canyon. These parameters can be combined into one parameter $k\eta_0^2$, given by

$$k\eta_1^2 = \omega\eta_1^2 / \beta = 2\pi\eta_1^2 / \lambda \tag{17}$$

where k is the wave number and λ is the wavelength of the incident SH-wave. A dimensionless frequency Ω can be defined as

$$\Omega = \omega\eta_1^2 / \pi\beta \tag{18}$$

In terms of the focal length of the parabolic canyon, $h\left(= \eta_0^2 / \pi\beta \right)$, Ω becomes

$$\Omega = 2\omega h / \pi\beta \tag{19}$$

The dimensionless frequency Ω can also be expressed in terms of the wavelength of the incident SH-wave:

$$\Omega = \frac{2\eta_1^2}{\lambda} = \frac{4h}{\lambda} \tag{20}$$

The choice of Ω has been motivated by its physical meaning, as a link between the dimension of the parabolic canyon (focal length), and the frequency and wavelength of the incident SH-wave.

The Weber functions are computed numerically by the use of their recursive relations in the reverse direction with respect to their orders (Abramowitz & Stegan 1972). They are then used to calculate the coefficient of each term of the series for the scattered wave in Equation (15). A sufficient number of coefficients of the infinite series are calculated so that the remaining coefficients will each contribute less than the floating-point error present in a digital computer.

Fig. 1.2 presents the displacement amplitudes, $|W|$, plotted versus the dimensionless frequency, Ω, at two points on the surface of the half-space close to the canyon for five angles of incidence $\gamma = 0^\circ, 15^\circ, 30^\circ, 45^\circ$ and 60°. The two surface points at which displacements are calculated correspond to the point on the surface of the half-space at a distance of one focal length from the tip to the left of the canyon $\left(x/h = -1\right)$, and he point at the tip of the canyon $\left(x/h = 0\right)$, respectively. An angle of incidence of $\gamma = 0^\circ$ corresponds to horizontal incidence from the left. For plane SH-wave of unit amplitudes incident upon a quarter-space, the resulting displacement amplitude at the corner point is

4, independent of the angles of incidence. For horizontal incidence $\left(\gamma = 0^{\circ}\right)$, the corner point at the tip of the semi-parabolic canyon $\left(x/h = 0 \right)$ behaves like that of a quarter-space with increasing frequency Ω, so that the displacement amplitudes approach the value of 4 with increasing frequency, as shown by the solid curve at the bottom graph of the figure. As the angles of incidence increase from 0° to 60°, such trend is still observed, as shown by the corresponding five bottom curves in the figure, but the convergence to 4 becomes slower and slower with increasing angle. For incidence angle of 60°, the incident plane SH-wave is diffracted at the bottom part of the parabolic canyon far from the half-space long before it reaches the half-space near the tip of the canyon. AS stated earlier, the analysis here is restricted to cases of plane SH-wave coming from the side of the half-space towards the front of the canyon. Hence, only the cases of almost horizontal incidence at or below 45° will be considered.

The upper set of five curves in Fig. 2 corresponds to displacement amplitudes for various angles of incidence namely, for $\gamma = 0^{\circ}, 15^{\circ}, 30^{\circ}, 45^{\circ}$ and 60° at the surface point, one focal length from the corner point. They are more oscillatory as the dimensionless frequency changes from 0 to 2, as a result of scattering and diffraction of the plane SH-wave on or near the tip (corner point) of the canyon. It may also be note that as Ω approaches zero, all displacement amplitudes approach 2, the free-field surface displacement amplitude. This is as expected, since as the frequency approaches zero, the wavelength of the incident waves approaches infinity, so that the wave will overlook the presence of the canyon.

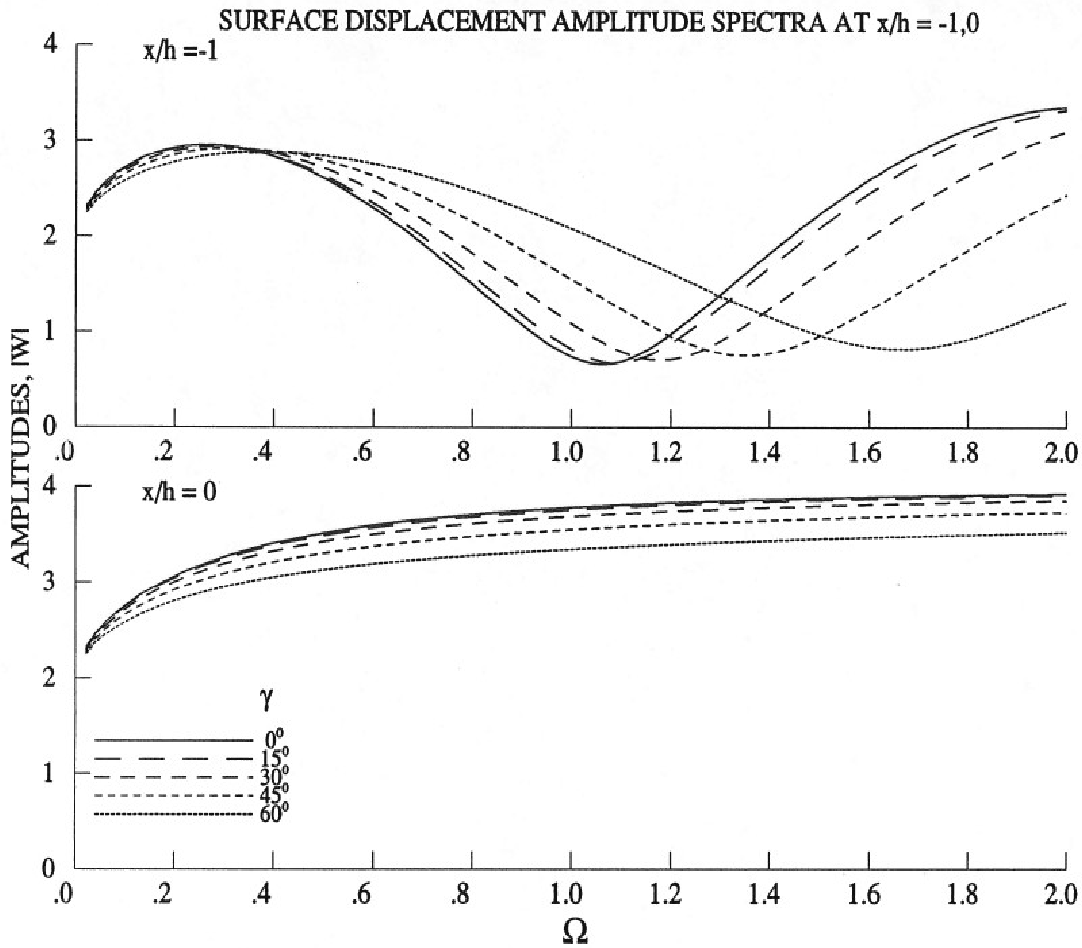

Fig. 1.2 Surface Displacement Amplitude, $|W|$, Plotted vs. the Dimensionless Frequency, $\Omega(=\omega h/\pi\beta)$, at Two Points on the Surface: (a) $x/h=-1$, One Focal Length on the Half-space Surface to the Left of the Tip of the Canyon, and (b) $x/h=0$, the Tip of the Canyon. The Five Curves on Each Graph Correspond to the Five Angles of Incidence, $\gamma = 0^{\circ}, 15^{\circ}, 30^{\circ}, 45^{\circ}$ and 60°

Figures 1.3 and 1.4 represent the displacement amplitudes, $|W|$, plotted versus the dimensionless distance x/h and the dimensionless frequency, Ω, for angles of incidence of $0^{\circ}, 15^{\circ}, 30^{\circ}$ and 45°, respectively. The incident SH-wave W^i is assumed as before to have unit amplitude. The dimensionless distance is measured in units of focal length from the tip (corner point) of the canyon. Points on the surface of the half-space to the left of the canyon are measured in negative units of focal length from the tip of the canyon. Thus $x/h = -2$ corresponds to the point on the surface of the half-space at distance 2h to the left of the tip of the canyon. Similarly, points on the surface of the canyon are measured according to their horizontal distances in positive units of focal length from the tip of the canyon. The shape of the surface on and near the canyon on which the displacement is calculated is outlined as a dotted line on the top-left graph of each figure, with the arrow indicating the corresponding direction of the incident SH-wave W^i. The incident plane SH-wave is assumed to be coming from the left, i.e. from $x/h < 0$ in all cases.

For the case of horizontal incidence $(\gamma = 0)$ in Fig. 1.3, the incident wave depends only on x, taking the form (from Equation 4)

$$W^i = \exp(ikx) \tag{21}$$

and the resultant wave becomes, from Equation (16)

$$W = 2\left[D_0\left(\eta\sqrt{2ik}\right) - \frac{iD_0^{'}\left(\eta_0\sqrt{2ik}\right)}{iD_{-1}^{'}\left(\eta_0\sqrt{-2ik}\right)} D_{-1}\left(\eta\sqrt{-2ik}\right) \right] D_{0}\left(\xi\sqrt{-2ik}\right) \tag{22}$$

with only the term for $n = 0$ remaining. It is seen from Equation (22) that the term inside $[\bullet]$ becomes constant at $\eta = \eta_0$, the surface of the canyon, while

$$\left| D_0\left(\xi\sqrt{-2ik}\right) \right| = \left| e^{-ik\xi^2 / 4} \right| = 1 \tag{23}$$

The displacement amplitude in Fig. 1.3 and 1.4 show some interesting features of the model, the most prominent being that there are no frequencies or points on the surface of the model that lead to displacement amplitudes higher than 4. In the absence of the canyon, the free-field surface displacement amplitudes at all points would be equal to 2 (Equation 6), for incident SH-wave with unit amplitudes. This means that the highest amplification for this model does not exceed 2. The amplification of 2 or displacement amplitude of 4 is attained in the limit of high frequencies at the corner point $x/h = 0$. This amplification is almost attained there at frequency $\Omega = 1.5$ (Fig. 2 and 3) for horizontal incidence $(\gamma = 0)$. It is interesting to note that the same observation has been made previously for the cases of incident SH-wave reflecting at the left rim of a semi-circular cylindrical canyon (Trifunac 1973), or the left rim of a semi-elliptical cylindrical canyon (Wong & Trifunac 1974) and at the left rims of shallow circular cylindrical canyons (Cao & Lee 1989). For all these cases, at the high frequencies, the waves reflect from the rim

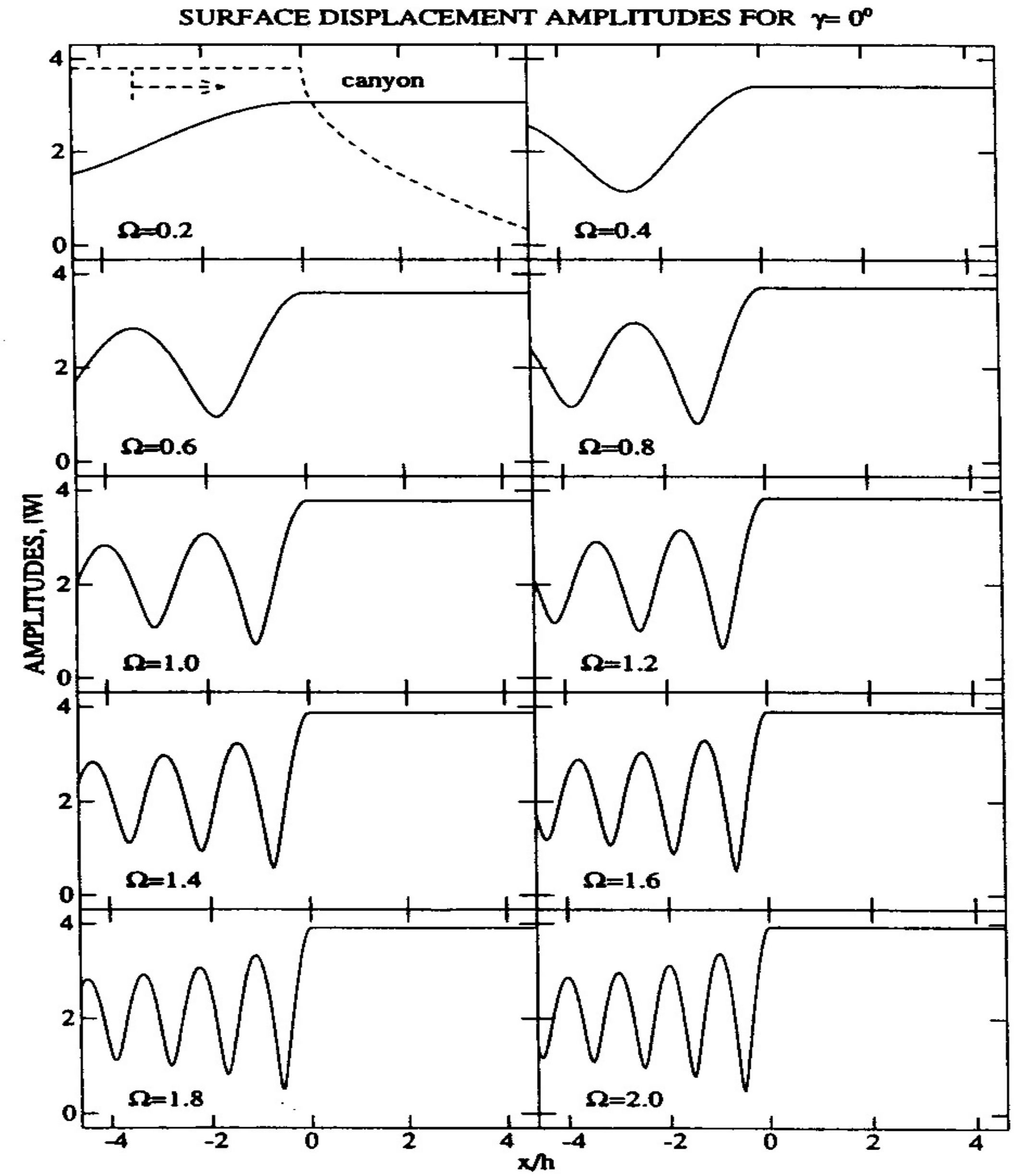

Fig. 1.3 Surface displacement amplitudes, |W|, for $\gamma = 0°$, plotted vs. the dimensionless distance *x/h* in the interval (-4, 4) measured from the tip of the canyon and for dimensionless frequencies $\Omega\ (= \omega h / \pi\beta\ )$ from 0.2 to 2.0 in steps of 0.2. $x/h \leqq 0$ corresponds to points on the half-space surface, and $x/h > 0$ to points on the surface of the semi-parabolic canyon.

as they would from the corner of a quarter-space. For the various angles of incidence shown $\left(\gamma = 0^{\circ}, 15^{\circ}, 30^{\circ} \text{ and } 45^{\circ}\right)$ in Figures 3-5, the parabolic canyon acts as a barrier, reflecting a large amount of energy back in the direction from which it came $\left(x/h < 0 \right)$, resulting in a standing-wave pattern superimposed onto the motion progressing to the right. This is evident for all angles of incidence, whether horizontal (Fig. 1.3) or oblique (Fig. 1.4). For the case of oblique incidence, (Fig. 1.4), the displacement amplitudes on the parabolic canyon are not constant, but they tend to be smoother than those at the surface of the half-space to the left of the canyon.

It should be pointed out that the displacement amplitudes at the surface of the canyon in Fig. 1.4, corresponding to SH-wave incident at 45° and of dimensionless frequencies $\Omega = 1.6, 1.8 \text{ and } 2.0$, are not plotted all the way beyond $x/h = 4$, unlike all the other displacement amplitudes. This is because at those higher frequencies and for angles of incidence at or greater than 45°, convergence of the series in Equation (13) at points along the canyon with $x/h \geq 4$ is not achieved. This fact is consistent with the findings of Thau (1966), who noted that the convergence of the series becomes slower as he angle of incidence γ increases and as the points become farther from the tip of the canyon.

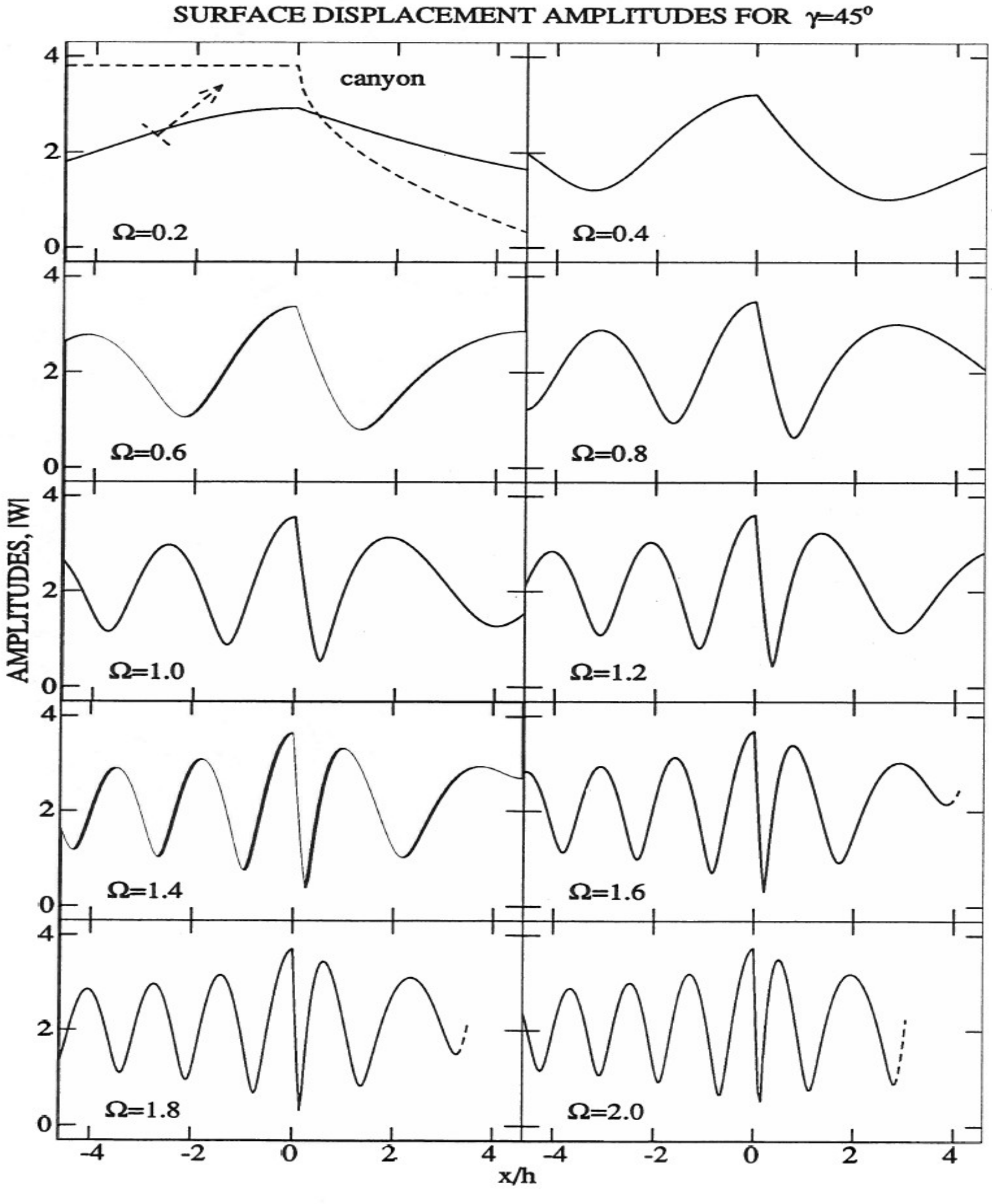

Fig. 1.4 Surface Displacement Amplitudes $|W|$ for $\gamma = 45^\circ$, Plotted vs. the dimensionless Distance x/h in (-4, 4), and Dimensionless Frequencies $\Omega(=\omega h/\pi\beta)$

Fig. 1.5 present the phase diagrams for the corresponding displacement amplitudes (Fig. 1.3 and 1.4), plotted versus the dimensionless distance x/h and the dimensionless frequency, Ω. In the absence of the canyon, the phase angle at the surface of the half-space is given by

$$\phi = k\left(\cos\gamma\right)x \tag{24}$$

which is linear in x, with slope proportional to the wavenumber k and the cosine of the incident angle. All phase diagrams in the figure have been shifted arbitrarily to have a common zero phase around $x/h = 0$ (i.e. the tip of the canyon). The phase values presented in the figures are in units of π. A common range of -4 to 4 units of π is chosen for all the phase figures. In the presence of the parabolic canyon, the phases of the resultant motion near the canyon deviate significantly from that of uniform free-filed motion. Compared with the corresponding figures of displacement amplitudes, abrupt jumps in phases are observed at points in front of the canyon where the displacement amplitudes are very small. Points where such jumps of almost $\pm\pi$ occur experience predominantly torsional vibrations. It should be noted that corresponding to displacement phase shown on Fig. 5: for SH-wave incident at 45°, the phases for dimensions; frequencies $\Omega = 1.6, 1.8,$ and 2.0 are again not plotted all the way beyond $x/h = 4$, as in the case of the corresponding amplitudes in Fig. 1.4.

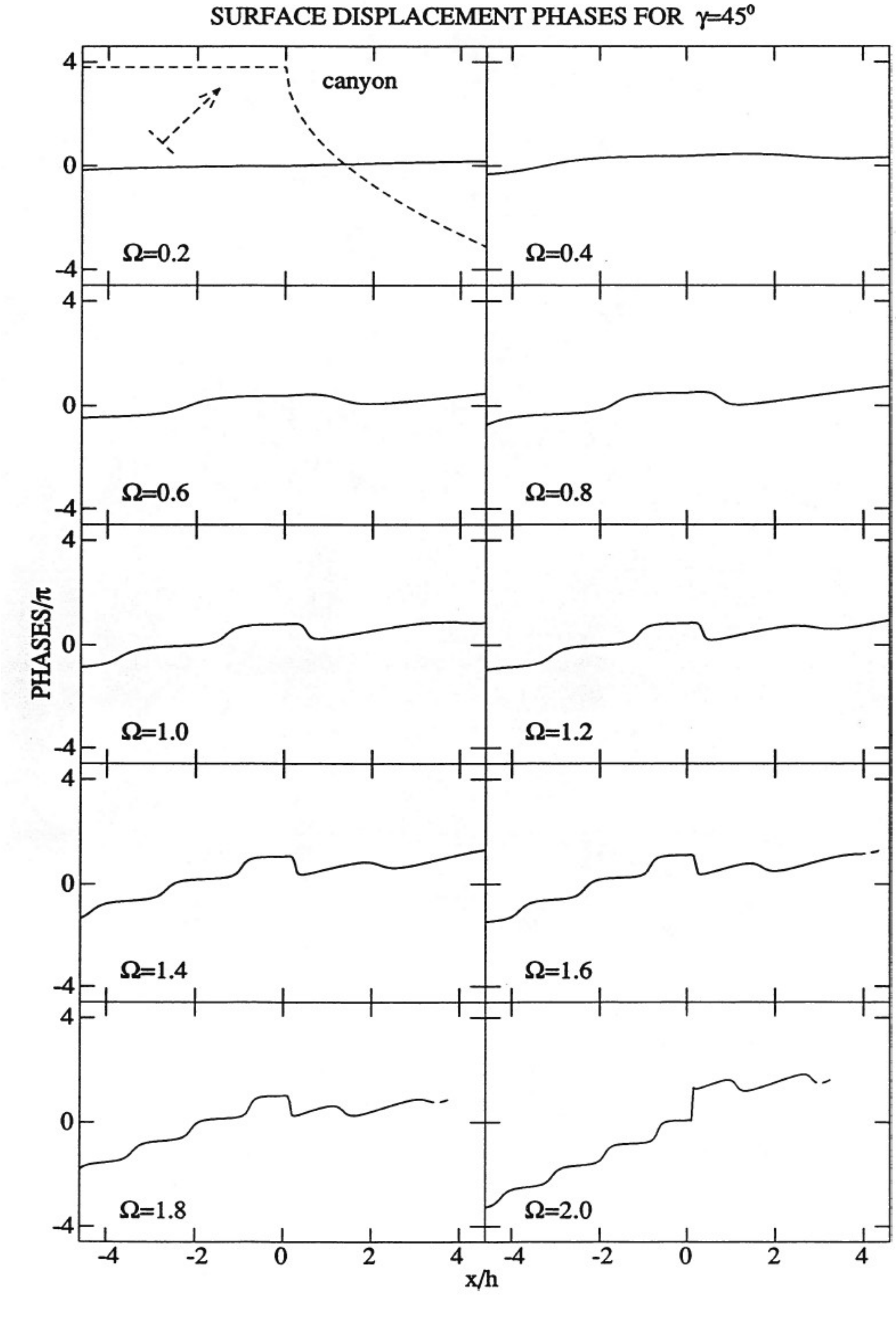

Fig. 1.5 Surface Displacement Phases for $\gamma = 45^\circ$, Plotted vs. the Dimensionless Distance x/h in (-4, 4), and Dimensionless Frequencies $\Omega(=\omega h/\pi\beta)$

I.3.4 Conclusions – Limitations in Lee (1990)

The model studied although is one of the most straightforward models, can explain several features that are common to many other regular and irregular forms of surface topography. The method of analysis presented above is simple, and demonstrates and confirms once again that topographic irregularity is an important factor which contributes to the overall ground amplification pattern at the given site. Such amplification of surface displacements, however, never exceeds 2. The closest to 2 is near the corner point of the canyon, which acts as the corner point of a quarter-space sufficiently at high frequencies.

The pattern of displacement amplitudes depends to a large extent on the directions and frequencies of the incoming waves. On the surface of the half-space to the left of the canyon, the displacement amplitudes oscillate rapidly between 0 and 4, forming an almost standing-wave pattern at all angles of incidence shown.

Trifunac (1973), in his analysis of the scattering of plane SH-wave by a semi-circular canyon, observed that the amplitudes of the resultant SH-wave at the surface on or near the canyon do not exceed 4. Since the amplitudes of the plane waves on the surface of the half-space in the absence of the canyon would be 2 everywhere (Equation 6), this means that the amplification in the presence of the canyon is no higher than 2. He concluded that other 2-D topographic features with corners no smaller than 90° will also have surface amplification of no more than 2. The present case of a semi-parabolic canyon on an elastic half-space is one such example reinforcing this observation.

However, it is known that the numerical scheme implemented in the calculations in the paper above (Lee, 1990) limits the solutions to

1) Dimensionless frequency $\Omega\left(= {\omega h}/{\pi\beta}\right)$ can be calculated no higher than 2,

2) The upper limit of Ω is much less at angles of incidence of $\gamma \geq 45^{\circ}$, and

3) Convergence of the scattered waves at $\gamma = 60^{\circ}$ is almost impossible beyond the vertex of the canyon.

I.4 Objective

Based on the previous studies of the diffraction of SH wave, this thesis will extend the study to the diffraction of elastic SH wave through two different parabolic geometries. The thesis is divided into two parts. The first part, Chapters I to V, studied the anti-plane displacements, rotations and stress concentration factors around a semi-parabolic canyon. The second part, Chapters VI to VIII, studied the anti-plane displacements, rotations and stress concentration factors around a semi-parabolic hill.

In the following chapters, anti-plane (SH) waves through the semi-parabolic canyon and hill will be presented. This includes:

a) Chapter II – Improved solution of displacement around semi-parabolic canyon at higher frequencies
b) Chapter III – The rotational components of motions: Torsion
c) Chapter IV – The rocking components of motions
d) Chapter V – The Dynamic shear stress concentration factors
e) Chapter VI – Diffraction of anti-plane SH waves by a semi-parabolic hill
f) Chapter VII – The rotational components of SH waves around a semi-parabolic hill
g) Chapter VIII – The shear stress components of SH waves around a semi-parabolic hill
h) Conclusions

all to be presented in the subsequent chapters.

I.5 Summary

In Chapter I here, it was found that much of the research work on the diffraction of elastic waves by surface and subsurface topographies were conducted on finite topographies, and hardly any work existed for semi-infinite topographies. This thesis extends the work on finite topographies to a case of semi-infinite topographies, namely, a semi-parabolic canyon and a semi-parabolic hill.

Chapter II. Improved Solution of Displacement around Semi-Parabolic Canyon at Higher Frequencies

II.1 Introduction

It has been long that engineers try to find models and equations that can accurately present the numerical solution for parabolic coordinate. Due to computation limitation on boundary condition determination and ability with numerical calculation engineers were only able to define numerical solution for surface displacement with low frequency. As technology improves and more resources available, it is now possible for engineers to improve the models created and obtain more accurate results numerically. This chapter will expand the results of Lee (1990) on anti-plane displacements in half-space near the parabolic canyon developed in Chapter I, the equations defined to solve wave function numerically for semi-parabolic cylindrical canyon in an elastic half-space, to obtain the surface displacement with dimensionless frequency up to $\Omega = 10$ with angles of incidence $\gamma = 0^{\circ}, 15^{\circ}$ and 30° (and up to $\Omega = 6$ with angles of incidence $\gamma = 45^{\circ}$ and 60°). There will also be discussion on the three-dimensional (3D) plots for the first time.

Based on the first chapter, the resultant wave was determined as

$$W = W^{ff} + W^{s} = \\ 2\sec\left(\gamma/2\right)\sum_{n=0}^{\infty}\frac{(-1)^n}{2n!}\tan^{2n}\left(\gamma/2\right)\left[D_{2n}\left(\overline{\lambda}\eta\right) - \frac{D'_{2n}\left(\lambda\eta_1\right)}{D'_{-2n-1}\left(\lambda\eta_1\right)}D_{-2n-1}\left(\lambda\eta\right)\right]D_{2n}\left(\lambda\xi\right) \tag{1}$$

which a_n is the n^th^ coefficient of the free-field waves, defined as

$$a_n = \frac{(-1)^n}{(2n)!}\tan^{2n}\left(\frac{\gamma}{2}\right) \tag{2}$$

which $\bar{\lambda} = \sqrt{2ik}$ and $\lambda = \sqrt{-2ik}$ are the wave numbers of the Weber Function. On the flat space surface to the left of the parabolic canyon where $\xi = 0$, the displacement can be evaluated as

$$\begin{aligned} W &= W^{ff} + W^{s}\Big|_{\xi=0} \\ &= 2e^{ikx\cos\gamma}\cos(ky\sin\gamma)\Big|_{y=0} + W^{s}\Big|_{\xi=0} \\ &= 2e^{ikx\cos\gamma} + 2\sec\left(\gamma/2\right)\sum_{n=0}^{\infty}(-i)\,a_n\,\frac{D'_{2n}(\lambda\eta_1)}{D'_{-2n-1}(\lambda\eta_1)}D_{-2n-1}(\lambda\eta)D_{2n}(0) \end{aligned} \tag{3}$$

where the exponential forms of the free filed waves are used instead of the series, the scattered waves in series stay the same.

On the surface of the parabolic canyon, where $\eta = \eta_1$, the resultant waves, W in Equation (1) takes the form I as

$$W\Big|_{\eta=\eta_1} = 2\sec\left(\gamma/2\right)\sum_{n=0}^{\infty}a_n\left[D_{2n}(\bar{\lambda}\eta_1) - \frac{iD'_{2n}(\bar{\lambda}\eta_1)}{D'_{-2n-1}(\lambda\eta_1)}D_{-2n-1}(\lambda\eta_1)\right]D_{2n}(\lambda\xi) \tag{4a}$$

Or

$$W\Big|_{\eta=\eta_1} = 2\sec\left(\gamma/2\right)\sum_{n=0}^{\infty}a_n\left[\frac{D_{2n}(\bar{\lambda}\eta_1)iD'_{2n}(\bar{\lambda}\eta_1) - iD'_{2n}(\bar{\lambda}\eta_1)D_{-2n-1}(\lambda\eta_1)}{D'_{-2n-1}(\lambda\eta_1)}\right]D_{2n}(\lambda\xi) \tag{4b}$$

The express in the numerator of the fraction in the square-bracket term above can further be simplified. For $f(z), g(z)$ the solution of a linear 2nd order differential equation, the Wronskian, $w(f,g)$ is defined as

$$w(f,g) = f(z)g'(z) - f'(z)g(z) \tag{5}$$

for functions $f(z)$ and $g(z)$. For the Weber Functions in order or n, take

$$z_1 = \bar{\lambda}\eta_1 \tag{6}$$

or

$$-iz_1 = \lambda\eta_1 \tag{7}$$

for

$$\begin{aligned} f(z) &= D_{2n}(z_1) \\ g(z) &= D_{-2n-1}(-iz_1) \end{aligned} \tag{8}$$

Then

$$\begin{aligned} w(f,g) &= w\left[D_{2n}(z_1), D_{-2n-1}(-iz_1)\right] \\ &= D_{2n}(z_1)\frac{d}{dz_1}D_{-2n-1}(-iz_1) - \frac{d}{dz_1}D_{2n}(z_1)D_{-2n-1}(-iz_1) \\ &= (-i)D_{2n}(z_1)D'_{-2n-1}(-iz_1) - D'_{2n}(z_1)D_{-2n-1}(-iz_1) \end{aligned} \tag{9}$$

It is shown that

$$w\left[D_{2n}(z_1), D_{-2n-1}(-iz_1)\right] = ie^{-i\pi\left[\frac{1}{2}\left(2n+\frac{1}{2}\right)+\frac{1}{4}\right]} = (-1)^n \tag{10}$$

By further expanding equation (10), it gives

$$D_{2n}(z_1)D'_{-2n-1}(-iz_1) - iD'_{2n}(z_1)D_{-2n-1}(-iz_1) = i(-1)^n \tag{11}$$

Thus the resultant displacement at $\eta = \eta_0$, the surface of the canyon, takes the form from equation (4b) as:

$$W\big|_{\eta=\eta_1} = 2\sec\left(\gamma/2\right)\sum_{n=0}^{\infty}\frac{ia_n(-1)^n}{D'_{-2n-1}(\lambda\eta_1)}D_{2n}(\lambda\xi) \tag{12}$$

An expression that is much simpler to manage. This expression will now be used to evaluate the displacement at the surface of the canyon. This simple form allows the expression to be evaluated at much higher frequencies for better convergence than what was done previously. Based on the solution, it provides results of following figures presents the anti-plane (SH) diffraction near parabolic canyon surface displacement amplitudes for $\gamma = 0^\circ, 15^\circ$, 30°, 45° and 60°. The equation not only allows results with higher frequency but also allows 3D results.

The resulting motion at every point will be characterized here by the displacement amplitude and phase, $|W|$ and φ. The incident SH-wave is assumed to have unit amplitude, so that the resulting free-filed surface displacement amplitude corresponding to the plane wave (Equation 3), in the absence of the canyon will be 2. The resultant amplitude $|W|$ of the displacement in Equation (12) thus represents the amplification or de-amplification due to the presence of the canyon. Both the amplitude and phase will depend on the angle of incidence of the SH-wave, the frequency ω, shear wave velocity β and the parameter η_0, where $\eta = \eta_0$ defines the surface of the semi-parabolic canyon. These parameters can be combined into one parameter $k\eta_0^2$, given by

$$k\eta_0^2 = \omega\eta_0^2 / \beta = 2\pi \eta_0^2 / \lambda \tag{13}$$

Where k is the wave number and λ is the wavelength of the incident SH-wave. A dimensionless frequency, Ω, can be defined as

$$\Omega = \omega\eta_0^2 / \pi\beta \tag{14}$$

In terms of the focal length of the parabolic canyon, $h\left(= \eta_0^2 / 2\right)$, **Ω** becomes

$$\Omega = 2\omega h / \pi\beta \tag{15}$$

The dimensionless frequency **Ω** can also be expressed in terms of the wavelength of the incident SH-wave:

$$\Omega = 2\eta_0^2 / \lambda = 4h / \lambda \tag{16}$$

The choice of **Ω** has been motivated by its physical meaning, as a link between the dimension of the parabolic canyon (focal length), and the frequency and wavelength of the incident SH-wave.

II.2 Horizontal Angle of Incidence $\gamma = 0^{\circ}$

Fig. 2.1 represents the displacement amplitudes $|W|$ plotted versus the dimensionless distance s/h at the dimensionless frequency, Ω=1.0, 2.0 … to 10.0, for the horizontal angle of incidence of $\gamma = 0^{\circ}$. The incident plan SH-wave W^{i} is assumed to have unit amplitude. The displacement amplitudes are calculated at points on the half-space and parabolic surfaces. The dimensionless distance s/h is measured in units of the focal length of the parabolic canyon from the tip (vertex, corner point) of the canyon, where $s/h = 0$. Points on the surface of the half-space to the left of the canyon will have negative units of focal length. Where $s/h = -3$ corresponds to the point on the surface of the half-space surface at distance of 3 focal lengths to the left of the tip of the canyon. Similarly, points on the surface of the canyon are measured as positive distances along the canyon surface in units of focal length from the canon's tip. The shape of the half-space and canyon surface on which the displacements are calculated is outlined as a dotted line on the top-left graph of the figure, with the arrow indicating the corresponding direction of the incident SH wave, W^{i}, which is assumed to be coming from the left-side toward the canyon (from where $s/h < 0$).

For the case of horizontal incidence $\gamma = 0^{\circ}$ here in Fig. 2.1, the incidence wave W^{i}, will depend only on the x-coordinate, of the form

$$W^{i} = \exp(ikx) \tag{17}$$

and the resultant wave $W = W^{ff} + W^{s}$, from Equation (1), will take on only the single term, $n = 0$ since $\tan^{2n}\left(\frac{\gamma}{2}\right)$ in Equation (2) is zero for $n > 0$ (meaning $a_n = 0$ for $n > 0$, and $a_0 = 1$):

$$W = 2\left[D_0\left(\bar{\lambda}\eta\right) - \frac{iD_0'\left(\bar{\lambda}\eta_1\right)}{D_{-1}'\left(\lambda\eta_1\right)} D_{-1}\left(\lambda\eta\right)\right] D_0\left(\lambda\xi\right) \tag{18}$$

It is seem form this equation that at the surface of the parabolic canyon, when $\eta = \eta_1$

$$W\Big|_{\substack{\gamma=0 \\ \eta=\eta_1}} = 2\left[D_0\left(\bar{\lambda}\eta_1\right) - \frac{iD_0'\left(\bar{\lambda}\eta_1\right)}{D_{-1}'\left(\lambda\eta_1\right)} D_{-1}\left(\lambda\eta_1\right)\right] D_0\left(\lambda\xi\right) = \frac{2i}{D_{-1}'\left(\lambda\eta_1\right)} D_0\left(\lambda\xi\right) \tag{19}$$

Using the Wronskian relation of Equation (10) which is exactly as the $n = 0$ term in Equation (12). At the half-space surface, when $\xi = 0$, $D_0(0) = 1$, so the displacement is

$$W\Big|_{\gamma=0} = 2\left[D_0\left(\bar{\lambda}\eta\right) - \frac{iD_0'\left(\bar{\lambda}\eta_1\right)}{D_{-1}'\left(\lambda\eta_1\right)} D_{-1}\left(\lambda\eta\right)\right] \tag{20}$$

Further Equation (19) shows that the displacement amplitude, $|W|$, at the canyon surface is constant:

$$\left|W\right|\Big|_{\substack{\gamma=0 \\ \eta=\eta_1}} = \frac{2}{\left|D_{-1}'\left(\lambda\eta_1\right)\right|}\left|D_0\left(\lambda\xi\right)\right| = \frac{2}{\left|D_{-1}'\left(\lambda\eta_1\right)\right|}\left|e^{-\frac{ik\xi^2}{2}}\right| = \frac{2}{\left|D_{-1}'\left(\lambda\eta_1\right)\right|} \tag{21}$$

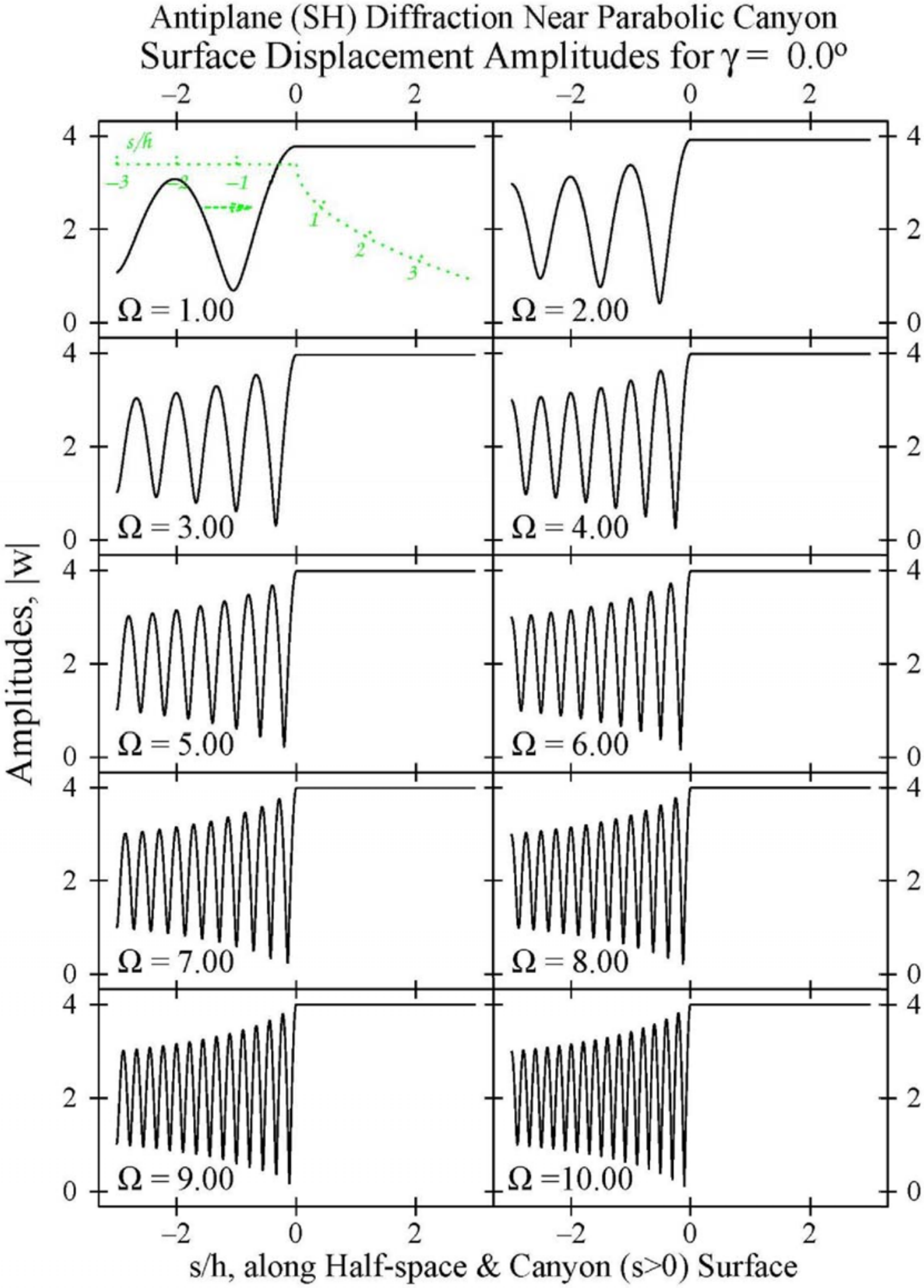

Fig. 2.1 Displacement Amplitudes for Horizontal Incidence, $\gamma = 0^{\circ}$

And the constant approaches four with $|\lambda\eta_1|$ not too small. This is a prominent feature of the displacement amplitudes observed in Fig. 2.1, together with the fact that the constant amplitude at the surface is close to four at all frequencies.

On the half-space surface, with free-field amplitude of two, the free-field plane waves and the scattered and diffracted waves would interfere to produce a standing wave pattern which oscillates around the mean free-field amplitude of two. Thus there are points with amplitudes much above two, there are points with amplitudes much lower than 2, being closest to zero just before the corner point of the parabolic canyon $\left(s/h = 0 \right)$ before the amplitude would jump to the constant amplitude of four along the canyon. A notable feature of the pattern is that at no point along the half-space surface would the amplitude be above four and the amplitude along the canyon surface would also be very close to, but no higher than four. In other words, the highest amplification resulting from diffraction in this model is no more than $\left|\frac{W_{\max}}{W^{ff}}\right| = \left|\frac{4}{2}\right| = 2$. As will be observed for all the angles of incidence in later section, the displacement amplitude at the vertex of the canyon $\left(s/h = 0 \right)$ is always close to four, corresponding to the corner of a quarter spaces.

Such observations of the anti-plane SH standing wave pattern in front of the parabolic canyon is consistent with all previous work of the anti-plane SH diffraction problems from surface topographies. These previous work include the works of Trifunac (1973) on the scattering and diffract semi-circular canyon, Trifunac (1971) on semi-circular alluvial valley, Trifunac (1972) on soil structure interaction by a circular rigid foundation. The same standing wave pattern is observed in front of the circular topographies. This however, is not limited to circular topographies. Wong & Trifunac (1974a, b, and c) observed the same standing wave pattern respectively in front of a semi-elliptical canyon, semi-elliptical alluvial valley and a semi-elliptical rigid foundation. Later, Lee & Cao (1989), Cao & Lee (1989, 1990) and Todorovska &Lee (1991a); demonstrated the same standing wave patterns in front of shallow circular canyons and valley for both in-plane and anti-plane waves. Todorovska & Lee (1990, 1991b) also observed the pattern for shallow canyons and alluvial valleys due to Rayleigh waves. All such observations are consistent with the phenomena that the corner point between the canyon and the half-space surface behaves as a quarter half-space where waves are reflected back into the left side of the half-space and interact with the incoming waves to create a standing wave pattern.

Fig. 2.2 is the same plot of the displacement amplitudes plotted vs. the dimensionless distance s/h horizontal incident and the dimensionless frequency Ω, as on Fig. 2.1 for $\gamma = 0$. Unlike Fig. 2.1, which is two-dimensional, this figure is a three-dimensional (3-D) plot of displacement vs. the distance axis s/h in the range -3 to 3 and the frequency axis Ω in the range 0 to 10. This 3-D plot confirms the standing –wave pattern to the left of the canyon where the incident waves come from and the constant amplitude asymptote to 4 along the canyon surface for and only for the case of horizontal incidence $\gamma = 0$.

Please note that the work of Lee (1990) on the same subject area back then can only calculate the displacement amplitudes up to frequency of $\Omega = 2$. This was due to the problem of convergence. As pointed out in the previous section, the use of the Wronskian relations dramatically simplified the resultant wave Equation (18) and displacement amplitudes can now be computed up to $\Omega = 10$, a significant increase.

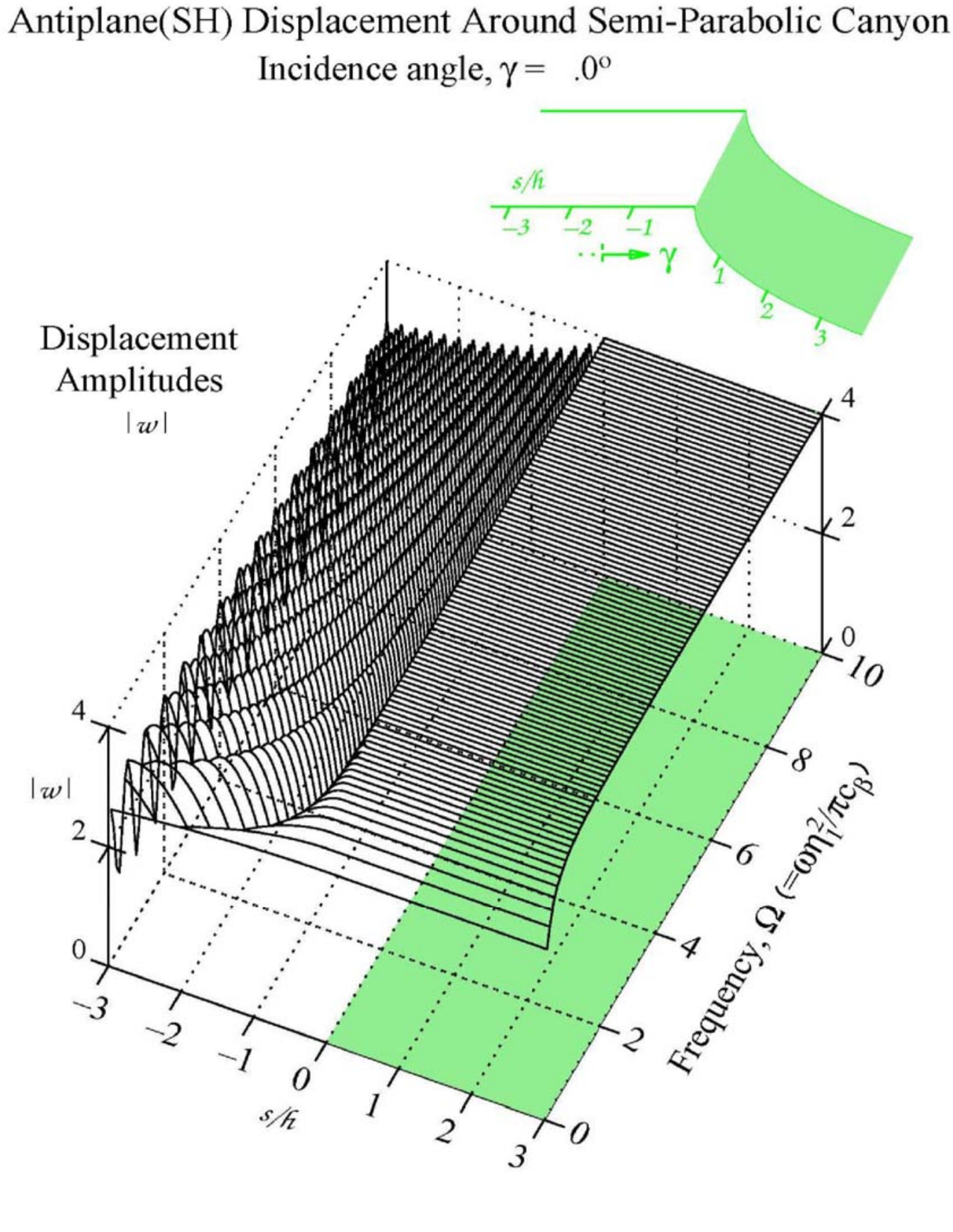

Fig. 2.2 3D Displacement Amplitudes for Horizontal Incidence, $\gamma = 0^{\circ}$

II.3 Oblique Angles of Incidences $\gamma = 15^{\circ}, 30^{\circ}, 45^{\circ}$ and 60°

With the calculations of horizontal incidence $\left(\gamma = 0^{\circ}\right)$ completed and presented, we now turn to the cases of oblique incidences in this section. Fig. 2.3 represents the displacement amplitudes, $\left|W\right|$, plotted vs. the same dimensionless distances s/h for various dimensionless frequencies Ω, for the case of angle of incidence, $\gamma = 15^{\circ}$. All descriptions of the distances and frequencies remain the same as $\gamma = 0^{\circ}$ and will not be repeated here.

The incident plane wave of unit amplitude and oblique incidence $\gamma > 0^{\circ}$ is coming from the left propagate in the positive x and positive y directions (upwards) be reflected from the half-space surface, creating reflected plan waves with the same angle of reflection, propagating in the positive x-direction and positive y-direction (downwards). As given in the previous section, the free-field wave W^{ff} is the input wave, made up of the sum of incident and reflected plan wave (from Equation 1):

$$W = W^{ff} + W^{s} = 2\sec\left(\gamma/2\right)\sum_{n=0}^{\infty} a_n D_{2n}\left(\bar{\lambda}\eta\right) D_{2n}\left(\lambda\xi\right) \tag{22}$$

This is now an infinite sum of parabolic cylinder Weber wave functions of all integer orders, $n = 0,1,2,...$ and the same is true for the scattered waves and resultant waves. Thus, as expected, the displacement amplitudes along the parabolic canyon is not constant any more, unlike the case of horizontal incidence, $\gamma = 0^{\circ}$

The dimensionless frequencies, $\Omega = {\omega\eta_0^2}/{\pi\beta} = {2\eta_0^2}/{\lambda} = {4h}/{\lambda}$ in the ten graphs of Fig. 2.3 are respectively $\Omega = 1, 2, 3, ...,$ up to 10 as before. Recall in Lee (1990), for the same SH waves diffracted from the same parabolic canyon, Fig. 4 of the paper there was also the figure of the displacement amplitudes of incident angle $\gamma = 15^\circ$, but is only plotted up to Ω=2. In that paper the equation for displacement is equation (16) of Lee (1990):

$$W = 2\sec\left(\frac{\gamma}{2}\right)\sum_{n=0}^{\infty}\left[D_{2n}\left(\bar{\lambda}\eta\right) - \frac{iD_{2n}^{'}\left(\bar{\lambda}\eta_1\right)}{D_{-2n-1}^{'}\left(\lambda\eta_1\right)}D_{2n-1}\left(\lambda\eta\right)\right]D_{2n}\left(\lambda\xi\right) \tag{23}$$

From Equation (2)

$$a_n = \frac{(-1)^n}{(2n)!}\tan^{2n}\left(\frac{\gamma}{2}\right) \tag{24}$$

the displacement amplitudes at each incident angles γ were computed using the above equations as presented by Lee (1990). Back then, Lee (1990) pointed out that the Weber Function $D_{2n}(\bullet)$ were computed numerically using the recursive relations in the reverse direction with respect to their orders, algorithm given by Abramowitz & Stegan (1972). With this numerical algorithm, Lee (1990), plotted the displacement amplitudes along ${x}/{h}$ only up to dimensionless frequency $\Omega = {\omega\eta_0^2}/{\pi\beta} = {4h}/{\lambda} = 2$ for angles of incidence of $0^\circ, 15^\circ, 30^\circ$ and 45°, respectively in Figure 3 to 6. It was found that displacement tin the infinite sum of Equation (23) is more difficult and gets harder and harder as the angles of γ increases. It was found that for angle of incidence γ increases. It was found that for angle of incidence $\gamma > 45^\circ$, say at 60°, out at $\left|{x}/{h}\right| > 1$, the convergence of the infinite sum failed even at low frequencies. Hence no such displacement curves for $\gamma > 45^{\circ}$ were presented in Lee (1990).

Over 20+ years later with now the development of high speed PCs and improved numerical algorithms, it is worthwhile to re-examine the convergence of the infinite sum, Equation (23), used in the calculation of the displacements in the vicinity of the parabolic surfaces. In fact, not long after the paper of Lee (1990) was published, the book by Zhang & Jin (1996) titled: *Computation of Special Functions* appeared. It published a set of computer programs (130 in all) for computing special mathematical functions. Among which is the subroutine for computing the parabolic cylinder functions $D_{\upsilon}(z)$ for a sufficient range of order υ and argument z.

The new subroutine from Zhang & Jin (1996) did allow the computation of the displacement amplitudes for horizontal incidence $(\gamma = 0^{\circ})$ to be carried out up to higher dimensionless frequency at $\Omega = {\omega\eta_0^2}/{\pi\beta} = {4h}/{\lambda} = 10$ (and beyond!) as shown in the 10 graphs in Fig. 2.1 above. Recall that the case of horizontal incidence $(\gamma = 0^{\circ})$ involves only the one term $n = 0$, Equation (19), thus there's no convergence problem. The cases of oblique, non-horizontal incidences $(\gamma > 0^{\circ})$ pose a different situation. As Equation (23) shows, the computation of displacement amplitudes for oblique incidence $(\gamma > 0^{\circ})$ involves the summation of an infinite sum. The availability of the new algorithm for calculating the parabolic cylinder function $D_{\upsilon}\left(z\right)$ for a higher order υ and argument z helps but still does not significantly accelerate the convergence of the infinite sum at frequencies higher than $\Omega > 5$. The acceleration of the convergence of the infinite sum of displacement is achieved, as stated in the previous section, by replacing the summation in Equation (23) using the Wronskian relations. This is how the results in Fig. 2.3 are computed, for dimensionless frequencies up to **Ω**=10.

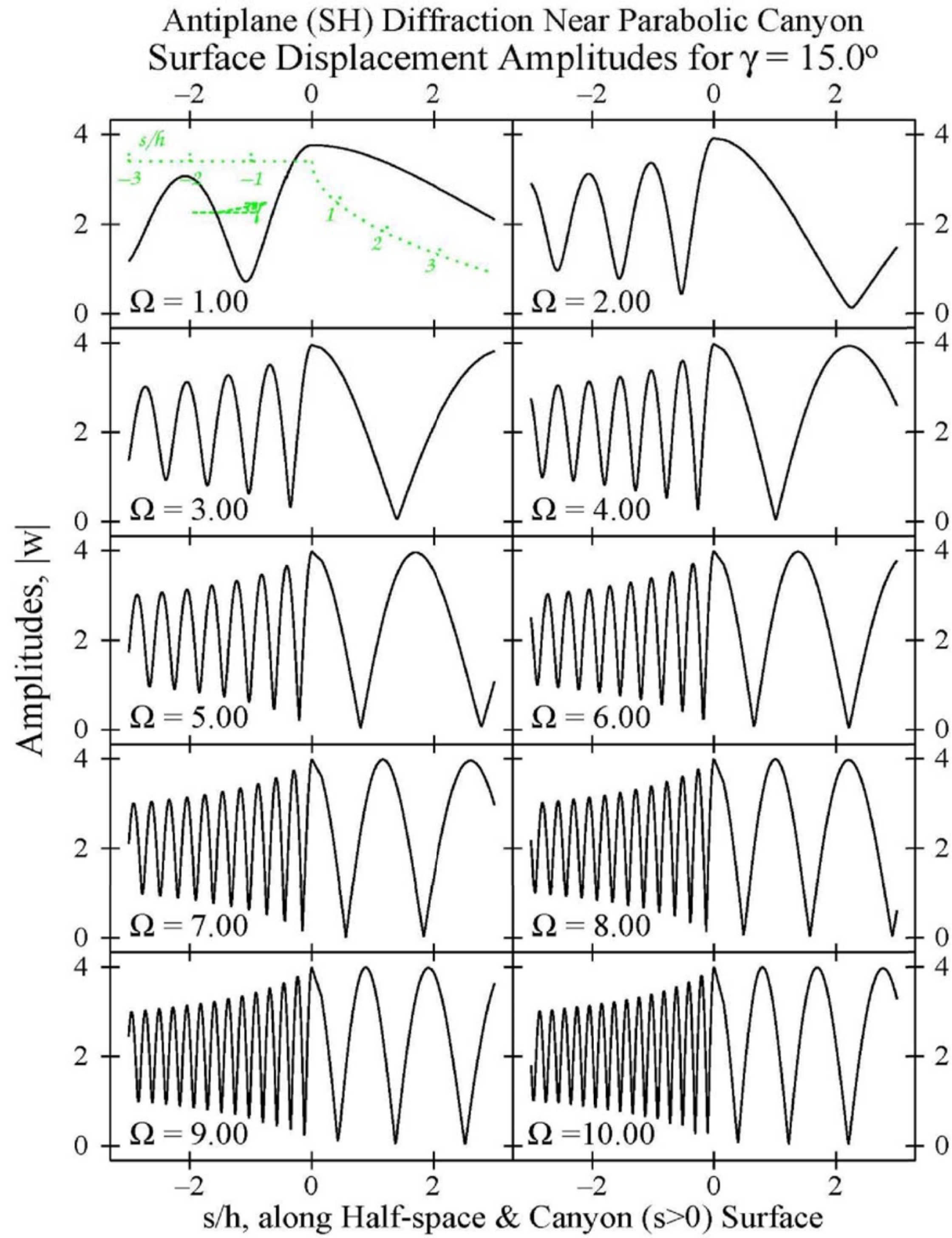

Fig. 2.3 Displacement Amplitudes for Oblique Incidence, $\gamma = 15^{\circ}$

The displacement amplitudes in Fig. 2.3 for $\gamma = 15^{\circ}$ show the same interesting features of the model as for the case of $\gamma = 0^{\circ}$ in Fig. 2.1. The main difference between the two figures being that for case of incident angle $\gamma = 15^{\circ}$, the displacement amplitudes at the surface of the parabolic canon are no longer constant close to four. Instead, they behave again as standing waves that vary in amplitudes consistently between zero and four. This is because every point of the canyon surface is in front, facing the incidence waves, thus resulting also in standing wave patterns. The displacement amplitudes on the half-space surface to the left and in front of the canyon, on the other hand, are just like that of $\gamma = 0^{\circ}$, in Fig. 2.1, being highly oscillatory, starting out to be of amplitude four at the vertex of the canyon $\left({}^{s}\!/\!{}_{h} = 0 \right)$, and the oscillatory amplitudes fall off from four gradually to an amplitude of two at the field far from the canyon.

Fig. 2.4 represents the displacement amplitudes $|W|$ plotted versus the same dimensionless distances ${}^{s}\!/\!{}_{h}$ for dimensionless frequencies of up to $\Omega = 10$, now for the case of angle of incidence $\gamma = 30^{\circ}$. All descriptions of the distances and frequencies remain the same as $\gamma = 0^{\circ}$ (Fig. 2.1) and $\gamma = 15^{\circ}$ (Fig. 2.3)

As pointed out earlier, as the angles of incidence γ increases from 0° to 30°, the input coefficients of the free-field waves (Equation (24)), $a_n = \dfrac{(-1)^n}{(2n)!} \tan^{2n}\left(\dfrac{\gamma}{2}\right)$, together with the large Weber Function terms, $D_{2n}\left(\overline{\lambda}\eta\right)D_{2n}\left(\lambda\xi\right)$ and $D_{-2n-1}\left(\lambda\eta\right)D_{2n}\left(\lambda\xi\right)$ terms of the free-filed and scattered waves, converge slower and slower.

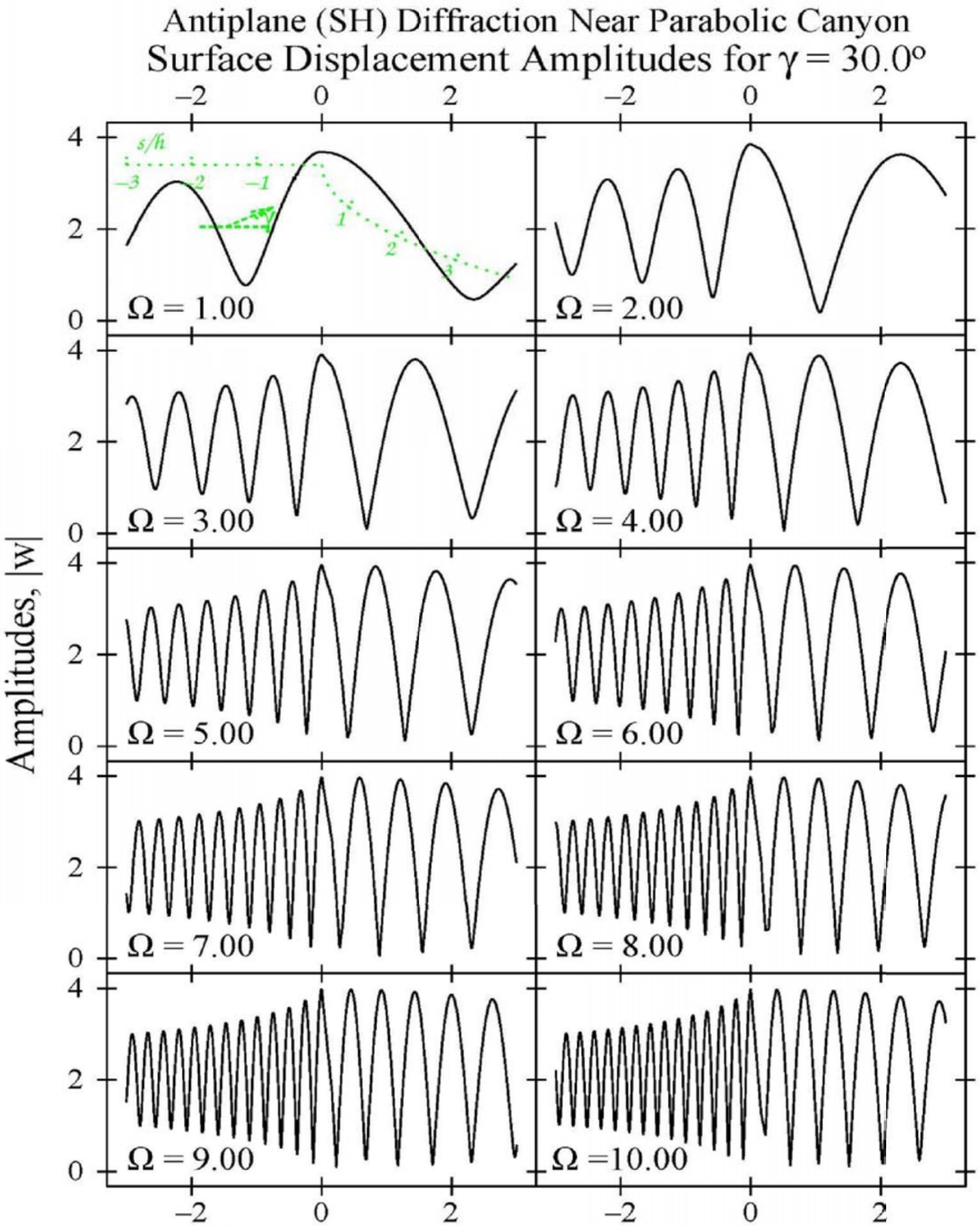

Fig.2.4 Displacement Amplitudes for Oblique Incidence, $\gamma = 30^{\circ}$

At $\gamma = 30^{\circ}$, the use of the Wronskian terms at $\eta = \eta_1$ still allow us to get good displacement amplitudes up to dimensionless frequency of **Ω**=10 in Fig. 2.4 above.

The displacement amplitudes at $\gamma = 30^{\circ}$, both on the parabolic canyon surface, and the half-space surface to its left, show the same trend as that at $\gamma = 15^{\circ}$. Though it is now more oscillatory even on the canyon surface and is oscillatory between zero and four only close to the vertex; gradually oscillating between zero and less than four as it move away from the vertex to the right.

Fig. 2.5 represents the same displacement amplitude curves $|W|$ for angle of incidence of $\gamma = 45^{\circ}$. As pointed out above, as the incidence angle increases, the free-field waves, W^{ff} in Equation (22), the resultant wave W of Equation (23) and the free-field coefficients, per Equation (24), $a_n = \frac{(-1)^n}{(2n)!}\tan^{2n}\left(\frac{\gamma}{2}\right)$ is getting harder and harder to converge. At $\gamma = 45^{\circ}$, back in Lee (1990), even at frequencies as low as **Ω**=2, the calculations failed to converge at the canyon surface beyond $s/h > 2$. As shown in Figure 6 of Lee (1990). In the present chapter here, as shown in the previous section, using the Wronskian relations, Equation (10), the resultant displacement amplitudes at the canyon surface $\eta = \eta_1$, becomes

$$W = 2\sec\left(\gamma/2\right)\sum_{n=0}^{\infty}\frac{ia_n(-1)^n}{D'_{-2n-1}(\lambda\eta_1)}D_{2n}(\lambda\xi) \qquad \text{Equation (12) of previous section}$$

As a result, we are now able to compute the displacement up to frequencies $\Omega = 10$ along the canyon as for as $s/h = 2$, as shown in Fig. 2.5.

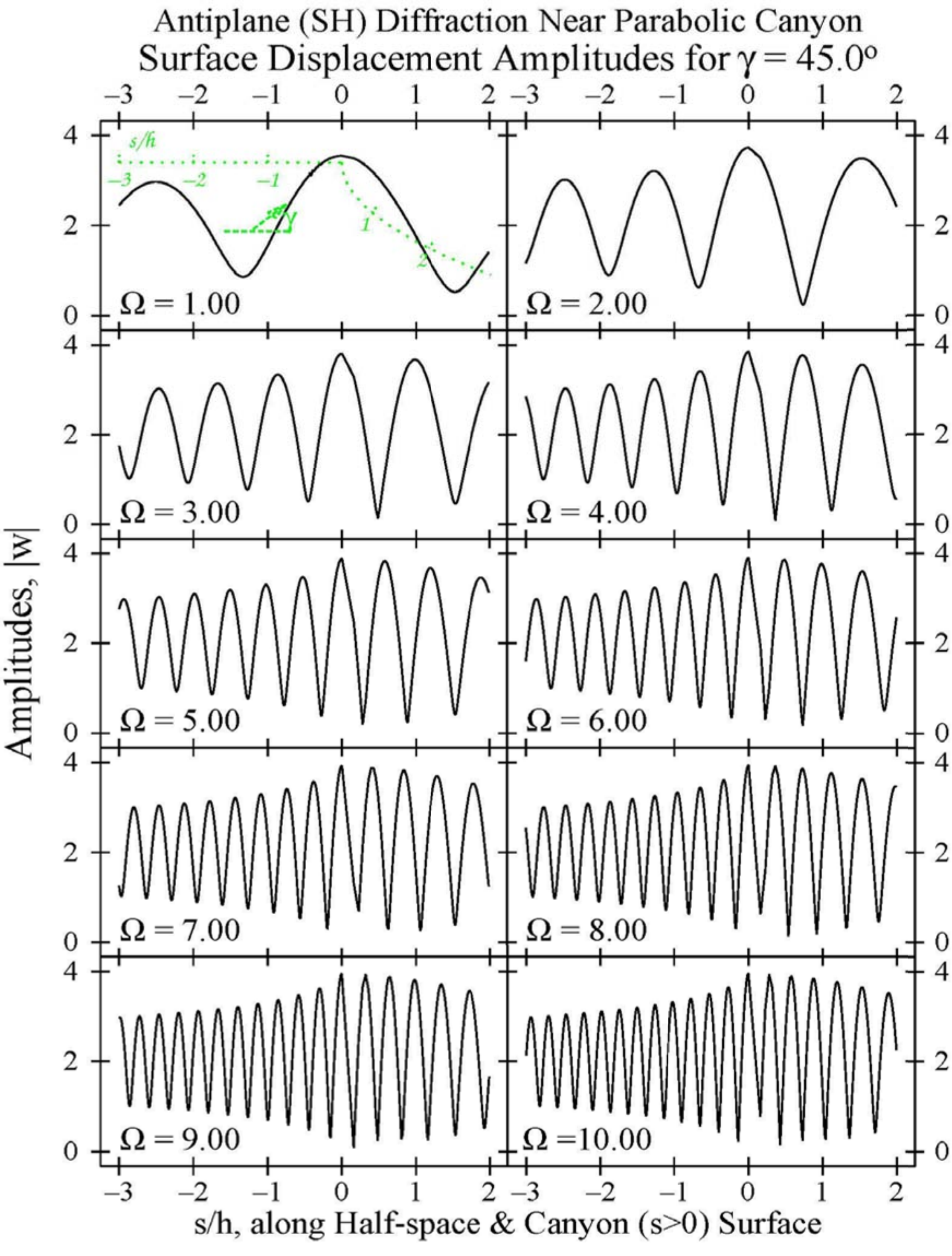

Fig. 2.5 Displacement Amplitudes for Oblique Incidence, $\gamma = 45^{\circ}$

For incidence angle of $\gamma = 60^\circ$, Lee (1990) cannot get any displacement amplitudes computed at any frequencies because the convergence is bad even at low frequencies. With the new numerical implementation using the Wronskian relation as described in the above section, it is now possible to compute and plot the displacement amplitudes for incidence angle of $\gamma = 60^\circ$.

Fig. 2.6 now shows the displacement amplitudes curves, $|W|$, for angle of incidence of $\gamma = 60^\circ$, computed up to dimensionless frequencies of $\Omega = 5$ and beyond, the convergence is already too difficult at the canyon surface at distance of $s/h = 2$ from the vertex. The figure below plotted the displacement amplitudes there as dashed lines showing the part where convergence is difficult and questionable.

Of interest for all the figures is the displacement amplitude at the tip of the canyon $\left(s/h = 0\right)$, for all angles of incidence. An angle of incidence of $\gamma = 0^\circ$ corresponds to horizontal incidence from the left. For plane SH-wave incident upon a quarter-space, the resulting displacement amplification at the corner point is 4, independent of the angles of incidence. Here the corner point at the tip of the semi-parabolic canyon $\left(s/h = 0\right)$ behaves like that of a quarter-space with increasing frequency Ω, so that the displacement amplitudes approach the value of 4 with increasing frequency, as shown by all the figures.

As the angles of incidence increase from 0° to 60°, such trend is still observed in all the figures here.

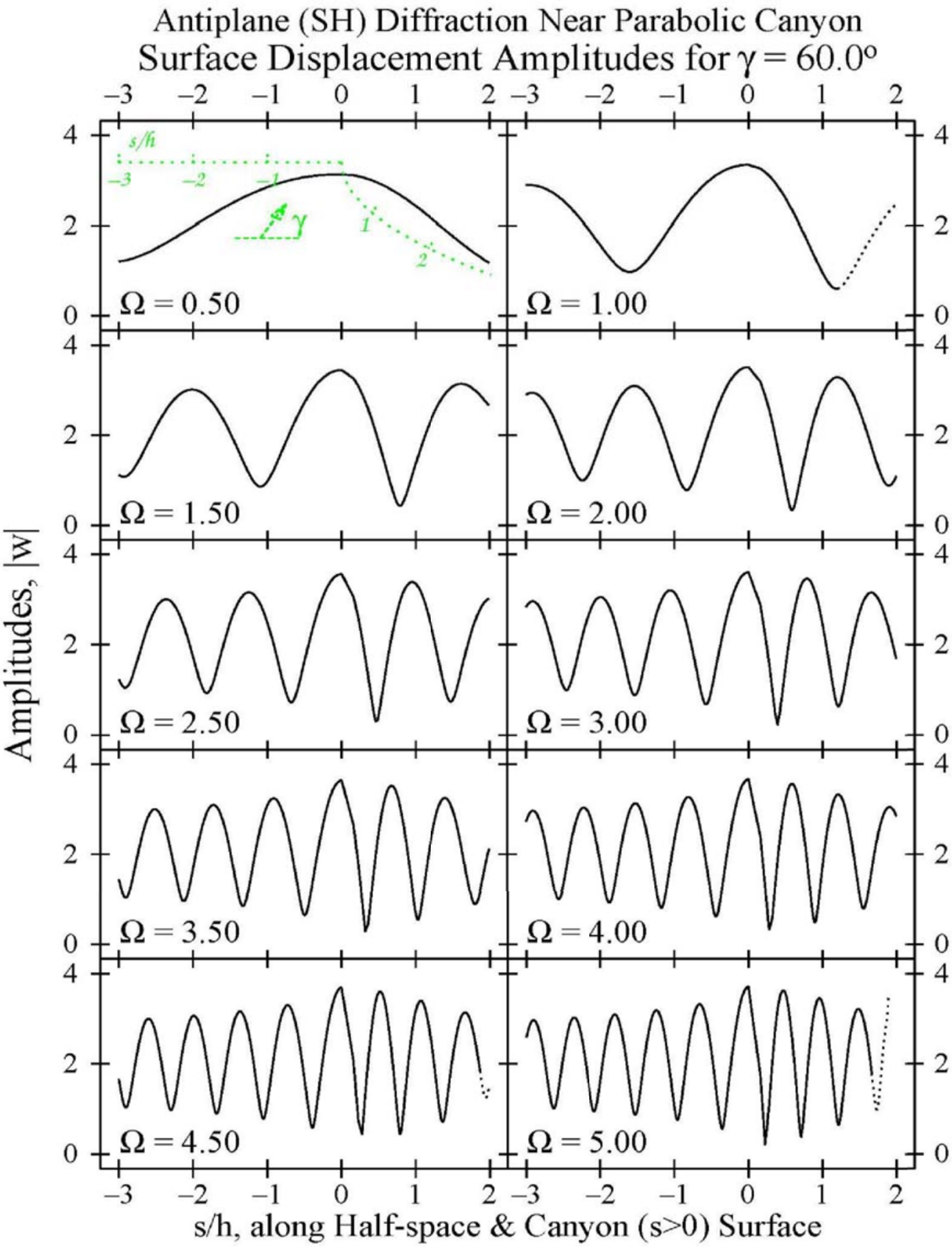

Fig. 2.6 Displacement Amplitudes for Oblique Incidence, $\gamma = 60$

Finally, Fig. 2.7 to Fig. 2.10 are the same plots of the displacement amplitudes plotted vs.

1) the dimensionless distance s/h measured along the half-space and canyon surface, and

2) the dimensionless frequency $\Omega = \omega\eta_0^2/\pi\beta = 2\eta_0^2/\lambda = 4h/\lambda$

as in Fig. 2.3 to 2.6 respectively for incidence angles of $\gamma = 15^\circ, 30^\circ, 45^\circ$ and 60°

Unlike Fig. 2.3 to 2.6, which are two-dimensional, these figures are now three-dimensional (3-D) plots of displacement vs. the distance axis s/h within the range -3 to 3 and the frequency axis Ω in the range from 0 up to 10. This 3-D plots confirm the standing-wave patterns on the half-space surface to the left of the canyon where the incident waves come from for all angles of incidence. Unlike the case of horizontal incidence $\gamma = 0^\circ$, where the constant amplitude asymptote to 4 along the canyon surface was observed from very low frequencies on, the displacement amplitudes along the canyon surfaces are also oscillatory for oblique angles of incidence as observed here.

It is again of interest to note the displacement amplitudes at the vertex $\left(s/h = 0\right)$ at all frequencies for all the figures. It is observed that the amplitude of 4 is achieved for all angles of incidence at very low frequency of $\Omega > 0$ and beyond, this confirms the fact that the vertex of the parabolic canyon behaves as the corner of a quarter spaces in an elastic medium.

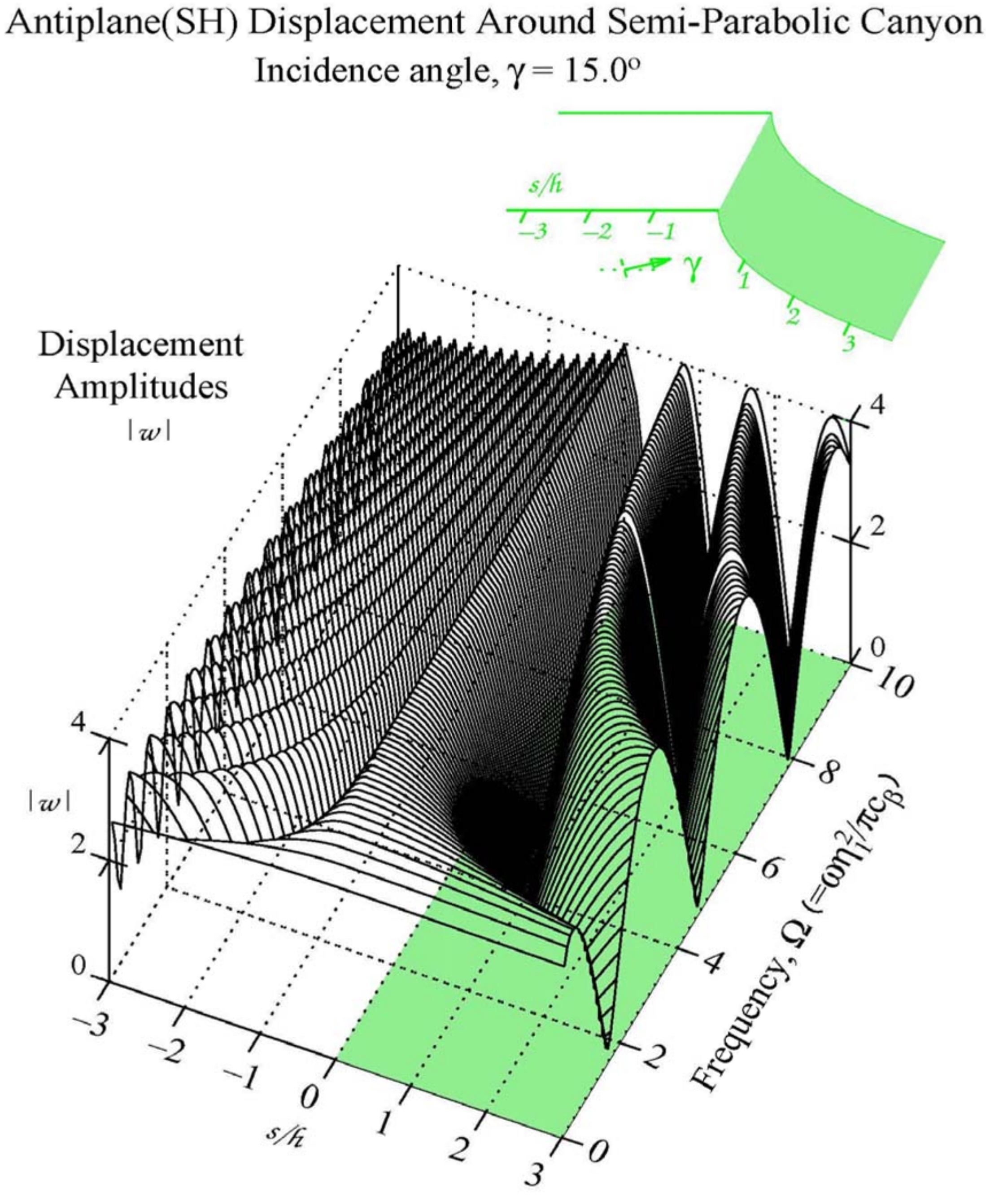

Fig. 2.7 3D Displacement Amplitudes for Oblique Incidence, $\gamma = 15^\circ$

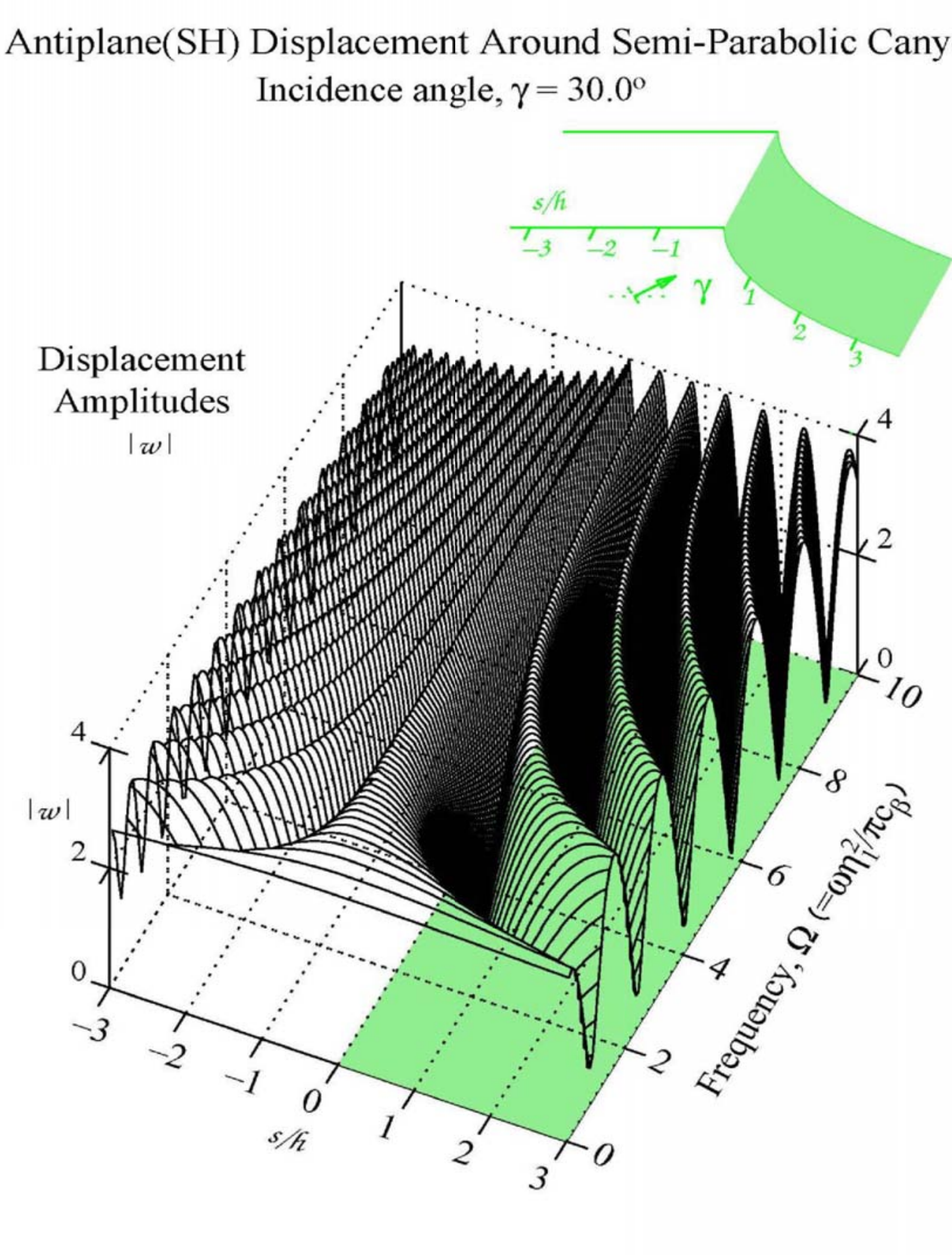

Fig. 2.8 3D Displacement Amplitudes for Oblique Incidence, $\gamma = 30^{\circ}$

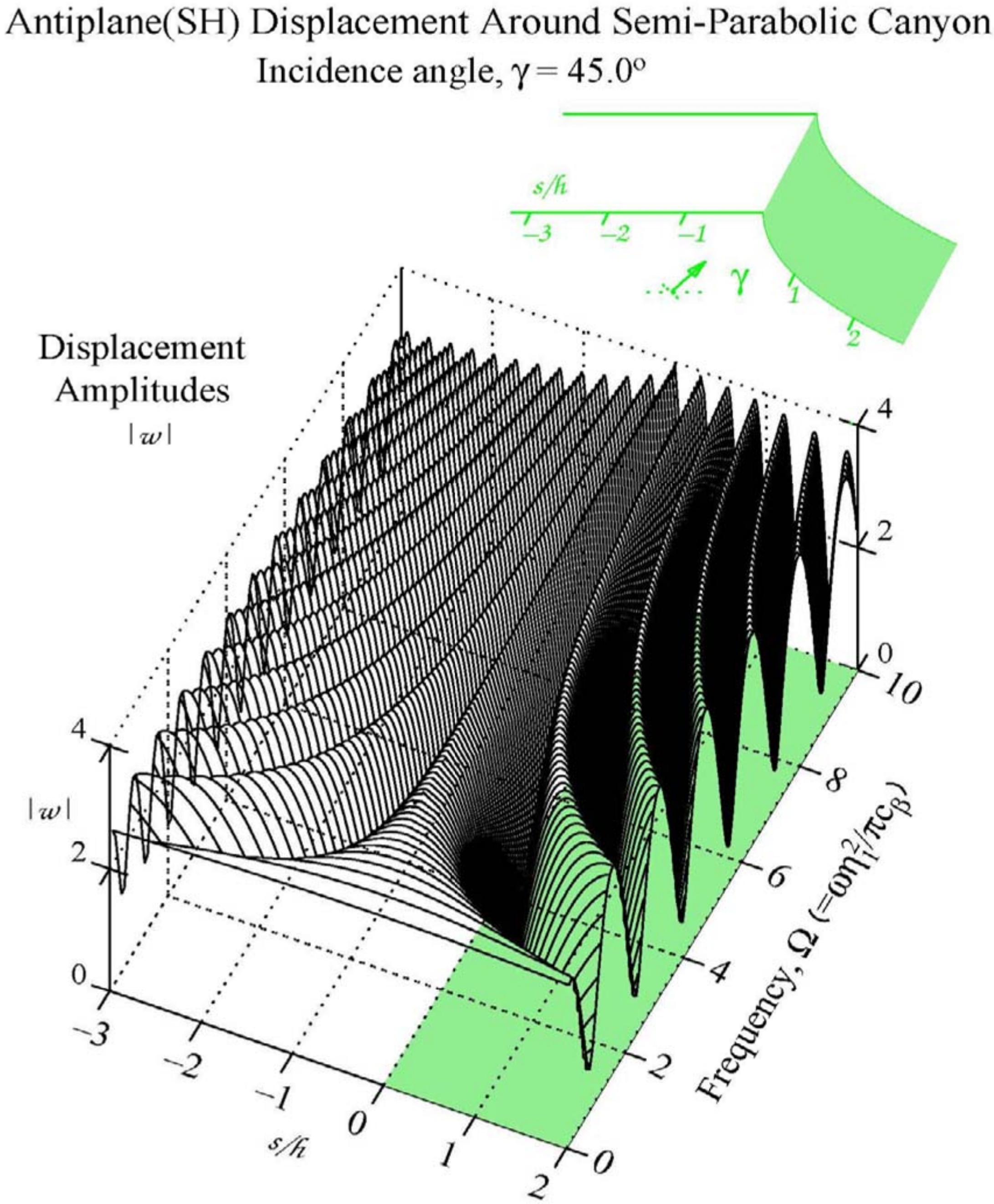

Fig. 2.9 3D Displacement Amplitudes for Oblique Incidence, $\gamma = 45^{\circ}$

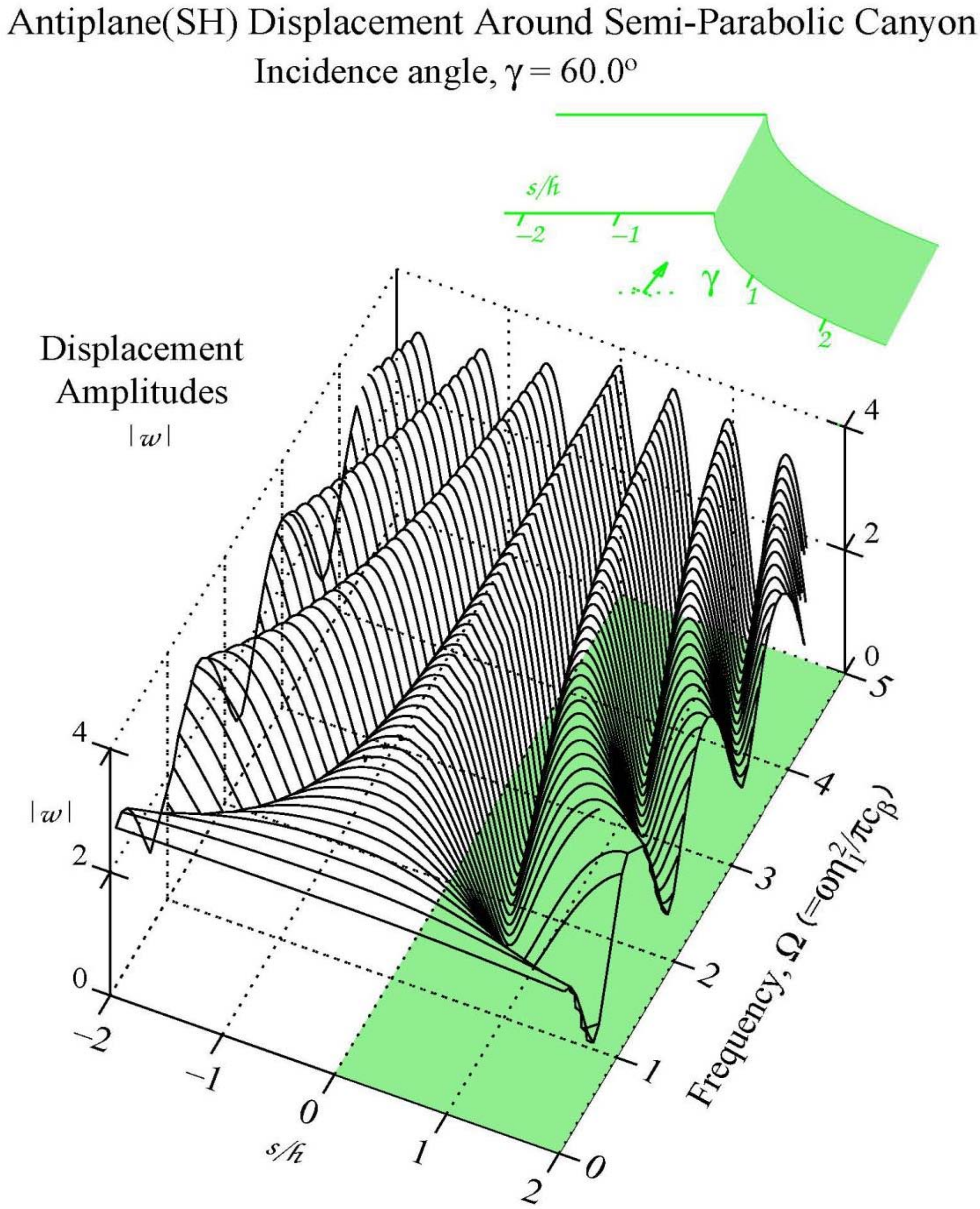

Fig. 2.9 3D Displacement Amplitudes for Oblique Incidence, $\gamma = 60^{\circ}$

II.4 Summary

In Chapter II, the work of Lee (1990) on the anti-plane (SH) wave diffraction around a semi-parabolic canyon in an elastic half-space was extended to higher frequencies, with frequencies to be presented here as high as five times that presented by Lee (1990). This is made possible by the simplification of the terms of the wave functions with the use of the Wronskian relations. In the frequency range and incidence angles presented, amplifications as high as four is observed along the canyon surface.

Chapter III. The Rotational Components of Motions: Torsion

III.1 Introduction – The Rotational Motions

In the last fifty years, the rotational components of motions namely, and in particular, the torsional and rocking components of strong earthquake ground motions, have attracted the attentions of engineer and researchers in the field of earthquake engineers and strong-motion seismology. It is becoming more and more evident that these rotational motions, together with the translational motions may and will contribute significantly to the overall response of structures in the presence of surface and sub-surface civil and geological topographies. In fact such rotational effects of earthquake waves have indeed been observed by many for hundreds of years, take for example, the cases of rotated chimneys, tombstones, statues and monuments relative to their supports. Oldham (1899) had the first documented observation of rotational movement of a large scale structure due to earthquake. The paper described the rotation of George Inglis, a monument built in 1850 at Chatak, India, due to the 1897 Great Shillong Earthquake (W.H.K. Lee, 2009). This monument that the form of an obelisk erected over 20m high from a base 4m wide on each side. During the earthquake, the topmost 2-meter section was broken off and fell to the south, and the next 3-meter section was thrown to the east. The remnant is only about 7m high and is rotated ~15° relative to the base.

Trifunac (2006) outlined the importance of the rotational components of earthquakes in his paper: Effects of Torsional and Rocking Excitations in the Responses of Structures. V. Lee & J. Liang, in their paper, Rotational Components of Strong-Motion Earthquakes, presented at the 14^{th} World Conference on Earthquake Engineering held at Beijing, China on Oct 12-17, 2008, also stressed the importance of these rotational components of waves associated with the dynamic response of elastic and poro-elastic half-space (Lee & Liang, 2008). In their paper, three objectives were stated:

1) To stress the importance of the rotational components of accelerogtrams, and promote the growth and development of strong-motion instruments for recording, together with the translational components, the rotational components of the accelerations of earthquake motions.
2) With the availability of rotational components of acceleration being so limited, we need to develop theories and algorithms for generating rotational motions from the corresponding available translational components of motions at each recording sites.
3) The use existing instrumentation to record, collect and process rotational time histories of acceleration in future seismic events if possible. This can then be used as a set of database to analyze and understand the rotational components of accelerograms, and to check the validity of development theories of generating the rotational components of motions from translations.

W.H.K. Lee et al (2009), in their recent article on Recent Advances in Rotational Seismology stated that

"… Rotational seismology is an emerging field of study concerned with all aspects of rotational motions induced by earthquakes, explosions, and ambient vibrations …"

In fact, the first International Workshop and Conference on Rotational Seismology and Engineering Applications was held in the United States Geological Survey (USGS) office in Menlo Park, California in September 2007. It had many interesting articles on rotational motions in Seismology and appeared as articles of a *Bulletin of the Seismological Society of America Special Issue* on Rotational Seismology and Engineering Applications (Lee, Celebi et al. 2009a, Lee et al, 2009b). W.H.K. Lee (2009) also pointed out that

"… Traditionally, only translational ground motions are observed in seismology. However, we should also measure the three components of rotational motion and the six or more components of strain (Lee, Celebi et al. 2009a)…"

We will indeed study the two components of rotations associated with the anti-plane (SH) wave motions in this and the next chapters (III and IV) and study the two components of shear stress associated with the waves in Chapter V.

With this general introduction on the importance of rotational motions completed, this chapter will continue with the discussion of the torsional component of rotations and next chapter will continue with the discussion of the rocking component of rotations. More citations of articles on both torsion and rocking will be given in this and next chapter to follow. The general rotational motions will first be defined here in the next section.

III.2 The Rotational Components Defined

Start with the general displacement vector, $\widetilde{U}$ of motions, and the rotational vector, $\widetilde{\omega}$, both with thee components,

$$\widetilde{U} = \left(U_x, U_y, U_z\right) = \left(U, V, W\right) \tag{1}$$

$\widetilde{\omega}$ is defined as:

$$\widetilde{\omega} = \tfrac{1}{2}\nabla \times \widetilde{U} = \tfrac{1}{2}\begin{pmatrix} \hat{i} & \hat{j} & \hat{k} \\ \partial/\partial x & \partial/\partial y & \partial/\partial z \\ U & V & W \end{pmatrix} = \tfrac{1}{2}\begin{pmatrix} \partial W/\partial y - \partial V/\partial z \\ \partial U/\partial z - \partial W/\partial x \\ \partial V/\partial x - \partial U/\partial y \end{pmatrix} \tag{2}$$

For the present case of anti-plane (SH) displacement with only the z-component of motions, namely $\widetilde{U} = W\hat{k} = W\left(x, y\right)\hat{k}$, as a function of x and y only, the rotational motion takes the form

$$\widetilde{\omega} = \begin{pmatrix} \omega_x \\ \omega_y \\ 0 \end{pmatrix} = \tfrac{1}{2}\begin{pmatrix} \partial W/\partial y \\ -\partial W/\partial x \\ 0 \end{pmatrix} \tag{3}$$

The rotation motion thus has only two components, the horizontal component, which is

1) The rotation about the vertical y-axis, the torsional motion, given by

$$\omega_y = \omega_{Tor} = -\tfrac{1}{2}\,\partial W/\partial x \tag{4a}$$

and

2) The rotation about the horizontal x-axis, the rocking motion, given by

$$\omega_x = \omega_{Rock} = \tfrac{1}{2}\,\partial W/\partial y \tag{4b}$$

For the incident waves W^i of unit amplitude with incident angle at γ, wave speed c_β and wave number $k = k_\beta = \omega / c_\beta$ given by

$$W^i = \exp^{ik(x\cos\gamma - y\sin\gamma)} \tag{5}$$

Where $|W^i| = 1$, the corresponding rotational vector for the incident wave, $\tilde{\omega}^i$ from Equation (3) is

$$\tilde{\omega}^i = \begin{pmatrix} \omega_x^i \\ \omega_y^i \\ 0 \end{pmatrix} = \tfrac{1}{2} \begin{pmatrix} \partial W^i / \partial y \\ -\partial W^i / \partial x \\ 0 \end{pmatrix} = \left(-\tfrac{1}{2}\right) \begin{pmatrix} ik\sin\lambda \\ ik\cos\gamma \\ 0 \end{pmatrix} W^i \tag{6}$$

So that the amplitude of the rotation vector of the incident wave, $|\tilde{\omega}^i|$ is

$$|\tilde{\omega}^i| = \left(|\omega_x^i|^2 + |\omega_y^i|^2\right)^{1/2} = k/2\,|W^i| = k/2 \tag{7}$$

which will be used as a normalization factor for all rotation components of what follows in this and subsequent chapters.

III.3 The torsional Component of Rotation

Although engineers have been aware of the importance on the rotational components for over hundreds of years, it has been common practice that the rotational components are neglected from studies. Recently more and more papers appeared in the subject of torsional responses, especially on how it is related to structures.

As pointed out, such rotations are often neglected and no instrument is available for measuring them. Lee & Trifunac (1985), using the method of Wong & Trifunac (1978) for generating artificial strong motion accelerogram, generated synthetic torsional accelerograms and their response spectra. They pointed out then that the torsional component of strong-motion is gaining attention as it is becoming evident that it may contribute significantly to the overall response of structures to earthquake motions (Luco, 1976).

K. L. Ryan (2004), in the PhD dissertation titled: Estimating the Seismic Response of Base-Isolated Buildings Including Torsion, Rocking, and Axial-Load Effects, identify that excluding the rotational components effect could understate the peak deformation by up to 50%. Aviles & Suarez (2006) showed the practical significance of torsional motions in their paper, Natural and Accidental Torsion in One-Story Structures on Elastic Foundation under Non-Vertically Incident SH-Waves. Ibsen et al (2006) studied Dynamic Stiffness Due to Torsion, Sliding and Rocking. Schreiber et al (2009) also pointed out that the effects of rotations have been neglected in studies on the seismic properties of civil engineering structures in the past. This was mainly because their influence was thought to be small and there were no suitable sensors available to measure the system response of buildings to rotations properly.

The torsional motion resulting from the anti-plan (SH) wave component of displacement will next be computed. For $W = W(x, y)$ in rectangular coordinators and expressed in parabolic coordinators as $W = W(\eta, \xi)$ given by Equation (1) of section II.1 in the last chapter, this will be given by (Equation (6) of Section III.2):

$$\omega_{Tor} = \omega_y = \tfrac{1}{2}\left(\nabla \times W\hat{k}\right)\cdot\hat{j} = -\tfrac{1}{2}\,\partial W/\partial x = -\tfrac{1}{2}\left(\frac{\partial W}{\partial \eta}\frac{\partial \eta}{\partial x} + \frac{\partial W}{\partial \xi}\frac{\partial \xi}{\partial x}\right) \quad (8)$$

With $\eta, \xi \geq 0$ in the half-space medium,

$$\begin{aligned} \eta &= +\left[\left(x^2 + y^2\right)^{1/2} - x\right]^{1/2} = \sqrt{2r}\cos\left(\theta/2\right) \\ \xi &= +\left[\left(x^2 + y^2\right)^{1/2} + x\right]^{1/2} = \sqrt{2r}\sin\left(\theta/2\right) \end{aligned} \quad (9a)$$

With

$$\begin{aligned} r &= \left(x^2 + y^2\right)^{1/2} = \tfrac{1}{2}\left(\xi^2 + \eta^2\right) \\ x &= \tfrac{1}{2}\left(\xi^2 + \eta^2\right) \\ y &= \xi\eta \end{aligned} \quad (9b)$$

So that

$$\frac{\partial \eta}{\partial x} = \frac{1}{2\left[\left(x^2+y^2\right)^{1/2} - x\right]^{1/2}} \left({}^{1}\!/_{2} \frac{2x}{\left(x^2+y^2\right)^{1/2}} - 1 \right)$$
$$= \frac{1}{2\eta}\left[-\frac{\left(\left(x^2+y^2\right)^{1/2} - x\right)}{\left(x^2+y^2\right)^{1/2}} \right] = \frac{1}{2\eta}\frac{-\eta^2}{r} \tag{10a}$$

or
$$\frac{\partial \eta}{\partial x} = \frac{-\eta}{\xi^2+\eta^2} \tag{10b}$$

By the same method,

$$\frac{\partial \xi}{\partial x} = \frac{1}{2\left[\left(x^2+y^2\right)^{1/2} + x\right]^{1/2}} \left({}^{1}\!/_{2} \frac{2x}{\left(x^2+y^2\right)^{1/2}} + 1 \right)$$
$$= \frac{1}{2\xi}\left[-\frac{\left(x + \left(x^2+y^2\right)^{1/2}\right)}{\left(x^2+y^2\right)^{1/2}} \right] = \frac{1}{2\xi}\frac{\xi^2}{r} \tag{11a}$$

Or
$$\frac{\partial \xi}{\partial x} = \frac{\xi}{\xi^2+\eta^2} \tag{11b}$$

With these expressions, one gets

$$\omega_{Tor} = \left(-{}^{1}\!/_{2}\right)\frac{1}{\left(\xi^2+\eta^2\right)}\left(\xi\frac{\partial W}{\partial \xi} - \eta\frac{\partial W}{\partial \eta}\right) \tag{12}$$

ω_{Tor} will be the torsional motion of the resultant waves everywhere in the half-space.

Consider the input free-filed motion, W^{ff} in both rectangular and parabolic coordinates

$$W^{ff} = 2e^{ikx\cos\gamma}\cos\left(ky\sin\gamma\right) = 2\sec\left(\frac{\gamma}{2}\right)\sum_{n=0}^{\infty} a_n D_{2n}\left(\lambda\xi\right) \tag{13}$$

Equation (13) gives the torsional motion of the free-field waves as

$$\begin{aligned}\omega_{Tor}^{ff} &= -\tfrac{1}{2}\frac{\partial W^{ff}}{\partial x} = \left(-\tfrac{1}{2}\right) ik\cos\gamma\left(2e^{ikx\cos\gamma}\cos\left(ky\sin\gamma\right)\right)\\ \omega_{Tor}^{ff} &= \left(-\tfrac{1}{2}\right)\left(i2k\cos\gamma\right)W^{ff}\end{aligned} \tag{14a}$$

In parabolic coordinates, Equation (12) gives

$$\omega_{Tor}^{ff} = \left(-\tfrac{1}{2}\right)\frac{2\sec\left(\gamma/2\right)}{\left(\xi^2+\eta^2\right)}\sum_{n=0}^{\infty} a_n\left[\lambda\xi D_{2n}\left(\overline{\lambda\eta}\right)D_{2n}^{'}\left(\lambda\xi\right)-\overline{\lambda}\eta D_{2n}^{'}\left(\overline{\lambda}\eta\right)D_{2n}\left(\lambda\xi\right)\right] \tag{14b}$$

Recall the scattered waves from Equation (1) of Chapter II:

$$W^s = 2\sec\left(\gamma/2\right)\sum_{n=0}^{\infty}\left(-i\right)a_n\frac{D_{2n}^{'}\left(\lambda\eta_1\right)}{D_{-2n-1}^{'}\left(\lambda\eta_1\right)}D_{-2n-1}\left(\lambda\eta\right)D_{2n}\left(\lambda\xi\right) \quad \text{from Chap II Eqn (1)}$$

With this, the torsional motion of the scattered waves can similarly be computed as:

$$\begin{aligned}&\omega_{Tor}^{s} = \left(-\tfrac{1}{2}\right)\frac{2\sec\left(\gamma/2\right)}{\left(\xi^2+\eta^2\right)}\times\\ &\sum_{n=0}\frac{\left(-i\right)a_n D_{2n}^{'}\left(\overline{\lambda}\eta_1\right)}{D_{-2n-1}^{'}\left(\lambda\eta_1\right)}\left[\lambda\xi D_{-2n-1}\left(\lambda\eta\right)D_{2n}^{'}\left(\lambda\xi\right)-\lambda\eta D_{-2n-1}^{'}\left(\lambda\eta\right)D_{2n}\left(\lambda\xi\right)\right]\end{aligned} \tag{15}$$

Equations (13), (14) and (15) show that on the half-space surface to the left of the canyon, where $y=0$ (and $\xi=0$), the resultant torsional motion of the waves, $\omega_{Tor} = \omega_{Tor}^{ff}+\omega_{Tor}^{s}\Big|_{\substack{y=0\\(\xi=0)}}$ is given by

$$\omega_{Tor}\Big|_{\substack{y=0\\(\xi=0)}} = \left(-\tfrac{1}{2}\right) i2k\cos\gamma e^{ik\cos\gamma x} + \left(-\tfrac{1}{2}\right)\frac{2\sec\left(\gamma/2\right)}{\left(\xi^2+\eta^2\right)}\times$$
$$\sum_{n=0}^{\infty}\frac{(-i)\,a_n D'_{2n}\left(\bar{\lambda}\eta_1\right)}{D'_{-2n-1}\left(\lambda\eta_1\right)}\left[\lambda\xi D_{-2n-1}(\lambda\eta)D'_{2n}(\lambda\xi)-\lambda\eta D'_{-2n-1}(\lambda\eta)D_{2n}(\lambda\xi)\right]\Big|_{\xi=0} \tag{16a}$$

Or

$$\omega_{Tor}\Big|_{\substack{y=0\\(\xi=0)}} = \left(-\tfrac{1}{2}\right) i2k\cos\gamma e^{ik\cos\gamma x} + \left(-\tfrac{1}{2}\right)\frac{2\sec\left(\gamma/2\right)}{\eta^2}\times$$
$$\sum_{n=0}^{\infty}\frac{(+i)\,a_n D'_{2n}\left(\bar{\lambda}\eta_1\right)}{D'_{-2n-1}\left(\lambda\eta_1\right)}\left[\lambda\eta D'_{-2n-1}(\lambda\eta)D_{2n}(0)\right] \tag{16b}$$

On the surface of the canyon, where $\eta=\eta_1$, Equations (14a, b) and (15) respectively for the free-filed, ω_{Tor}^{ff}, and scattered, ω_{Tor}^{s}, torsional motions, will be used at $\eta=\eta_1$ for $\left(\omega_{Tor}^{ff}+\omega_{Tor}^{s}\right)\Big|_{\eta=\eta_1}$, where

$$\omega_{Tor}^{ff}\Big|_{\eta=\eta_1} = \left(-\tfrac{1}{2}\right)\frac{2\sec\left(\gamma/2\right)}{\left(\xi^2+\eta_1^2\right)}\sum_{n=0}^{\infty}a_n\left[\lambda\xi D_{2n}\left(\bar{\lambda}\eta_1\right)D'_{2n}(\lambda\xi)-\bar{\lambda}\eta D'_{2n}\left(\bar{\lambda}\eta_1\right)D_{2n}(\lambda\xi)\right] \tag{17}$$

$$\omega_{Tor}^{s}\Big|_{\eta=\eta_1} = \left(-\tfrac{1}{2}\right)\frac{2\sec\left(\gamma/2\right)}{\left(\xi^2+\eta_1^2\right)}\times$$
$$\sum_{n=0}^{\infty}\frac{(-i)\,a_n D'_{2n}\left(\bar{\lambda}\eta_1\right)}{D'_{-2n-1}\left(\lambda\eta_1\right)}\left[\lambda\xi D_{-2n-1}\left(\bar{\lambda}\eta_1\right)D'_{2n}(\lambda\xi)-\bar{\lambda}\eta_1 D'_{-2n-1}\left(\bar{\lambda}\eta_1\right)D_{2n}(\lambda\xi)\right] \tag{18}$$

The first term in the sum from both waves in Equation (17) and (18) respectively for the free-field, ω_{Tor}^{ff}, and scattered ω_{Tor}^{s}, torsional motions at $\eta=\eta_1$, can be combined and simplified as:

1^{st} term of $\left(\omega_{Tor}^{ff}+\omega_{Tor}^{s}\right)\Big|_{\eta=\eta_1}=$

$$\left(-\tfrac{1}{2}\right)\frac{2\sec\left(\gamma/2\right)}{\left(\xi^2+\eta^2\right)}\sum_{n=0}^{\infty}a_n\left(\lambda\xi\right)\left[D_{2n}\left(\lambda\eta_1\right)-\frac{(i)D_{2n}^{'}\left(\overline{\lambda}\eta_1\right)}{D_{-2n-1}^{'}\left(\lambda\eta_1\right)}D_{-2n-1}\left(\lambda\eta_1\right)\right]D_{2n}^{'}\left(\lambda\xi\right) \tag{19}$$

The term in the squared bracket is identical to that encountered earlier in Equation (3a) of Section II.1 which is simplified to Equation (6) of Section II.1 of Chapter II

$$\left[D_{2n}\left(\lambda\eta_1\right)-\frac{(i)D_{2n}^{'}\left(\overline{\lambda}\eta_1\right)}{D_{-2n-1}^{'}\left(\lambda\eta_1\right)}D_{-2n-1}^{'}\left(\lambda\eta_1\right)\right]=\frac{i(-1)^n}{D_{-2n-1}^{'}\left(\lambda\eta_1\right)} \qquad \text{Equation (6) of II.1}$$

So that

$$1^{st}\text{ term of }\left(\omega_{Tor}^{ff}+\omega_{Tor}^{s}\right)\Big|_{\eta=\eta_1}=\left(-\tfrac{1}{2}\right)\frac{2\sec\left(\gamma/2\right)}{\left(\xi^2+\eta^2\right)}\sum_{n=0}^{\infty}\left(\lambda\xi\right)\frac{a_n i(-1)^n}{D_{-2n-1}^{'}\left(\lambda\eta_1\right)}D_{2n}^{'}\left(\lambda\xi\right) \tag{20}$$

Similarly, the 2nd term in the two sums in Equations (17) and (18) can be combined as

$$\begin{aligned}&2^{nd}\text{ term of }\left(\omega_{Tor}^{ff}+\omega_{Tor}^{s}\right)\Big|_{\eta=\eta_1}\\&=\left(-\tfrac{1}{2}\right)\frac{2\sec\left(\gamma/2\right)}{\left(\xi^2+\eta^2\right)}\sum_{n=0}^{\infty}a_n\left(\overline{\lambda}-i\lambda\right)\eta_1 D_{2n}^{'}\left(\overline{\lambda}\eta_1\right)D_{2n}\left(\lambda\xi\right)=0\end{aligned} \tag{21}$$

As they cancelled each other out with $\overline{\lambda}=i\lambda$. In other words, on the surface of the canyon, the torsional motions simplified to

$$\omega_{Tor}\Big|_{\eta=\eta_1}=\left(\omega_{Tor}^{ff}+\omega_{Tor}^{s}\right)\Big|_{\eta=\eta_1}=\left(-\tfrac{1}{2}\right)\frac{2\sec\left(\gamma/2\right)}{\left(\xi^2+\eta_1^2\right)}\left(\lambda\xi\right)\sum_{n=0}^{\infty}ia_n\left(-1\right)^n\frac{D_{2n}^{'}\left(\lambda\xi\right)}{D_{-2n-1}^{'}\left(\lambda\eta_1\right)} \tag{22}$$

Equation (22) can also be derived using the fact that the waves are stress-free at the surface of the canyon, namely $\partial W/\partial\eta\Big|_{\eta=\eta_1}=0$, so that

$$\omega_{Tor}\Big|_{\eta=\eta_1} = \left(-\tfrac{1}{2}\right)\frac{1}{\left(\xi^2+\eta_1^2\right)}\left(\xi\frac{\partial W}{\partial \xi} - \eta\frac{\partial W}{\partial \eta}\right)\Bigg|_{\eta=\eta_1} = \left(-\tfrac{1}{2}\right)\frac{1}{\left(\xi^2+\eta_1^2\right)}\xi\frac{\partial W}{\partial \xi}\Bigg|_{\eta=\eta_1} \tag{23}$$

which will also lead to the expression in Equation (22) above.

This completes the derivation of the equations for the torsional component of rotational motions everywhere. In the next section, the amplitudes of the torsional motions, normalized with the rotation vector amplitude of the incident waves, $\left|\widetilde{\omega^i}\right| = k/2$ (Equation 7) will be presented as

$$\overline{\omega}_{Tor} = \omega_{Tor}\Big/\left|\omega^i\right| = 2/k\left|\omega_{Tor}\right| = 2/k\left(\omega_{Tor}^{ff} + \omega_{Tor}^{s}\right) = 2/k\left(-1/2\,\partial W/\partial x\right) = -1/k\,\partial W/\partial x \tag{24}$$

Using Equation (24), the normalized torsional rotation motion amplitude at the half-space and parabolic canyon surface respectively takes the form, from Equations (16b) and (22)

$$\begin{aligned}\overline{\omega}_{Tor}\Big|_{\substack{y=0\\(\xi=0)}} &= -2i\cos\gamma e^{ik\cos\gamma x}\\ &-\frac{2\sec\left(\gamma/2\right)}{k\eta^2}\sum_{n=0}^{\infty}\frac{(+i)a_n D_{2n}'\left(\overline{\lambda}\eta_1\right)}{D_{-2n-1}'\left(\lambda\eta_1\right)}\left[\lambda\eta D_{-2n-1}'\left(\lambda\eta\right)D_{2n}\left(0\right)\right]\end{aligned} \tag{25a}$$

and

$$\overline{\omega}_{Tor}\Big|_{\eta=\eta_1} = -\frac{2\sec\left(\gamma/2\right)}{k\left(\xi^2+\eta_1^2\right)}\left(\lambda\xi\right)\sum_{n=0}^{\infty} i a_n\left(-1\right)^n\frac{D_{2n}'\left(\lambda\xi\right)}{D_{-2n-1}'\left(\lambda\eta_1\right)} \tag{25b}$$

III.4 Torsional Motions: Horizontal Angle of Incidence $\gamma = 0^{\circ}$

Fig. 3.1 represents the normalized torsion amplitudes (Equation 23), $\left|\overline{\omega}_{Tor}\right|$, plotted versus the dimensionless distance s/h at the dimensionless frequency,**Ω**=1.0, 2.0, …, 10.0, for the horizontal angle of incidence o $\gamma = 0^{\circ}$. The incident, plan SH-wave, W^{i}, is assumed to have unit amplitude. As in Fig. 2.1 for displacement amplitudes, the torsion amplitudes are calculated at points on the half—space and parabolic surfaces. The same dimensionless distance s/h, is measured in units of the focal length of the parabolic canyon from the tip (vertex, corner point) of the canyon, where $s/h = 0$. Refer to the description of Fig. 2.1 in the last chapter for details. Here the dashed line in each graph is the (normalized) free-field torsional rotation amplitude, which is two for $\gamma = 0^{\circ}$

The shape of the half-space and canyon surface on which the displacements are calculated is outlined as a dotted line on the tope-left graph of the figure, as in Fig. 2.1, and it is now green. The green arrow again indicates the corresponding direction of the incident SH wave, W^{i} which is assumed to be coming from the left-side towards the canyon.

For the case of horizontal incidence, $\gamma = 0^{\circ}$, here in Fig. 3.1, the incidence wave W^{i} will depend only on the x-coordinate, of the form $W^{i} = \exp^{(ikx)}$, and the resultant wave $W = W^{ff} + W^{s}$, from Equation (1) of Chapter II, will take on only the single term, $n = 0$,

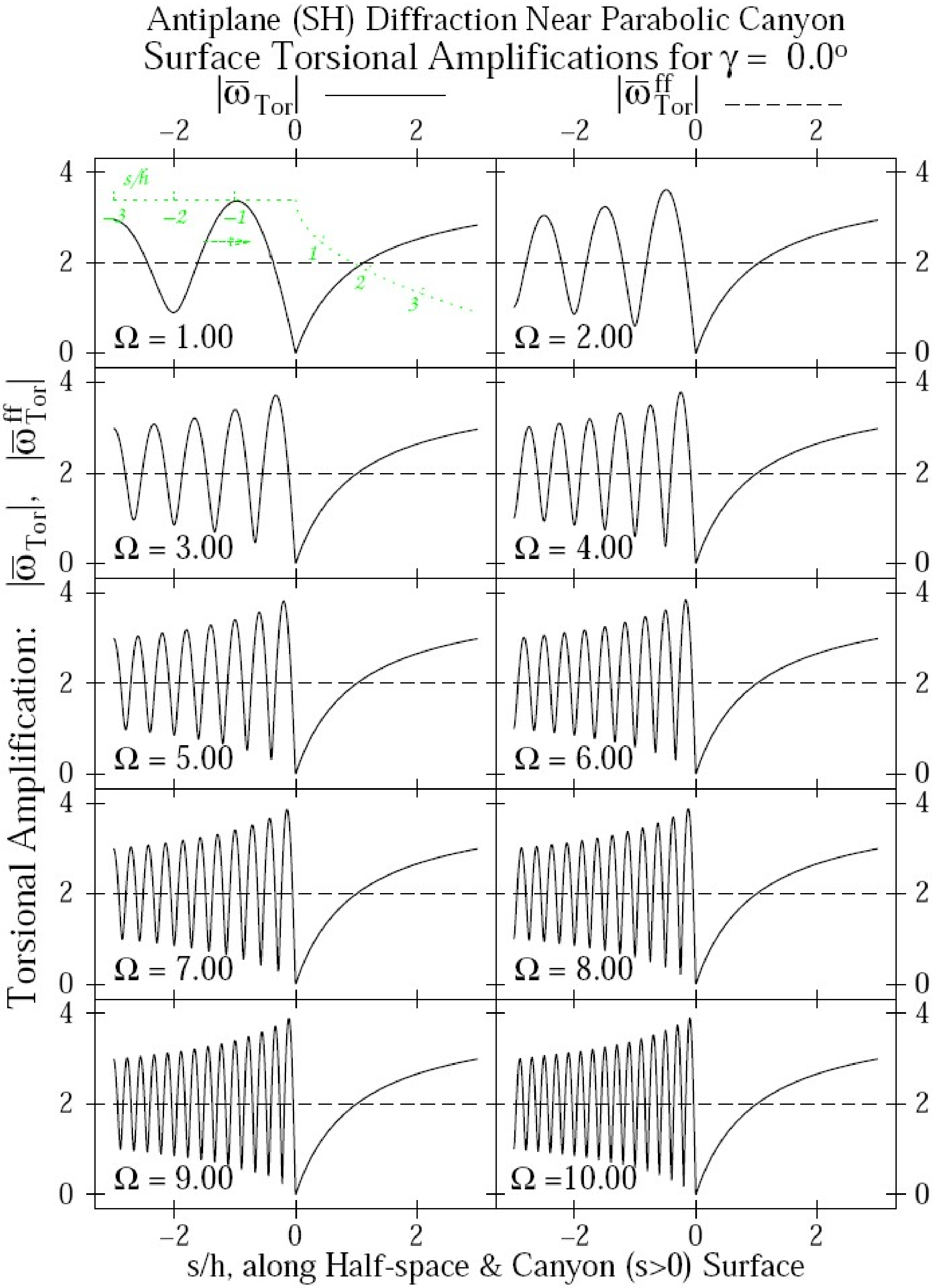

Fig. 3.1 Torsion Amplitudes for Horizontal Incidence, $\gamma = 0^{\circ}$

since $\tan^{2n}\left(\frac{\gamma}{2}\right)$ in Equation (2) of Chapter II is zero for $n>0$ (meaning $a_n = 0$ for $n>0$, and $a_0 = 1$). The 1-term translational displacement W for $\gamma = 0^\circ$ is

$$\begin{aligned} W\Big|_{\substack{\gamma=0\\ \eta=\eta_1}} &= 2\left[D_0\left(\bar{\lambda}\eta_1\right) - \frac{iD_0'\left(\bar{\lambda}\eta_1\right)}{D_{-1}'\left(\lambda\eta_1\right)}D_{-1}\left(\lambda\eta_1\right)\right]D_0\left(\lambda\xi\right) \\ &= \frac{2i}{D_{-1}'\left(\lambda\eta_1\right)}D_0\left(\lambda\xi\right) \end{aligned} \qquad \text{Chap II Eqn (19)}$$

and the corresponding 1-term torsional motion, (using Wronskian) from Equation (22)

$$\omega_{Tor}\Big|_{\substack{y=0\\ \eta=\eta_1}} = \left(\omega_{Tor}^{ff} + \omega_{Tor}^{s}\right)\Big|_{\substack{\gamma=0\\ \eta=\eta_1}} = \left(-1/2\right)\frac{2}{\left(\xi^2+\eta_1^2\right)}\left(\lambda\xi\right)\frac{iD_0'\left(\lambda\xi\right)}{D_{-1}'\left(\lambda\eta_1\right)} \qquad (26a)$$

with the corresponding normalized torsional rotation amplitudes (Equation 25b) as

$$\left|\overline{\omega}_{Tor}\right|_{\substack{\gamma=0\\ \eta=\eta_1}} = \left|\omega_{Tor}/\omega^i\right| = 2/k\left|\omega_{Tor}\right|_{\substack{\gamma=0\\ \eta=\eta_1}} = \left|\frac{2\lambda\xi}{k\left(\xi^2+\eta_1^2\right)D_{-1}'\left(\lambda\eta_1\right)}D_0'\left(\lambda\xi\right)\right| \qquad (26b)$$

using $\left|\varpi_{Tor}\right| = k/2$ as a normalization factor. Further, with $D_0\left(z\right) = e^{-z^2/4}$ and $D_0'\left(z\right) = \left(-z/2\right)e^{-z^2/4}$, Equation (26) for the torsion amplitude at the canyon surface for horizontal incidence, $\gamma = 0^\circ$ simplifies to (with $\lambda = \sqrt{-2ik}, \left|\lambda\right|^2 = 2k$)

$$\left|\overline{\omega}_{Tor}\right|_{\substack{\gamma=0\\ \eta=\eta_1}} = \left|\omega_{Tor}/\omega^i\right| = \frac{2\left|\lambda\right|\xi}{k\left(\xi^2+\eta_1^2\right)D_{-1}'\left(\lambda\eta_1\right)}\left|\left(-z/2\right)e^{-z^2/4}\right|_{z=\lambda\xi} = \frac{2\xi^2}{\left(\xi^2+\eta_1^2\right)\left|D_{-1}'\left(\lambda\eta_1\right)\right|} \qquad (27)$$

So unlike the case of the displacement amplitudes (Equation 21, Chapter II), this is not a constant, but instead, a quotient of quadratic function of ξ^2, being 0 at the vertex $\xi = 0$. Far from there, as ξ increases, the amplitude approached the asymptote

$$\left|\varpi_{Tor}\right|_{\substack{\gamma=0\\ \eta=\eta_1}} \sim \frac{2}{\left|D'_{-1}\left(\lambda\eta_1\right)\right|} \text{ as } \xi \to \infty \tag{28}$$

an asymptote close to 4, as in the case of translation displacement (Equation (21), Chapter II). On the half-space surface, the torsional motion in Fig. 3.1 does resemble that of the translational motion, namely, the free-field torsional motions interfere with the scattered and diffracted torsional motions to result in a standing wave pattern. Comparison of Fig. 3.1 of the torsional motion here with Fig. 2.1 of the translational motions confirms this. Such observation of the standing wave pattern in front of the – parabolic canyon is thus again consistent with all previous work of the anti-plan SH diffraction problems from surface topographies. Recall from Section II.2 of Chapter II where it stated that the previous work of Trifunac (1971, 1972, 1973), Wong & Trifunac (1974a, b, c), Lee & Cao (1989), Cao & Lee (1989, 1990), Todorovska & Lee (1990, 1991a, b) all demonstrated the same standing wave patterns in front of shallow circular canyon. As pointed out, all such observations are consistent with the phenomena that the corner point between the canyon and the half-space surface behave as a quarter half-space where waves are reflected back into the left side of the half-space and interact with the incoming waves to create a standing wave pattern. This section of torsional motions confirms the same phenomena for this component of rotation motions.

Fig. 3.2 is the same 3D plot of the torsional amplitudes plotted vs. the dimensionless distance s/h horizontal incident and the dimensionless frequency **Ω**, as on Fig. 3.1 for $\gamma = 0^{\circ}$. Unlike Fig. 3.1, which is 2D, this figure as in Fig. 2.2 of the translational motions in Chapter II, is a three-dimensional plot of torsional motions vs. the distance axis s/h in the range of -3 to 3 and the frequency axis Ω in the range 0 to 10.

As in the previous chapters, the shape of the half-space and canyon surface model on which the displacements are calculated is outlined on the top-left graph of the figures and it is now in green color. The green arrow is the direction of the incident SH wave, W^i, which is assumed to be coming from the left-side towards the canyon.

This 3-D plot confirms the standing-wave pattern to the left of the canyon where the incident waves come from and the constant amplitude asymptote along the canyon surface for the case of horizontal incidence $(\gamma = 0^\circ)$

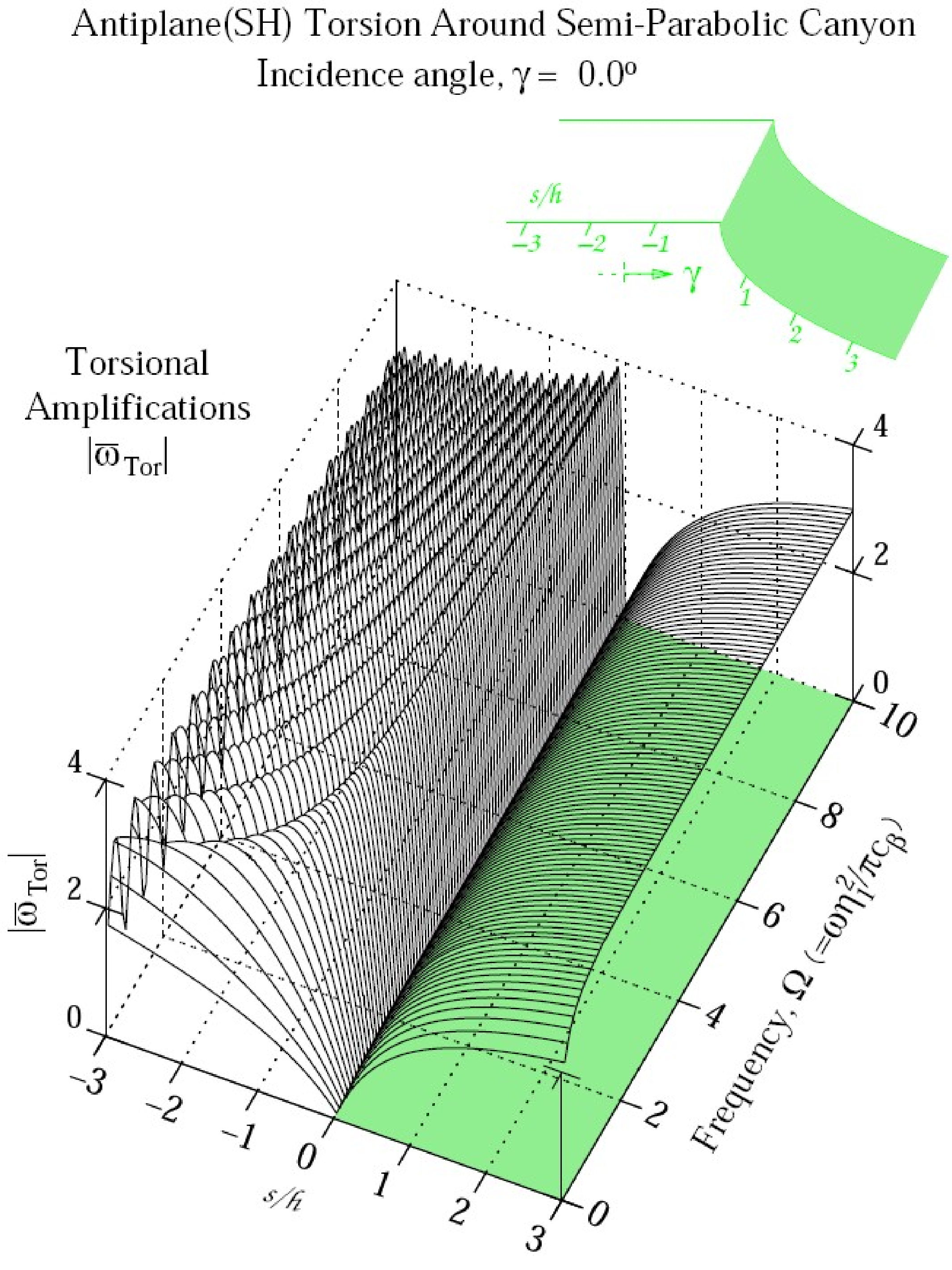

Fig 3.3 3D Torsion Amplitudes for Horizontal incidence, $\gamma = 0^{\circ}$

III.5 Torsional Motions Oblique Angles of Incidences: $\gamma=0^{\circ},15^{\circ},30^{\circ},45^{\circ}$ and 60°

With the presentations of the torsional motions of horizontal incidence $\gamma = 0^{\circ}$ completed, we now turn to the cases of oblique incidences in this section. Fig. 3.3 presents the normalized torsional motion amplitudes, $\left|\varpi_{Tor}\right|$, plotted vs. the same dimensionless distance s/h for various dimensionless frequencies Ω, for the case of angle of incidence, $\gamma = 15^{\circ}$. All descriptions of the dimensionless distances and frequencies remain the same as $\gamma = 0^{\circ}$. The dashed line again is the normalized free-field torsional rotation amplitudes.

With the translational and rotational motions of the free-field and scattered waves now all given by infinite series for oblique incidence $\gamma > 0^{\circ}$, the convergence of the infinite series will be considered in the calculations, as in the cases of the translational motions presented in the last chapter (Chapter II). On the half-space surface $y = 0\left(\xi = 0\right)$, torsional motion ω_{Tor}, and the corresponding normalized motion ϖ_{Tor} are

$$\begin{aligned}\omega_{Tor}\Big|_{\substack{y=0\\(\xi=0)}} &= \left(-\tfrac{1}{2}\right) i2k\cos\gamma e^{ik\cos\gamma x}\\ &+\left(-\tfrac{1}{2}\right)\frac{2\sec\left(\gamma/2\right)}{\eta^2}\sum_{n=0}^{\infty}\frac{(+i)\,a_n D'_{2n}\left(\bar{\lambda}\eta_1\right)}{D'_{-2n-1}\left(\lambda\eta_1\right)}\left[\lambda\eta D'_{-2n-1}\left(\lambda\eta\right)D_{2n}\left(0\right)\right]\end{aligned} \quad \text{(16b) Above}$$

$$\begin{aligned}\varpi_{Tor}\Big|_{y=0} = \left(2/k\right)\omega_{Tor}\Big|_{y=0} &= -i2\cos\gamma e^{ik\cos\gamma x}\\ &-\frac{2\sec\left(\gamma/2\right)}{k\eta^2}\sum_{n=0}^{\infty}\frac{(+i)\,a_n D'_{2n}\left(\bar{\lambda}\eta_1\right)}{D'_{-2n-1}\left(\lambda\eta_1\right)}\left[\lambda\eta D'_{-2n-1}\left(\lambda\eta\right)D_{2n}\left(0\right)\right]\end{aligned} \quad (31)$$

involving both the 1-term free-field and the infinite sum of scattered waves. On the surface of the parabolic canyon, ω_{Tor} and the corresponding normalized motion ϖ_{Tor} are

$$\left(\omega_{Tor}^{ff}+\omega_{Tor}^{s}\right)\Big|_{\eta=\eta_1}=\left(-1/2\right)\frac{2\sec\left(\gamma/2\right)}{\left(\xi^2+\eta_1^2\right)}\left(\lambda\xi\right)\sum_{n=0}^{\infty}ia_n\left(-1\right)^n\frac{D_{2n}^{'}\left(\lambda\xi\right)}{D_{-2n-1}^{'}\left(\lambda\eta_1\right)} \quad (22)\ \text{Above}$$

$$\varpi_{Tor}\Big|_{\eta=\eta_1}=\left(2/k\right)\omega_{Tor}\Big|_{\eta=\eta_1}=\frac{-2\sec\left(\gamma/2\right)}{k\left(\xi^2+\eta_1^2\right)}\left(\lambda\xi\right)\sum_{n=0}^{\infty}ia_n\left(-1\right)^n\frac{D_{2n}^{'}\left(\lambda\xi\right)}{D_{-2n-1}^{'}\left(\lambda\eta_1\right)} \quad (32)$$

which is equal to zero at the vertex of the canyon, where $\xi=0$

The convergence of the infinite sum of the torsional motions in Equation (32) here is again accelerated by the use of the Wronskian relation, as is the case for the translational motions in Chapter II. Recall that Lee (1990) was able to calculate the translational motions of Chapter II only up to the dimensionless frequencies of $\Omega=\omega\eta_0^2/\pi\beta=2\eta_0^2/\lambda=4h/\lambda=2$ and convergence failed beyond **Ω** = 2. The use of the Wronskian relation now enables the calculation of the torsional motions, as in the case of the translational motions, up to **Ω**=10! Here the ten graphs of Fig. 3.3 are again respectively for **Ω** = 1, 2, 3, … up to 10 as before.

The torsion rotational amplitudes in Fig. 3.3 for $\gamma=15^{\circ}$ show the same interesting features of the model as for the case of $\gamma=0^{\circ}$ in Fig. 3.1, namely, the rotational amplitudes on the half-space surface to the left and in front of the canyon, are just like that of $\gamma = 0^\circ$, in Fig.3.1 being highly oscillatory with an amplitude as high as four and averaging to two and converging to an amplitude of two at the field far from the canyon. Further, they both are ZERO at the vertex of the canyon where ${s}/{h} = 0$.

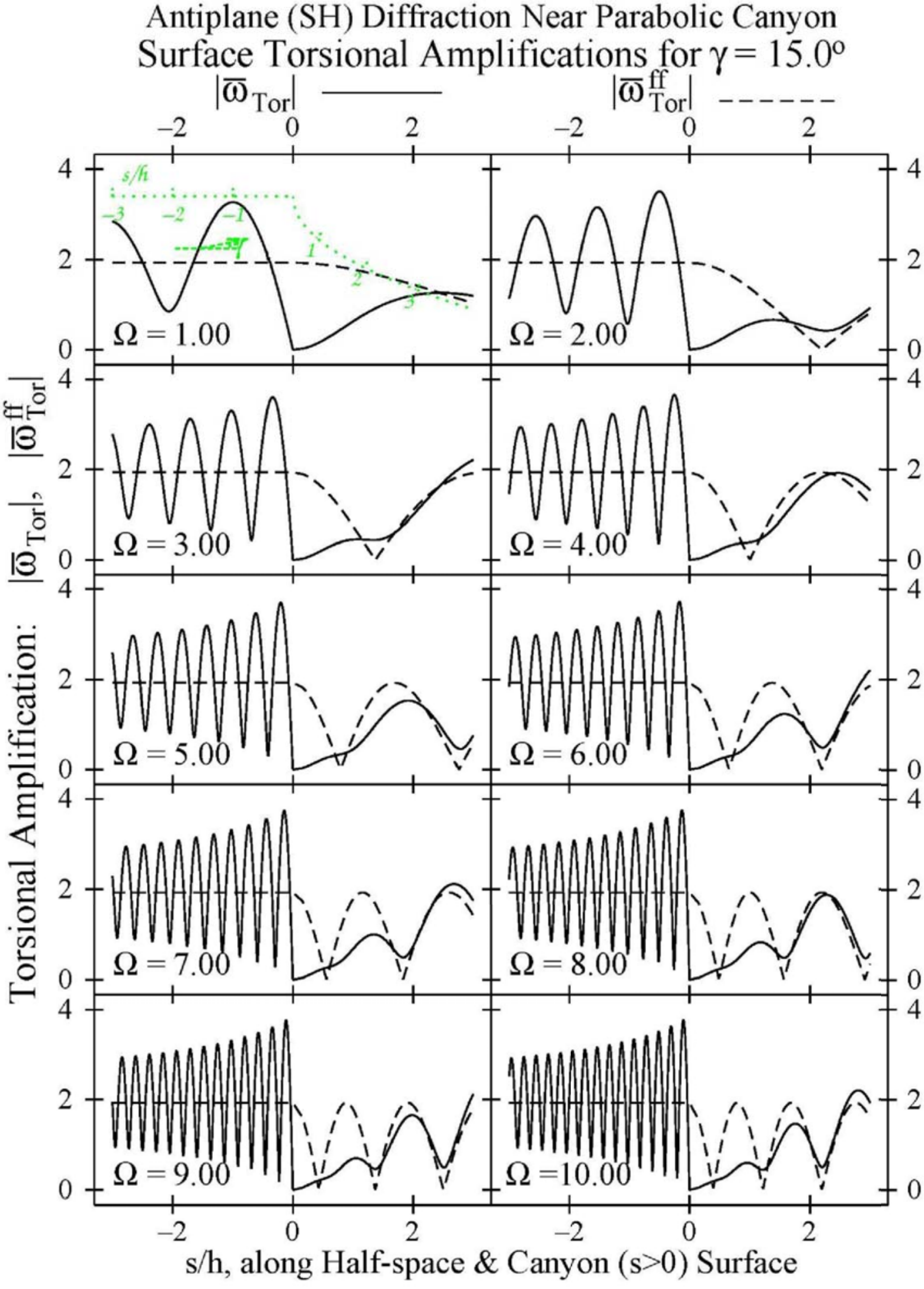

Fig. 3.3 Torsion Amplitudes for Oblique Incidence, $\gamma = 15^{\circ}$

The main difference between the two figures (Fig. 3.1 and Fig. 3.3) being that for the case of incident angle $\gamma = 15^{\circ}$ here, the rotational amplitudes at the surface of the parabolic canyon are no longer approaching an asymptotic constant (as in Fig. 3.1). Instead, they behave again as standing waves that vary in amplitudes consistently between zero and about two. This is because every point of the canyon surface is in front, facing the incidence waves, thus resulting also in standing wave patterns.

Fig. 3.4 represents (normalized) torsional motion amplitudes, $\left|\varpi_{Tor}\right|$, plotted versus the same dimensionless distance s/h for dimensionless frequencies of up to Ω = 10, now for the case of angle of incidence $\gamma = 30^{\circ}$. All descriptions of the distances and frequencies remain the same as $\gamma = 0^{\circ}$ (Fig. 3.1) and $\gamma = 15^{\circ}$ (Fig. 3.3).

As pointed out in the previous Chapter II for translation displacement amplitudes, as the angles of incidence γ increases from 0° to 30°, the input coefficients of the free-field waves (Chapter II Equation (24)), $a_n = \dfrac{(-1)^n}{(2n)!}\tan^{2n}\left(\dfrac{\gamma}{2}\right)$, together with the large Weber function terms, $D_{2n}\left(\bar{\lambda}\eta\right)D_{2n}\left(\lambda\xi\right)$ and $D_{-2n-1}\left(\lambda\eta\right)D_{2n}\left(\lambda\xi\right)$ terms of the free-field and scattered waves, converge slower and slower for the translational displacement amplitudes. The same is true here in Chapter III for the torsional rotation amplitudes. Here at $\gamma = 30^{\circ}$, the use of the Wronskian terms at $\eta = \eta_1$ still allow us to get good torsional rotation amplitudes up to dimensionless frequency of Ω = 10 in Fig. 3.4. This is analogues to the case of displacement amplitudes for $\gamma = 30^{\circ}$, Fig. 2.4 of Chapter II.

The torsional rotation amplitudes at $\gamma = 30^{\circ}$, both on the parabolic canyon surface, and the half-space surface to its left, show the same trend as that at $\gamma = 15^{\circ}$. Though it is now more oscillatory than the case of horizontal incidence, $\gamma = 0^{\circ}$, even on the canyon surface.

Fig. 3.5 represents the (normalized) torsional rotation amplitudes, $\left|\varpi_{Tor}\right|$, now for angle of incidence of $\gamma = 45^{\circ}$. As pointed out above, using the Wronskian relations, the resultant torsional rotation amplitudes at the canyon surface, $\eta = \eta_1$, as giving by Equation (32) above, enables the computation of the displacement up to frequencies as high as Ω = 10 along the canyon, but for only as far as $s/h = 2$, as shown in Fig. 3.5.

This is consistent with the results presented in Chapter II for the corresponding displacement amplitudes. This consistency can be expected, as the displacement and torsional rotation amplitudes are respectively given by:

$$W\Big|_{\eta=\eta_1} = 2\sec\left(\gamma/2\right)\sum_{n=0}^{\infty}\frac{ia_n\left(-1\right)^n}{D'_{-2n-1}\left(\lambda\eta_1\right)}D_{2n}\left(\lambda\xi\right) \qquad \text{Chapter II Eqn (12)}$$

$$\omega_{Tor}\Big|_{\eta=\eta_1} = \left(2/k\right)\omega_{Tor}\Big|_{\eta=\eta_1} = \frac{-2\sec\left(\gamma/2\right)}{k\left(\xi^2+\eta_1^2\right)}\left(\lambda\xi\right)\sum_{n=0}^{\infty}ia_n\left(-1\right)^n\frac{D'_{2n}\left(\lambda\xi\right)}{D'_{-2n-1}\left(\lambda\eta_1\right)} \quad \text{Eqn (32) above}$$

so that the summation above involves the same coefficients, namely $\frac{ia_n\left(-1\right)^n}{D'_{-2n-1}\left(\lambda\eta_1\right)}$, times $D_{2n}\left(\lambda\xi\right)$ for displacement and $D'_{2n}\left(\lambda\xi\right)$ for torsional rotations.

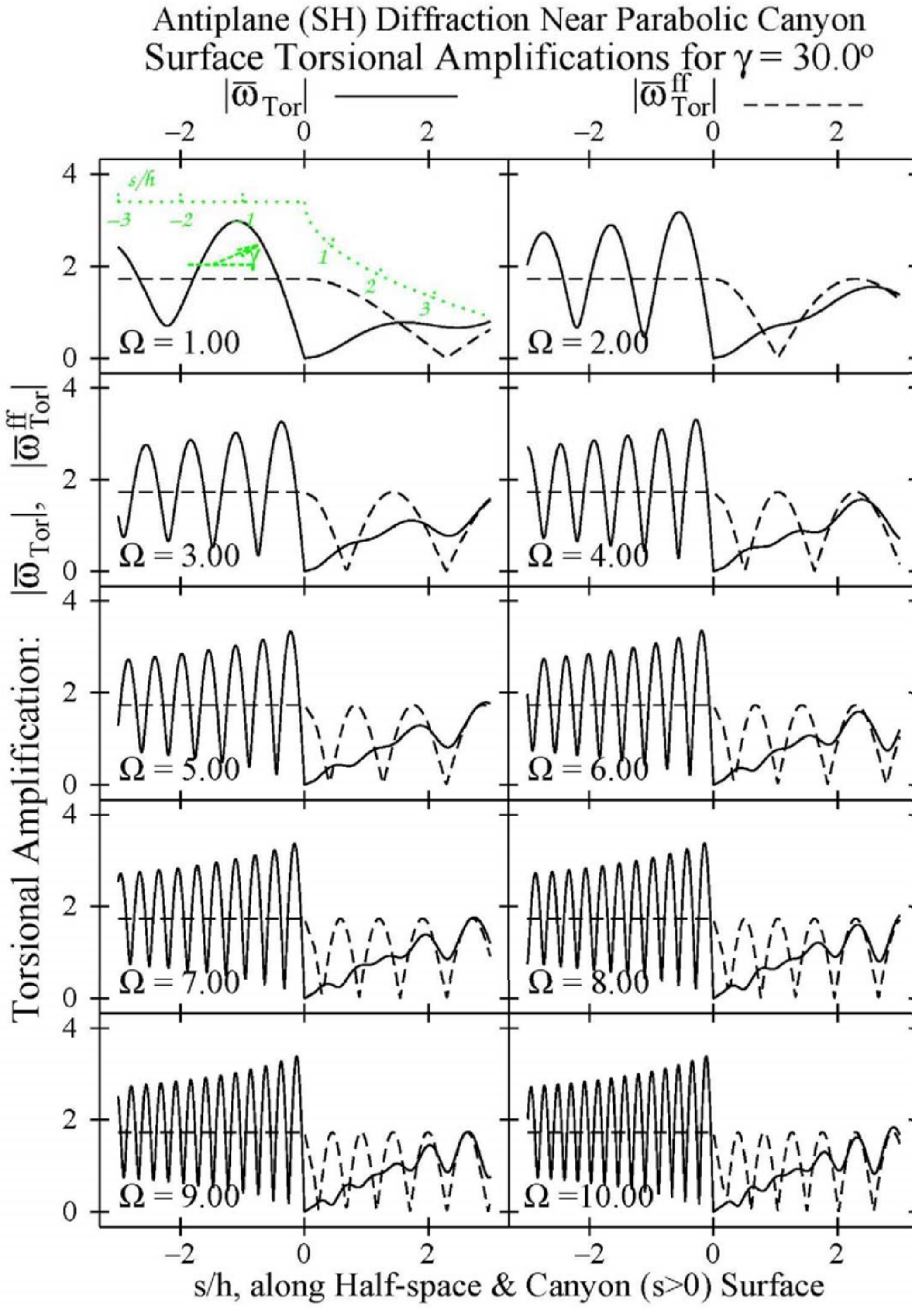

Fig. 3.4 Torsion Amplitudes for Oblique Incidence, $\gamma = 30^{\circ}$

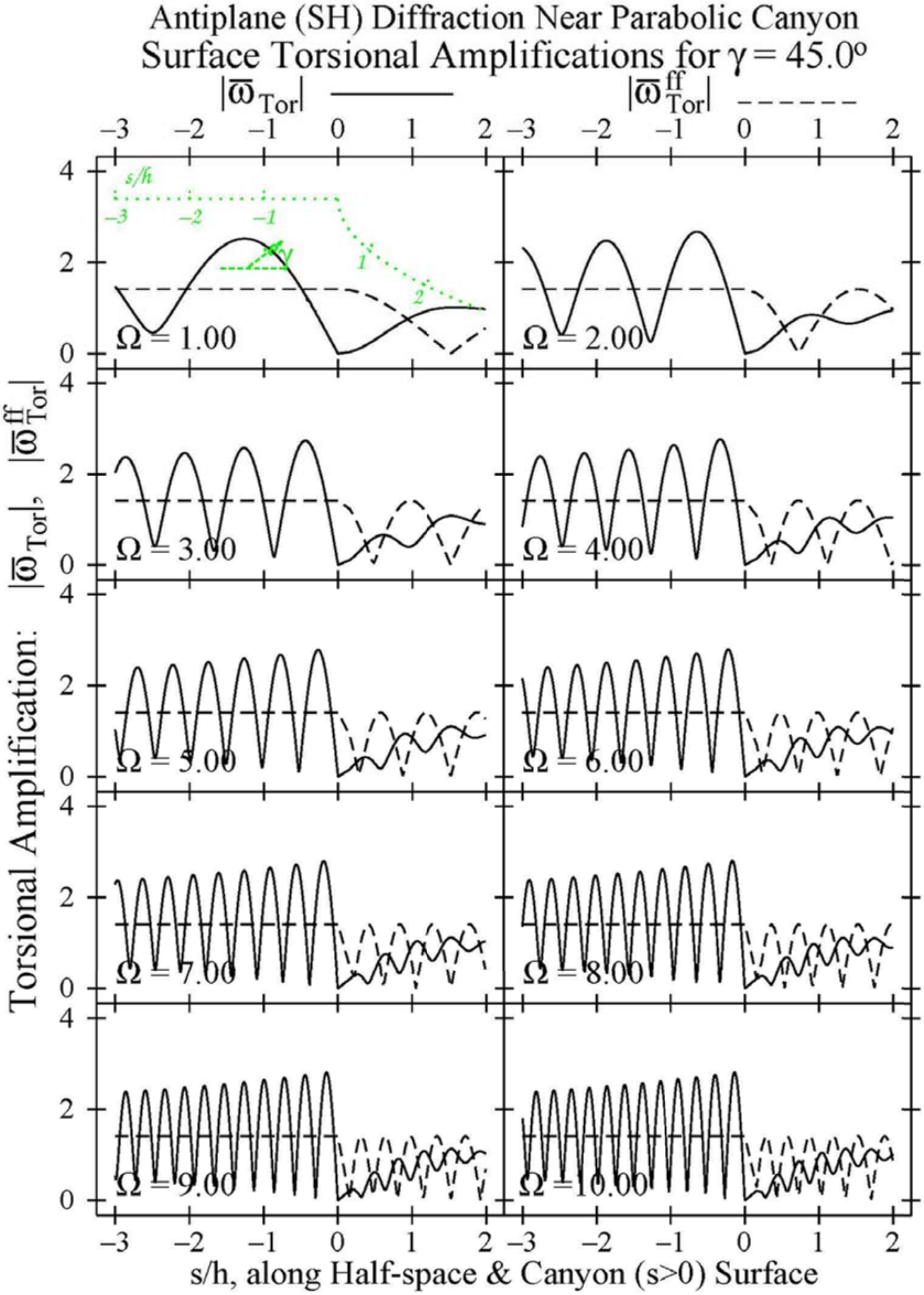

Fig. 3.5 Torsion Amplitudes for Oblique Incidence, $\gamma = 45^{\circ}$

Finally, for incidence angle of $\gamma = 60^{\circ}$, recall that for translational displacements, Lee (1990) cannot get any displacement amplitudes computed at any frequencies because the convergence is bad even at low frequencies. With the new numerical implementation using the Wronskian relation as described in Chapter II previously, it is now possible to compute and plot both the displacement $|W|$ (Chapter II) and torsional rotation amplitudes here for incidence angle of $\gamma = 60^{\circ}$.

Fig. 3.6 now shows the torsion rotation amplitudes curves, $|\varpi_{Tor}|$ for angle of incidence of $\gamma = 60^{\circ}$, computed up to dimensionless frequencies of Ω = 5, a great improvement. It should be pointed that at frequencies around Ω = 5 and beyond, as in the case of translational displacements in Chapter II, the convergence is already difficult at the canyon surface for torsional amplitudes at distance of $s/h = 2$ from the vertex. The figure below plotted the displacement amplitudes there as dotted dashed lines, showing the part where convergence is difficult and questionable.

Of interest for all the figures is the torsional rotation amplitude at the tip (vertex) of the canyon ($s/h = 0$), for all angles of incidence. Namely, it has zero torsion at the corner point, where $\xi = 0$, as indicated by Equation (32) above, due to the presence of the term $(\lambda\xi)$ independent of the angles of incidence. This is a contrast to the translational displacement amplitude of four there at the corner point, corresponding to that of a quarter space.

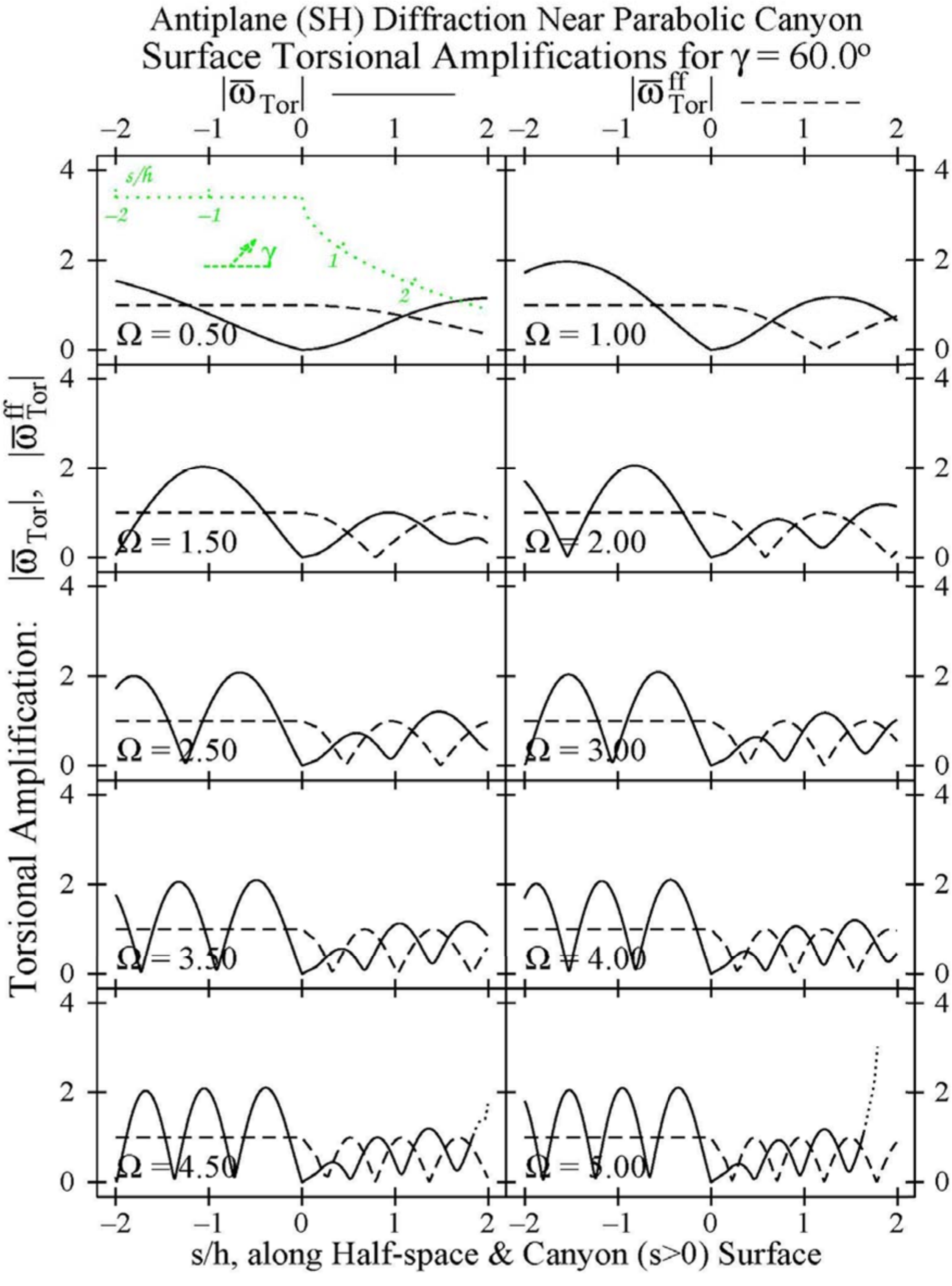

Fig. 3.6 Torsion Amplitudes for Oblique Incidence, $\gamma = 60^{\circ}$

Finally, Fig. 3.7 to Fig. 3.10 are the 3D plots of the torsional rotation amplitudes plotted vs.

1) The dimensionless distance s/h measured along the half-space and canyon surface, and

2) The dimensionless frequency $\Omega = \omega\eta_0^2/\pi\beta = 2\eta_0^2/\lambda = 4h/\lambda = 2$

as the 2D plots in Fig. 3.3 to 3.6 respectively for incidence angles of $\gamma = 15^\circ, 30^\circ, 45^\circ$ and 60°

Unlike Fig. 3.3 to 3.6 which are two-dimensional, these figures are now three-dimensional plots of torsional amplitudes vs. the distance axis s/h within the range -3 to 3 and the frequency axis Ω in the range from 0 up to 10. This 3D plots confirm the standing-wave patterns to the left of the canyon where the incident waves come from for all angles of incidence. Unlike the case of horizontal incidence, $\gamma = 0^\circ$, where the constant amplitude asymptote to 4 along the canyon surface was observed from very low frequencies on (Fig. 3.2), the displacement amplitudes along the canyon surfaces are also oscillatory for oblique angles of incidence as observed here.

It is again of interest to note that the torsional rotation amplitude is zero at the vertex where $\xi = 0$ $\left(s/h = 0\right)$ at all frequencies for all angles of incidence, as seen from the figures. This is as indicated by Equation (32) above, due to the presence of the term

$(\lambda\xi)$. As $\xi \to \infty$ along the surface of the canyon $\eta = \eta_1$, the amplitude approaches (Equation (28)) $\left|\varpi_{Tor}\right|_{\substack{\gamma=0\\ \eta=\eta_1}} \sim \dfrac{2}{\left|D_{-1}^{'}(\lambda\eta_1)\right|}$ as $\xi \to \infty$ an asymptote of 4 (as in Chapter II for translation), but it will be very, very far from the vertex beyond the range plotted.

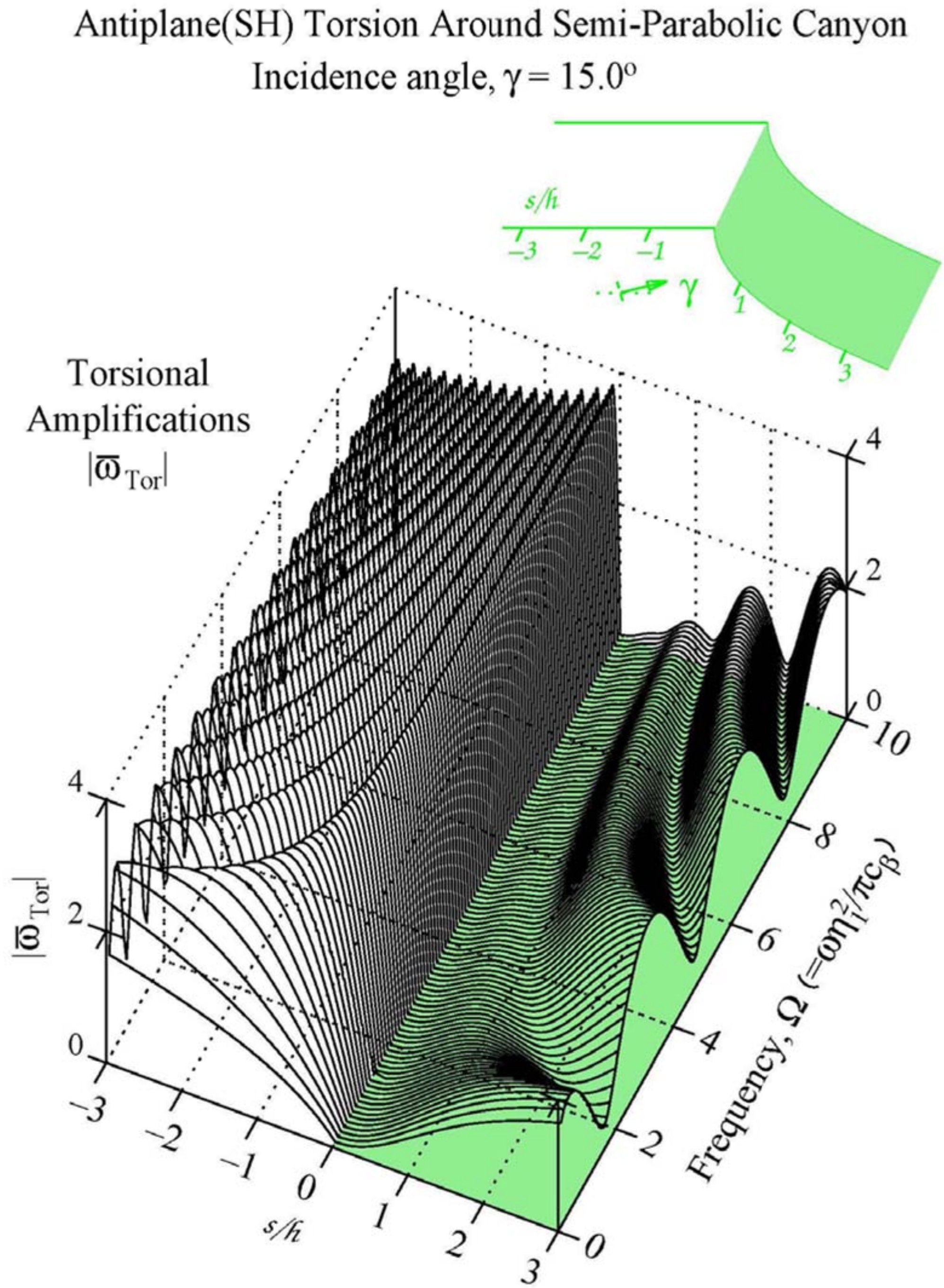

Fig. 3.7 3D Torsion Amplitudes for Oblique Incidence, $\gamma = 15^{\circ}$

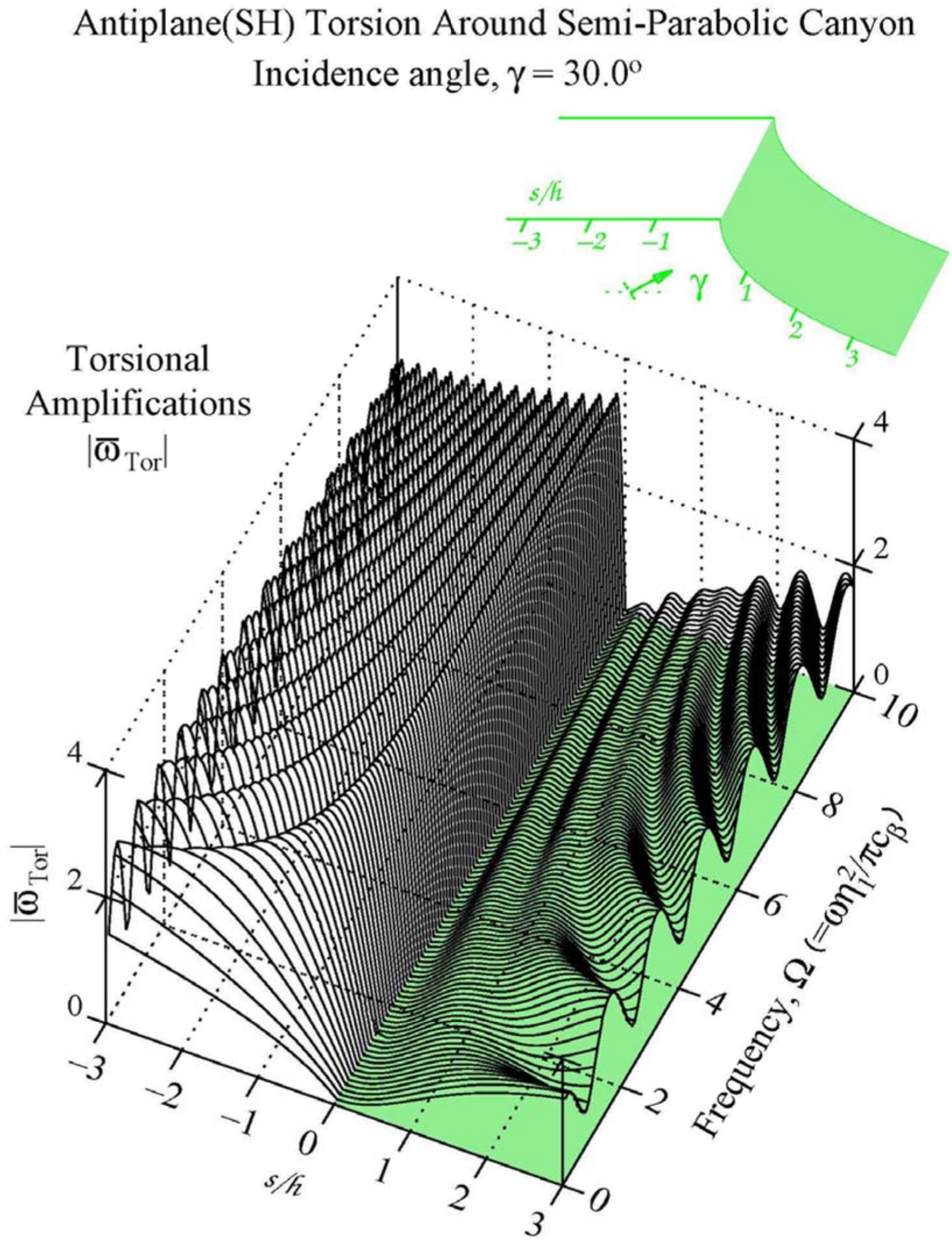

Fig. 3.8 3D Torsion Amplitudes for Oblique Incidence, $\gamma = 30^\circ$

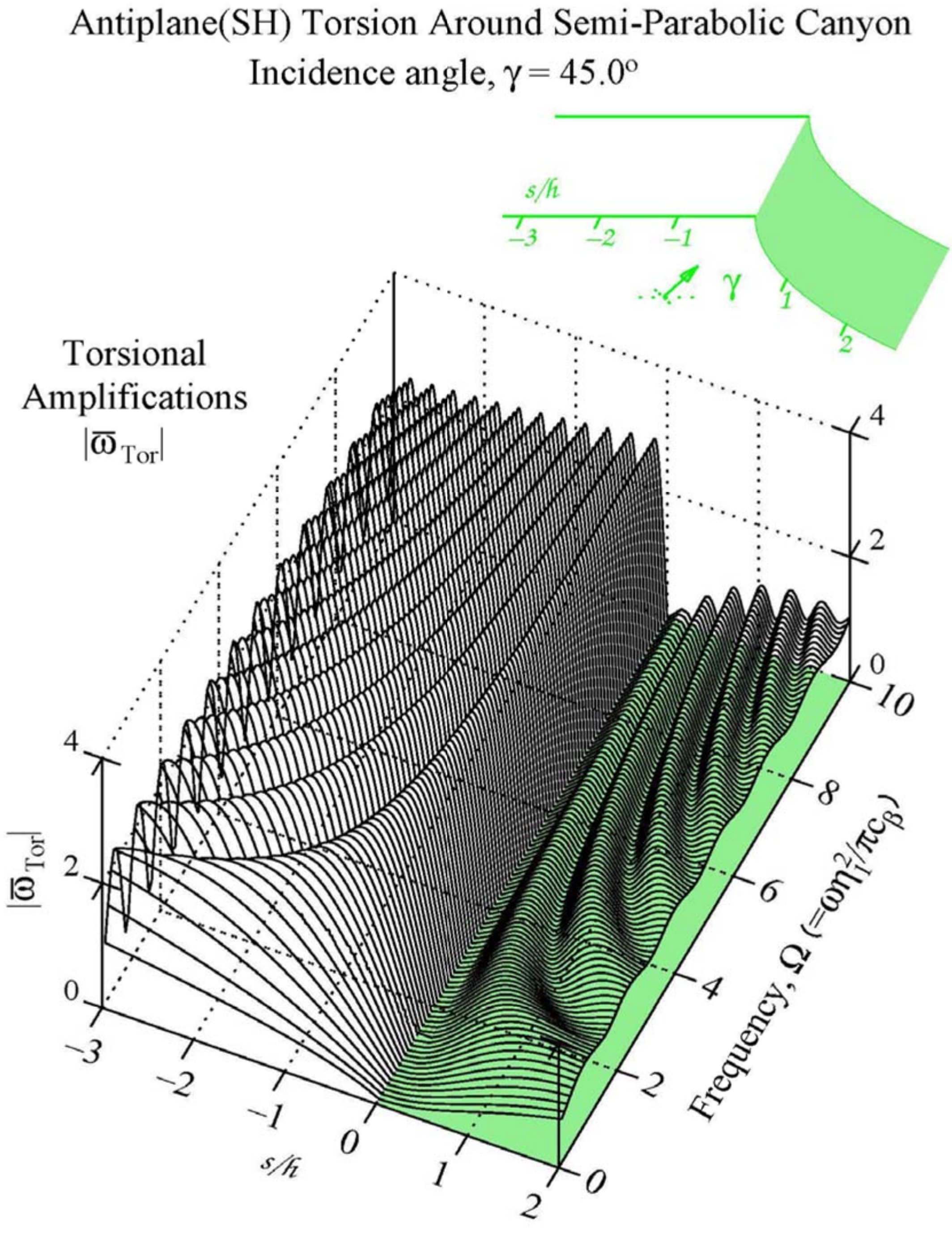

Fig. 3.9 3D Torsion Amplitudes for Oblique Incidence, $\gamma = 45^{\circ}$

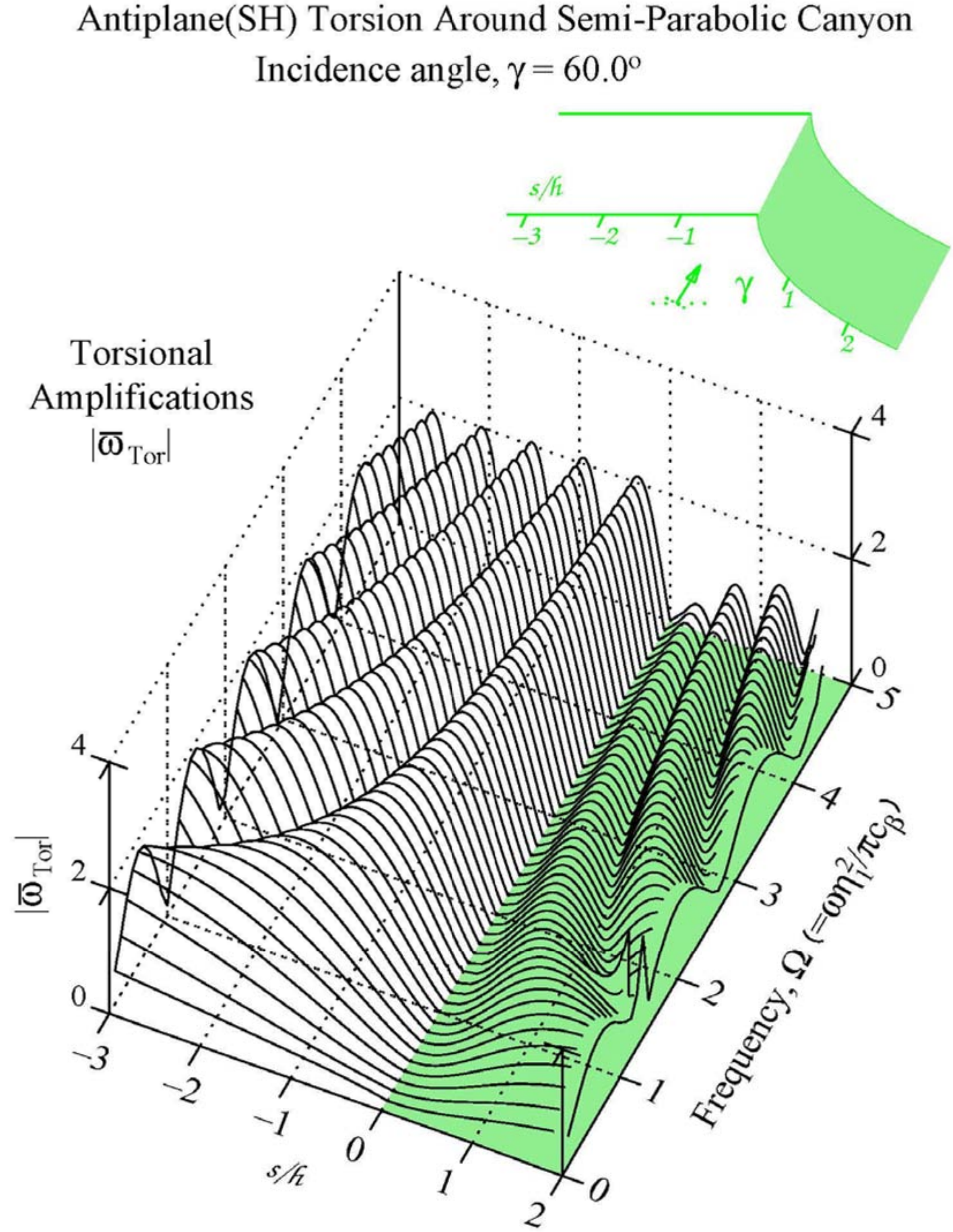

Fig. 3.10 3D Torsion Amplitudes for Oblique Incidence, $\gamma = 60^{\circ}$

III.6 Summary

Chapter III extends the work of Chapter II to compute the rotational components of motions. For anti-plane (SH) wave motions, it is shown that two components of motions are present: the torsional and rocking motions. Chapter II studies the torsional component of rotation. As in the translational motions, the use of the Wronskian relations again allow the torsional motions to be computed up to the dimensionless frequency of $\Omega = 10$. Torsional motions as high as 4 are observed in front of the semi-parabolic canyon.

Chapter IV. The Rocking Components of Motions

IV.1 Introduction

As stated in the introduction of the previous chapter (Chapter III. The Rotational Components of Motions), the rotational components of motions are gaining more and more importance in earthquake engineering and seismological studies, as they can affect significant changes in structural and topographical responses. The reader can again refer to the article by Lee, Celebi, Todorovska & Igel (2009) titled: Introduction to the Special Issue on Rotational Seismology and Engineering Applications for a complete reference to the development and importance of rotational motions. The previous chapter presented the responses due to the torsional motions. This chapter turns now to the responses due to the rocking motions.

As in the case of torsional motions pointed out in Chapter III, such rocking motion is often neglected and no instruments are available for measuring them. Back in early 1980’s, Luco & Wong (1982) in their study of the earthquake response of symmetric elastic structures subjected to SH waves and Rayleigh waves excitation, investigated the effects of the additional rocking associated with the vertical component of the excitation. Lee & Trifunac (1987), using the same method for torsion as in Lee & Trifunac (1985) generated synthetic rocking accelerograms and their response spectra.

Many more recent articles on surface displacements already pointed out to the importance of such rotational motions. Godinho et al (2009) pointed out the importance of such rotations in their articles: Numerical Simulation of Ground Rotations along 2D Topographical Profiles under the Incidence of Elastic Plane Waves. Hung et al (2008) studied the rocking response of bridge foundations. Hu et al (2010) computed such rocking responses in their article: Rocking Vibrations of a Rigid Embedded Foundation in a Poroelastic Half-Space.

IV.2 The Rocking Component of Rotation

The rocking motion resulting from the anti-plane (SH) wave component of displacement will next be computed. For $W = W(x, y)$ in rectangular coordinators and expressed in parabolic coordinators as $W = W(\eta, \xi)$ given by Equation 1 of Section II.1 in Chapter II, this will be given by

$$\begin{aligned} \omega_{Rock} &= \omega_x = \tfrac{1}{2}\left(\nabla \times W\hat{k}\right)\cdot \hat{i} \\ &= \tfrac{1}{2}\,\partial W / \partial y = \tfrac{1}{2}\left(\frac{\partial W}{\partial \eta}\frac{\partial \eta}{\partial y} + \frac{\partial W}{\partial \xi}\frac{\partial \xi}{\partial y}\right) \end{aligned} \tag{1}$$

With $\eta, \xi \geq 0$ in the half-space medium, and as in the last chapter on torsion, we have

$$\begin{aligned} \eta &= +\left[\left(x^2+y^2\right)^{1/2} - x\right]^{1/2} = \sqrt{2r}\cos\left(\frac{\theta}{2}\right) \\ \xi &= +\left[\left(x^2+y^2\right)^{1/2} + x\right]^{1/2} = \sqrt{2r}\sin\left(\frac{\theta}{2}\right) \end{aligned} \tag{2a}$$

with

$$\begin{aligned} r &= \left(x^2+y^2\right)^{1/2} = \tfrac{1}{2}\left(\xi^2+\eta^2\right) \\ x &= \tfrac{1}{2}\left(\xi^2-\eta^2\right) \\ y &= \xi\eta \end{aligned} \tag{2b}$$

so

$$\begin{aligned} \frac{\partial \eta}{\partial y} &= \frac{1}{2\left[\left(x^2+y^2\right)^{1/2} - x\right]^{1/2}}\left(\tfrac{1}{2}\frac{2y}{\left(x^2+y^2\right)^{1/2}}\right) \\ &= \frac{1}{2\eta}\left[-\frac{\xi\eta}{\tfrac{1}{2}\left(\xi^2+\eta^2\right)}\right] = \frac{\xi}{\left(\xi^2+\eta^2\right)} \end{aligned} \tag{3a}$$

and

$$\frac{\partial\xi}{\partial y}=\frac{1}{2\left[\left(x^2+y^2\right)^{1/2}+x\right]^{1/2}}\left(1/2\frac{2y}{\left(x^2+y^2\right)^{1/2}}\right)$$
$$=\frac{1}{2\xi}\left[-\frac{\xi\eta}{1/2\left(\xi^2+\eta^2\right)}\right]=\frac{\eta}{\left(\xi^2+\eta^2\right)} \tag{3b}$$

with these expressions, one gets

$$\omega_{Rock}=\frac{1}{2\left(\xi^2+\eta^2\right)}\left(\xi\frac{\partial W}{\partial\eta}+\eta\frac{\partial W}{\partial\xi}\right) \tag{4}$$

ω_{Rock} will be the rocking motion of the resultant waves everywhere in the half-space.

Consider again the input free-field motion w^{ff} in both rectangular and parabolic coordinates

$$W^{ff}=2e^{ikx\cos\gamma}\cos\left(ky\sin\gamma\right)=2\sec\left(\frac{\gamma}{2}\right)\sum_{n=0}^{\infty}a_nD_{2n}\left(\bar{\lambda}\eta\right)D_{2n}\left(\lambda\xi\right) \tag{5}$$

Equation (4) gives the torsional motion of the free-field waves as

$$\omega_{Rock}^{ff}=1/2\frac{\partial W^{ff}}{\partial y}=\left(-1/2\right)k\sin\gamma\left(2e^{ikx\cos\gamma}\sin\left(ky\sin\gamma\right)\right) \tag{6}$$

In parabolic coordinates, Equation (4) gives

$$\omega_{Rock}^{ff}=\left(1/2\right)\frac{2\sec\left(\frac{\gamma}{2}\right)}{\left(\xi^2+\eta^2\right)}\sum_{n=0}^{\infty}a_n\left[\bar{\lambda}\xi D_{2n}^{'}\left(\bar{\lambda}\eta\right)D_{2n}\left(\lambda\xi\right)+\lambda\eta D_{2n}\left(\bar{\lambda}\eta\right)D_{2n}^{'}\left(\lambda\xi\right)\right] \tag{7}$$

Recall the scattered waves from Equation (1) of Chapter II:

$$W^s = 2\sec\left(\gamma/2\right)\sum_{n=0}^{\infty}(-i)\,a_n \frac{D'_{2n}(\lambda\eta_1)}{D'_{-2n-1}(\lambda\eta_1)} D_{-2n-1}(\lambda\eta)\,D_{2n}(\lambda\xi) \quad \text{From Chapter II Eqn (1)}$$

With this, the rocking motion of the scattered waves can similarly be computed as

$$\omega^s_{Rock} = \left(1/2\right)\frac{2\sec\left(\gamma/2\right)}{\left(\xi^2+\eta^2\right)}\times$$
$$\sum_{n=0}^{\infty}(-i)\,a_n \frac{D'_{2n}(\lambda\eta_1)}{D'_{-2n-1}(\lambda\eta_1)}\left[\lambda\xi D'_{-2n-1}(\lambda\eta)\,D_{2n}(\lambda\xi)+\lambda\eta D_{-2n-1}(\lambda\eta)\,D'_{2n}(\lambda\xi)\right] \tag{8}$$

On the half-space surface to the left of the canyon, where $\gamma = 0$ (and ξ=0), Equation (6) shows that the rocking motion of the free-field was, ω^{ff}_{Rock}, is zero, since

$$\omega^{ff}_{Rock}\Big|_{\xi=0} =$$
$$\left(1/2\,\frac{2\sec\left(\gamma/2\right)}{\cancel{\xi}^2+\eta^2}\right)\sum a_n\left[\bar{\lambda}\cancel{\xi} D'_{2n}\left(\bar{\lambda}\eta\right)D_{2n}(\lambda\xi)+\lambda\eta D_{2n}\left(\bar{\lambda}\eta\right)\cancel{D}'_{2n}(\lambda\xi)\right]\Bigg|_{\xi=0} = 0 \tag{9}$$

Similarly, the rocking motion of the scattered waves, ω^s_{Rock}, is also zero, as

$$\omega^s_{Rock}\Big|_{\xi=0} = \left.\begin{array}{l}\left(1/2\,\dfrac{2\sec\left(\gamma/2\right)}{\xi^2+\eta^2}\right)\times \\ \displaystyle\sum_n \frac{(-i)\,a_n D'_{2n}\left(\bar{\lambda}\eta_1\right)}{D'_{-2n-1}(\lambda\eta_1)}\left[\lambda\cancel{\xi} D'_{-2n-1}(\lambda\eta)\,D_{2n}(\lambda\xi)+\lambda\eta D_{-2n-1}(\lambda\eta)\,\cancel{D}'_{2n}(\lambda\xi)\right]\end{array}\right|_{\xi=0} = 0 \tag{10}$$

The resultant rocking motion $\omega_{Rock}\Big|_{y=0} = \omega_{Rock}^{ff} + \omega_{Rock}^{s}\Big|_{\substack{y=0 \\ (\xi=0)}} = 0$, at the surface of the half-space, from Equation (9) and (10), is thus zero

$$\omega_{Rock}\Big|_{y=0} = \omega_{Rock}^{ff} + \omega_{Rock}^{s}\Big|_{\substack{y=0 \\ (\xi=0)}} = 0 \tag{11}$$

On the surface of the canyon, where $\eta = \eta_1$, Equation (7) and (8), respectively from the free-field ω_{Rock}^{ff}, and scattered, ω_{Rock}^{s}, rocking motions, will take the form $\omega_{Rock}^{ff} + \omega_{Rock}^{s}\Big|_{\eta=\eta_1}$, where

$$\omega_{Rock}^{ff}\Big|_{\eta=\eta_1} = \left(\tfrac{1}{2}\right)\frac{2\sec\left(\gamma/2\right)}{\xi^2+\eta_1^2}\sum_{n=0}^{\infty} a_n\left[\bar{\lambda}\xi D_{2n}^{'}\left(\bar{\lambda}\eta_1\right)D_{2n}\left(\lambda\xi\right) - \lambda\eta D_{2n}\left(\bar{\lambda}\eta_1\right)D_{2n}^{'}\left(\lambda\xi\right)\right] \tag{12}$$

and

$$\begin{aligned}\omega_{Rock}^{s}\Big|_{\eta=\eta_1} &= \left(\tfrac{1}{2}\right)\frac{2\sec\left(\gamma/2\right)}{\xi^2+\eta_1^2}\times \\ &\sum_{n=0}^{\infty}\frac{(-i)\,a_n D_{2n}^{'}\left(\bar{\lambda}\eta_1\right)}{D_{-2n-1}^{'}\left(\lambda\eta_1\right)}\left[\lambda\xi D_{-2n-1}^{'}\left(\lambda\eta_1\right)D_{2n}\left(\lambda\xi\right) + \lambda\eta_1 D_{-2n-1}\left(\lambda\eta_1\right)D_{2n}^{'}\left(\lambda\xi\right)\right]\end{aligned} \tag{13}$$

The first term in the sum from both waves in Equation (12) and (13) for the free-field ω_{Rock}^{s} rocking motions, can be combined ad simplified to zero:

1^{st} term of $\left(\omega_{Rock}^{ff}+\omega_{Rock}^{s}\right)\Big|_{\eta=\eta_1} =$

$$\left(\tfrac{1}{2}\right)\frac{2\sec\left(\gamma/2\right)}{\left(\xi^2+\eta_1^2\right)}\sum_{n=0}^{\infty}\xi a_n\left[\bar{\lambda}D_{2n}'\left(\lambda\eta_1\right)-\frac{(-i)\lambda D_{2n}'\left(\bar{\lambda}\eta_1\right)}{\cancel{D}_{-2n-1}'\left(\lambda\eta_1\right)}\cancel{D}_{-2n-1}\left(\lambda\eta_1\right)\right]D_{2n}\left(\lambda\xi\right)=0 \qquad (14)$$

since $\bar{\lambda}=i\lambda$

With the 2nd term of both sums remaining, they are combined as

2^{nd} term of $(\omega_{Rock}^{ff}+\omega_{Rock}^{s})\Big|_{\eta=\eta_1} =$

$$\left(\tfrac{1}{2}\right)\frac{2\sec\left(\gamma/2\right)}{\left(\xi^2+\eta_1^2\right)}\sum_{n=0}^{\infty}\left(\lambda\eta_1\right)a_n\left[D_{2n}\left(\bar{\lambda}\eta_1\right)+(-i)\frac{D_{2n}'\left(\bar{\lambda}\eta_1\right)}{D_{-2n-1}'\left(\lambda\eta_1\right)}D_{-2n-1}\left(\lambda\eta_1\right)\right]D_{2n}'\left(\lambda\xi\right) \qquad (15)$$

The term in the squared bracket is again identical to that encountered earlier in Equation (3a) of Chapter II, and Equation (18) of Chapter III, which is simplified to Equation (6) of Section II.1 of Chapter II, using the Wronskian relation,

$$\left[D_{2n}\left(\lambda\eta_1\right)-\frac{(i)D_{2n}'\left(\bar{\lambda}\eta_1\right)}{D_{-2n-1}'\left(\lambda\eta_1\right)}D_{-2n-1}'\left(\lambda\eta_1\right)\right]=\frac{i(-1)^n}{D_{-2n-1}'\left(\lambda\eta_1\right)} \qquad \text{Chapter II, Equation (6)}$$

In other words, on the surface of the canyon, the rocking motions simplified to:

$$\left(\omega_{Rock}^{ff}+\omega_{Rock}^{s}\right)\Big|_{\eta=\eta_1}=\left(\tfrac{1}{2}\right)\frac{2\sec\left(\gamma/2\right)}{\left(\xi^2+\eta_1^2\right)}\left(\lambda\eta_1\right)\sum_{n=0}^{\infty}\frac{ia_n(-1)^n}{D_{-2n-1}'\left(\lambda\eta_1\right)}D_{2n}'\left(\lambda\xi\right) \qquad (16)$$

This completes the derivation of the equations for the rocking component of rotational motions everywhere. It is interesting to compare the above equation of rocking at the parabolic canyon surface with the corresponding equation of torsion at the same point.

From Equation (22) of Chapter III, on the surface of the canyon, the torsional motion is given by

$$\left(\omega_{Tor}^{ff}+\omega_{Tor}^{s}\right)\Big|_{\eta=\eta_1}=\left(-\tfrac{1}{2}\right)\frac{2\sec\left(\gamma/2\right)}{\left(\xi^2+\eta_1^2\right)}\left(\lambda\xi\right)\sum_{n=0}^{\infty}ia_n\left(-1\right)^n\frac{D_{2n}^{'}\left(\lambda\xi\right)}{D_{-2n-1}^{'}\left(\lambda\eta_1\right)}\ \text{Chapter III, Eq (22)}$$

an expression which is similar to that of, but different from, the rocking motions of Equation (16) above.

In the next section, the amplitudes of the rocking motions, normalized with the rotation vector amplitude of the incident waves, $\left|\tilde{\omega}^{i}\right|$ (Chapter III, Equation (7)), will next be presented:

$$\begin{aligned}\omega_{Rock}&=\omega_{Rock}\Big/\left|\omega^{i}\right|=\left(2/k\right)\omega_{Rock}=2/k\left(\omega_{Rock}^{ff}+\omega_{Rock}^{s}\right)\\&=2/k\left(1/2\,\partial W/\partial y\right)=1/k\left(\partial W/\partial y\right)\end{aligned}\tag{17}$$

Using Equation (17), the normalized rocking motion amplitude at the half-space and parabolic canyon surface takes the form, form Equations (11) and (16)

$$\begin{aligned}&\omega_{Rock}\Big|_{y=0}=0\qquad\rightarrow\qquad\overline{\omega}_{Rock}\Big|_{y=0}=0\\&\overline{\omega}_{Rock}\Big|_{\eta=\eta_1}=2/k\,\omega_{Rock}\Big|_{\eta=\eta_1}=\frac{2\sec\left(\gamma/2\right)}{k\left(\xi^2+\eta_1^2\right)}\left(\lambda\eta_1\right)\sum_{n=0}^{\infty}\frac{ia_n\left(-1\right)^n}{D_{-2n-1}^{'}\left(\lambda\eta_1\right)}D_{2n}^{'}\left(\lambda\xi\right)\end{aligned}\tag{18}$$

IV.3 Rocking Motions: Horizontal Angle of Incidence $\gamma = 0^{\circ}$

Fig 4.1 represents the normalized rocking amplitudes Equation (17), $\left|\varpi_{Rcok}\right|$, plotted versus the dimensionless distance s/h at the dimensionless frequency, $\Omega = 1.0, 2.0, \ldots$ to 10.0, for the horizontal angle of incidence of $\gamma = 0^{\circ}$. The incident, plan SH wave, W^{i}, is assumed to have unit amplitude. As in Fig. 3.1 for torsion amplitudes, the rocking amplitudes are calculated at points on the half-space and parabolic surfaces. The same dimensionless distance, s/h is measured in units of the focal length of the parabolic canyon from the tip (vertex, corner point) of the canyon, where $s/h = 0$. Refer to the description of Fig. 2.1 in Chapter II and Fig. 3.1 in the last chapter for details.

The shape of the half-space and canyon surface on which the displacements are calculated is outlined as a dotted line on the top-left graph of the figure, as in Fig. 3.1 of the last chapter for torsion, and it is now green. The green arrow again indicates the corresponding direction of the incident SH wave, W^{i}, which is assumed to be coming from the left-side towards the canyon.

For the case of horizontal incidence, $\gamma = 0^{\circ}$, here in Fig. 4.1, the incidence wave W^{i} will depend only on the x-coordinate, of the form $W^{i} = \exp^{(ikx)}$ and the resultant wave

$W = W^{ff} + W^{s}$, from Equation (1) of Chapter II, will take on only the single tern, n = 0, since $\tan^{2n}\left(\frac{\gamma}{2}\right)$ in Equation (2) of Chapter II is zero for $n > 0$ (meaning $a_n = 0$ for $n > 0,$ and $a_0 = 1)$. The translational displacement motion, W again is

$$W = 2\left[D_0\left(\bar{\lambda}\eta\right) - \frac{iD_0^{'}\left(\bar{\lambda}\eta_1\right)}{D_{-1}^{'}\left(\lambda\eta_1\right)} D_{-1}\left(\lambda\eta\right) \right] D_0\left(\lambda\xi\right) \qquad \text{Chapter II Equation (18)}$$

and the corresponding rocking motion, from Equation (4) of the previous section:

$$\omega_{Rock} = \frac{1}{2\left(\xi^2 + \eta^2\right)} \left(\xi \frac{\partial W}{\partial \eta} + \eta \frac{\partial W}{\partial \xi} \right) \qquad \text{Equation (5) above}$$

Recall from Equation (11) above that the rocking motion is zero at the half-space surface, where y = 0

$$\omega_{Rock}\Big|_{y=0} = \omega_{Rock}^{ff} + \omega_{Rock}^{s}\Big|_{\substack{y=0 \\ (\xi=0)}} = 0 \qquad \text{Equation (12) above}$$

as shown in Fig. 4.1 below, the dashed line is the free-field rocking, ω_{Rock}^{ff} is also zero at the half-space surface.

At the surface of the parabolic canyon, it takes the form (also from Equation (7) and (14) above), respectively for the free-field and scattered waves, from Equation (18), with just the n = 0 terms for $\gamma = 0 \ \left(\sec\left(\frac{\gamma}{2}\right) = 1,\ \lambda = \sqrt{-2ik},\ \left|\lambda\right|^2 = 2k \right)$:

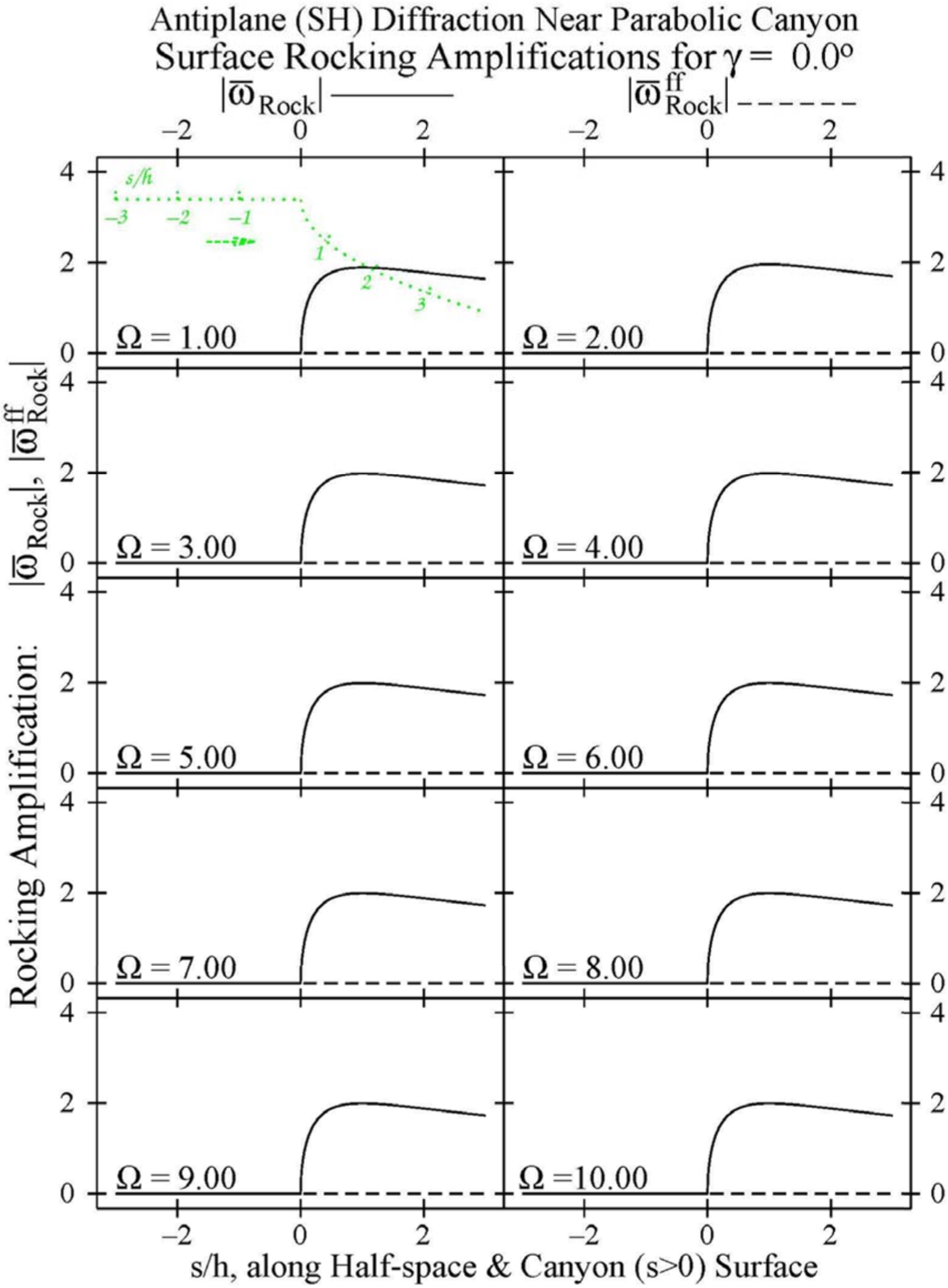

Fig. 4.1 Rocking Amplitudes for Horizontal Incidence, $\gamma = 0^{\circ}$

$$\left|\overline{\omega}_{Rock}\right|_{\eta=\eta_1} = {}^{2}\!/_{k}\left|\omega_{Rock}\right|\Big|_{\eta=\eta_1} = \frac{2}{k\left(\xi^2+\eta_1^2\right)}\left|\lambda\eta_1\right|\left|\frac{D_0^{'}\left(\lambda\xi\right)}{D_{-1}^{'}\left(\lambda\eta_1\right)}\right|$$
$$= \frac{2\left|\lambda\right|\eta_1}{k\left(\xi^2+\eta_1^2\right)\left|\dfrac{D_0^{'}\left(\lambda\xi\right)}{D_{-1}^{'}\left(\lambda\eta_1\right)}\right|}\left|\left(-{}^{z}\!/_{2}\right)e^{-z^2/4}\right|_{z=\lambda\xi} = \frac{2\eta_1\xi}{\left(\xi^2+\eta_1^2\right)\left|D_{-1}^{'}\left(\lambda\eta_1\right)\right|} \tag{19}$$

At the vertex of the parabolic canyon, where $\eta=\eta_1, \xi=0$, when the half-space surface meets the parabolic surface, the rocking motion is zero, as it is on the half-space surface. Along the canyon surface, as ξ increases, the rocking motion amplitude gradually increases from zero, and reaches a maximum at $\xi=\xi_1$, a point on the canyon surface $\eta=\eta_1$ where from equation (19)

$$\frac{d}{d\xi}\left(\left|\overline{\omega}_{Rock}\right|\right) = \frac{d}{d\xi}\left(\frac{2\eta_1\xi}{\left(\xi^2+\eta_1^2\right)\left|D_{-1}^{'}\left(\lambda\eta_1\right)\right|}\right) = 0, \text{ or}$$
$$\frac{\left(\xi^2+\eta_1^2\right)-\xi\left(2\xi\right)}{\left(\xi^2+\eta_1^2\right)^2} = 0 \qquad \Rightarrow \qquad \xi=\xi_1=\eta_1 \tag{20}$$

At $\xi=\xi_1=\eta_1$, where $\dfrac{d}{d\xi}\left(\left|\overline{\omega}_{Rock}\right|\right)=0$, $\left|\overline{\omega}_{Rock}\right| = \left|\overline{\omega}_{Rock}\right|\Big|_{\max}$ is given by, from Equation (19),

$$\left|\overline{\omega}_{Rock}\right|\Big|_{\max} = \left|\overline{\omega}_{Rock}\right|\Big|_{\xi=\eta_1} = \frac{2\eta_1\xi}{\left(\xi^2+\eta_1^2\right)\left|D_{-1}^{'}\left(\lambda\eta_1\right)\right|}\Bigg|_{\xi=\eta_1} = \frac{1}{\left|D_{-1}^{'}\left(\lambda\eta_1\right)\right|} \tag{21}$$

which is an amplitude close to 2.

Further and further away from the vertex, as $\xi \to \infty$, Equation (19) above shows that the rocking amplitudes approach zero.

Fig. 4.2 is the same 3D plot of the rocking amplitudes plotted vs. the dimensionless distance s/h and the dimensionless frequency **Ω**, as on Fig. 4.1 for horizontal incidence $\gamma = 0^{\circ}$.

As in the previous chapters, the shape of the half-space and canyon surface model on which the displacements are calculated is outlined on the top-left graph of the figure, and it is now in green color. The green arrow is the direction of the incident SH wave, W^{i} which is assumed to be coming from the left-side towards the canyon.

The 3D plot shows that the rocking motion is practically the same at all frequencies. It started as zero at the vertex of the canyon, where $\eta = \eta_1$, $\xi = 0$ and quickly reaches the maximum of $\left|\overline{\omega}_{Rock}\right|_{\max} = 1 \Big/ \left|D_{-1}^{'}\left(\lambda \eta_1\right)\right|$ close to amplitude of 2, and practically stays constant as shown in the figure. This is similar to the translational amplitude for $\gamma = 0$, $\left|W\right|\Big|_{\substack{\gamma=0 \\ \eta=\eta_1}} = \dfrac{2}{\left|D_{-1}^{'}\left(\lambda \eta_1\right)\right|}$, Chapter II Equation (21) with amplitude of 4.

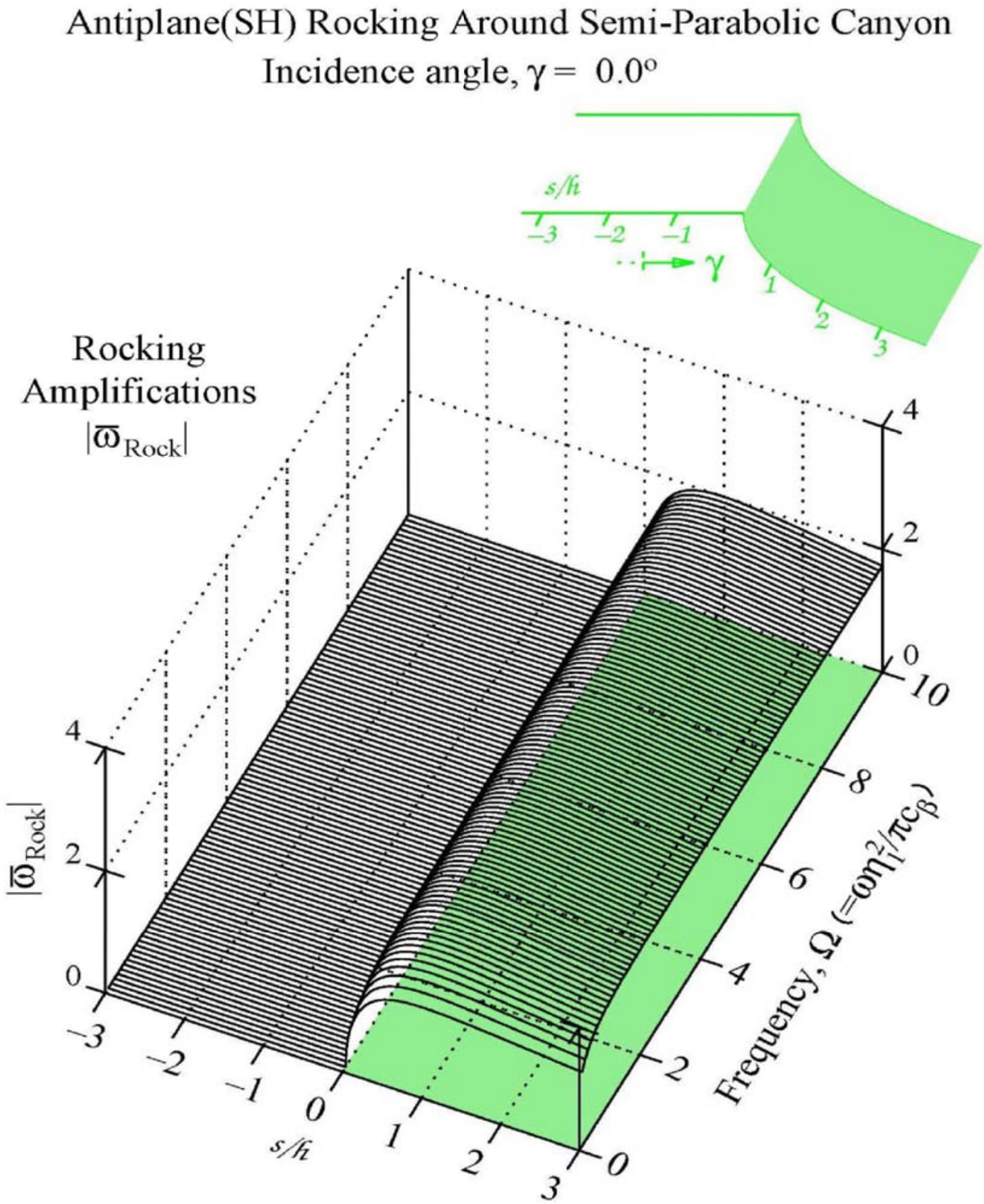

Fig. 4.2 3D Rocking Amplitudes for Horizontal Incidence, $\gamma = 0^{\circ}$

IV.4 Rocking Motions – Oblique Angles of Incidences: $\gamma = 15^\circ, 30^\circ, 45^\circ$ and 60°

With the presentations of the rocking motions of horizontal incidence $\left(\gamma = 0^\circ\right)$ completed, we now turn to the case of rocking motions for oblique incidences in this section, as in Section III.5 of Chapter III for torsional motions at oblique angles of incidences $\gamma = 15^\circ, 30^\circ, 45^\circ$ and 60°. The only difference between the two sections will be the fact that only 3D plots for rocking motions will be presented in this section.

Fig. 4.3 presents the normalized rocking motion amplitudes, $\left|\overline{\omega}_{Rock}\right|$ plotted vs. the same dimensionless distance s/h and dimensionless frequencies Ω for the case of angle of incidence $\gamma = 15^\circ$. All descriptions of the plot remain the same as the figures in the previous section for $\gamma = 0^\circ$ and will not be repeated here.

As in the translational and torsional motions, with the free-field waves and scattered waves now all given by infinite series for oblique incidence $\gamma > 0^\circ$ the convergence of the infinite series, as before in the previous two chapters (Chapter II and III) will again be considered in the calculations, with the difference being this time convergence needs only to be considered along the parabolic surface, since rocking motions are unanimously zero on the half-space surface for all angles of incidence:

$$\omega_{Rock}\Big|_{y=0} = \omega_{Rock}^{ff} + \omega_{Rock}^{s}\Big|_{\substack{y=0\\(\xi=0)}} = 0 \qquad \text{Equation (11) above}$$

As shown in Fig. 4.3 below.

On the surface of the parabolic canyon, the rocking motion is given by

$$\left(\omega_{Rock}^{ff} + \omega_{Rock}^{s}\right)\Big|_{\eta=\eta_1} = \left(1\!\!\diagup\!2\right)\frac{2\sec\left(\gamma\!\!\diagup\!2\right)}{\left(\xi^2+\eta_1^2\right)}\left(\lambda\eta_1\right)\sum_{n=0}^{\infty}\frac{ia_n\left(-1\right)^n}{D'_{-2n-1}\left(\lambda\eta_1\right)}D'_{2n}\left(\lambda\xi\right) \qquad \text{Equation (16) above}$$

which is equal to zero at the vertex of the canyon, where $\xi = 0$, since for all n, at $\xi = 0$ $D'_{2n}\left(\lambda\xi\right) = 0$. The convergence of the infinite sum of the rocking motions in Equation (16) used here is again accelerated by the use of the Wronskian relation, as is the case for the translational motions in Chapter II and torsional motions in Chapter III.

The rocking rotational amplitudes in Fig 4.3 for $\gamma = 15^{\circ}$ show an interesting feature of the model in being different from the case of $\gamma = 0^{\circ}$ in Fig. 4.2. Fig. 4.2 shows that at the canyon surface, at all frequencies, the rocking amplitudes start as zero on the vertex and quickly reaches the maximum of $\left|\overline{\omega}_{Rock}\right|\Big|_{\max} = \dfrac{1}{\left|D'_{-1}\left(\lambda\eta_1\right)\right|}$ (Equation (22)), an amplitude

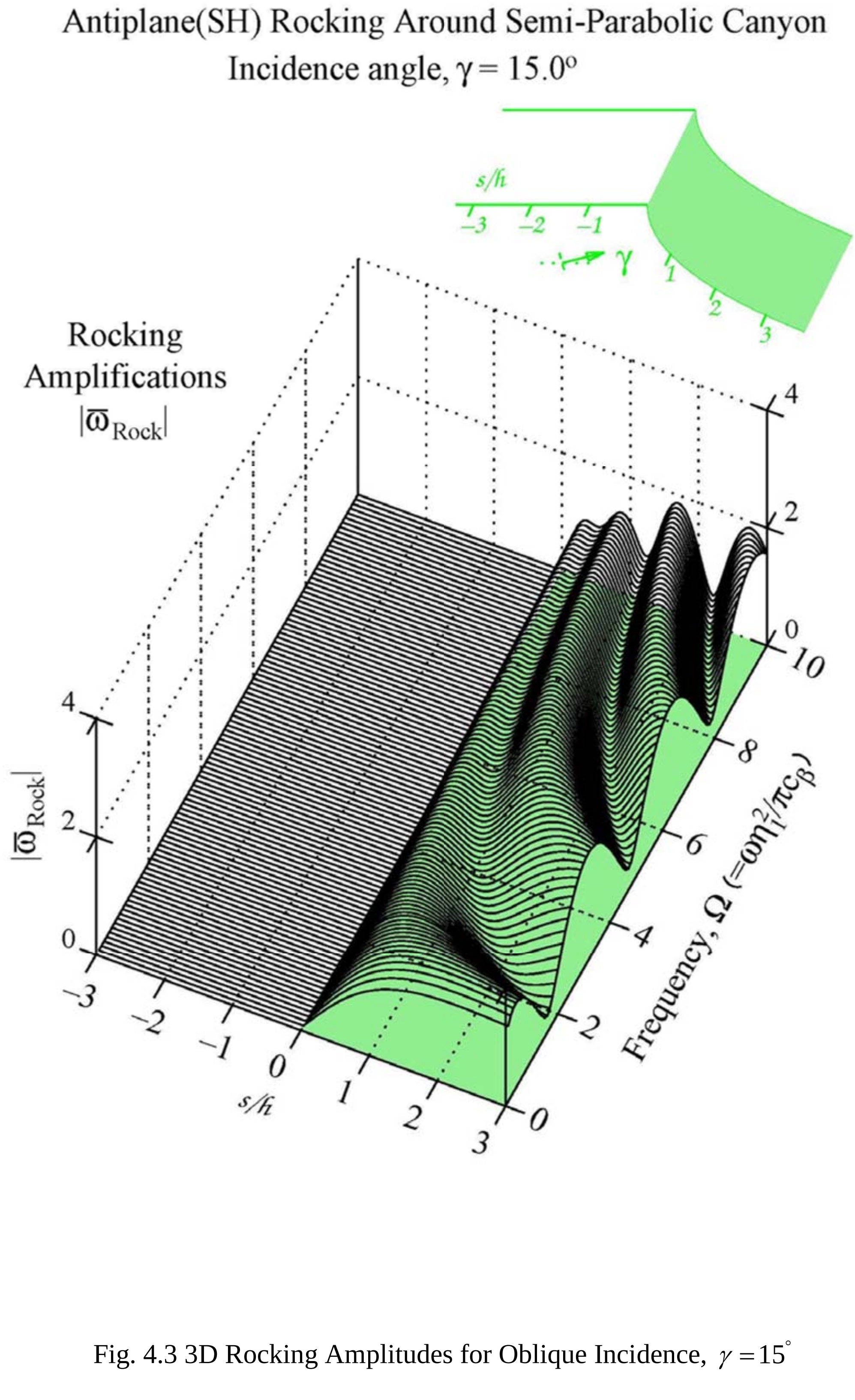

Fig. 4.3 3D Rocking Amplitudes for Oblique Incidence, $\gamma = 15^{\circ}$

close to two and starts almost constant there, as shown in the figure. For Oblique incidence of $\gamma = 15^{\circ}$ the rocking amplitudes are more oscillatory, which increases with increasing frequency **Ω**. As in torsion, the rocking motions behave again as standing wave, because every point of the canyon surface is in front, facing the incidence waves, thus resulting also in standing wave patterns.

Fig. 4.4 presents the normalized rocking motion amplitudes, $\left|\overline{\omega}_{Rock}\right|$ plotted vs. the same dimensionless distances s/h and dimensionless frequencies **Ω**, for the case of angle of incidence $\gamma = 30^{\circ}$. All descriptions of the plot remain the same as the previous two figures.

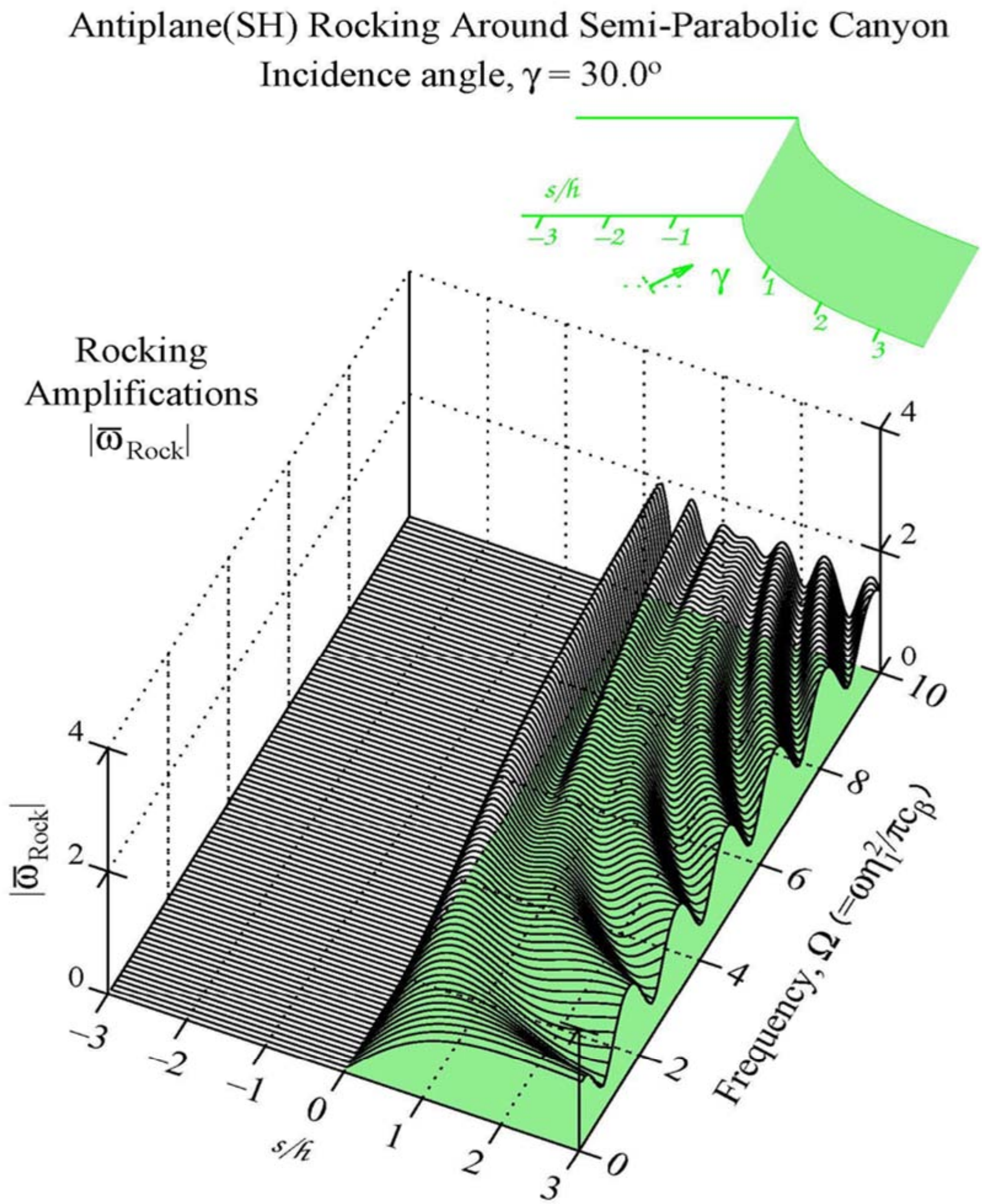

Fig. 4.4 3D Rocking Amplitudes for Oblique Incidence, $\gamma = 30^{\circ}$

Fig. 4.5 and 4.6 are the normalized rocking motion amplitudes $\left|\overline{\omega}_{Rock}\right|$ plotted vs. the same dimensionless distance s/h and dimensionless frequencies **Ω**, respectively for the case of angles of incidence $\gamma = 45^\circ$ and $\gamma = 60^\circ$. All descriptions of the plot remain the same as previous three figures for $\gamma = 0^\circ, 15^\circ$ and 30°

As pointed out in the previous Chapter II for translation displacement amplitudes, as the angles of incidence γ increases from 0° to 60° the input coefficients of the free-field waves (Chapter II, Equation 24) $a_n = \dfrac{(-1)^n}{(2n)!}\tan^{2n}\left(\dfrac{\gamma}{2}\right)$ together with the large Weber function terms, $D_{2n}\left(\overline{\lambda}\eta\right)D_{2n}\left(\lambda\xi\right)$ and $D_{-2n-1}\left(\lambda\eta\right)D_{2n}\left(\lambda\xi\right)$ terms of the free-field and scattered waves converge slower and slower for the translational displacement amplitudes. The same is true in Chapter III for the torsional rotation amplitudes and here in Chapter IV for the rocking rotation amplitudes.

At $\gamma = 30^\circ$ the use of the Wronskian terms at $\eta = \eta_1$ still allow one to get good rocking, rotation amplitudes up to dimensionless frequency of **Ω** = 10 in Fig. 4.4 above. At $\gamma = 45^\circ$, the Wronskian terms still allow one to get good rocking, rotation amplitudes up to a frequency of **Ω** =10, but for only as far as $s/h = 2$ shown in Fig. 4.5. Finally, for incidence angle of $\gamma = 60^\circ$ in Fig. 4.6, the calculation for rocking amplitudes is now only up to dimensionless frequencies of $\Omega = 5$.

All these trends and observations are consistent with the results presented in Chapter II for the corresponding displacement amplitudes and Chapter III for the corresponding torsion rotation amplitudes.

This consistency is expect, of no surprise, as the displacement, torsional and rocking rotational motions are respectively given by

$$W\big|_{\eta=\eta_1} = 2\sec\left(\gamma/2\right)\sum_{n=0}^{\infty}\frac{ia_n\left(-1\right)^n}{D'_{-2n-1}\left(\lambda\eta_1\right)}D_{2n}\left(\lambda\xi\right) \qquad \text{Chapter II Equation (12)}$$

$$\omega_{Tor}\big|_{\eta=\eta_1} = \frac{-2\sec\left(\gamma/2\right)}{k\left(\xi^2+\eta_1^2\right)}\left(\lambda\xi\right)\sum_{n=0}^{\infty}ia_n\left(-1\right)^n\frac{D'_{2n}\left(\lambda\xi\right)}{D'_{-2n-1}\left(\lambda\eta_1\right)} \qquad \text{Chapter III Equation (32)}$$

$$\bar{\omega}_{Rock}\big|_{\eta=\eta_1} = \frac{2\sec\left(\gamma/2\right)}{k\left(\xi^2+\eta_1^2\right)}\left(\lambda\eta_1\right)\sum_{n=0}^{\infty}\frac{ia_n\left(-1\right)^n}{D'_{-2n-1}\left(\lambda\eta_1\right)}D'_{2n}\left(\lambda\xi\right) \qquad \text{Equation (18) above}$$

so that the summation above involves the same coefficients namely, summation of the terms $\dfrac{ia_n\left(-1\right)^n}{D'_{-2n-1}\left(\lambda\eta_1\right)}$ times

1) $D_{2n}\left(\lambda\xi\right)$ for displacement.

2) $\left(\lambda\xi\right)D'_{2n}\left(\lambda\xi\right)$ for torsional rotation, and

3) $\left(\lambda\eta_1\right)D'_{2n}\left(\lambda\xi\right)$ for rocking rotation

In other words, they all have the same range of convergence at each angle of incidence, as shown in Chapters II, III and IV

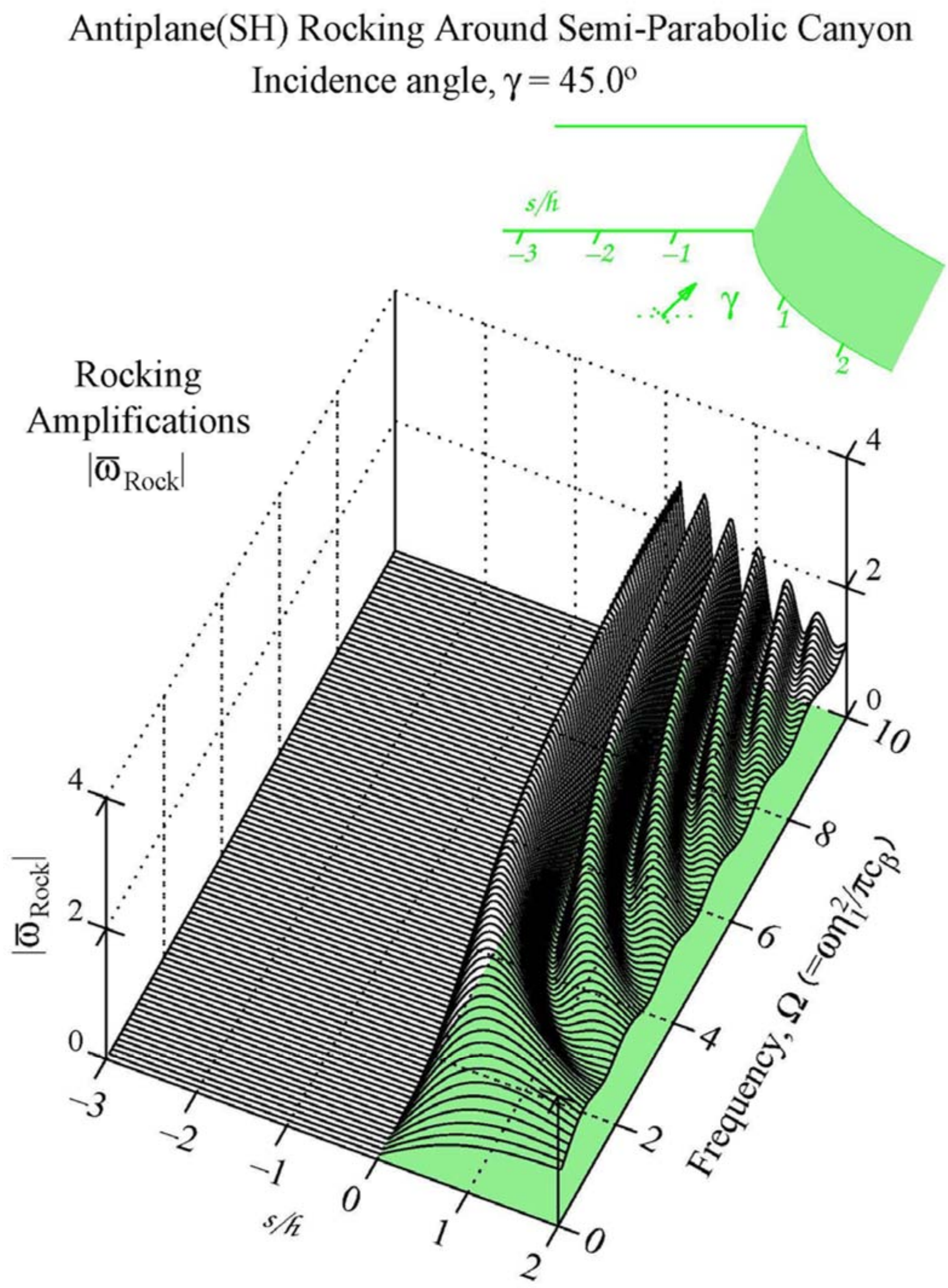

Fig 4.5 3D Rocking Amplitudes for Oblique Incidence, $\gamma = 45^{\circ}$

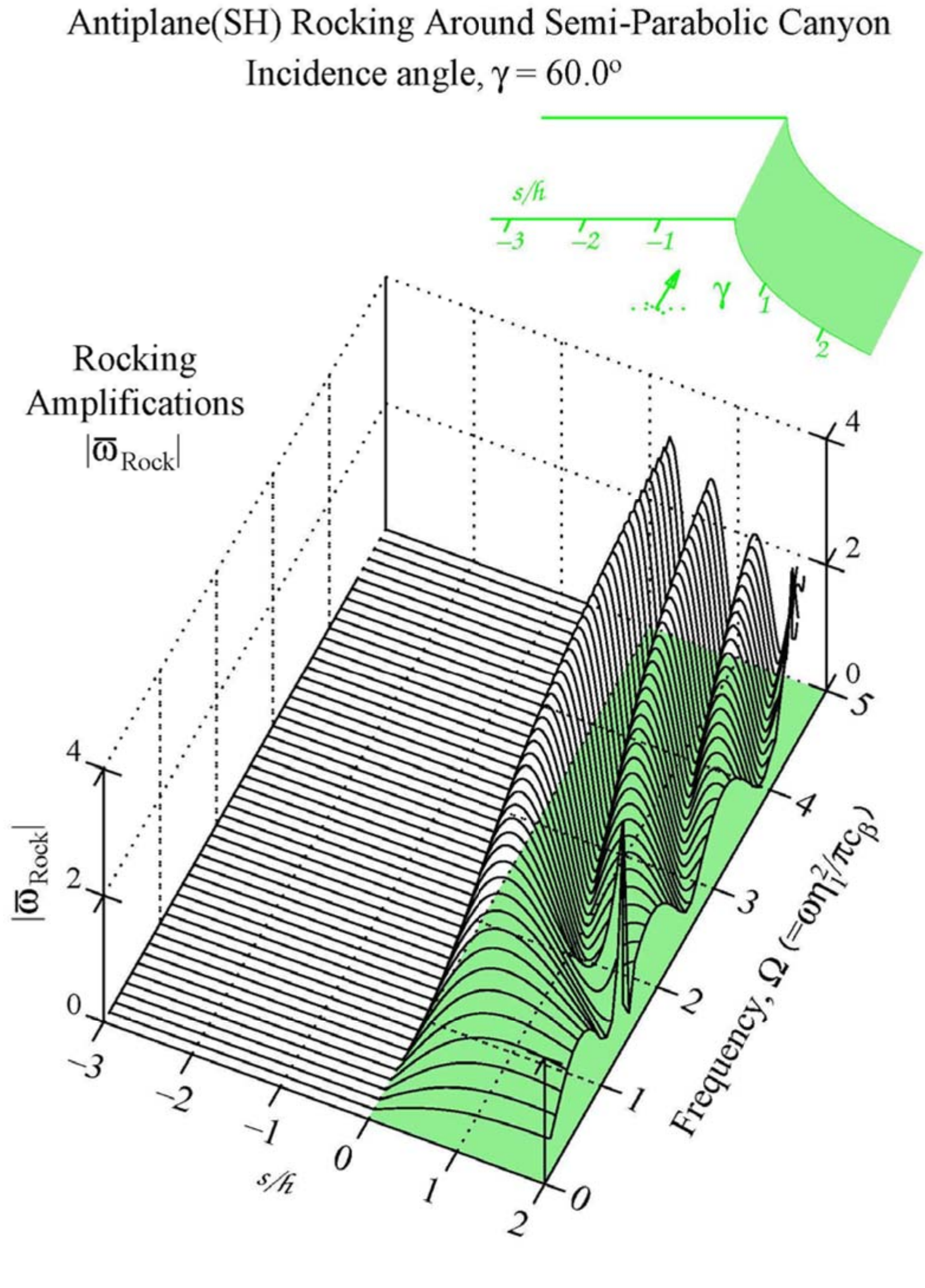

Fig 4.6 3D Rocking Amplitudes for Oblique Incidence, $\gamma = 60^{\circ}$

IV.5 Resultant Rotation Motions for Horizontal & Oblique Angles of Incidences: $\gamma = 0^\circ, 15^\circ, 30^\circ, 45^\circ$ and 60°

Recall from Chapter III, where the rotation components of motions are first defined:

$$\tilde{\omega} = \begin{pmatrix} \omega_x \\ \omega_y \\ 0 \end{pmatrix} = \frac{1}{2} \begin{pmatrix} \partial W / \partial y \\ -\partial W / \partial x \\ 0 \end{pmatrix} \qquad \text{Chapter III Equation (3)}$$

and for anti-plane (z-component) motion, the rotational motion is shown to have only two components, the horizontal components, which are

1) The rotation about the vertical y-axis, the torsional motion given by

$$\omega_y = \omega_{Tor} = -\frac{1}{2} \partial W / \partial x \qquad \text{Chapter III Equation (4a)}$$

And

2) The rotation about the horizontal x-axis, the rocking motion given by

$$\omega_x = \omega_{Rock} = \frac{1}{2} \partial W / \partial y \qquad \text{Chapter III Equation (4b)}$$

In this section, the resultant rotation amplitude is studied, where

$$|\omega| = \left(|\omega_x|^2 + |\omega_y|^2 \right)^{1/2} = \left(|\omega_{Rock}|^2 + |\omega_{Tor}|^2 \right)^{1/2} \qquad (22)$$

The resultant rotation will again be normalized with respect to that of the incident waves.

Recall from Chapter II, for the incident waves W^i of unit amplitude with incident angle at γ wave speed c_β and wave number $k = k_\beta = \omega / c_\beta$ given by

$$W^i = \exp^{ik(x\cos\gamma - y\sin\gamma)} \qquad \text{Chapter III Equation (5)}$$

where $\left|W^i\right| = 1$ the corresponding rotational vector for the incident wave, $\tilde{\omega}^i$ is

$$\tilde{\omega}^i = \begin{pmatrix} \omega_x^i \\ \omega_y^i \\ 0 \end{pmatrix} = \frac{1}{2}\begin{pmatrix} \partial W^i / \partial y \\ -\partial W^i / \partial x \\ 0 \end{pmatrix} = \left(-\frac{1}{2}\right)\begin{pmatrix} ik\sin\lambda \\ ik\cos\gamma \\ 0 \end{pmatrix} W^i \qquad \text{Chapter III Equation (6)}$$

so that the amplitude of the rotation vector of the incident wave, $\left|\tilde{\omega}^i\right|$ is

$$\left|\tilde{\omega}^i\right| = \left(\left|\omega_x^i\right|^2 + \left|\omega_y^i\right|^2\right)^{1/2} = k/2 \left|W^i\right| = k/2 \qquad \text{Chapter III Equation (7)}$$

which will be used as a normalization factor for all rotation components. This is exactly the same normalization factor used for the torsional motion in Chapter II and the rocking motion of the earlier sections of this chapter. The normalization rotation amplitude will next be defined as:

$$\begin{aligned} \left|\overline{\omega}\right| &= \left|\omega\right| / \left|\omega^i\right| = 2/k \left|\omega\right| = 2/k \left(\left|\omega_{Rock}\right|^2 + \left|\omega_{Tor}\right|^2\right)^{1/2} \\ &= \left(\left|\overline{\omega}_x\right|^2 + \left|\overline{\omega}_y\right|^2\right)^{1/2} = \left(\left|\overline{\omega}_{Rock}\right|^2 + \left|\overline{\omega}_{Tor}\right|^2\right)^{1/2} \end{aligned} \qquad (23)$$

Recall that the rocking motion at the surface of the half-space, y = 0 is zero:

$$\omega_{Rock}\Big|_{y=0} = \omega_{Rock}^{ff} + \omega_{Rock}^{s}\Big|_{\substack{y=0\\(\xi=0)}} = 0 \qquad \text{Equation (12) above}$$

so that the normalized resultant rotation motion there at the half-space surface is

$$\left|\overline{\omega}\right|_{y=0} = \left|\overline{\omega}_{Tor}\right|_{y=0} \tag{24}$$

with no (zero) contribution from the rocking motion.

At the surface of the canyon, $\eta = \eta_1$ the normalized torsional and rocking motions are respectively:

$$\omega_{Tor}\Big|_{\eta=\eta_1} = \frac{-2\sec\left(\gamma/2\right)}{k\left(\xi^2+\eta_1^2\right)}\left(\lambda\xi\right)\sum_{n=0}^{\infty} ia_n\left(-1\right)^n \frac{D_{2n}^{'}\left(\lambda\xi\right)}{D_{-2n-1}^{'}\left(\lambda\eta_1\right)} \qquad \text{Chapter III Equation (32)}$$

$$\overline{\omega}_{Rock}\Big|_{\eta=\eta_1} = \frac{2\sec\left(\gamma/2\right)}{k\left(\xi^2+\eta_1^2\right)}\left(\lambda\eta_1\right)\sum_{n=0}^{\infty} \frac{ia_n\left(-1\right)^n}{D_{-2n-1}^{'}\left(\lambda\eta_1\right)} D_{2n}^{'}\left(\lambda\xi\right) \qquad \text{Equation (18) above}$$

which, from Equation (23) give the resultant rotation at $\eta = \eta_1$ as:

$$\begin{aligned}\overline{\tilde{\omega}}\Big|_{\eta=\eta_1} &= \overline{\omega}_x\hat{i} + \overline{\omega}_y\,\hat{j}\Big|_{\eta=\eta_1} = \overline{\omega}_{Rock}\,\hat{i} + \overline{\omega}_{Tor}\,\hat{j}\Big|_{\eta=\eta_1} \\ &\frac{2\sec\left(\gamma/2\right)}{k\left(\xi^2+\eta_1^2\right)}\left(\sum_{n=0}^{\infty}\frac{ia_n\left(-1\right)^n}{D_{-2n-1}^{'}\left(\lambda\eta_1\right)}D_{2n}^{'}\left(\lambda\xi\right)\right)\lambda\left(\eta_1\hat{i} - \xi\hat{j}\right)\end{aligned} \tag{25}$$

with amplitude

$$
\left.\tilde{\overline{\omega}}\right|_{\eta=\eta_1} = \left(\left|\overline{\omega}_{Rock}\right|^2 + \left|\overline{\omega}_{Tor}\right|^2\right)^{1/2}_{\eta=\eta_1} = \left(\left|\overline{\omega}_x\right|^2 + \left|\overline{\omega}_y\right|^2\right)^{1/2}_{\eta=\eta_1}
$$

$$
= 2\sec\left(\gamma/2\right)\frac{|\lambda|\left(\xi^2+\eta_1^2\right)^{1/2}}{k\left(\xi^2+\eta_1^2\right)}\left|\sum_{n=0}^{\infty}\frac{ia_n(-1)^n}{D'_{-2n-1}(\lambda\eta_1)}D'_{2n}(\lambda\xi)\right| \tag{26}
$$

or, with $\lambda = \sqrt{-2ik}$, $|\lambda|^2 = 2k$

$$
\left.\left|\overline{\omega}\right|\right|_{\eta=\eta_1} = \frac{4\sec\left(\gamma/2\right)}{|\lambda|\left(\xi^2+\eta_1^2\right)^{1/2}}\left|\sum_{n=0}^{\infty}\frac{ia_n(-1)^n}{D'_{-2n-1}(\lambda\eta_1)}D'_{2n}(\lambda\xi)\right| \tag{27}
$$

Fig. 4.7 to Fig. 4.11 are the five 3D plots of the normalized resultant rotation amplitudes plotted vs.

1) The dimensionless distance s/h measured along the half-space and canyon surface and
2) The dimensionless frequency $\Omega = \omega\eta_0^2/\pi\beta = 2\eta_0^2/\lambda = 4h/\lambda$,

respectively for incidence angles $\gamma = 0^\circ, 15^\circ, 30^\circ, 45^\circ$ and 60°. As in the corresponding plots of normalized torsional and rocking rotation amplitudes, all trends of features stayed the same.

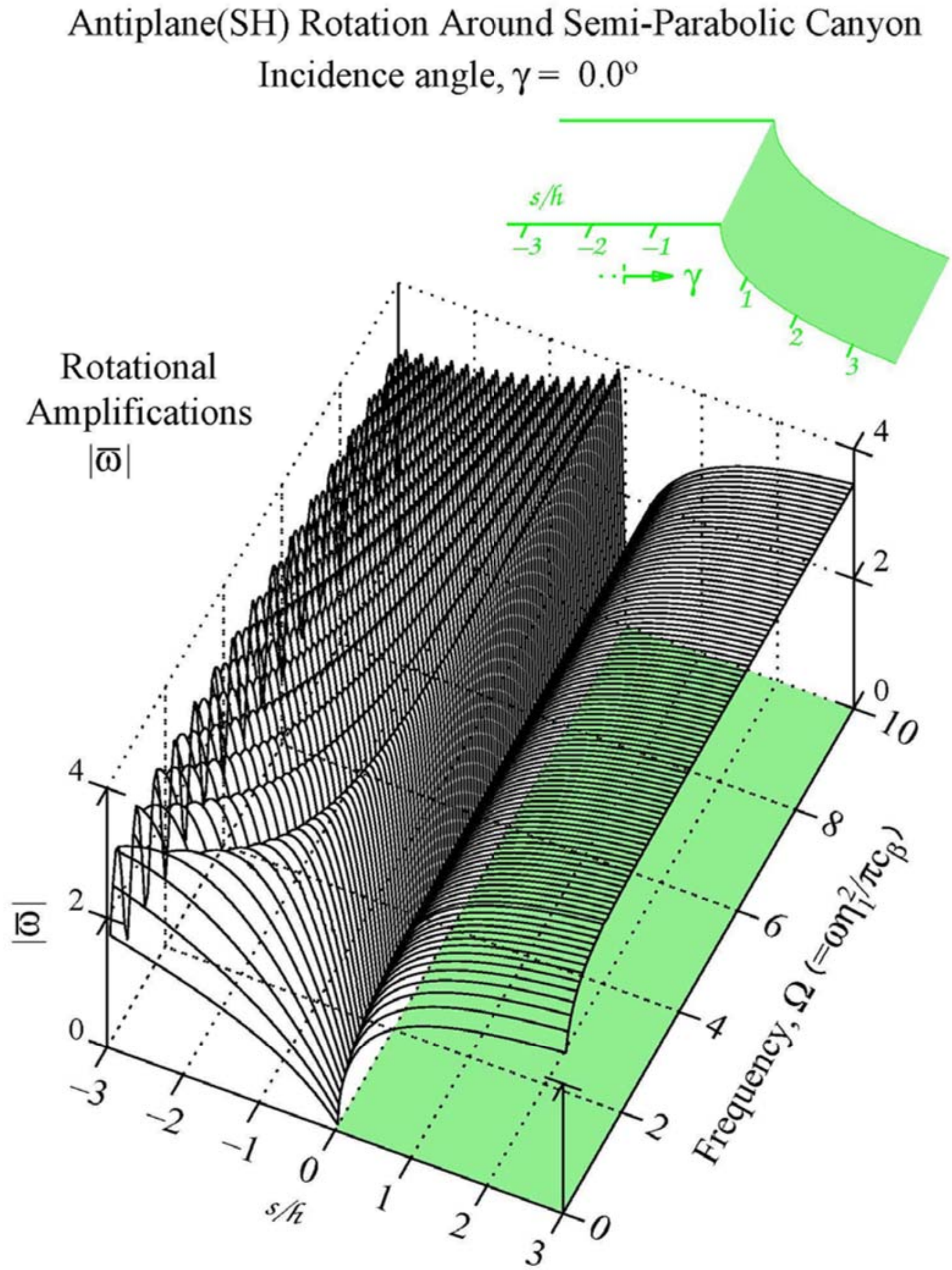

Fig. 4.7 3D Rotation Amplitudes for Horizontal Incidence, $\gamma = 0^{\circ}$

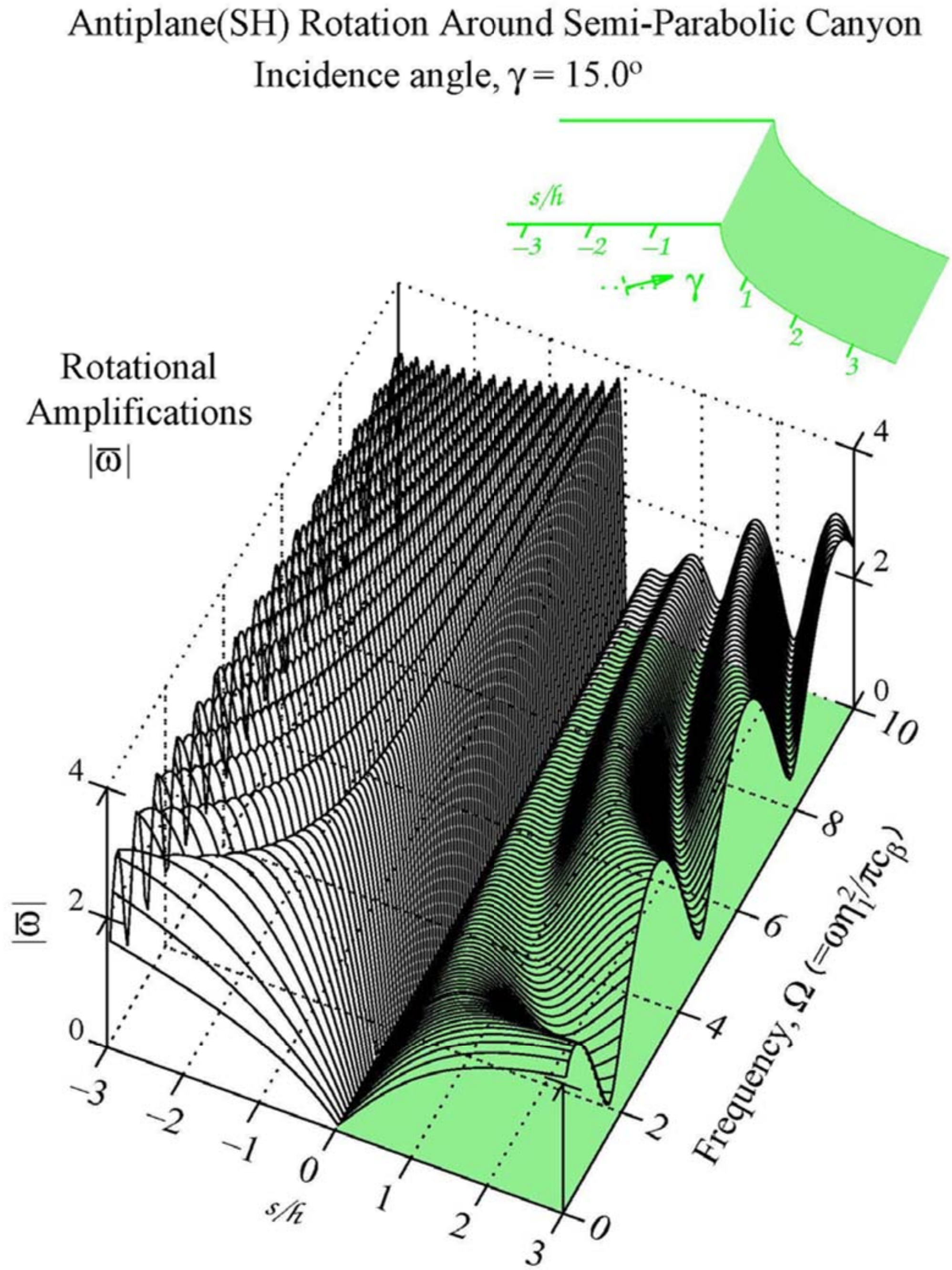

Fig. 4.8 3D Rotation Amplitudes for Oblique Incidence, $\gamma = 15^{\circ}$

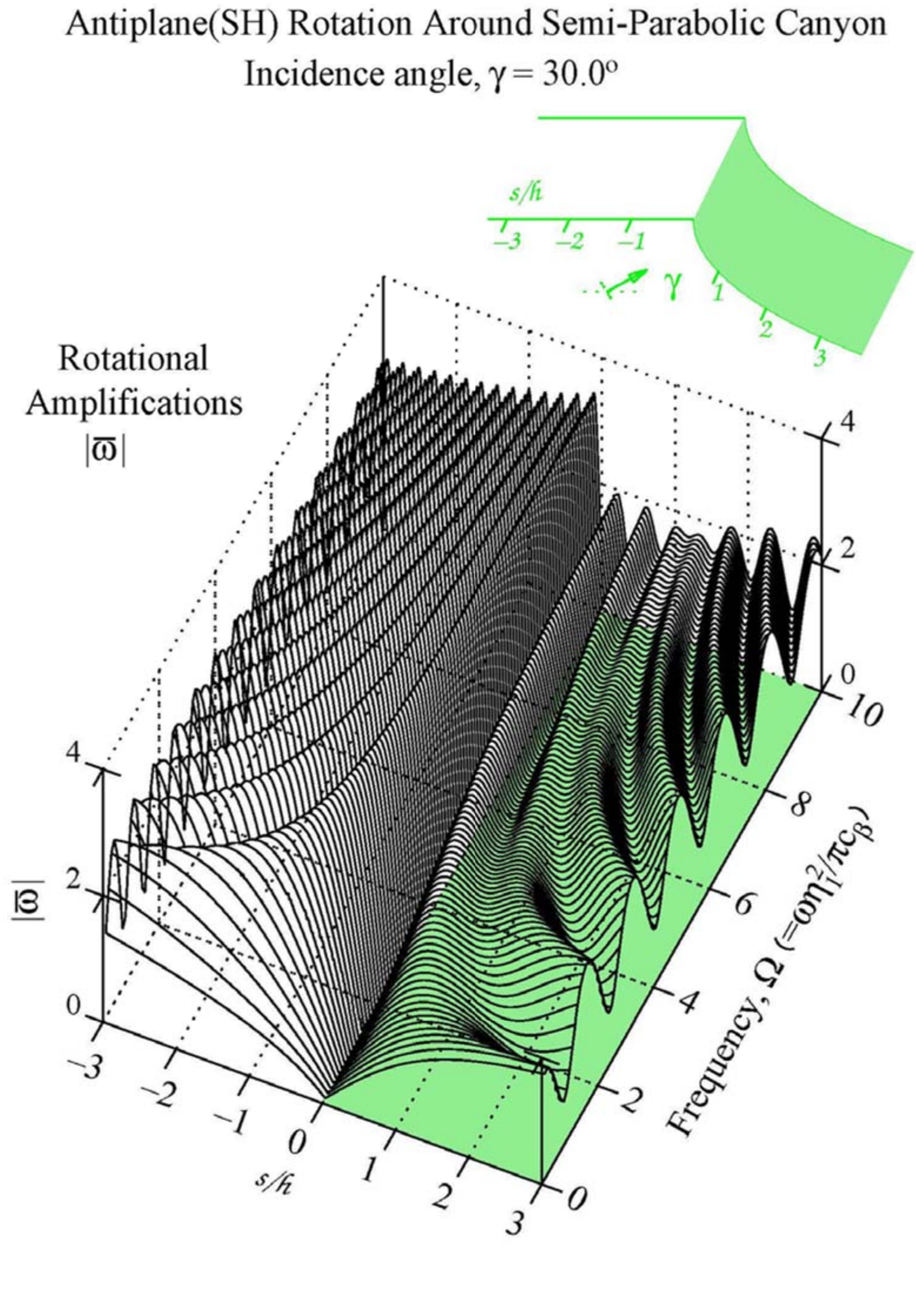

Fig. 4.9 3D Rotation Amplitudes for Oblique Incidence, $\gamma = 30^\circ$

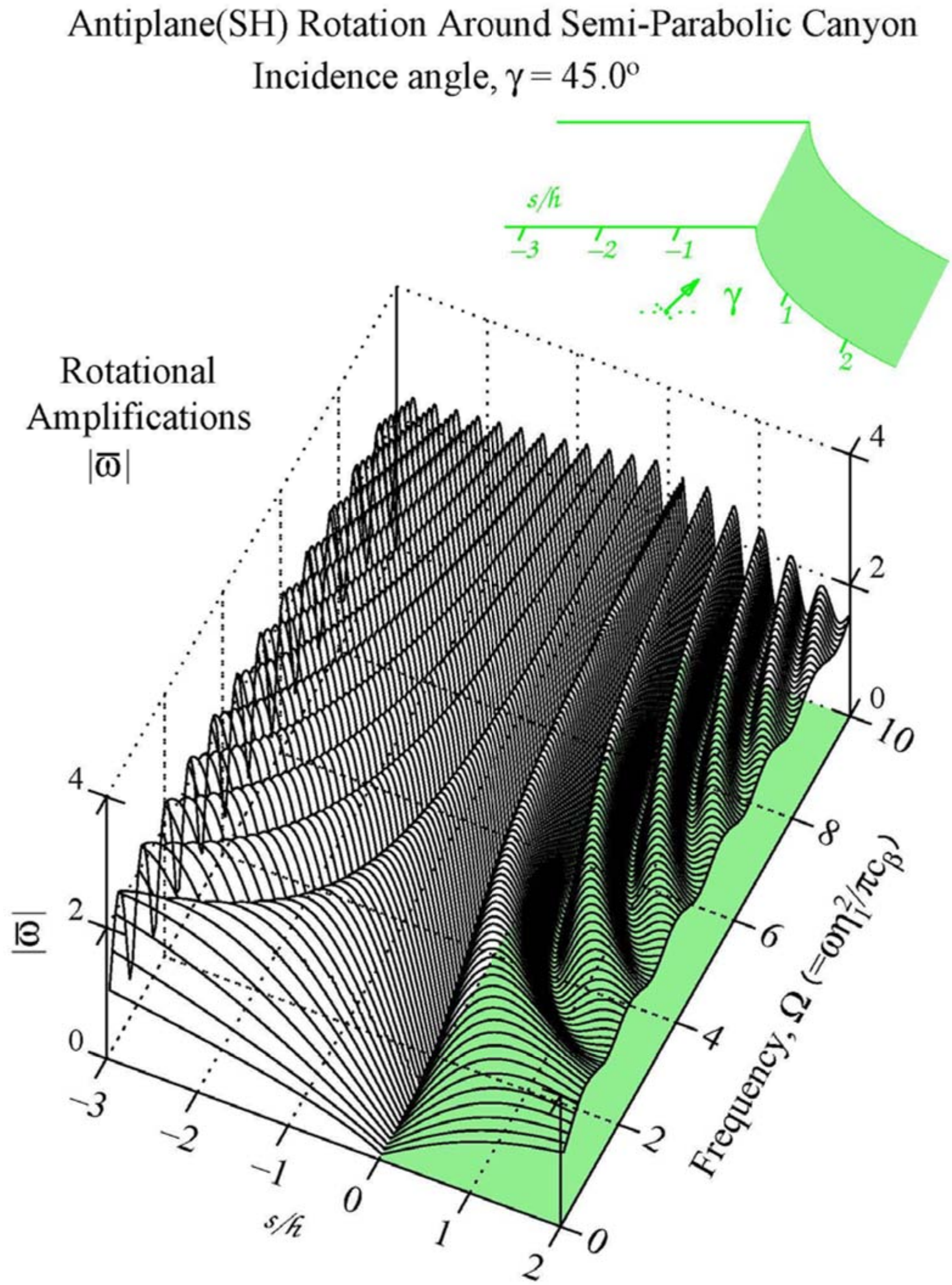

Fig. 4.10 3D Rotation Amplitudes for Oblique Incidence, $\gamma = 45^{\circ}$

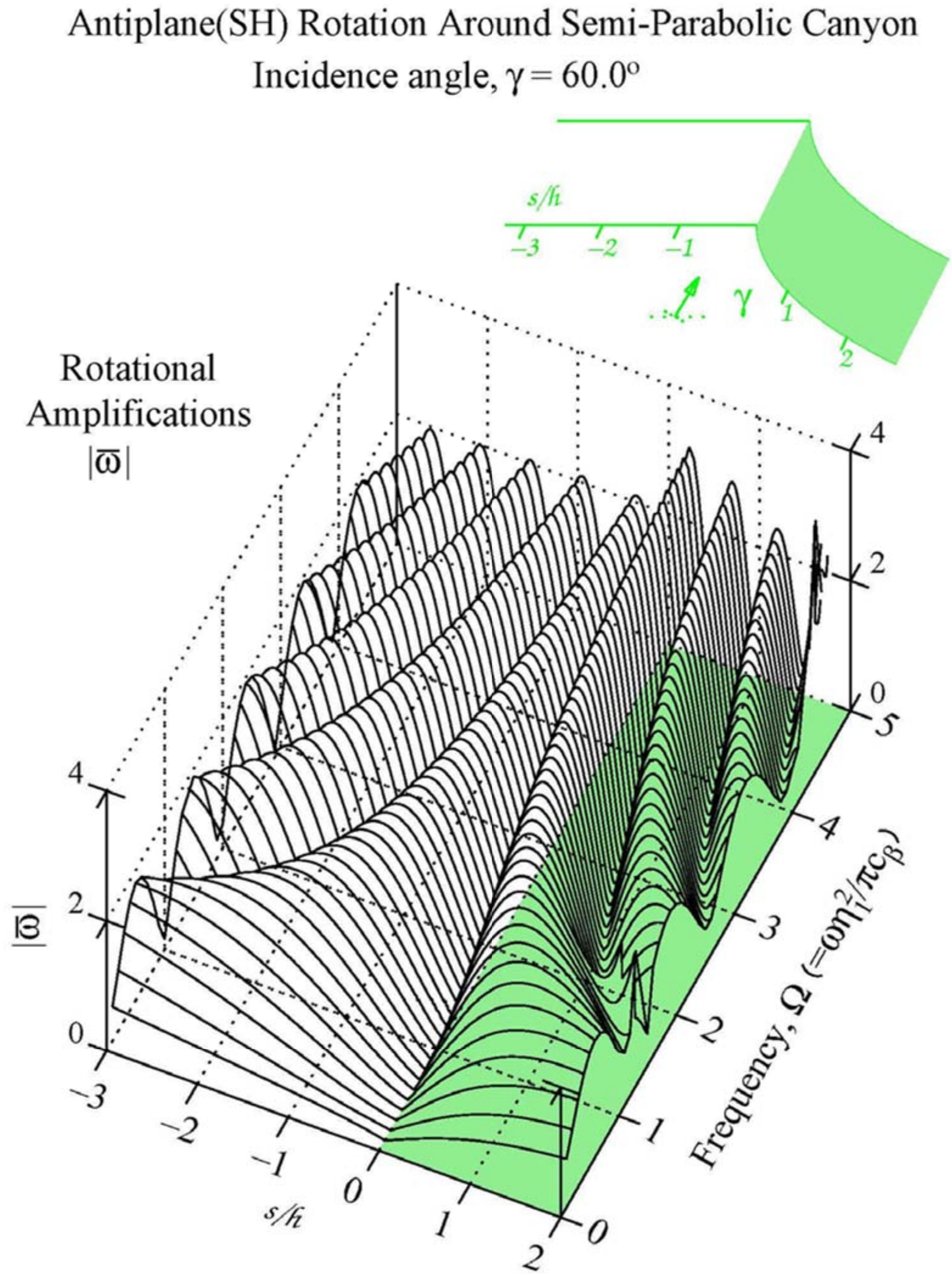

Fig. 4.11 3D Rotation Amplitudes for Oblique Incidence, $\gamma = 60^{\circ}$

IV. 6 Summary

The rocking component of rotations are derived and studied in Chapter IV. It showed that the rocking motion is zero at the half-space surface and the corresponding rocking motions on the semi-parabolic canyon surface are smaller than the corresponding torsional motions. Finally the resultant rotational motions combining torsion and rocking is presented. It shows that the resultant rotational motions are large both on the half-space and canyon surfaces.

Chapter V. The Dynamic Shear Stress Concentration Factor

V. 1 Introduction

As pointed out by Pao & Mow (1973), one of the major problems and analyses associated with the diffraction of elastic waves is the determination of stress concentration, which deals with Chapter I, Pao & Mow (1973) the sharp change and increase of stress over a nominal value in a localized region of a structural member due to geometric discontinuities in the presence of surface and sub-surface topographies, such as canyons, corners, cavities and notches.

The importance of understanding stress concentration in engineering design was noted since the beginning of the last century. Please refer to Chapter I of Pao & Mow (1973) for a detailed historical introduction (up till the early 1970's) on the subject of Stress Concentration. The reminder of this section is brief excerpts from there.

In as early as 1925, Timoshenko & Dietz (1925) stressed that

"… *It can be concluded that in many practical cases a very high stress concentration is produced by holes, grooves, and shape variations of cross sections. In the case of ductile material, this stress concentration does not have a weakening effect under static loading. In the case of brittle materials or ductile material under the action* *of stress reversal, however, the weakening effect of stress concentration may become of prime importance and it must be taken into account in consideration in actual design ... "*

Since then, Pao & Mow (1973) pointed out that the general progress in both theoretical analyses and experimental simulations and measurements greatly simulated the interest of the engineering public in stress concentration. Such understanding and importance was spread wider by the coming of the Second World War (1939-1945). During the war, ships and airplanes were produced in large numbers on both sides of the Atlantic. With the ships and airplanes in operation during the war, fractures in the full structures of ships and fatigue failures of aircraft components were reported in numerous times, serious enough to endanger the operations of the vessels.

Extension investigations and studies, as pointed out by Pao & Mow (1973), were made during and after the war to find out if such failures were caused by faulty design or defective welding. Right after the war, Timoshenko (1947) summarized the findings in a review on the link between fatigue failure and stress concentration factors. Since then, many theoretical and experimental results were conducted by many scientists and engineers. Their important results were compiled in one volume by Peterson (1953) in a publication titled Stress Concentration Design Factors, which had results for stress concentrations at grooves, notches, shoulder fillers, holes in plates & shafts and miscellaneous design elements.

It was around that decade (the 1950's), under the work of Takeuchi (1950), Ying & Truell (1956), White (1958) and Knopoff (1959), that the correct, true origin of Stress Concentration was identified with the diffraction of elastic waves. That is when Nishimura & Jimbo (1955) in their article, A Dynamic Problem of Stress Concentration – Stresses in the Vicinity of a Spherical Matter Included in an Elastic Solid under Dynamic Force, defined the dynamic stress concentration factor as:

$$\text{Dynamic Stress Concentration Factor at a Point} = \frac{\text{Stresses due to the Total Waves there}}{\text{Stress due to the Incident Wave (Without the Obstacle) there}}$$

This will be the stress concentration factor to be defined, computed and presented in this chapter.

From the 1970's till now, about forty years in time, articles, publication and textbooks on stress concentration factors continued to appear. The following is a list of some of those articles:

- K. Walker (1970) The Effect of Stress Ratio During Crack Propagation and Fatigue for 2024-T3 and 7075-T6 Aluminum
- Pao & Mow (1973) The Diffraction of Elastic Waves and Dynamic Stress Concentration
- J. M. Whitney (1974) Stress Fracture Criteria for Laminated Composites Containing Stress Concentrations
- D.P. Rooke, D.J. Cartwright, et al (1976) Compendium of Stress Intensity Factors

- Shigley, Mischke, Budynas & Liu (1989) Mechanical Engineering Design
- G.C. Cheng, H.M. Loree, R.D. Kamm & M.C. Fishbein (1993) Distribution of Circumferential Stress in Ruptured and Stable Atherosclerotic Lesions. A Structural Analysis with Histopathological Correlations
- R. E. Peterson (1997) Stress Concentration Design Factors
- Young (2002) Roark's Formulas for Stress and Strain
- Gao, Ji, Jager & Arzt (2003) Materials Become Insensitive to Flaws at Nanoscale: Lessons from Nature
- Wang (2003) Expressions of Stres Concentration Factors for an Eccentric Circular Hole in a Tension Orthotropic Finite-Width Strip
- C.E. Packard & C.A. Schuh – Acta Materialia, 2007 Initiation of Shear Bands near a Stress Concentration in Metallic Glass
- L Van Miegroet, et al – Structural and Multidisciplinary Optimization, 2007 Stress Concentration Minimization of 2D Filets using X-FEM and Level Set Description

V. 2 The Components of Shear Stresses

In the $x-y$ plane, where $z=$ constant, the components of stress due to the anti-plane (SH) component of waves, namely the incident and reflected plane waves and the scattered waves, are (and only) the shear stresses. Since the scattered and diffracted waves from the parabolic canyon are in the form of parabolic wave functions in parabolic coordinates, and the free-field incident and reflected plane waves are also expressed in parabolic coordinates, one can first consider the shear stress components also in the same parabolic coordinates. They are then the two components, $\tau_{z\eta}$ and $\tau_{z\xi}$ given by:

$$\begin{aligned} \tau_{z\eta} &= 2\mu\varepsilon_{z\eta} = \mu\frac{\partial W}{\partial \eta} \\ \tau_{z\xi} &= 2\mu\varepsilon_{z\xi} = \mu\frac{\partial W}{\partial \xi} \end{aligned} \tag{1}$$

$\tau_{z\eta}$ is the component of shear stress along and tangential to the lines $\eta=$ constant, and $\tau_{z\xi}$ is the component of shear stress along and tangential to the lines $\xi=$ constant. Since the contours of the lines $\eta=$ constant and $\xi=$ constant are orthogonal lines, the two components of shear stresses, as expected, are orthogonal components at each point.

Recall from Chapter II for the general expression for W given in Equation (1):

$$\begin{aligned} W &= W^{ff} + W^{s} \\ &= 2\sec\left(\gamma/2\right)\sum_{n=0}^{\infty} a_n\left[D_{2n}\left(\bar{\lambda}\eta\right) - \frac{iD'_{2n}\left(\lambda\eta_1\right)}{D'_{-2n-1}\left(\lambda\eta_1\right)}D_{-2n-1}\left(\lambda\eta\right)\right]D_{2n}\left(\lambda\xi\right) \end{aligned}$$ Chapter II Equation (1)

with a_n is the n[th] coefficient of the free-field waves, $a_n = \frac{(-1)^n}{(2n)!}\tan^{2n}\left(\frac{\gamma}{2}\right)$ and $\overline{\lambda} = \sqrt{2ik}$ and $\lambda=\sqrt{-2ik}$ are the wave numbers of the Weber Function. The expression for $\tau_{z\eta}$ and $\tau_{z\xi}$ can easily be derived:

$$\tau_{z\eta} = 2\mu\sec\left(\gamma/2\right)\sum_{n=0}^{\infty}a_n\left[\overline{\lambda}D_{2n}^{'}\left(\overline{\lambda}\eta\right) - \frac{iD_{2n}^{'}\left(\overline{\lambda}\eta_1\right)}{D_{-2n-1}^{'}\left(\lambda\eta_1\right)}\lambda D_{-2n-1}^{'}\left(\lambda\eta\right)\right]D_{2n}\left(\lambda\xi\right) \quad (2)$$

and

$$\tau_{z\xi} = 2\mu\sec\left(\gamma/2\right)\sum_{n=0}^{\infty}a_n\left[D_{2n}\left(\overline{\lambda}\eta\right) - \frac{iD_{2n}^{'}\left(\overline{\lambda}\eta_1\right)}{D_{-2n-1}^{'}\left(\lambda\eta_1\right)}D_{-2n-1}\left(\lambda\eta\right)\right]\lambda D_{2n}^{'}\left(\lambda\xi\right) \quad (3)$$

At the surface of the half-space, to the left of the parabolic canyon, where $y = 0$ and $\xi=0$, the shear stress $\tau_{z\xi}$ vanishes as $\tau_{zy}\big|_{y=0} = \tau_{z\xi}\big|_{\xi=0} = 0$ and only the shear stress $\tau_{z\eta}$ remains. On the other hand, at the surface of the parabolic canyon, where $\eta = \eta_1$ the shear stress $\tau_{z\eta}\big|_{\eta=\eta_1} = 0$ and $\tau_{z\xi}$ at $\eta = \eta_1$ simplifies to:

$$\begin{aligned}\tau_{z\xi}\big|_{\eta=\eta_1} &= 2\mu\sec\left(\gamma/2\right)\sum_{n=0}^{\infty}a_n\left[D_{2n}\left(\overline{\lambda}\eta\right) - \frac{iD_{2n}^{'}\left(\overline{\lambda}\eta_1\right)}{D_{-2n-1}^{'}\left(\lambda\eta_1\right)}D_{-2n-1}\left(\lambda\eta\right)\right]\lambda D_{2n}^{'}\left(\lambda\xi\right) \\ &= 2\mu\sec\left(\gamma/2\right)\sum_{n=0}^{\infty}a_n\left[\frac{i(-1)^n}{D_{-2n-1}^{'}\left(\lambda\eta_1\right)}\right]\lambda D_{2n}^{'}\left(\lambda\xi\right)\end{aligned} \quad (4)$$

Again, using the Wronskian relation to simplify the square term in the summation.

It is appropriate next also to consider the rectangular components of these shear stresses, namely the horizontal and vertical components of the shear traction:

$$\begin{aligned} \tau_{zx} &= 2\mu\varepsilon_{zx} = \mu\frac{\partial W}{\partial x} \\ \tau_{zy} &= 2\mu\varepsilon_{zy} = \mu\frac{\partial W}{\partial y} \end{aligned} \tag{5}$$

and the corresponding component of shear traction vector in the x-y plane

$$\tilde{\tau}_{zt} = \begin{pmatrix} \tau_{zx} \\ \tau_{zy} \end{pmatrix} = \mu \begin{pmatrix} \partial W / \partial x \\ \partial W / \partial y \end{pmatrix} \tag{6}$$

and the shear traction (resultant) amplitude is

$$|\tau_{zt}| = \left(|\tau_{zx}|^2 + |\tau_{zy}|^2\right)^{1/2} = \mu\left(\left|\partial W / \partial x\right|^2 + \left|\partial W / \partial y\right|^2\right)^{1/2} \tag{7}$$

The same normalization can be carried out here for the shear stress components τ_{zx} and τ_{zy}. Start with the shear stress components of the incident waves:

$$\tilde{\tau}^{i}_{zt} = \begin{pmatrix} \tau^{i}_{zx} \\ \tau^{i}_{zy} \end{pmatrix} = \mu \begin{pmatrix} \partial / \partial x \\ \partial / \partial y \end{pmatrix} W^{i} = \mu i k \begin{pmatrix} \cos\gamma \\ -\sin\gamma \end{pmatrix} W^{i} \tag{8}$$

where the subscript of the stress vector $\tilde{\tau}^{i}_{zt}$ is ‘z’ and ‘t’, with ‘z’ denoting the component of motion and ‘t’ denoting the resultant tangential or shear component in the x-y plane. It has the shear traction amplitude:

$$\left|\tau^i\right| = \left(\left|\tau^i_{zx}\right|^2 + \left|\tau^i_{zy}\right|^2\right)^{1/2} = \mu k \tag{9}$$

This will be used as the normalization factor for all the shear stress terms to be presented, and the normalized shear stresses, τ_{zx} and τ_{zy} to be presented in all subsequent sections will take the form

$$\begin{aligned}
\bar{\tau}_{zx} &= \tau_{zx}\big/\left|\tau^i\right| = \mu\left(\partial W/\partial x\right)\big/\mu k = 1/k\left(\partial W/\partial x\right) \\
\bar{\tau}_{zy} &= \tau_{zy}\big/\left|\tau^i\right| = \mu\left(\partial W/\partial y\right)\big/\mu k = 1/k\left(\partial W/\partial y\right)
\end{aligned} \tag{10}$$

and the normalized shear traction amplitude is

$$\left|\bar{\tau}_{zt}\right| = \left(\left|\bar{\tau}_{zx}\right|^2 + \left|\bar{\tau}_{zy}\right|^2\right)^{1/2} = 1/k\left(\left|\partial W/\partial x\right|^2 + \left|\partial W/\partial y\right|^2\right)^{1/2} \tag{11}$$

The shear stress amplitudes $\left|\bar{\tau}_{zx}\right|, \left|\bar{\tau}_{zy}\right|$ and $\left|\bar{\tau}_{zt}\right|$ will also be referred in what follows as the stress concentration factors.

It is observed that the equations for the shear stresses in Equation (5) is of the same form as the form as the rotational components of motions given in Chapter III

$$\tilde{\omega} = \begin{pmatrix} \omega_x \\ \omega_y \\ 0 \end{pmatrix} = \begin{pmatrix} \omega_{Rock} \\ \omega_{Tor} \\ 0 \end{pmatrix} = \tfrac{1}{2} \begin{pmatrix} \partial W / \partial y \\ -\partial W / \partial x \\ 0 \end{pmatrix} \qquad \text{Chapter III Equation (3)}$$

where it is seen that the x-component shear stress τ_{zx} is of the same form as the torsional motion $\omega_y = \omega_{Tor}$, and the y-component shear stress τ_{zy} is of the same form as the rocking motions, $\omega_x = \omega_{Rock}$, both involving the first derivatives of x and y

$$\begin{aligned} \omega_{Tor} &= \omega_y = -\tfrac{1}{2}\left(\frac{\partial W}{\partial x}\right), \text{ while } \tau_{zx} = 2\mu\varepsilon_{zx} = \mu\frac{\partial W}{\partial x} \\ \omega_{Rock} &= \omega_x = -\tfrac{1}{2}\left(\frac{\partial W}{\partial y}\right), \text{ while } \tau_{zy} = 2\mu\varepsilon_{zy} = \mu\frac{\partial W}{\partial y} \end{aligned} \qquad (12)$$

together with the resultant rotation amplitude studied:

$$|\omega| = \left(|\omega_x|^2 + |\omega_y|^2\right)^{1/2} = \left(|\omega_{Rock}|^2 + |\omega_{Tor}|^2\right)^{1/2} \qquad \text{Chapter IV Equation (22)}$$

of the form, comparing with Equation (7) here

$$|\omega| = \frac{1}{2}\left(\left|\frac{\partial W}{\partial x}\right|^2 + \left|\frac{\partial W}{\partial y}\right|^2\right)^{1/2}, \text{ while } |\tau_{zt}| = \mu\left(\left|\frac{\partial W}{\partial x}\right|^2 + \left|\frac{\partial W}{\partial y}\right|^2\right)^{1/2} \qquad (13)$$

Recall Chater III and IV on torsional, rocking and resultant components of rotational motions, where the rotational motions are normalized to the rotation vector amplitude of the incident wave, $\left|\tilde{\omega}^i\right|$ where from Chapter III

$$\left|\tilde{\omega}^i\right| = \left(\left|\omega_x^i\right|^2 + \left|\omega_y^i\right|^2\right)^{1/2} = k/2\left|W^i\right| = k/2 \qquad \text{Chapter III Equation (7)}$$

so that the normalized components of torsion and rocking takes the form

$$\begin{aligned}\bar{\omega}_{Tor} &= \omega_{Tor}\Big/\left|\omega^i\right| = 2/k\left|\omega_{Tor}\right| = 2/k\left(\omega_{Tor}^{ff} + \omega_{Tor}^{s}\right)\\ &= 2/k\left(-1/2\,\partial W/\partial x\right) = -1/k\,\partial W/\partial x\end{aligned} \qquad \text{Chapter III Equation (24)}$$

$$\begin{aligned}\omega_{Rock} &= \omega_{Rock}\Big/\left|\omega^i\right| = \left(2/k\right)\omega_{Rock} = 2/k\left(\omega_{Rock}^{ff} + \omega_{Rock}^{s}\right)\\ &= 2/k\left(1/2\,\partial W/\partial y\right) = 1/k\left(\partial W/\partial y\right)\end{aligned} \qquad \text{Chapter IV Equation (17)}$$

and the resultant (normalized) rotational amplitude is

$$\begin{aligned}\left|\omega\right| &= \left(\left|\omega_x\right|^2 + \left|\omega_y\right|^2\right)^{1/2} = \left(\left|\omega_{Rock}\right|^2 + \left|\omega_{Tor}\right|^2\right)^{1/2}\\ &= 1/k\left(\left|\partial W/\partial x\right|^2 + \left|\partial W/\partial y\right|^2\right)^{1/2}\end{aligned} \qquad \text{Chapter IV Equation (22)}$$

Comparing Equation (10) with Equation (12) above, together with Equation (24) of Chapter III for torsion shows that

$$\bar{\tau}_{zx} = 1/k\left(\partial W/\partial x\right) = -\bar{\omega}_{Tor} \qquad (14)$$

or the normalized x-component shear stresses is identical to the negative of normalized torsion.

Similary comparing Equation (10) with Equation (12) above, together with Equation (17) of Chapter IV for rocking shows that

$$\overline{\tau}_{zy} = \frac{1}{k}\left(\frac{\partial W}{\partial y}\right) = -\overline{\omega}_{Rock} \tag{15}$$

or the normalized y-component shear stresses is identical to normalized rocking.

Finally, the resultant shear traction

$$\begin{aligned} \left|\overline{\tau}_{zt}\right| &= \left[\left|\overline{\tau}_{zx}\right|^2 + \left|\overline{\tau}_{zy}\right|^2\right]^{1/2} \\ &= \frac{1}{k}\left(\left|\frac{\partial W}{\partial x}\right|^2 + \left|\frac{\partial W}{\partial y}\right|^2\right)^{1/2} = \left|\overline{\omega}\right|, \text{ the resultant rotation} \end{aligned} \tag{16}$$

or the normalized shear traction amplitudes is identical to normalized resultant rotation amplitude.

Thus all previous figures of plots of torsion in Chapter III and rocking and rotation in Chapter IV can simply be plotted and relabeled respectively as the normalized x- and y-component shear stresses amplitudes and shear traction (resultant) amplitudes here in subsequent section, without any need for new calculation.

V.3 Dynamic Shear Stress Concentration Factors, $\left|\bar{\tau}_{zx}\right|$

Since $$\bar{\tau}_{zx} = {}^{1}\!/_{k}\left({}^{\partial W}\!/_{\partial x}\right) = -\bar{\omega}_{Tor} \qquad \text{Equation (14) above}$$

so as stated earlier, all derivations for expression for torsion in Chapter III will be used and will not be repeated here.

The normalized shear stress amplitude $\bar{\tau}_{zx}$ at the half-space and parabolic canyon surface respectively takes the form, from Chapter III, Equation (16b)

$$\begin{aligned}\bar{\tau}_{zx}\Big|_{\substack{y=0\\(\xi=0)}} &= \left(-\bar{\omega}_{Tor}\Big|_{\substack{y=0\\(\xi=0)}}\right) = 2i\cos\gamma e^{ik\cos\gamma x}\\ &+\frac{2\sec\left({}^{\gamma}\!/_{2}\right)}{k\eta^{2}}\sum_{n=0}^{\infty}\frac{(+i)\,a_n D'_{2n}\left(\bar{\lambda}\eta_1\right)}{D'_{-2n-1}\left(\lambda\eta_1\right)}\left[\lambda\eta D'_{-2n-1}\left(\lambda\eta\right)D_{2n}\left(0\right)\right]\end{aligned} \tag{17}$$

and from Chapter III, Equation (22)

$$\bar{\tau}_{zx}\Big|_{\eta=\eta_1} = \left(-\bar{\omega}_{Tor}\Big|_{\eta=\eta_1}\right) = \frac{2\sec\left({}^{\gamma}\!/_{2}\right)}{k\left(\xi^2+\eta_1^2\right)}\left(\lambda\xi\right)\sum_{n=0}^{\infty} ia_n\left(-1\right)^n\frac{D'_{2n}\left(\lambda\xi\right)}{D'_{-2n-1}\left(\lambda\eta_1\right)} \tag{18}$$

respectively. Its amplitude $\left|\bar{\tau}_{zx}\right|$ will also be called the stress concentration factor.

Fig. 5.1 is a three-dimensional plot of the normalized shear stress amplitudes, $\left|\overline{\tau}_{zx}\right|$, plotted versus the dimensionless distance s/h at the dimensionless frequency Ω for the horizontal angle of incidence of $\gamma = 0^{\circ}$. They are computed using Equations (17) and (19) for $\gamma = 0^{\circ}$ with only the term $n = 0$. Please refer to Section III.4 Torsional Motions: Horizontal Angel of Incidence $\gamma = 0^{\circ}$ for a detailed description of the figure, since from Equation (14) above, $\overline{\tau}_{zx} = 1/k \left(\partial W / \partial x \right) = -\overline{\omega}_{Tor}$.

As in the previous chapters, the shape of the half-space and canyon surface model on which the displacements are calculated is outlined on the top-left graph of the figure, and it is now in gold color. The gold arrow again indicates the corresponding direction of the incident SH wave W^i which is assumed to be coming from the left-side towards the canyon. The 1-term translational displacement W for $\gamma = 0^{\circ}$ is

$$W\Big|_{\substack{y=0 \\ \eta=\eta_1}} = \frac{2i}{D_{-1}^{'}\left(\lambda\eta_1\right)} D_0\left(\lambda\xi\right) \qquad \text{Chapter II Equation (19)}$$

and the corresponding 1-term shear stress amplitude $\left|\overline{\tau}_{zx}\right|$ from Equation (18) simplified to (as in Chapter III for torsion):

$$\left|\overline{\tau}_{zx}\right|_{\substack{y=0 \\ \eta=\eta_1}} \left(= \left|\overline{\omega_{Tor}}\right|_{\substack{y=0 \\ \eta=\eta_1}} \right) = \frac{2\xi^2}{\left(\xi^2+\eta_1^2\right)\left|D_{-1}^{'}\left(\lambda\eta_1\right)\right|} \qquad \text{Chapter III Equation (27)}$$

The shear stress along the canyon surface is not a constant, but instead, a quotient of quadratic function of ξ^2 being 0 at the vertex $\xi = 0$. Far from there, as ξ increases, the amplitude approaches the asymptote

$$\left|\overline{\tau}_{zx}\right|_{\substack{y=0\\ \eta=\eta_1}} \left(\left|\varpi_{Tor}\right|_{\substack{\gamma=0\\ \eta=\eta_1}}\right) \sim \frac{2}{\left|D_{-1}^{'}\left(\lambda\eta_1\right)\right|} \text{ as } \xi \to \infty \qquad \text{Chapter III Equation (28)}$$

an asymptote close to 4 as in the case of translation displacement (Equation (21) Chapter II). On the half-space surface, the shear stress amplitude $\left|\overline{\tau}_{zx}\right|$ in Fig 5.1 does resemble that of the translational motion, namely the free-field torsional motions interfere with the scattered and diffracted torsional motions to result in a standing wave pattern.

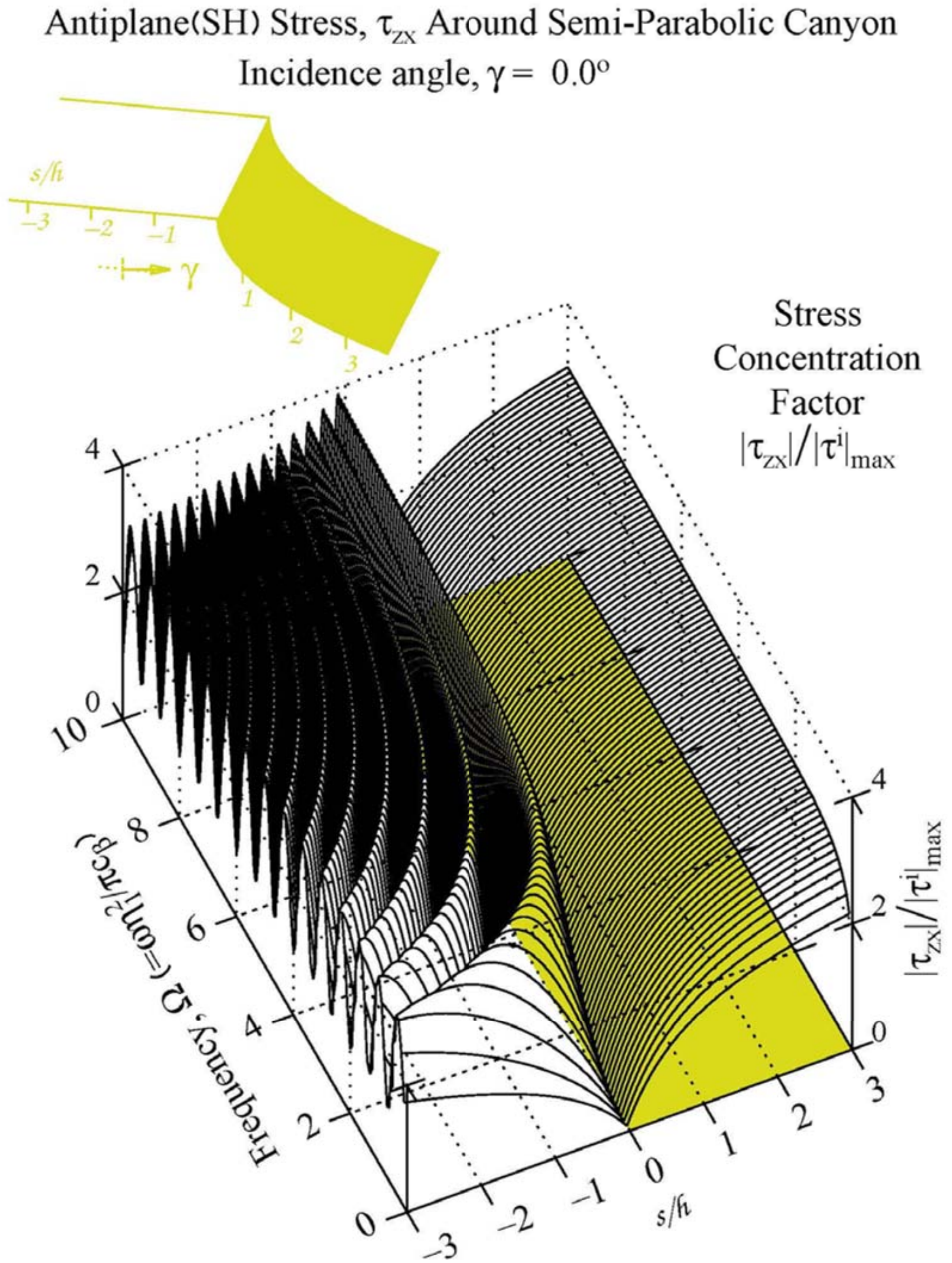

Fig. 5.1 3D Shear Stress Amplitudes, $\left|\overline{\tau}_{zx}\right|$ for Horizontal Incidence, $\gamma = 0^{\circ}$

Fig. 5.2 to Fig. 5.5 are the 3D plots of the normalized shear stress concentration factor, $\left|\overline{\tau}_{zx}\right|$ (= torsional rotation) amplitudes plotted vs.

1) The dimensionless distance s/h measured along the half-space and canyon surface and

2) The dimensionless frequency $\Omega = \omega\eta_0^2 / \pi\beta = 2\eta_0^2 / \lambda = 4h/\lambda$,

Respectively for incidence angles of $\gamma = 15^\circ, 30^\circ, 45^\circ$ and 60°. The reader are advised refer to Section III.5 Torsional Motions: Oblique Angles of Incidence $\gamma = 15^\circ, 30^\circ, 45^\circ$ and 60° for a detailed description of the figure, since from Equation (14) above, $\overline{\tau}_{zx} = 1/k \left(\partial W / \partial x \right) = -\overline{\omega}_{Tor}$. They are identical to Fig 3.7 to Fig. 3.10, the 3D plots of the torsional rotation amplitudes.

The normalized shear stress amplitudes in Fig. 5.2 through 5.5, as the case of torsional amplitudes in Chapter III, are consistent with the presented in Chapter II for the corresponding displacement amplitudes, with the same range of convergence. This is no surprise, as the displacement and shear stress are respectively given by

$$W\Big|_{\eta=\eta_1} = 2\sec\left(\gamma/2\right)\sum_{n=0}^{\infty} i a_n \frac{D_{2n}\left(\lambda\xi\right)}{D'_{-2n-1}\left(\lambda\eta_1\right)} \qquad \text{Chapter II Equation (12)}$$

$$\bar{\tau}_{zx}\Big|_{\eta=\eta_1} = \left(-\bar{\omega}_{Tor}\Big|_{\eta=\eta_1}\right) = \frac{2\sec\left(\gamma/2\right)}{k\left(\xi^2+\eta_1^2\right)}\left(\lambda\xi\right)\sum_{n=0}^{\infty} ia_n\left(-1\right)^n \frac{D'_{2n}\left(\lambda\xi\right)}{D'_{-2n-1}\left(\lambda\eta_1\right)} \qquad \text{Equation (18) above}$$

so that the summation above involves the same coefficients, $2\sec\left(\gamma/2\right)\frac{ia_n\left(-1\right)^n}{D'_{-2n-1}\left(\lambda\eta_1\right)}$, times $D_{2n}\left(\lambda\xi\right)$ for displacement and $\frac{\lambda\xi}{k\left(\xi^2+\eta_1^2\right)}D'_{2n}\left(\lambda\xi\right)$ for shear stress.

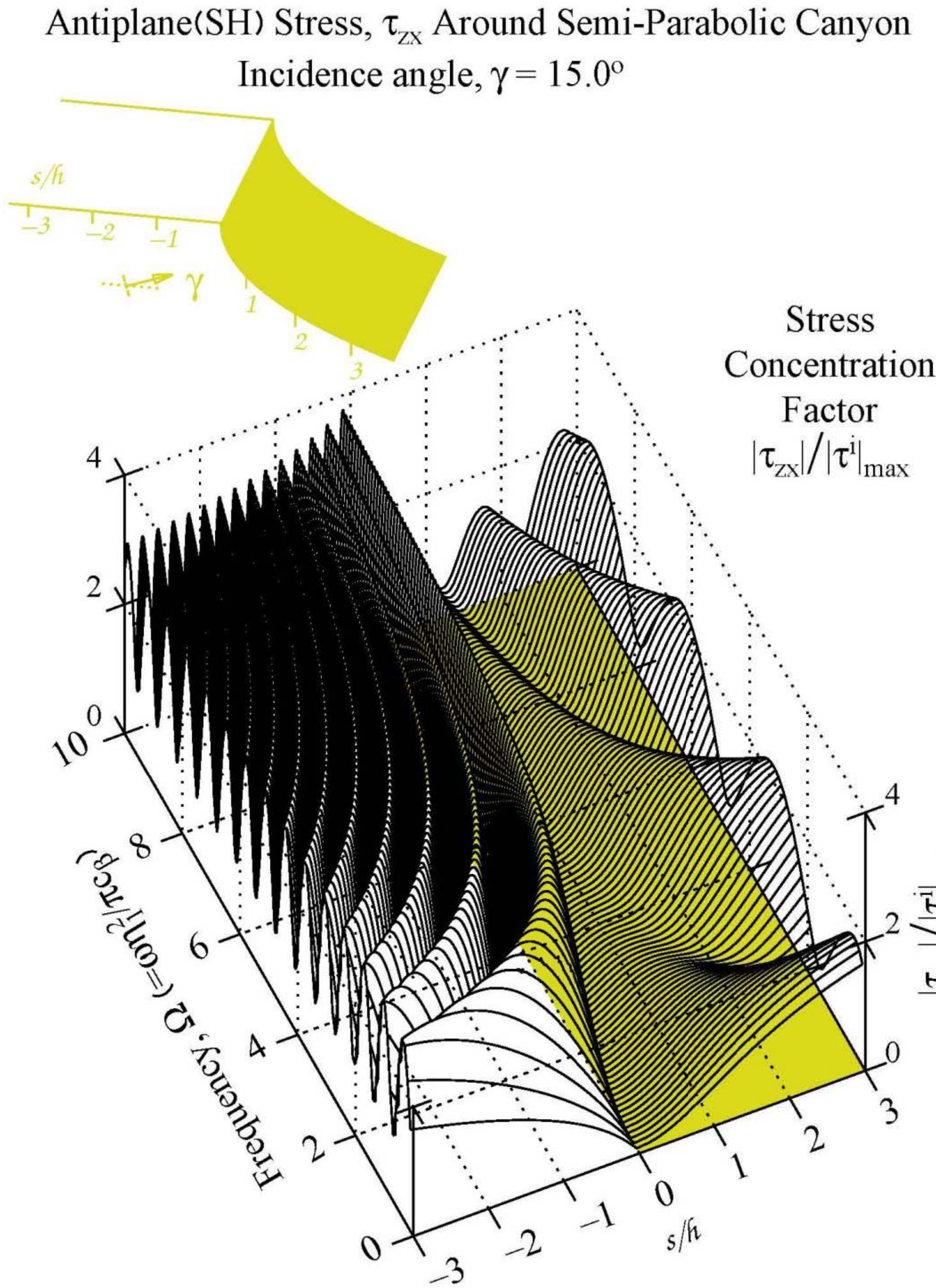

Fig. 5.2 3D Shear Stress Amplitudes, $\left|\bar{\tau}_{zx}\right|$ for Oblique Incidence, $\gamma = 15^{\circ}$

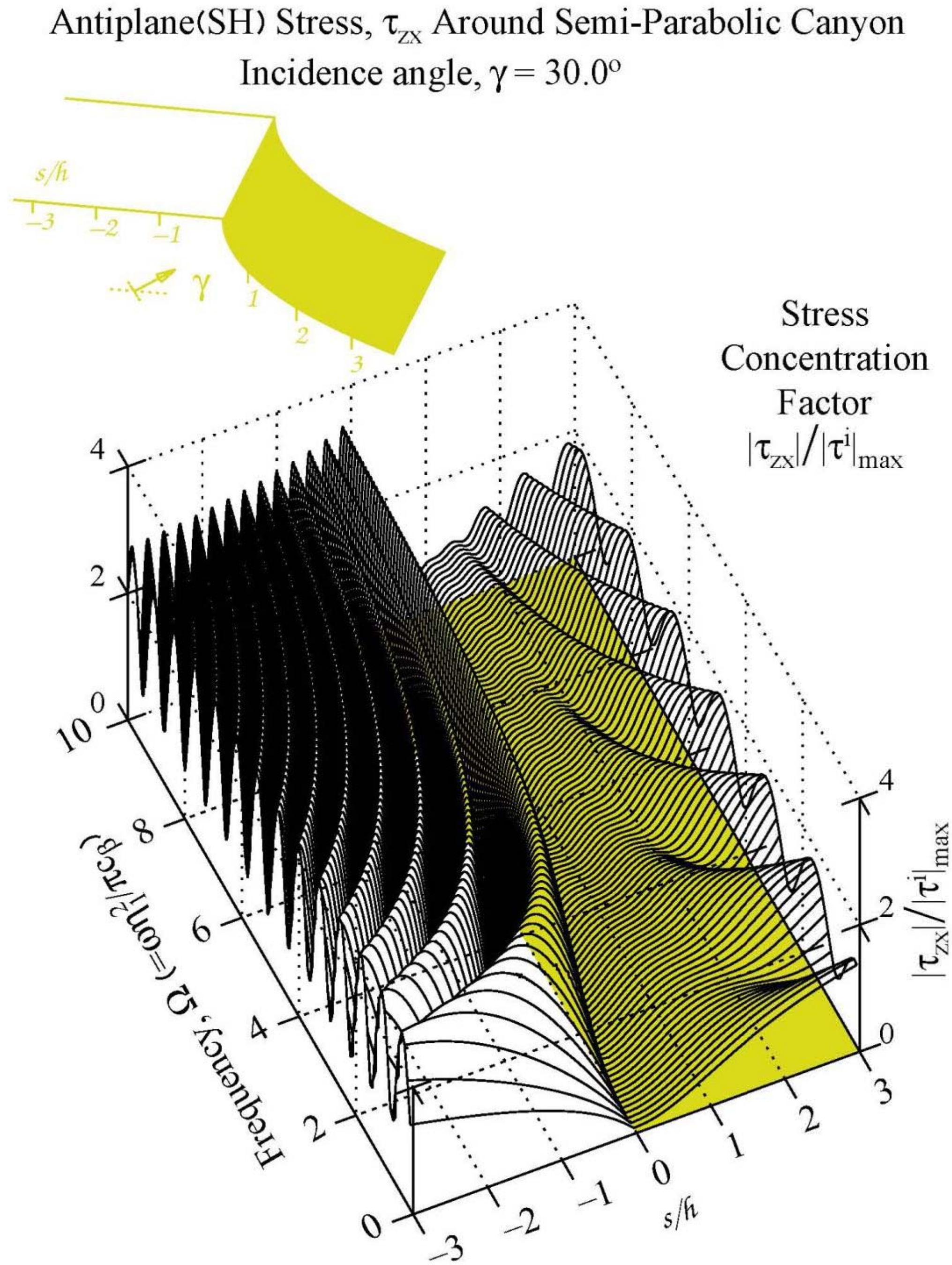

Fig. 5.3 3D Shear Stress Amplitudes, $\left|\bar{\tau}_{zx}\right|$ for Oblique Incidence, $\gamma = 30^\circ$

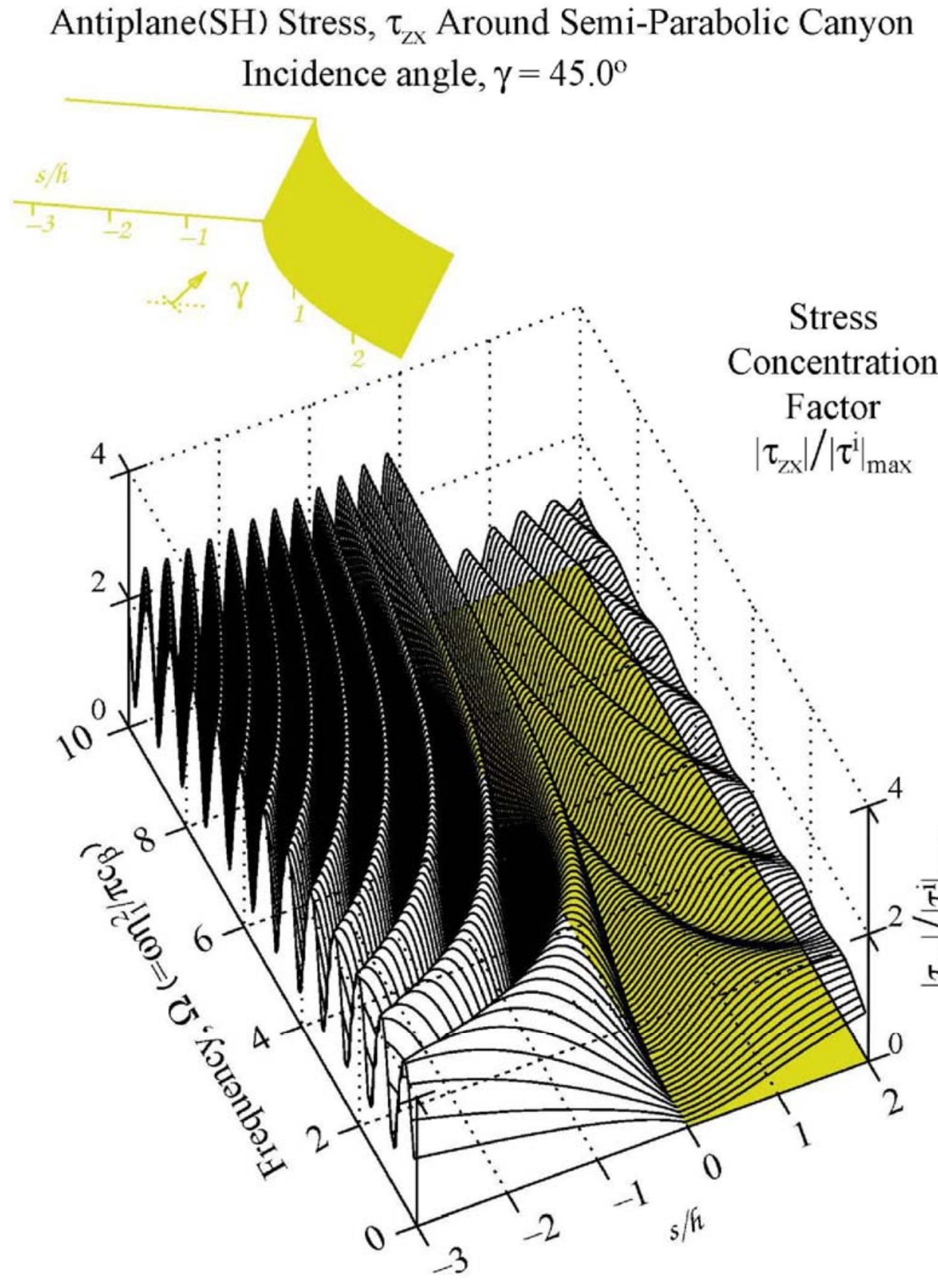

Fig. 5.4 3D Shear Stress Amplitudes, $\left|\bar{\tau}_{zx}\right|$ for Oblique Incidence, $\gamma = 45^\circ$

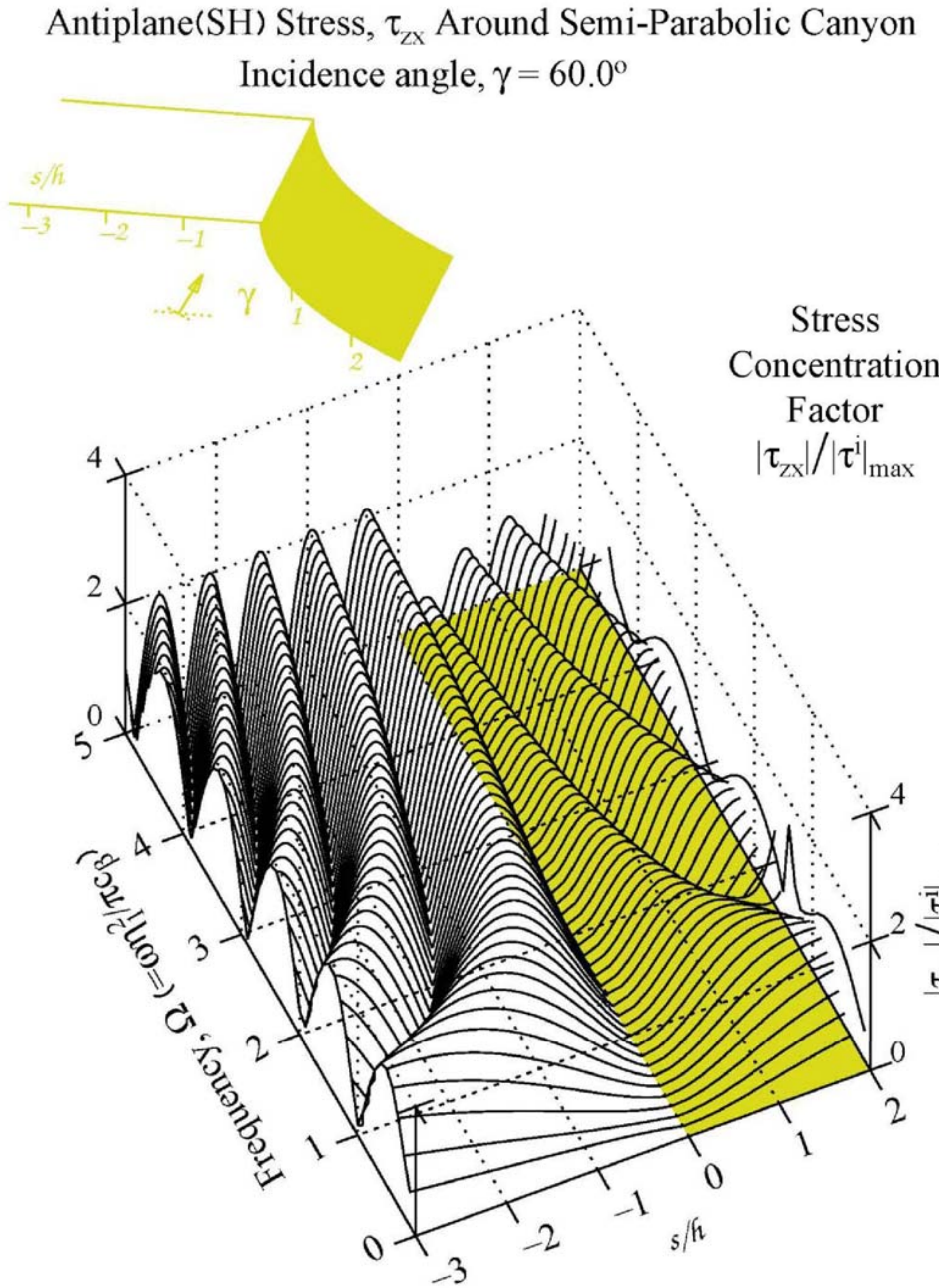

Fig. 5.5 3D Shear Stress Amplitudes, $\left|\bar{\tau}_{zx}\right|$ for Oblique Incidence, $\gamma = 60^{\circ}$

V. 4 Dynamic Shear Stress Concentration Factors, $\left|\bar{\tau}_{zy}\right|$

Since $\bar{\tau}_{zy} = {}^{1}\!/_{k}\left({}^{\partial W}\!/_{\partial y}\right) = -\bar{\omega}_{Rock}$ Equation (15) above

so as stated earlier, all derivations for expressions for rocking rotations in Chapter IV will be used and will not be repeated here.

The normalized shear stress amplitude $\left|\bar{\tau}_{zy}\right|$ at the half-space and parabolic canyon surface respectively takes the form, from Equation (19) of Chapter IV

$$\bar{\tau}_{zy}\Big|_{y=0}\left(=\varpi_{Rock}\Big|_{y=0}\right)=0 \tag{19}$$

and

$$\bar{\tau}_{zy}\Big|_{\eta=\eta_1}\left(=\bar{\omega}_{Rock}\Big|_{\eta=\eta_1}\right)=\frac{2\sec\left({}^{\gamma}\!/_{2}\right)}{k\left(\xi^2+\eta_1^2\right)}\left(\lambda\eta_1\right)\sum_{n=0}^{\infty}\frac{ia_n\left(-1\right)^n}{D'_{-2n-1}\left(\lambda\eta_1\right)}D'_{2n}\left(\lambda\xi\right) \tag{20}$$

respectively.

Fig. 5.6 is a 3D plot of the normalized shear stress amplitudes $\left|\bar{\tau}_{zy}\right|$ plotted vs. the dimensionless distance ${}^{s}\!/_{h}$ at the dimensionless frequency Ω for the horizontal angle of incidence of $\gamma=0^{\circ}$. They are computed using Equations (19) and (20) for $\gamma=0^{\circ}$ with only the term $n = 0$. Please refer to Section IV.3 Rocking Motions: Horizontal Angle of Incidence $\gamma = 0^{\circ}$ for a detailed description of the figure since form Equation (15) above, $\bar{\tau}_{zy} = {}^{1}\!/\!_{k}\left({}^{\partial W}\!/\!_{\partial y}\right) = -\bar{\omega}_{Rock}$

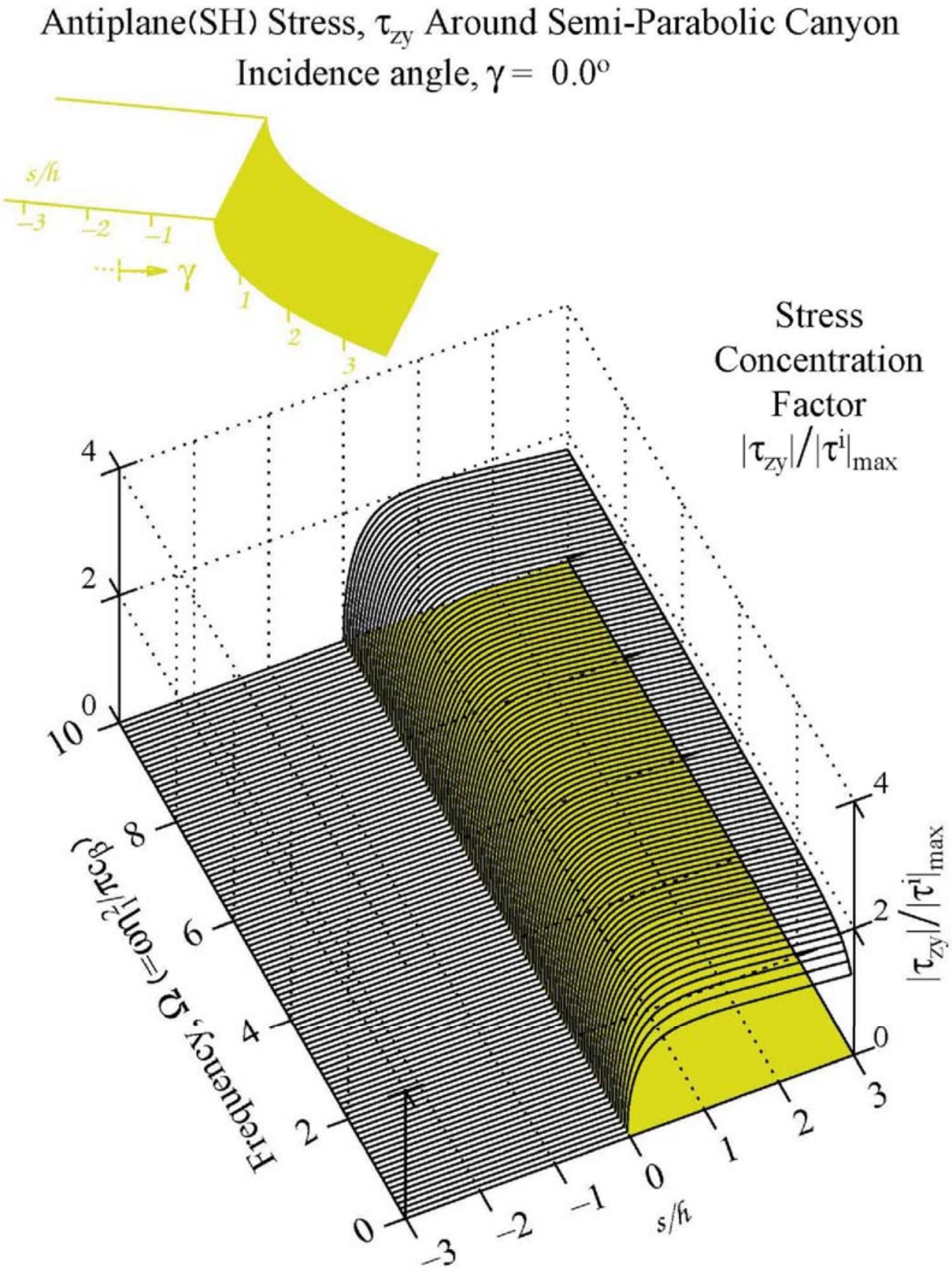

Fig. 5.6 3D Shear Stress Amplitudes, $\left|\bar{\tau}_{zy}\right|$ for Horizontal Incidence, $\gamma = 0^\circ$

Fig. 5.7 to Fig. 5.10 are the 3D plots of the normalized shear stress, $\left|\overline{\tau}_{zy}\right|$(= rocking rotation) amplitudes plotted vs.

1) The dimensionless distance s/h measured along the half-space and canyon surface and
2) The dimensionless frequency $\Omega = \omega\eta_0^2/\pi\beta = 2\eta_0^2/\lambda = 4h/\lambda$

respectively for incidence angles of $\gamma = 15^\circ, 30^\circ, 45^\circ$ and 60°. The reader are advised to refer to Section IV.4 – Rocking Motions: Oblique Angles of Incidence $\gamma = 15^\circ, 30^\circ, 45^\circ$ and 60° for a detailed description of the figures, since from equation (15) above, $\overline{\tau}_{zy} = 1/k\left(\partial W/\partial y\right) = -\overline{\omega}_{Rock}$. They are identical to Fig. 4.3 to Fig. 4.6, the 3D plots of the rocking rotation amplitudes. All trends are described there.

The normalized shear stress amplitudes $\left|\overline{\tau}_{zy}\right|$ in Fig. 5.7 through 5.10 as in the case of rocking amplitudes in Chapter IV are consistent with the results presented in Chapter II for the corresponding displacement amplitudes, Chapter III for the corresponding torsion rotation amplitudes, the shear stress $\left|\overline{\tau}_{zx}\right|$ in the previous section, all with the same range of convergence. This consistency is expected, of no surprise, as the displacement, normalized shear stress $\left|\overline{\tau}_{zx}\right|$ and $\left|\overline{\tau}_{zy}\right|$ are respectively given by

$$W\big|_{\eta=\eta_1} = 2\sec\left(\gamma/2\right)\sum_{n=0}^{\infty}\frac{ia_n\left(-1\right)^n}{D'_{-2n-1}\left(\lambda\eta_1\right)}D_{2n}\left(\lambda\xi\right) \qquad \text{Chapter II Equation (12)}$$

$$\bar{\tau}_{zx}\big|_{\eta=\eta_1} = \left(-\bar{\omega}_{Tor}\big|_{\eta=\eta_1}\right) = \frac{2\sec\left(\gamma/2\right)}{k\left(\xi^2+\eta_1^2\right)}\left(\lambda\xi\right)\sum_{n=0}^{\infty}ia_n\left(-1\right)^n\frac{D'_{2n}\left(\lambda\xi\right)}{D'_{-2n-1}\left(\lambda\eta_1\right)} \qquad \text{Equation (18) above}$$

$$\bar{\tau}_{zy}\big|_{\eta=\eta_1} \left(=\bar{\omega}_{Rock}\big|_{\eta=\eta_1}\right) = \frac{2\sec\left(\gamma/2\right)}{k\left(\xi^2+\eta_1^2\right)}\left(\lambda\eta_1\right)\sum_{n=0}^{\infty}\frac{ia_n\left(-1\right)^n}{D'_{-2n-1}\left(\lambda\eta_1\right)}D'_{2n}\left(\lambda\xi\right) \qquad \text{Equation (20) above}$$

so that the summation above involves the same coefficients namely summation of the terms $2\sec\left(\gamma/2\right)\frac{ia_n\left(-1\right)^n}{D'_{-2n-1}\left(\lambda\eta_1\right)}$, times

1) $D_{2n}\left(\lambda\xi\right)$ for displacement,

2) $\frac{\lambda\xi}{k\left(\xi^2+\eta_1^2\right)}D'_{2n}\left(\lambda\xi\right)$ for shear stresses $\bar{\tau}_{zx}$, and

3) $\frac{\lambda\eta_1}{k\left(\xi^2+\eta_1^2\right)}D'_{2n}\left(\lambda\xi\right)$ for shear stresses $\bar{\tau}_{zy}$

In other words, they all have the same range of convergence at each angle of incidence as shown in figures of Chapter II and here.

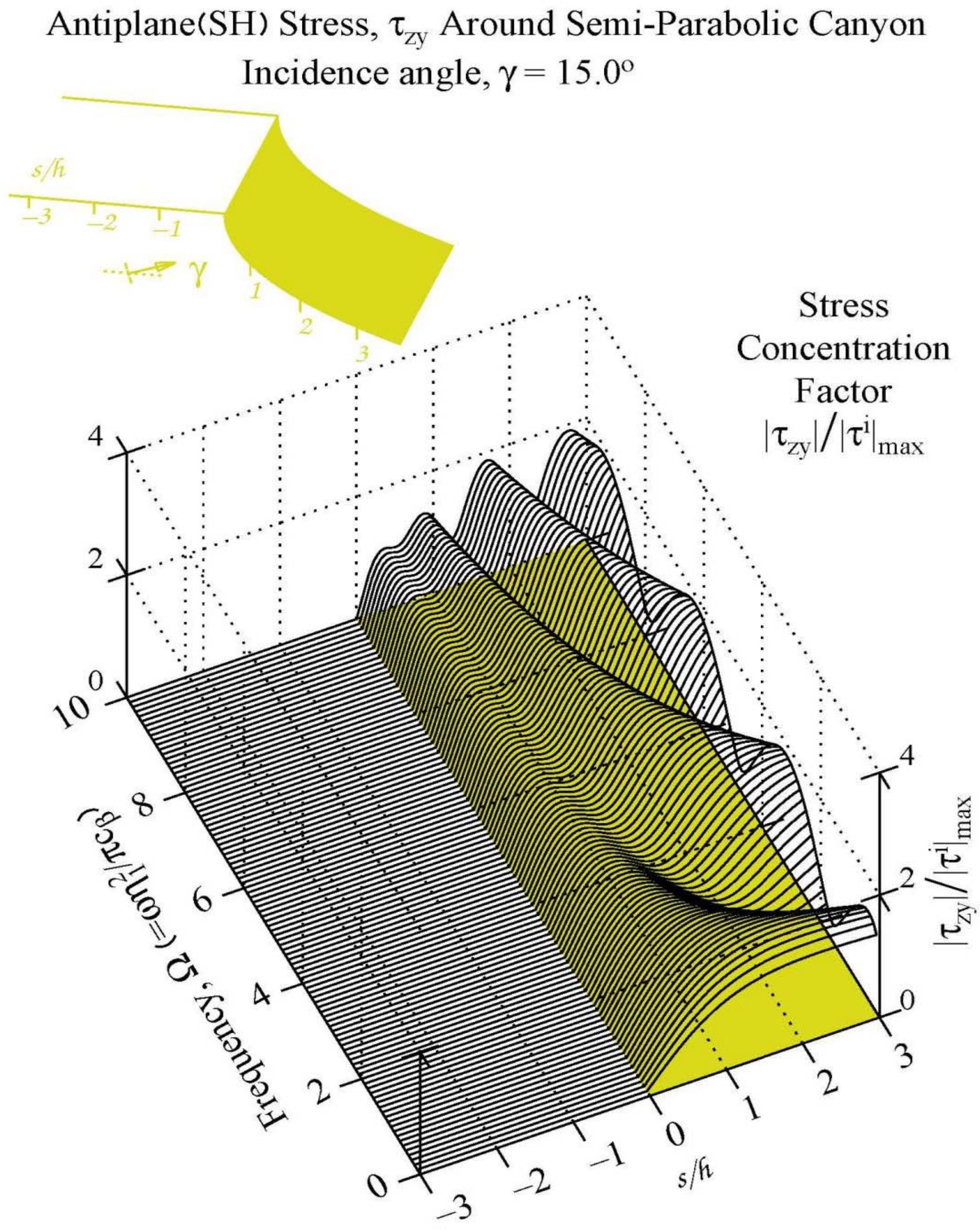

Fig. 5.7 3D Shear Stress Amplitudes, $\left|\bar{\tau}_{zy}\right|$ for Oblique Incidence, $\gamma = 15^\circ$

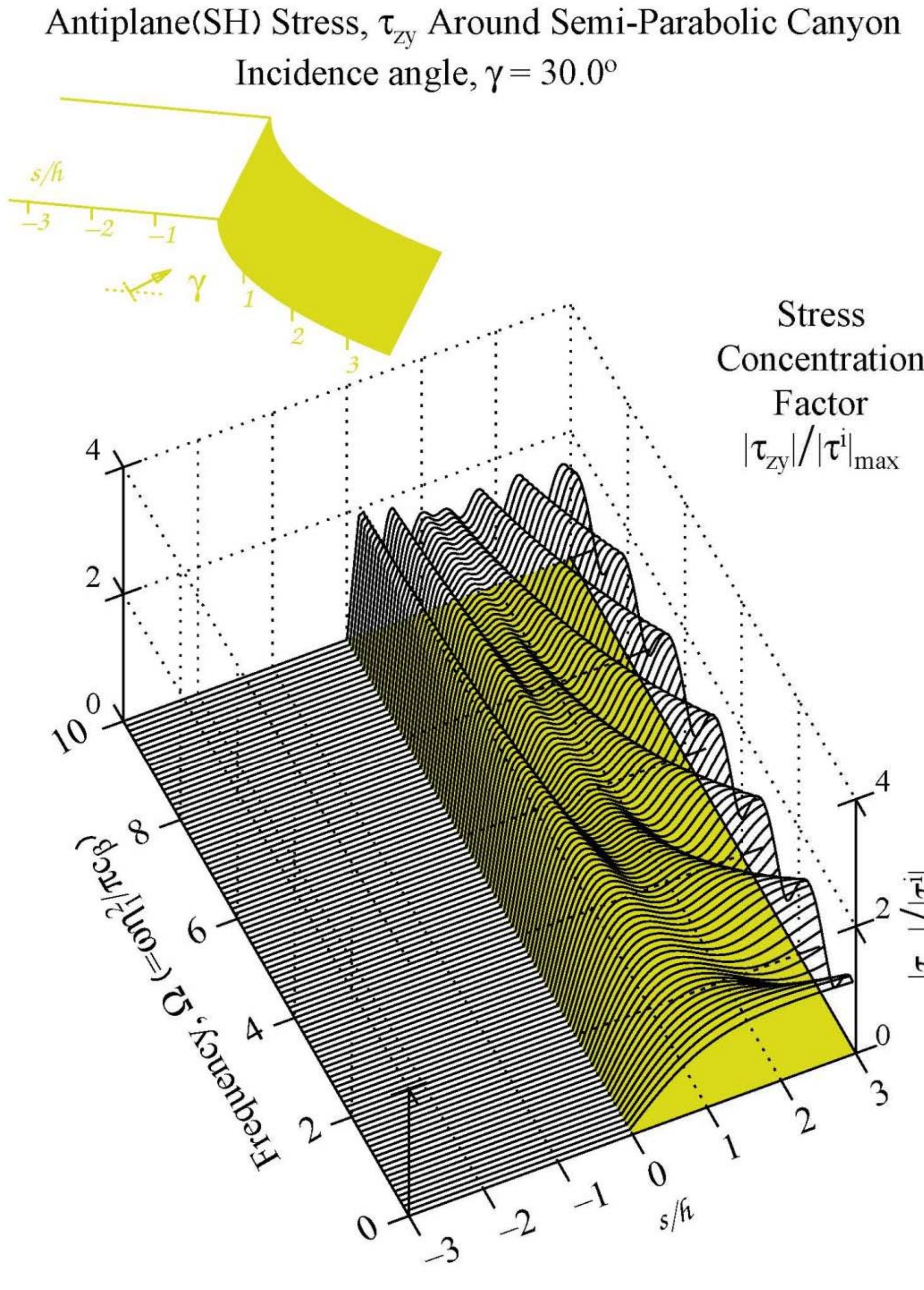

Fig. 5.8 3D Shear Stress Amplitudes, $\left|\bar{\tau}_{zy}\right|$ for Oblique Incidence, $\gamma = 30^\circ$

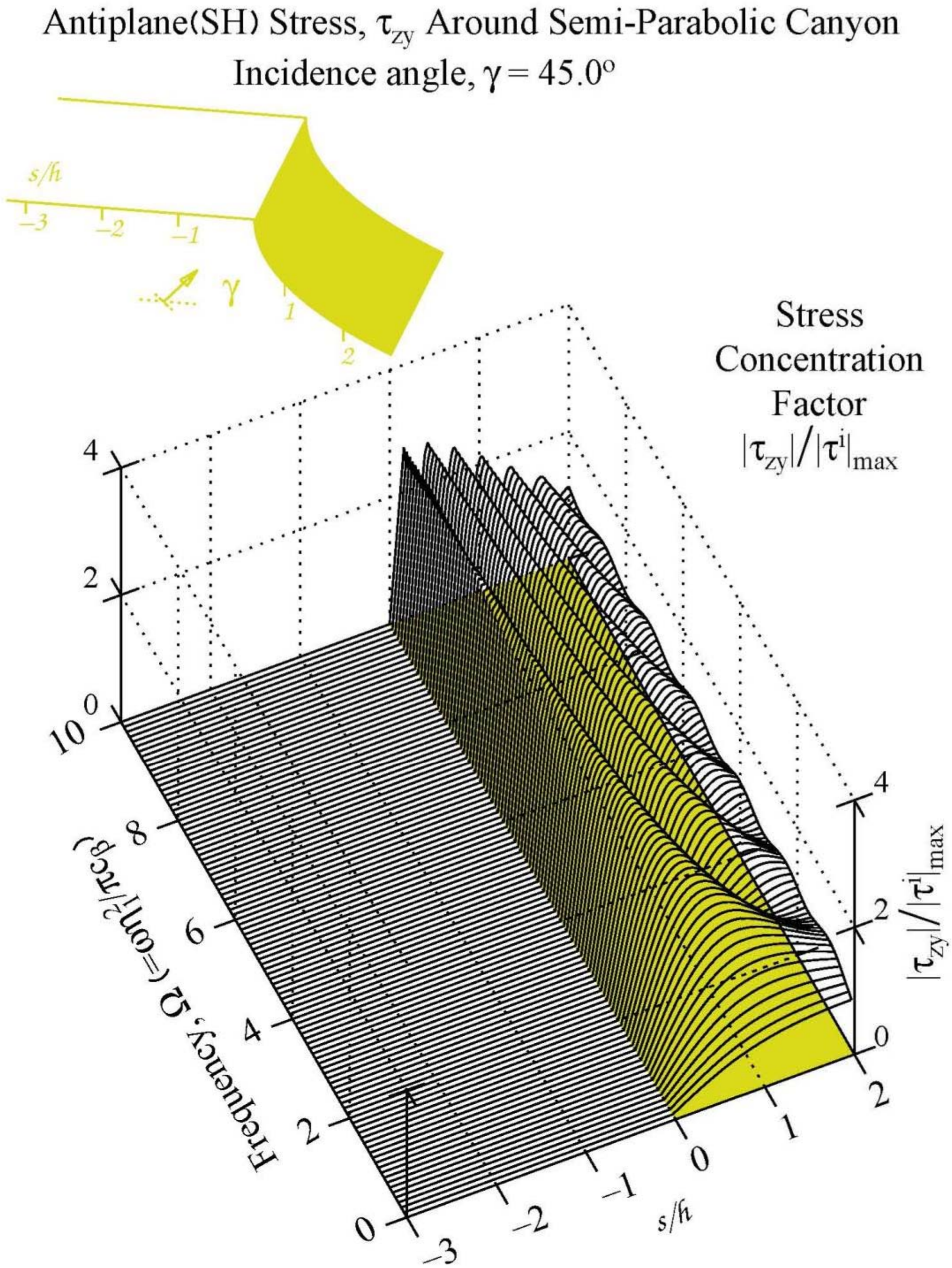

Fig. 5.9 3D Shear Stress Amplitudes, $\left|\bar{\tau}_{zy}\right|$ for Oblique Incidence, $\gamma = 45^{\circ}$

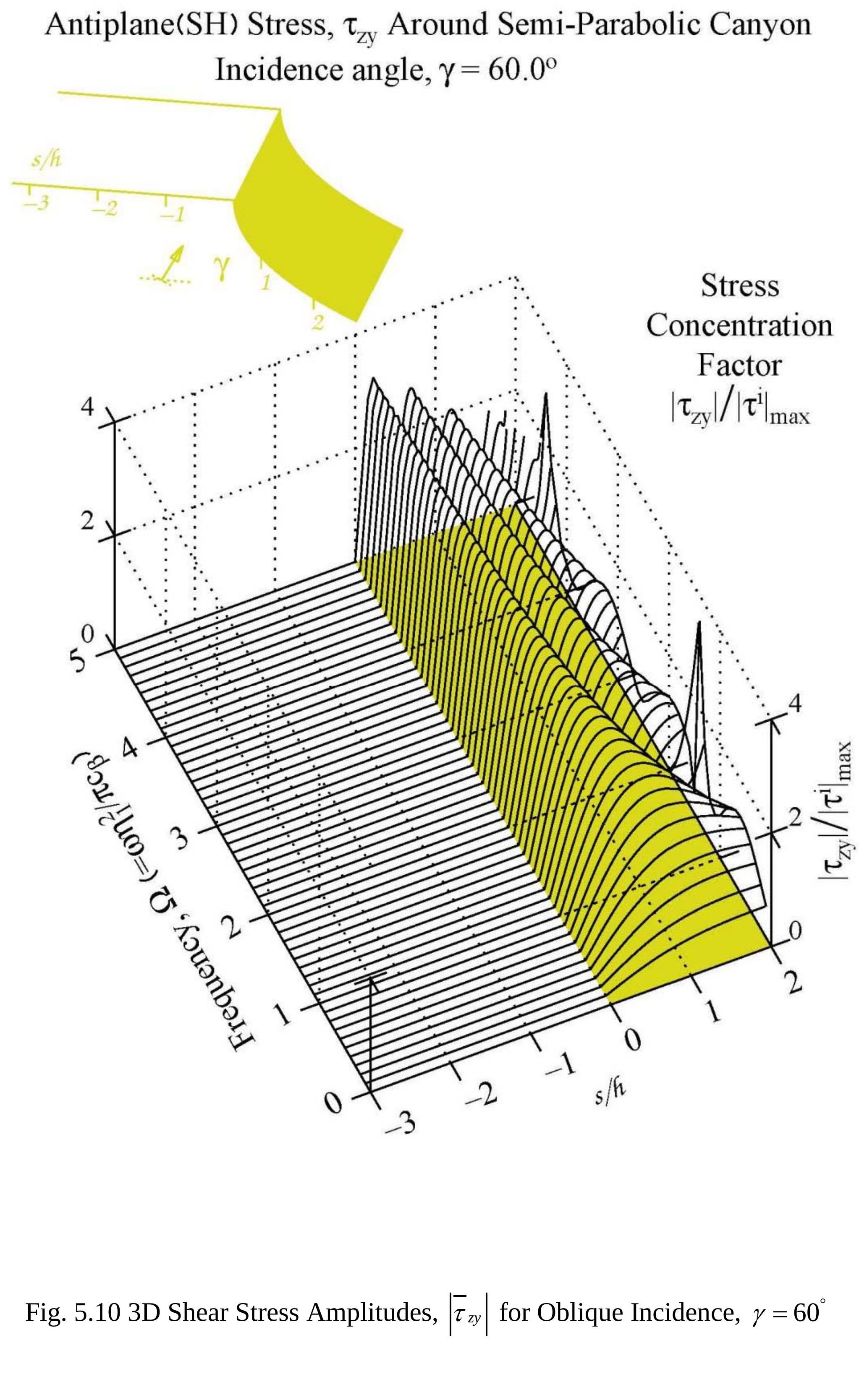

Fig. 5.10 3D Shear Stress Amplitudes, $\left|\bar{\tau}_{zy}\right|$ for Oblique Incidence, $\gamma = 60^{\circ}$

V.5 Dynamic Shear Traction Concentration Factors, $\left|\bar{\tau}_{zt}\right|$

Since the resultant shear traction is

$$\left|\bar{\tau}_{zt}\right| = \frac{1}{k}\left(\left|\frac{\partial W}{\partial x}\right|^2 + \left|\frac{\partial W}{\partial y}\right|^2\right)^{\frac{1}{2}} = \left|\bar{\omega}\right|, \text{ the resultant rotation} \qquad \text{Equation (16) above}$$

so as stated earlier, all derivations for expressions for resultant rotations in Chapter IV will be used and will not be repeated here.

The normalized shear stress amplitude $\bar{\tau}_{zy}$ at the half-space surface takes the same form as the rocking motion

$$\bar{\tau}_{zy}\Big|_{y=0}\left(=\varpi_{Rock}\Big|_{y=0}\right) = 0 \qquad \text{Equation (19) above}$$

so that the normalized resultant traction amplitude at the half-space surface is

$$\bar{\tau}_{zt}\Big|_{y=0} = \bar{\tau}_{zx}\Big|_{y=0} \qquad (21)$$

with no (zero) contribution from the $\bar{\tau}_{zy}$ component.

At the surface of the canyon, the normalized $\bar{\tau}_{zx}$ and $\bar{\tau}_{zy}$ components stress are respectively as

$$\bar{\tau}_{zx}\Big|_{\eta=\eta_1} = \left(-\bar{\omega}_{Tor}\Big|_{\eta=\eta_1}\right) = \frac{2\sec\left(\gamma/2\right)}{k\left(\xi^2+\eta_1^2\right)}\left(\lambda\xi\right)\sum_{n=0}^{\infty} ia_n\left(-1\right)^n \frac{D_{2n}^{'}\left(\lambda\xi\right)}{D_{-2n-1}^{'}\left(\lambda\eta_1\right)} \qquad \text{Equation (18) above}$$

$$\bar{\tau}_{zy}\Big|_{\eta=\eta_1}\left(=\bar{\omega}_{Rock}\Big|_{\eta=\eta_1}\right) = \frac{2\sec\left(\gamma/2\right)}{k\left(\xi^2+\eta_1^2\right)}\left(\lambda\eta_1\right)\sum_{n=0}^{\infty}\frac{ia_n\left(-1\right)^n}{D_{-2n-1}^{'}\left(\lambda\eta_1\right)}D_{2n}^{'}\left(\lambda\xi\right) \qquad \text{Equation (20) above}$$

Which from Equation (16), give the resultant rotation amplitude as

$$\begin{aligned}\bar{\tau}_{zt}\Big|_{\eta=\eta_1} &= \left[\left|\bar{\tau}_{zx}\right|^2+\left|\bar{\tau}_{zy}\right|^2\right]_{\eta=\eta_1}^{1/2}\left(=\left|\bar{\omega}\right|_{\eta=\eta_1}\right)\\ &= 2\sec\left(\gamma/2\right)\frac{\left|\lambda\right|\left(\xi^2+\eta_1^2\right)^{1/2}}{k\left(\xi^2+\eta_1^2\right)}\left|\sum_{n=0}^{\infty} ia_n\left(-1\right)^n\frac{D_{2n}^{'}\left(\lambda\xi\right)}{D_{-2n-1}^{'}\left(\lambda\eta_1\right)}\right|\end{aligned} \tag{22}$$

Or with $\lambda=\sqrt{-2ik}$, $\left|\lambda\right|=\sqrt{2k}$, $\left|\lambda\right|/k = 2/\sqrt{2k} = 2/\sqrt{\lambda}$

$$\left|\bar{\tau}_{zt}\right|_{\eta=\eta_1}\left(=\left|\varpi\right|_{\eta=\eta_1}\right) = \frac{4\sec\left(\gamma/2\right)}{\left|\lambda\right|\left(\xi^2+\eta_1^2\right)^{1/2}}\left|\sum_{n=0}^{\infty} ia_n\left(-1\right)^n\frac{D_{2n}^{'}\left(\lambda\xi\right)}{D_{-2n-1}^{'}\left(\lambda\eta_1\right)}\right| \tag{23}$$

Fig. 5.11 to Fig. 5.15 are the five 3D plots of the normalized shear traction amplitudes plotted vs.

1) The dimensionless distance s/h measured along the half-space and canyon surface and

2) The dimensionless frequency $\Omega = \omega\eta_0^2 / \pi\beta = 2\eta_0^2 / \lambda = 4h / \lambda$

respectively for incidence angles of $\gamma = 0^{\circ}, 15^{\circ}, 30^{\circ}, 45^{\circ}$ and 60°. As in the corresponding plots of normalized shear stress amplitudes of $\bar{\tau}_{zx}$ and $\bar{\tau}_{zy}$, all trends and features stayed the same.

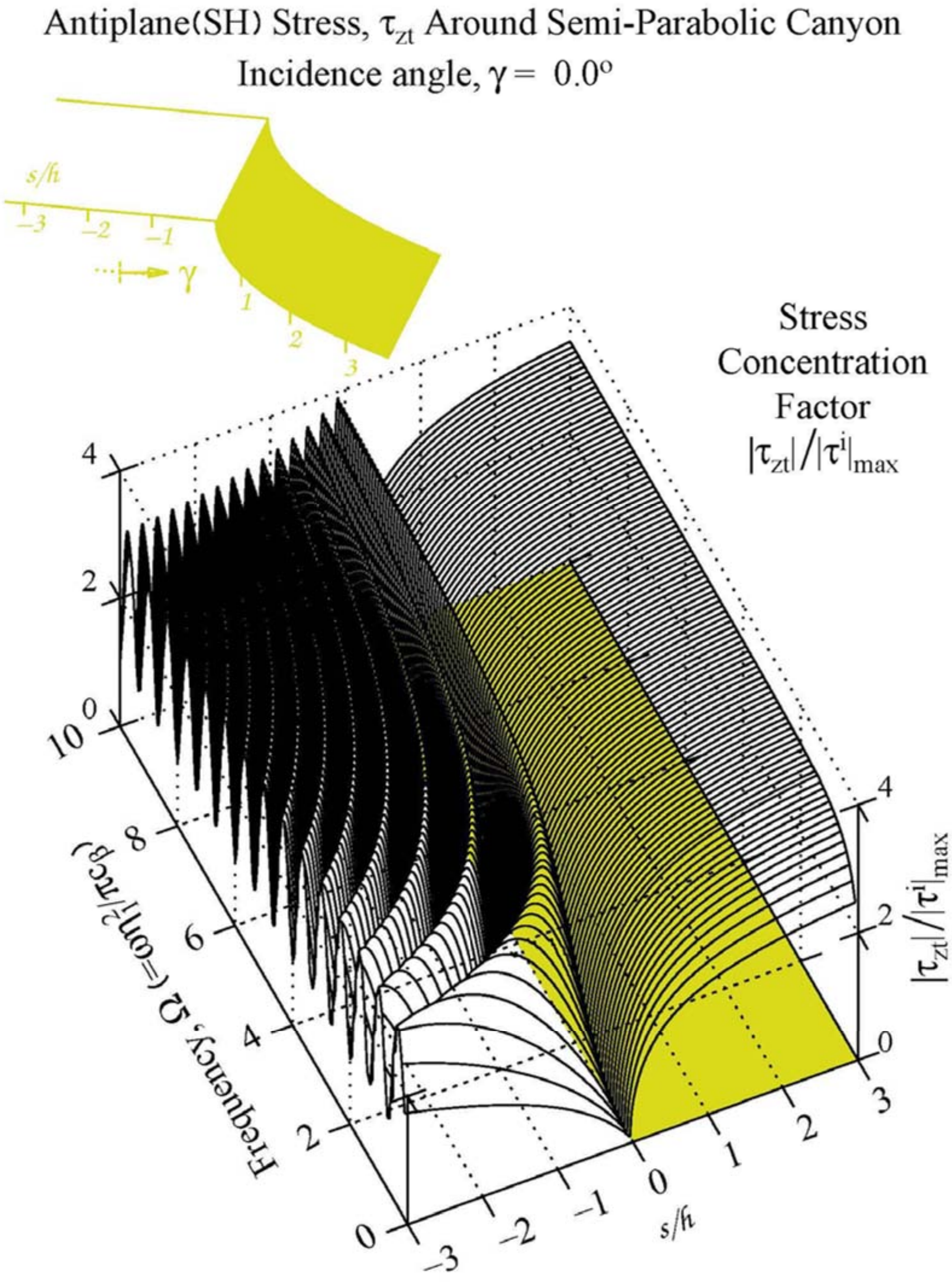

Fig. 5.11 3D Shear Traction Amplitudes, $\left|\overline{\tau}_{zt}\right|$ for Horizontal Incidence, $\gamma = 0^\circ$

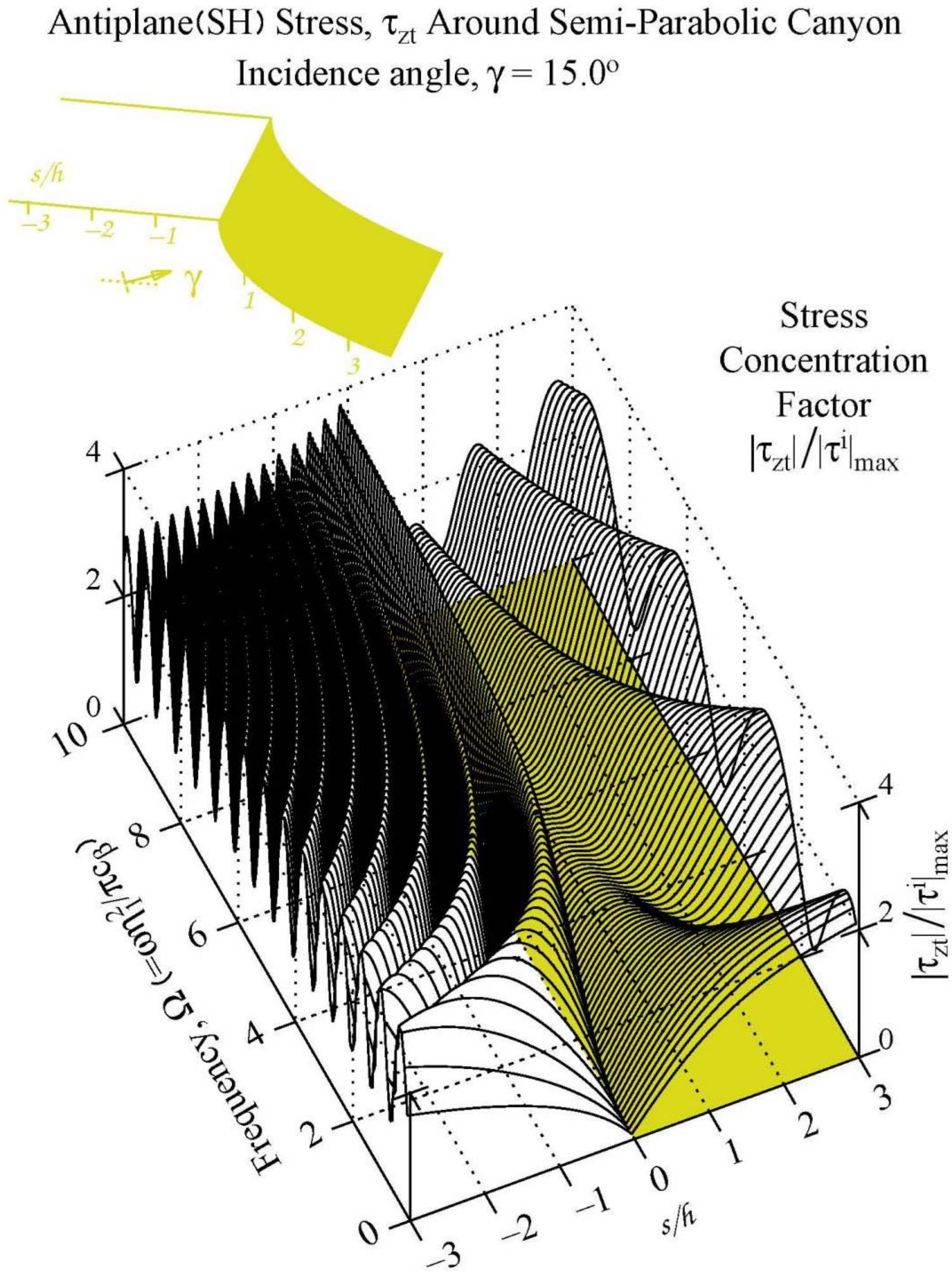

Fig. 5.12 3D Shear Traction Amplitudes, $\left|\bar{\tau}_{zt}\right|$ for Oblique Incidence, $\gamma = 15^{\circ}$

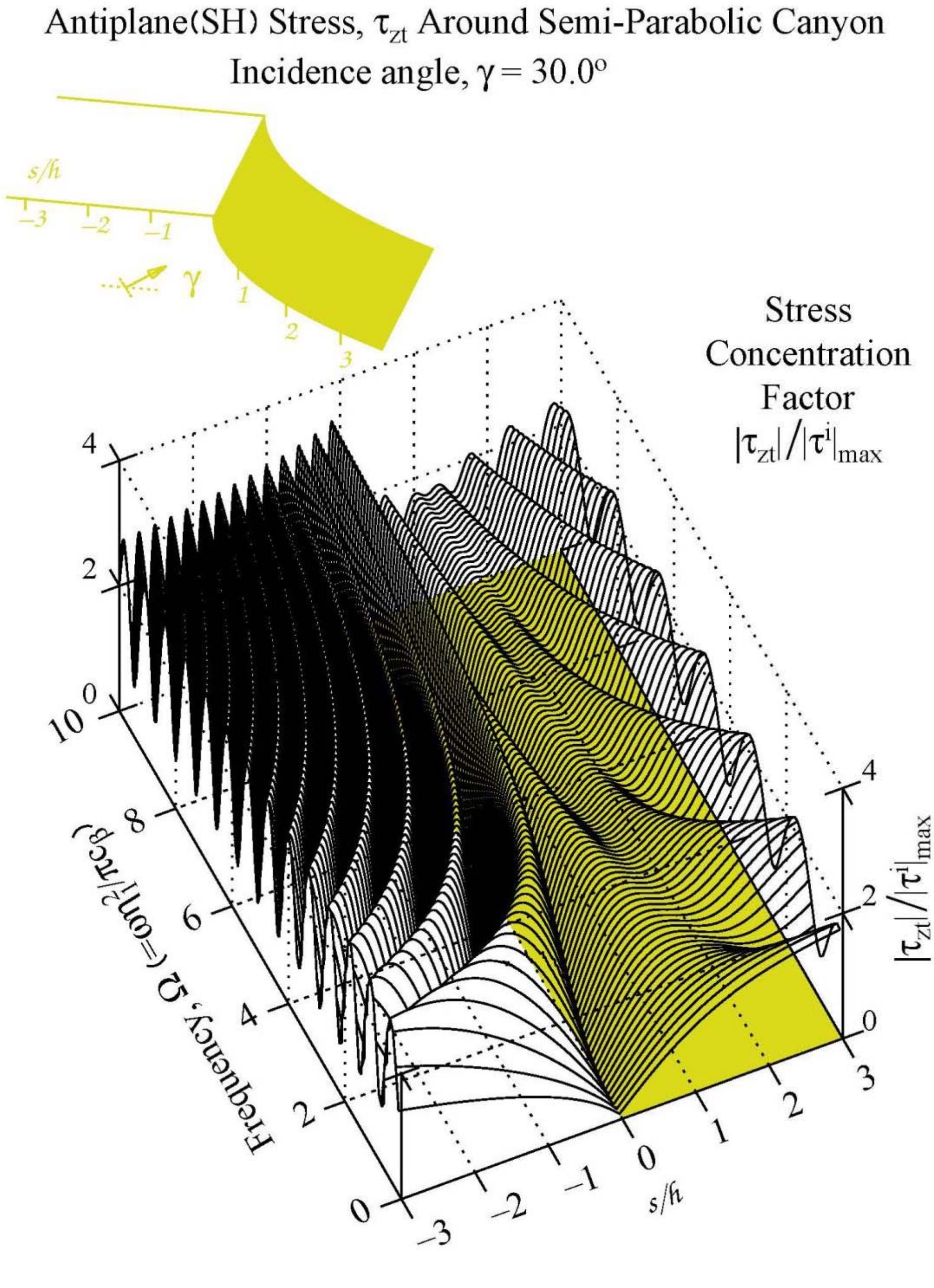

Fig. 5.13 3D Shear Traction Amplitudes, $\left|\bar{\tau}_{zt}\right|$ for Oblique Incidence, $\gamma = 30^{\circ}$

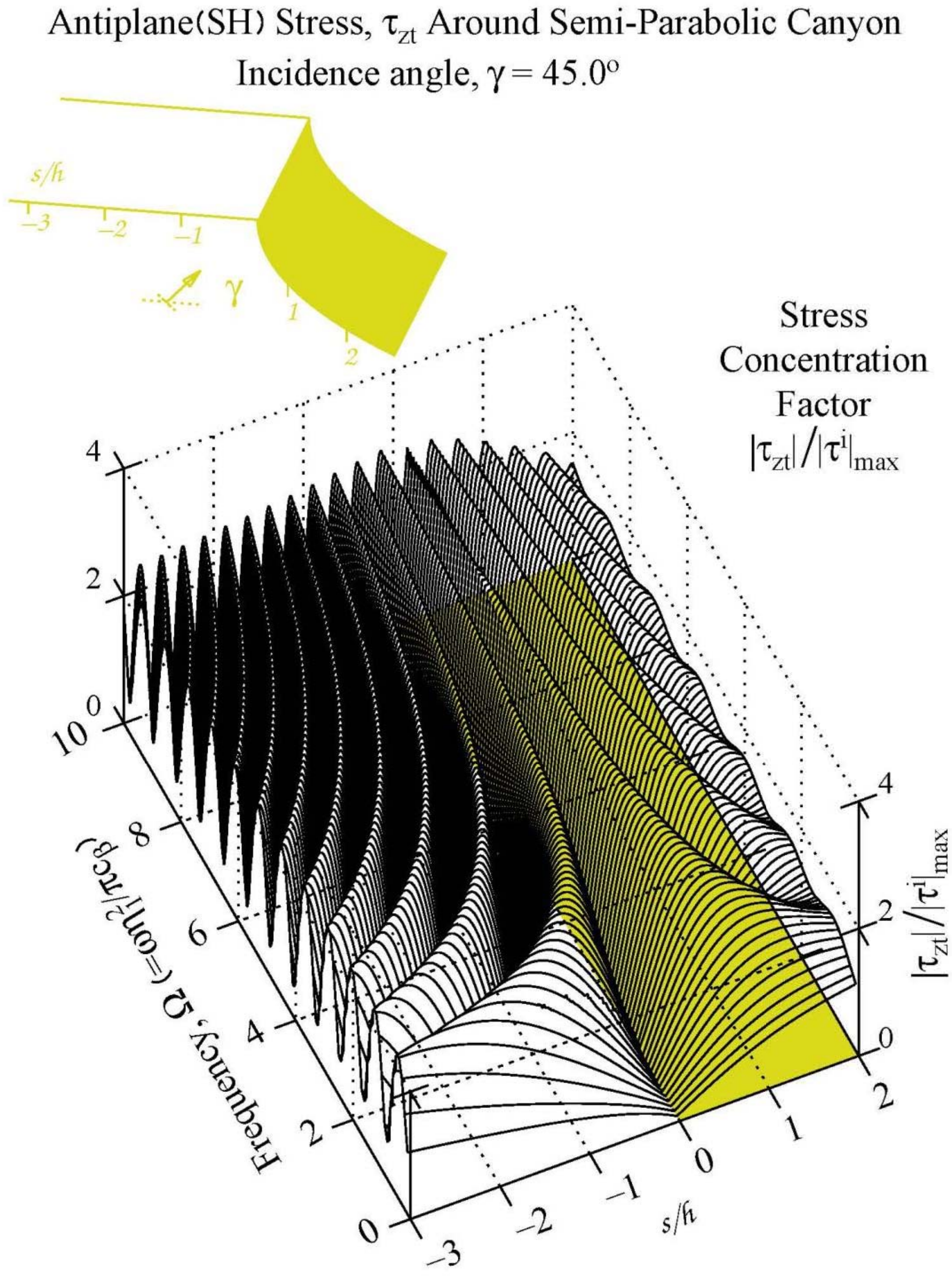

Fig. 5.14 3D Shear Traction Amplitudes, $\left|\bar{\tau}_{zt}\right|$ for Oblique Incidence, $\gamma = 45^{\circ}$

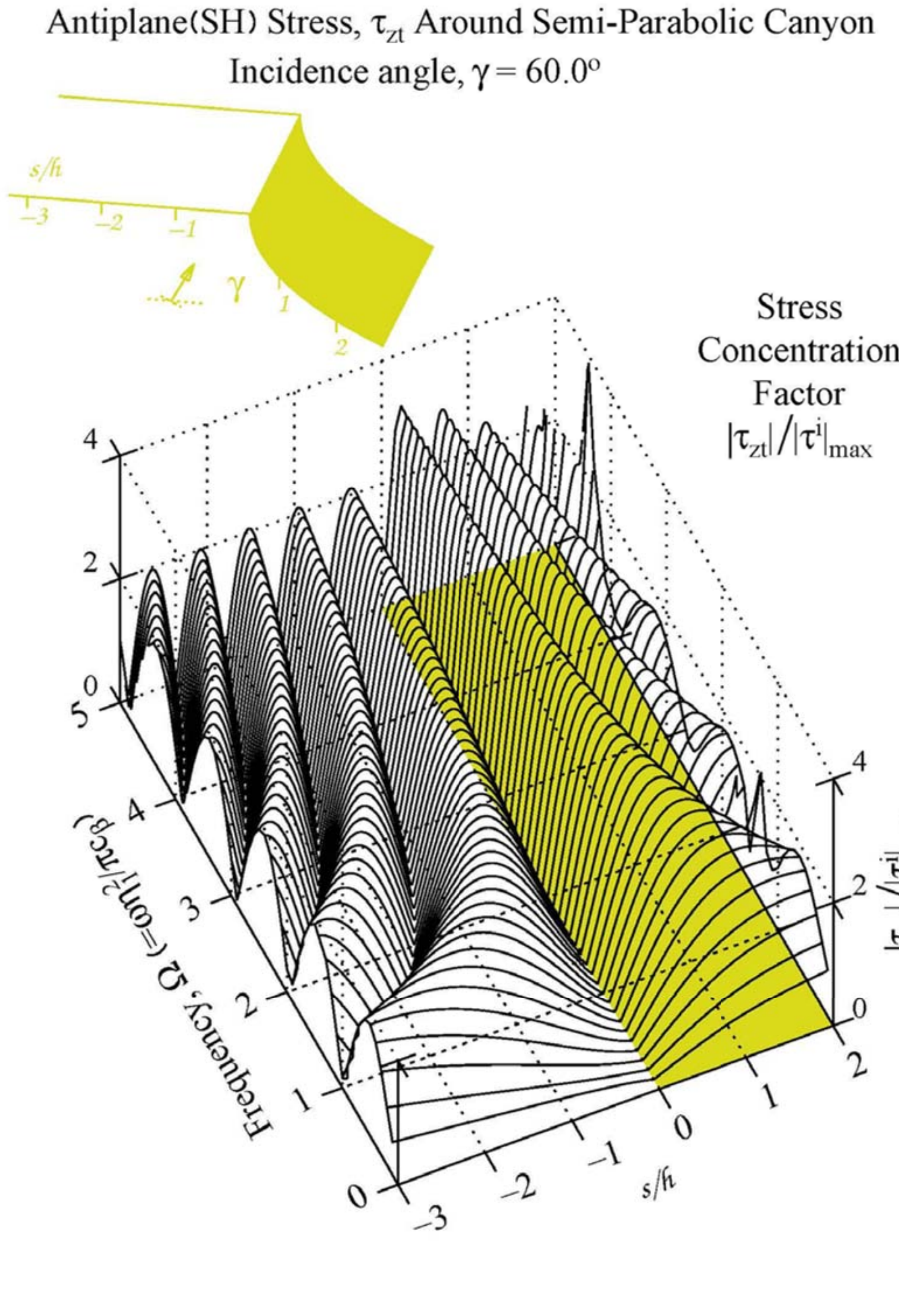

Fig. 5.15 3D Shear Traction Amplitudes, $\left|\overline{\tau}_{zt}\right|$ for Oblique Incidence, $\gamma = 60^{\circ}$

V. 6 Comparison Graphs for Anti-Plane Stress with Incidence Angles $\gamma = 0^\circ, 15^\circ, 30^\circ, 45^\circ$ and 60°

In order to gain a better understanding of the importance of the amplified displacement created due to the anti-plane stress in rocking, rotation and stress concentration factor, a comparison graph has been put together in Fig 5.16 to 5.20 with incident angles $\gamma = 0^\circ, 15^\circ, 30^\circ, 45^\circ$ and 60°. The shape of the half-space and canyon surface model on which the displacements are calculated are outlined on the top-left graph of the figure and is in gold color. The gold arrow is the direction of the incident SH wave W^i which is assumed to be coming from the left-side towards the canyon. These figures show the displacement amplitudes due to rocking (top), rotation (middle) and the combination resultant force for both rocking and rotation (bottom).

In normal engineering design practice, rocking, rotation and stress concentration factor are not being considered in design force as engineers' makes assumptions as the effects are small enough to be ignored or effects would cancel out in process. However, by putting the figures side by side, we can see the impact in displacement of each reaction, especially with the combination resultant force. Displacement is comparatively small for both rocking and rotation especially when location is far away from cliff, however, in reality, rocking and rotation comes in as package which is in form of the combination resultant force and the graph clearly show how the large impact these forces create in displacement.

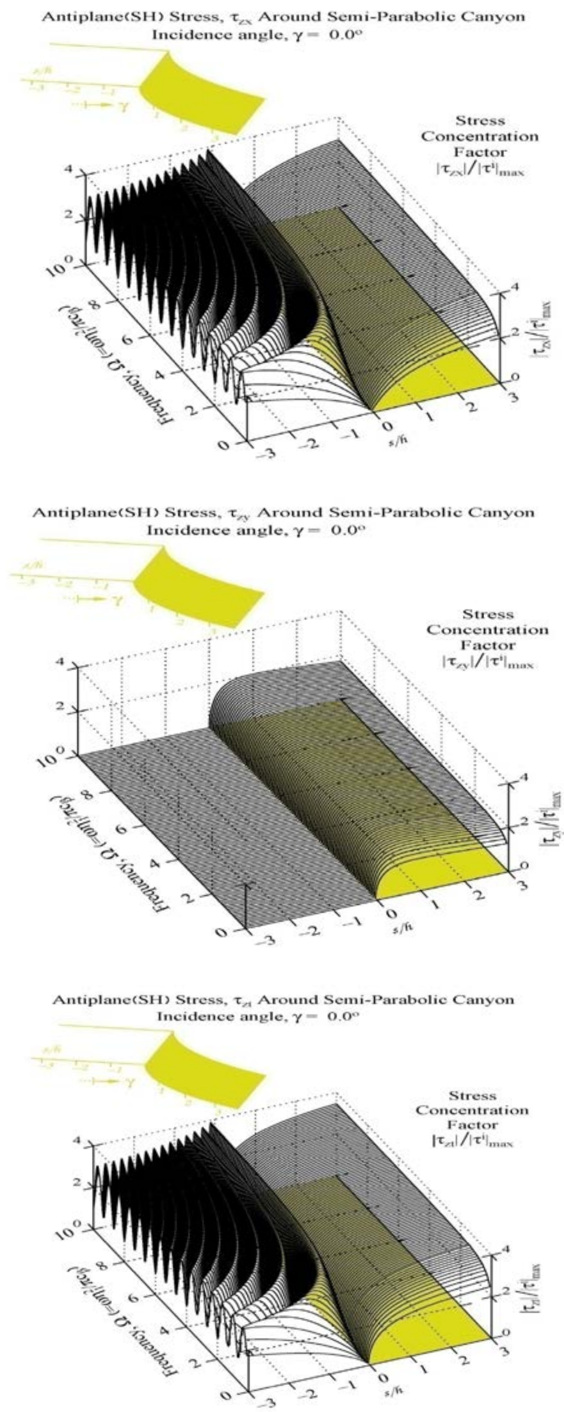

Fig. 5.16 3D Shear Stress Amplitudes, $\left|\bar{\tau}_{zx}\right|, \left|\bar{\tau}_{zy}\right|$ and $\left|\bar{\tau}_{zt}\right|$ Comparison for Horizontal Incidence $\gamma = 0^{\circ}$

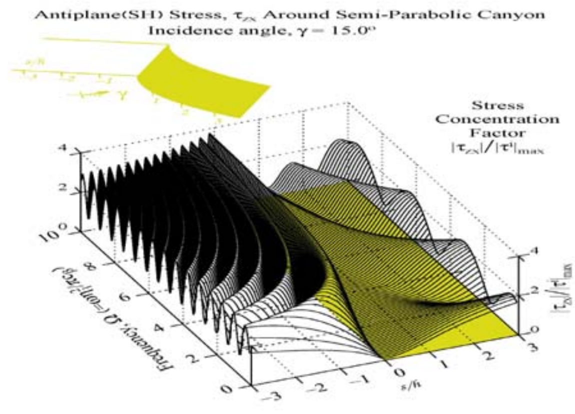

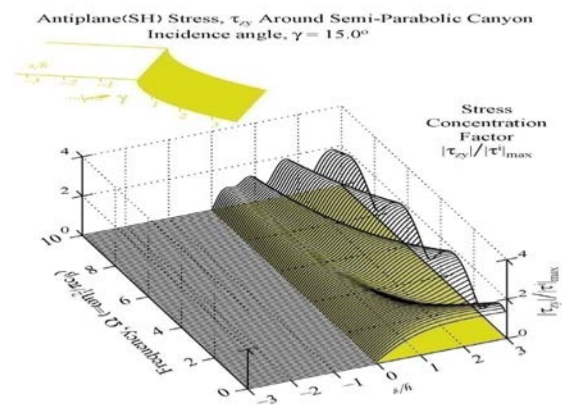

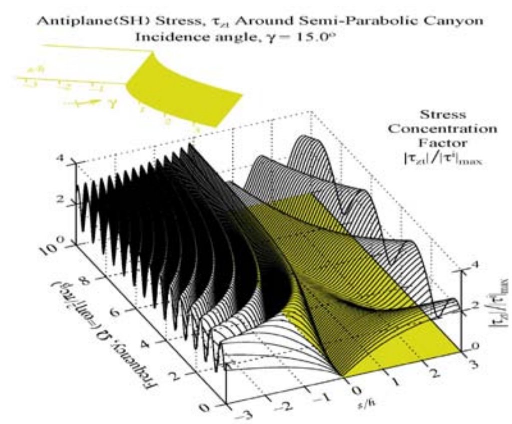

Fig. 5.17 3D Shear Stress Amplitudes, $\left|\bar{\tau}_{zx}\right|, \left|\bar{\tau}_{zy}\right|$ and $\left|\bar{\tau}_{zt}\right|$ Comparison for Oblique Incidence $\gamma = 15^{\circ}$

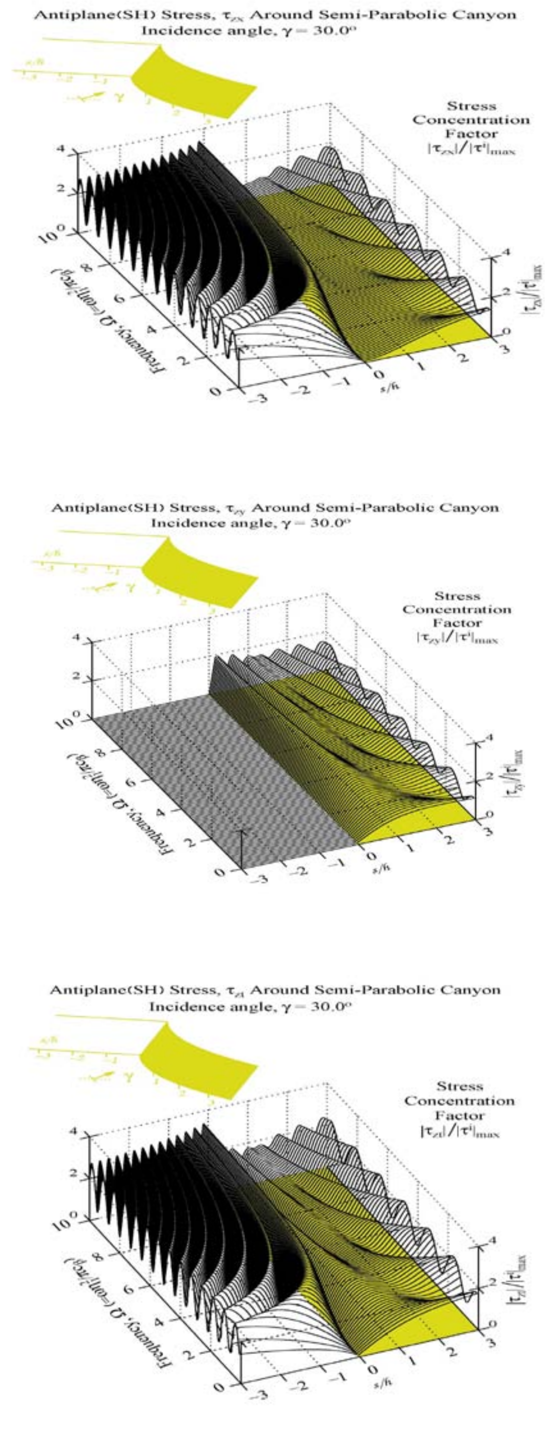

Fig. 5.18 3D Shear Stress Amplitudes, $\left|\bar{\tau}_{zx}\right|, \left|\bar{\tau}_{zy}\right|$ and $\left|\bar{\tau}_{zt}\right|$ Comparison for Oblique Incidence $\gamma = 30^{\circ}$

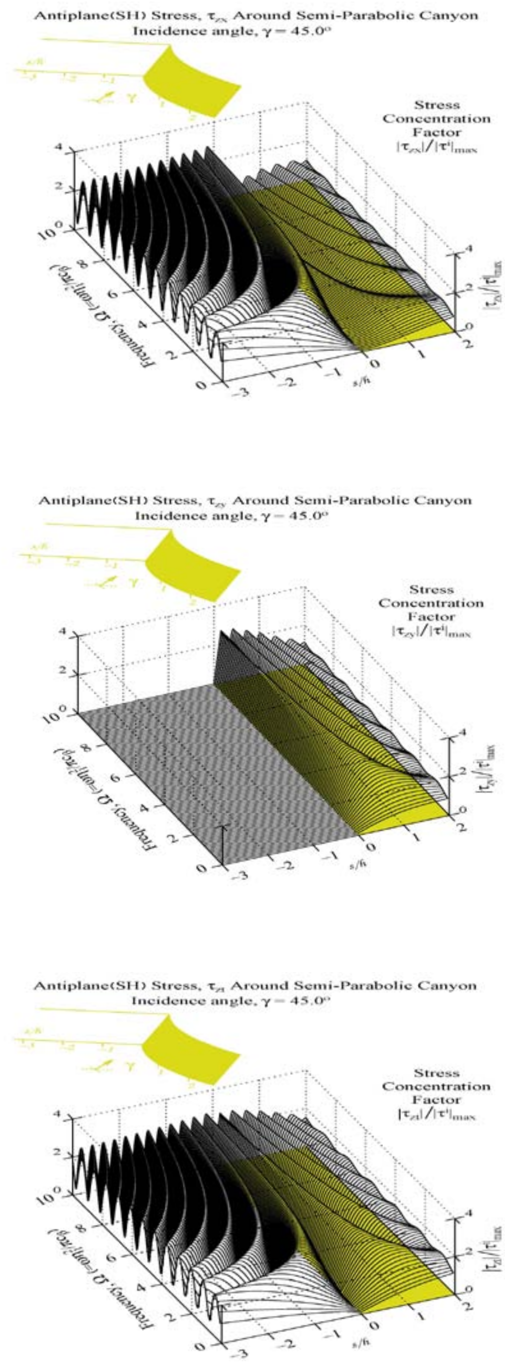

Fig. 5.19 3D Shear Stress Amplitudes, $\left|\bar{\tau}_{zx}\right|, \left|\bar{\tau}_{zy}\right|$ and $\left|\bar{\tau}_{zt}\right|$ Comparison for Oblique Incidence $\gamma = 45^{\circ}$

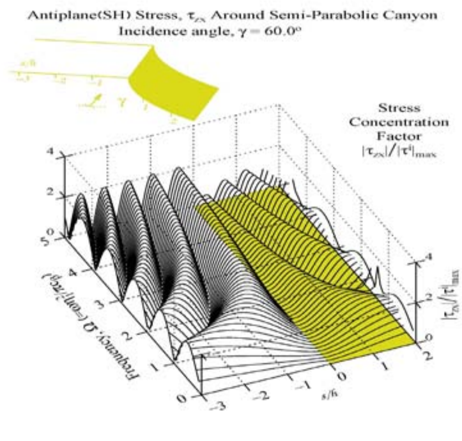

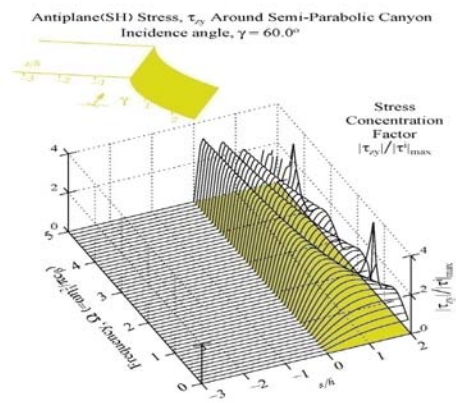

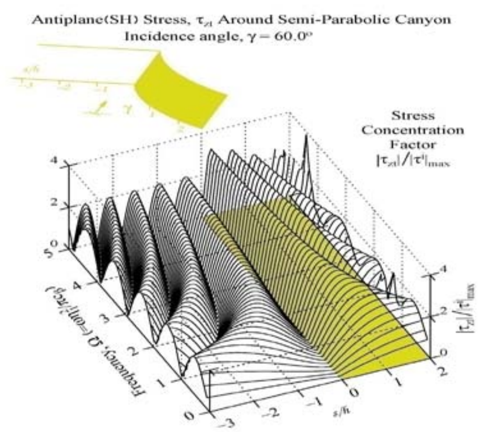

Fig. 5.20 3D Shear Stress Amplitudes, $\left|\overline{\tau}_{zx}\right|, \left|\overline{\tau}_{zy}\right|$ and $\left|\overline{\tau}_{zt}\right|$ Comparison for Oblique Incidence $\gamma = 60^{\circ}$

V. 7 Summary

Chapter V studies the stress concentration factors present in the model. For anti-plane (SH) wave motions, it is shown that two components of shear stresses are present: the τ_{zx} and τ_{zy} stresses, both being on the x-y plane. It was shown that the τ_{zx} and τ_{zy} stresses are identical respectively to the normalized torsion and rocking components of rotations, and thus the resultant traction stress concentration factors (=resultant rotational motions) are large both on the half-space and canon surfaces. As in the rotational motions, the shear traction concentration factors are large both on the half-space and canyon surfaces.

This completes the first part of the thesis dealing with semi-parabolic canyon. The second part, Chapter VI to Chapter VIII, deals with the semi-parabolic hill.

Chapter VI. Diffraction of Anti-Plane SH Waves by a Semi-Parabolic Hill

VI.1 Introduction

Hill topography is a common local surface irregularity which can cause scattering and diffraction of incoming seismic waves, resulting in significant amplifications and de-amplifications on and around the hill surface as well as on the nearby flat ground surfaces. The case of a semi-circular hill above a flat, elastic, homogeneous half-space surface is being studied as simplified hill topography for the modeling of real surface hill topographies. Analogous cases include a semi-circular surface canyon or alluvial valley and that of a sub-surface (underground) circular cavity or tunnel in a flat half-space. Due to the complexity of the topographies, incident plane SH wave studies were done as closed-form analytic solutions in the 70s by Trifunac (1971, 1973), Lee (1977), Lee & Trifunac (1979) for semi-circular canyon or valley and circular underground cavity or tunnel. The case of a semi-circular hill on a float half-space, however, was investigated more recently (Yuan & Men, 1992; Yuan & Liao, 1996). Since the hill topography presented a much higher degree of complexity, it was much more difficult to formulate a simple, closed-form analytic solution. Works on similar geometries, like trough or canyon, in electromagnetic waves were also completed recently (Hinders & Yaghjian, 1991; Park et al, 1993)

A simple, closed form analytic solution here would require the existence of an accurate wave function series solution, with coefficients in the series solution, with coefficients in the series that are solvable using a comprehensive numerical procedure. The solution needs to be compatible with the physics of the problem and satisfies all the physical boundary conditions present in the model of the problem, both analytically and numerically. Some of these problems have the coefficients of each term of the series solvable in terms of computable analytic expressions. Other more complicated problems have solutions given in an infinite set of linear matrix equations solvable by truncation to a finite matrix equation with a large enough number of terms to preserve the accuracy of the solutions. These problems with solutions that is numerically simpler to compute, can thus result in great certainty of the accuracy of the numerical solutions, and can often achieve that also at higher frequencies. These closed form solutions are thus often used as benchmark for comparison with solutions from other approximate numerical methods.

The case of a semi-circular hill on the surface of an elastic half-space was first investigated just over 10 years ago (Yuan & Men, 1992; Yuan & Liao, 1996). In their papers, the authors defined two auxiliary functions, one for the stress and the other for the displacement residues at the interface between the circular region of the hill with the empty space on top and the half-space medium below. Two sets of wave functions were defined, one that was finite everywhere inside the circular hill region, and the other representing outgoing waves from the circular hill to everywhere in the half-space. The coefficients of the wave series were then calculated by setting each term of both residual auxiliary functions to zero through Fourier series expansion. The solution can be considered as an implicit Rayleigh-Ritz method, or method of weighted residues. Subsequently Lee et al. (2006) redefined the solutions using the orthogonally of the cosine functions and the analytic solutions were able to extend the dimensionless frequency to a much higher range.

VI.2 The Semi-Circular Hill of Lee et al (2006)

VI.2.1 The Model

The cross section of the two-dimensional model studied in this paper is shown in Fig. 6.1. It is identical to that considered by Yuan & Men (1992). It represents an elastic, isotropic and homogeneous half-space with a semi-cylindrical hill of radius a. The free surface of the half-space consists of a flat surface Γ and circular-arc hill boundary L. The rectangular coordinate $\left(x, y\right)$ and corresponding polar coordinate $\left(r, \theta\right)$ systems are as defined in Fig. 6.1. The angle θ is measured from the horizontal x-axis clockwise toward the vertical y-axis which is pointing downwards into the half-space.

The half-space in Fig. 6.1 is divided into two regions, an interior and exterior region. The interior region C is the full circular region with the circular hill as the upper part and a semi-circular portion of the half-space as the lower part. This interior region has the boundary L between the hill and the empty space (air) on top and $\underline{L}$ between the interior and exterior regions of the half-space. The exterior region, H, is the rest of the half-space outside the region C. The flat surface of the half-space beyond the hill is denoted by Γ. The excitation of the half-space medium consists of a train of steady-state incident plane SH waves, $w^{(i)}$ with incidence angle γ and (anti-plane) particle motions in the z-direction. A simplified description of the procedure is included here.

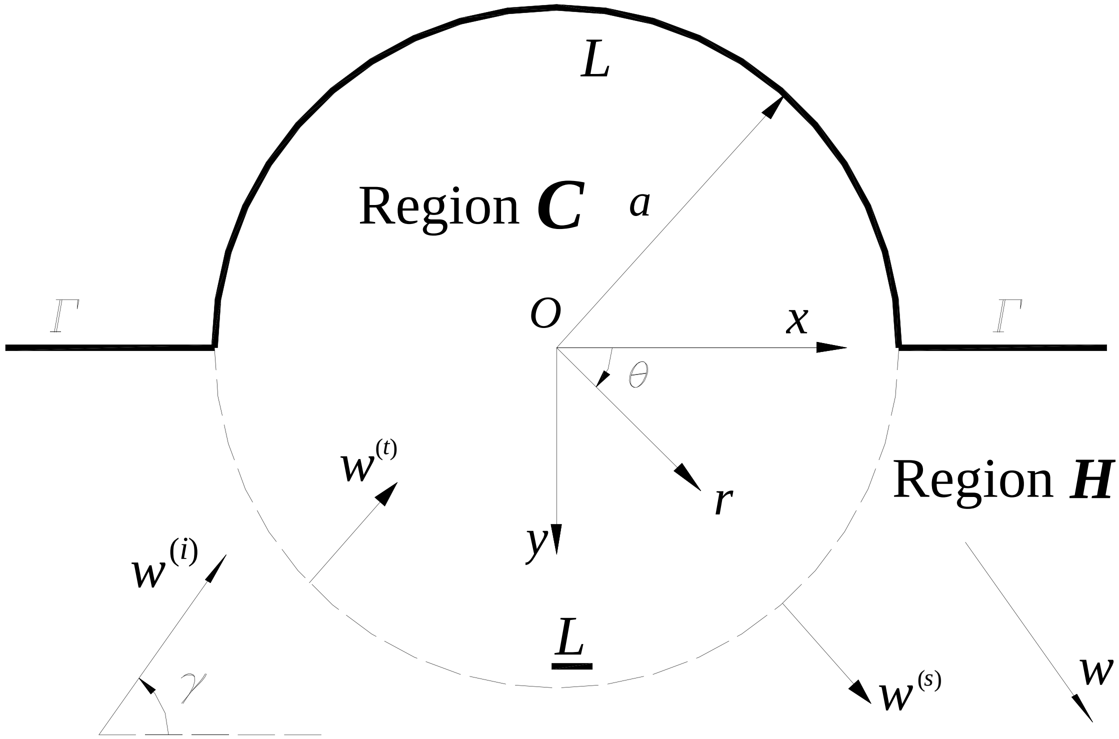

Fig. 6.1 The Semi-Circular Hill Model: Incident Plane SH-Waves

The free-field displacement, $w^{(ff)}$ consists of the sum of incident plane $w^{(fi)}$ and reflected plane, $w^{(r)}$ waves from the flat ground surface. Expanded as a cylindrical wave function series:

$$w^{(ff)}\left(r,\theta\right)=w^{(i)}+w^{(r)}=\sum_{n=0}^{\infty}a_{0,n}J_n\left(kr\right)\cos n\theta, \quad \text{with}$$
$$a_{o,n}=2\varepsilon_n i^n\cos n\gamma \qquad\qquad \text{for n=0,1,2,...} \tag{1}$$

where $J_n\left(\bullet\right)$ is the Bessel function of the first kind with order n, with $\varepsilon_0=1,\ \varepsilon_n=2$ for $n>0$. It is derived from the expansion theorem of Bessel function

(Abramowitz & Stegun, 1972; Pao & Mow, 1973) and used extensively (Lee & Cao, 1989; Lee & Karl, 1993a, b; Lee & Wu, 1994a, b; Lee et al, 2004; Liang et al, 2004).

The presence of the semi-circular hill on top of the half-space resulted in scattered and diffracted outgoing waves in the half-space H outside the circular region of the hill, $w^{(s)}$ and standing transmitted waves inside the circular region C of the hill, $w^{(t)}$. The scattered and transmitted waves, $w^{(s)}$ and $w^{(t)}$ can all be represented as wave function series, and respectively take the form

$$\begin{aligned} w^{(s)}(r,\theta) &= w_0 \sum_{n=0}^{\infty} A_n H_n^{(1)}(kr)\cos n\theta && a \le r \\ w^{(t)}(r,\theta) &= w_0 \sum_{n=0}^{\infty} J_n(kr)\left(B_n \cos n\theta + C_n \sin n\theta\right) && r \le a \end{aligned} \qquad (2)$$

where $H_n^{(1)}(\bullet)$ is the Hankel function of the first kind with order n, and A_n, B_n and C_n are the unknown coefficients of the new waves to be determined. The scattered waves $w^{(s)}$ in the half-space region $H(r \ge a, 0 \le \theta \le \pi)$ has for $n = 0,1,2$ ... $H_n^{(1)}(kr)$, Hankel functions of the first kind as wave functions to correspond to outgoing waves towards infinity, satisfying Sommerfeld's radiation condition (Pao & Mow, 1973). Only the cosine functions $\cos n\theta$ for $n = 0,1,2$ ... are used as they form a complete orthogonal set of functions in the half space region $H(0 \le \theta \le \pi)$, and are appropriate for the stress-free boundary condition at the half-space surface. The transmitted wave $w^{(t)}$ in the circular hill region $C\left(r \le a, -\pi \le \theta \le \pi\right)$ has for $n = 0,1,2\ \ldots\ J_n\left(kr\right)$, Bessel functions of the first kind as wave functions so that the waves are finite everywhere in the hill region C. Both the cosine and sine functions $\cos n\theta, \sin n\theta$ for $n = 0,1,2\ \ldots$ are used as both sets together form a complete orthogonal set of functions in the full circular region $\left(-\pi \le \theta \le \pi\right)$.

Each term in each of the wave functions of the total displacement field $w = w^{(ff)} + w^{(s)}$ in the half-space region H and the transmitted field $w^{(t)}$ in the circular region C, all satisfies the steady-state elastic wave equation (Helmholtz equation) (Pao & Mow 1973)

$$\frac{\partial^2 w}{\partial r^2} + \frac{1}{r}\frac{\partial w}{\partial r} + \frac{1}{r^2}\frac{\partial^2 w}{\partial \theta^2} + k_\beta^2 w = 0 \tag{3}$$

and, with each term of $w^{(ff)}$ and $w^{(s)}$ being a cosine function, they automatically satisfy the anti-plane (SH) traction-free boundary condition at the surface of the flat half-space Γ

$$\tau_{yz}\Big|_{y=0} = \tau_{\theta z}\Big|_{\theta=0,\pi} = \frac{\mu}{r}\frac{\partial w}{\partial \theta}\bigg|_{\theta=0,\pi} = 0 \tag{4}$$

The remaining boundary conditions for the waves are

1) The traction-free condition for the transmitted waves at the surface of the circular hill,

$$L\left(r=a,-\pi \le \theta \le 0\right) \text{ on top: } \tau_{rz}\Big|_{r=a} = \mu \frac{\partial w^{(t)}}{\partial r}\Bigg|_{r=a} = 0 \tag{5}$$

2) The continuity of displacement and stress at $\underline{L}$, between the half-space and the circular hill,

$$\text{At } r=a,\ 0<\theta<\pi \quad w^{(ff)} + w^{(s)}\Big|_{r=a} = w^{(t)}\Big|_{r=a}$$
$$\tau_{rz}\Big|_{r=a} = \mu \frac{\partial\left(w^{(ff)} + w^{(s)}\right)}{\partial r}\Bigg|_{r=a} = \mu \frac{\partial w^{(t)}}{\partial r}\Bigg|_{r=a} \tag{6}$$

VI.2.2 The Analytic Solution Using the Cosine Half-Range Expansion

Recall that the transmitted waves in the hill $w^{(t)}$ are defined in the whole circular region $C: r \le a, -\pi \le \theta \le \pi$, while the scattered waves $w^{(s)}$ are defined only in the half-space region $H: a \le r, 0 \le \theta \le \pi$. Further, the boundary conditions (Equation (8) and (9)) at $r = a$ facing the transmitted waves $w^{(t)}$ are composed of two disjoint sets, one set for continuity of stress and displacement in the lower half interface $\underline{L}, 0 \le \theta \le \pi$, and the other being he traction free condition in the upper half $L, -\pi \le \theta \le 0$.

To satisfy all the boundary conditions analytically, the circular region C is divided into the upper, $\overline{C}\left(-\pi \le \theta \le 0\right)$, and lower, $\underline{C}\left(0 \le \theta \le \pi\right)$, halves. In each of the half range region, the cosine functions along, $\left\{\cos m\theta, m = 0,1,2...\right\}$ form a complete set of orthogonal functions, and each sine function is thus expressible in terms of the cosine functions in each of the semi-circular half range:

$$\sin m\theta = \begin{cases} -\sum\limits_{n+m\ odd, n=0}^{\infty} s_{mn} \cos n\theta & \text{for } -\pi \le \theta \le 0 \\ +\sum\limits_{n+m\ odd, n=0}^{\infty} s_{mn} \cos n\theta & \text{for } 0 \le \theta \le \pi \end{cases} \tag{7a}$$

where

$$s_{mn} = \frac{\int_0^\pi \sin m\theta \cos n\theta d\theta}{\int_0^\pi \cos^2 n\theta d\theta} = \frac{2m\varepsilon_n}{\pi\left(m^2 - n^2\right)} \tag{7b}$$

so that the only difference between the two halves being the minus $(-)$ sign is for the upper $(-\pi \le \theta \le 0)$ and the positive $(+)$ one is for the lower $(0 \le \theta \le \pi)$ semi-circular region. The corresponding transmitted waves now take the form (again the '$-$' and '$+$' signs respectively for the upper and lower semi-circular regions)

$$w^{(t)}(r,\theta) = \begin{cases} \sum_{n=0}^{\infty}\left(B_n J_n(kr) - \sum_{n+m\ odd, m=1}^{\infty} C_m J_m(kr) s_{mn}\right)\cos n\theta & \text{for } -\pi \le \theta \le 0 \\ \sum_{n=0}^{\infty}\left(B_n J_n(kr) + \sum_{n+m\ odd, m=1}^{\infty} C_m J_m(kr) s_{mn}\right)\cos n\theta & \text{for } 0 \le \theta \le \pi \end{cases} \tag{8}$$

with the displacement wave functions of both the scattered and transmitted waves all in the form of cosine series, the boundary conditions in each region are now straight forward to apply.

From Equation (5), traction-free boundary condition at the surface of the circular hill, $L\left(r = a, -\pi \le \theta \le 0\right)$ on top: $\tau_{rz}\big|_{r=a} = \mu \frac{\partial w^{(t)}}{\partial r}\bigg|_{r=a} = 0$ give, using Equation (8), for $n = 0, 1, 2 ...$

$$J_n^{'}\left(ka\right)B_n = \sum_{n+m\ odd,m=1}^{\infty} s_{mn}J_m^{'}\left(ka\right)C_m \tag{9}$$

From Equation (6), displacement and stress continuity at the interface, $\underline{L}\left(r=a, 0\le\theta\le\pi\right)$, for $n=1,2...$

$$a_{0,n}J_n\left(ka\right)+H_n^{(1)}\left(ka\right)A_n = J_n\left(ka\right)B_n + \sum_{n+m\ odd,m=1}^{\infty} s_{mn}J_m\left(ka\right)C_m \tag{10}$$

$$a_{0,n}J_n^{'}\left(ka\right)+H_n^{(1)'}\left(ka\right)A_n = J^{'}\left(ka\right)B_n + \sum_{n+m\ odd,m=1}^{\infty} s_{mn}J_m^{'}\left(ka\right)C_m \tag{11}$$

Equation (9) ~ (11) are the three sets of equations for the three sets of unknowns A_n, B_n and C_n.

Fig. 6.2 is a plot of the anti-plane z-component displacement amplitude $\left|w\right|$ along x/a from -5 to +5 along the surface of the half-space for a semi-circular hill of radius ‘a’ at the dimensionless frequency of $\eta=\frac{\omega a}{\pi c_\beta}=\frac{2a}{\lambda}=5$ for four angles of incidences $\gamma=0^\circ, 30^\circ, 60^\circ$ and 90°. The amplitudes in the range of x/a in the range $\left[-1,1\right]$ are those on the surface of the semi-circular hill. It is Fig. 5 of Lee et al (2006).

This concept of expressing the sine functions in terms of the cosine functions will now be applied to the case of a semi-parabolic hill on top of an elastic half space, to be proposed in the next section.

Fig. 6.2 here will also be used to compare the displacement amplitudes around a semi-circular hill and a semi-parabolic hill in the section below.

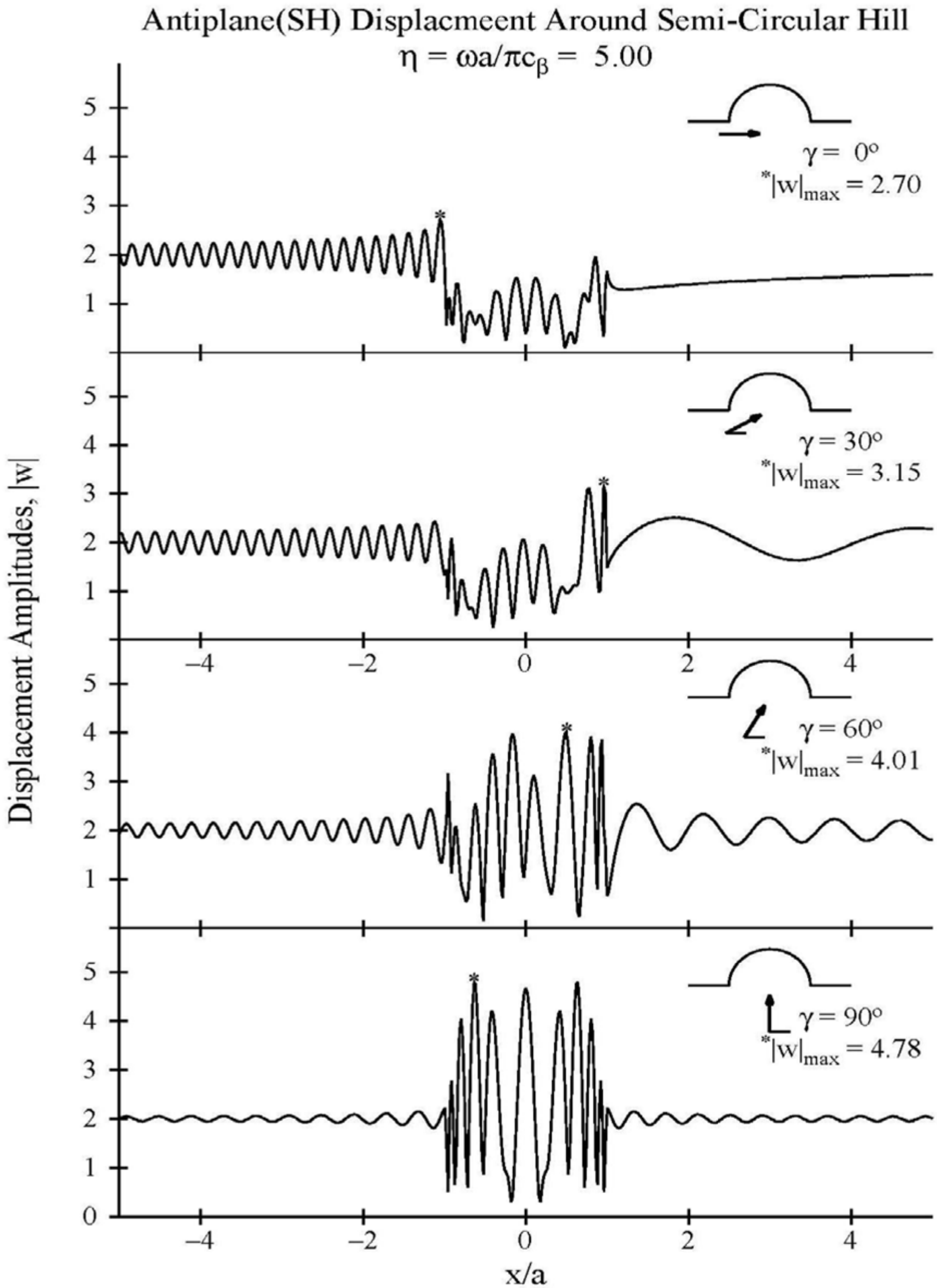

Fig. 6.2 Displacement Amplitude at Circular Hill at $\eta = 5$ (Lee et al, 2006)

VI.3 The Semi-Parabolic Hill

VI.3.1 The Model

The cross section of the two-dimensional model is shown in Fig. 6.1. It represents an elastic, isotropic and homogeneous half-space with a semi parabolic hill. The free surface of the half-space consists of a flat surface Γ and parabolic-arc hill boundary L

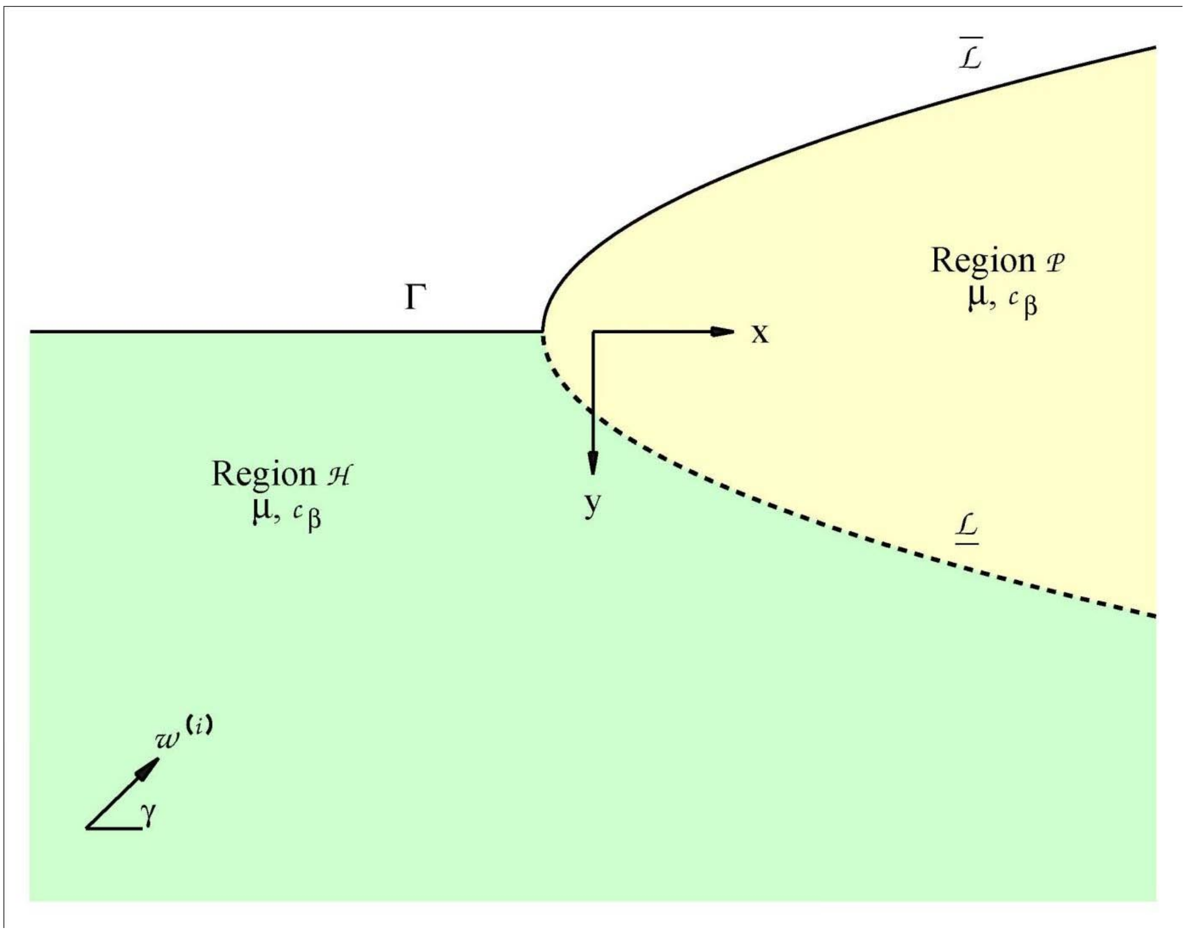

Fig. 6.3 A Semi-Parabolic Hill Model

The half-space in Fig. 6.3 is divided into two regions, an interior and exterior region. The interior region $\mathscr{P}$ is the parabolic hill region with the parabolic hill as the upper part and a semi-parabolic portion of the half-space as the lower part. This interior region has the boundary $\overline{L}$, between the hill and the empty space (air) on top and $\underline{L}$, between the interior and exterior regions of the half-space. The exterior region, $\mathscr{H}$ is the rest of the half-space outside the region $\mathscr{P}$. The float surface of the half-space beyond the hill is denoted by Γ. The excitation of the half-space medium consists of a train of steady-state incident plane SH waves $w^{(i)}$ with incidence angle γ and (anti-plane) particle motions in the z-direction. A simplified description of the procedure is included here.

The free field displacement, W^{ff} consists of the sum of incident plane, is represented as

$$W^{ff}(\eta,\xi) = 2\sec{\gamma/2}\sum_{n=0}^{\infty} a_n D_{2n}\left(\overline{\lambda}\eta\right) D_{2n}\left(\lambda\xi\right) \tag{12}$$

The presence of the semi-parabolic hill on top of the half-space resulted in scattered and diffracted outgoing waves in the half-space $\mathscr{H}$ outside the parabolic region of the hill, W^s and standing transmitted waves inside the parabolic region $\mathscr{P}$ of the hill, W^t. The scattered and transmitted waves W^s and W^t can all be represented as wave function series, and respectively take the form

$$W^s(\xi,\eta) = 2\sec\gamma/2 \sum_{n=0}^{\infty} A_n D_{-2n-1}(\lambda\eta) D_{2n}(\lambda\xi)$$
$$W^t(\xi,\eta) = 2\sec\gamma/2 \sum_{n=0}^{\infty} B_n D_n(\bar{\lambda}\eta) D_n(\lambda\xi) \tag{13}$$

where A_n and B_n are the unknown coefficients of the new waves to be determined. For $n = 0,1,2...$ the $D_{-2n-1}(\lambda\eta) D_{2n}(\lambda\xi)$ terms in the scattered $w^{(s)}$ waves in the half-space region $\mathscr{H}$ correspond to outgoing waves from the parabolic region $\mathscr{P}$ of the hill part, while the $D_n(\bar{\lambda}\eta) D_n(\lambda\xi)$ terms in the transmitted $w^{(t)}$ waves are the standing waves inside the parabolic region $\mathscr{P}$.

Similar to the semi-circular hill problem, the parabolic region $\mathscr{P}$ of the hill is going to be divided into two sub-regions: the upper and lower regions, respectively defined by $-\infty < \xi \le 0,\ \eta \le \eta_0$ for the upper hill region, and $0 \le \xi \le \infty,\ \eta \le \eta_0$ for the region inside $\mathscr{P}$ below the hill.

In each of these half sub-regions, the set of parabolic cylinder function $\{D_{2n}(\lambda\xi)\}$ with even orders are orthogonal and complete, and so the set of parabolic cylinder function $\{D_{2n+1}(\lambda\xi)\}$ with odd orders can thus be expressed in terms of the corresponding set with even orders, for $z = \lambda\xi$

$$D_{2n+1}(z)=\begin{cases}-\sum_n s_{2m+1,2n}D_{2n}(z) & -\infty < z \le 0\\ +\sum_n s_{2m+1,2n}D_{2n}(z) & 0\le z<\infty\end{cases}$$

$$\text{with}\quad s_{2m+1,2n}=\frac{\int_0 D_{2m+1}(z)D_{2n}(z)\,dz}{\int_0^\infty D_{2n}^2(z)\,dz} \tag{14}$$

Applying the above Equation (14) for $z=\lambda\xi,\ W^t$ can be re-written as follow

$$W^t=\begin{cases}\sum_n\left[B_{2n}D_{2n}\left(\bar{\lambda}\eta\right)-\sum_m B_{2m+1}D_{2m+1}\left(\bar{\lambda}\eta\right)s_{2m+1,2n}\right]D_{2n}(\lambda\xi) & -\infty<\xi\le 0\\ \sum_n\left[B_{2n}D_{2n}\left(\bar{\lambda}\eta\right)+\sum_m B_{2m+1}D_{2m+1}\left(\bar{\lambda}\eta\right)s_{2m+1,2n}\right]D_{2n}(\lambda\xi) & 0\le\xi<\infty\end{cases} \tag{15}$$

Which now the equation is easy to apply the boundary condition set as identified with semi-circular hill problem,

1) Traction-free condition at the surface of the parabola hill, $L(\xi<0,\ n=0,1,2\ ...)$

$$\left.\frac{\partial W^t}{\partial\eta}\right|_{\eta=\eta_0}=0$$
$$\bar{\lambda}\left[B_{2n}D'_{2n}\left(\bar{\lambda}\eta_0\right)-\sum_m B_{2m+1}D'_{2m+1}\left(\bar{\lambda}\eta\right)s_{2m+1,2n}\right]=0 \tag{16}$$

2) Displacement and stress continuity at the lower interface at $\underline{L}$ the interface between the half-space $\mathscr{H}$ and parabola hill $\mathscr{P}\left(\xi\ge 0,\ \eta=\eta_0\right)$, for n= 0, 1, 2, …

$$W^t = W^{ff} + W^s \Big|_{\eta=\eta_1} :$$

$$B_{2n} D_{2n}\left(\bar{\lambda}\eta_1\right) + \sum_m B_{2m+1} D_{2m+1}\left(\bar{\lambda}\eta_1\right) s_{2m+1,2n} = \left[a_n D_{2n}\left(\bar{\lambda}\eta_1\right) + A_n D_{-2n-1}\left(\lambda\eta_1\right) \right] \tag{17}$$

$$\frac{\partial W^t}{\partial \eta} = \frac{\partial W^{ff}}{\partial \eta} + \frac{\partial W^s}{\partial \eta}\bigg|_{\eta=\eta_1} :$$

$$B_{2n} D'_{2n}\left(\lambda\eta_1\right) + \sum_m B_{2m+1} D'_{2m+1}\left(\lambda\eta_1\right) s_{2m+1,2n} = \tag{18}$$

$$= 2B_{2n} D'_{2n}\left(\lambda\eta_1\right) = \left[a_n \left(\bar{\lambda}/\lambda\right) D'_{2n}\left(\bar{\lambda}\eta_1\right) + A_n D'_{-2n-1}\left(\lambda\eta_1\right) \right]$$

Equation (16, (17) and (18) are the three sets of equations for the three sets of unknowns A_n, B_{2n} and B_{2n+1}, the even and odd coefficients.

VI.3.2 The Expansion of Odd vs. Even Weber Functions

The success of the above method depends on the numerical implementation of the expansion of parabolic cylinder function $\left\{D_{2n+1}\left(\lambda\xi\right)\right\}$ of odd orders in terms of the corresponding set with even order, as given in Equation (14) above. This section will turn to the evaluation of the integral in the coefficients s_{mn} used in the above expansion. The following formula is known (Erdélyi et al, 1953)

$$\int_0^\infty D_\mu\left(\pm\xi\right)D_\nu\left(\xi\right)d\xi = \frac{\pi 2^{(\mu+\nu+1)/2}}{\mu-\nu}\left[\frac{1}{\Gamma\left(\tfrac{1}{2}-\tfrac{\mu}{2}\right)\Gamma\left(-\tfrac{\nu}{2}\right)} \mp \frac{1}{\Gamma\left(\tfrac{\mu}{2}\right)\Gamma\left(\tfrac{1}{2}-\tfrac{\nu}{2}\right)}\right] \quad (19)$$

$$\left(\mu>\nu,\ \text{if lower signs are taken}\right)$$

From which the following half-range expansion is derived (Erdélyi et al, 1953), of the form $D_\nu\left(x\right)=\sum_{n=0}^{\infty}s_{\nu,2n}D_{2n}\left(x\right)=\sum_{n=0}^{\infty}s_{\nu,2n+1}D_{2n+1}\left(x\right)$

For $x\ge 0$:

$$D_\nu\left(x\right)=\frac{2^{\nu/2}}{\Gamma\left(-\nu/2\right)}\sum_{n=0}^{\infty}\frac{\left(-1\right)^n D_{2n}\left(x\right)}{n!2^n\left(n-\nu/2\right)}=\frac{2^{\nu/2-1/2}}{\Gamma\left(1/2-\nu/2\right)}\sum_{n=0}^{\infty}\frac{\left(-1\right)^n D_{2n+1}\left(x\right)}{n!2^n\left(n+1/2-\nu/2\right)} \quad (20)$$

Putting $\nu=2m+1$ gives for $x\ge 0$:

$$D_{2m+1}\left(x\right)=\frac{2^{2m+1/2}}{\Gamma\left(-\left(2m+1\right)/2\right)}\sum_{n=0}^{\infty}\frac{\left(-1\right)^n D_{2n}\left(x\right)}{n!2^n\left(n-\left(2m+1\right)/2\right)}=\sum_{n=0}^{\infty}s_{2m+1,2n}D_{2n}\left(x\right) \quad (21)$$

With the coefficients $s_{2m+1,2n}$ available from Equation (21) to be substituted into Equation (16), (17), and (18), this enables the coefficients $\{A_n\},\{B_{2n}\},\{B_{2m+1}\}$ to be computed from a set of infinite number of equations. Normally, a large enough order or number of equations is taken to ensure that the remaining coefficients can be neglected without loss of error. Normally such order increases with increasing dimensionless frequency $\Omega = {2\eta_0^2}/{\lambda} = {4h}/{\lambda}$ (Equation (16), Chapter II)

This completes the solution of the boundary-valued problem of diffraction of semi-parabolic hill by SH waves. The numerical results will be presented in the next two Sections. As in previous Chapters, the plots are separated into two sections, with the first section of plots from Section VI.4 Horizontal Angle of Incidence $\gamma = 0^\circ$, followed by plots from Section VI.5 Oblique Angles of Incidences: $\gamma = 15^\circ, 30^\circ, 45^\circ$ and 60°.

VI.4 Horizontal Angle of Incidence $\gamma = 0^{\circ}$

Fig. 6.4 represents the displacement amplitudes $|W|$ plotted vs. the dimensionless distance s/h at the dimensionless frequency, $\Omega = 1.0, 2.0, \ldots$ to 10.0 for the horizontal angle of incidence of $\gamma = 0^{\circ}$. All descriptions are the same as Fig. 2.1in Section II.2 of Chapter II for displacements around a semi-parabolic canyon. They will be briefly stated in the next paragraph, and it will apply to all figures in this and subsequent chapters on semi-parabolic hills.

The incident, plane SH-wave W^{i} is as in the case of parabolic canyon in previous chapters, assumed to have unit amplitude. The displacement amplitudes are calculated at points on the half-space and the semi-parabolic hill surfaces. The dimensionless distance s/h is measured in units of the focal length of the semi-parabolic hill from the tip (vertex, corner point) of the hill, where $s/h = 0$. Points on the surface of the half-space to the left of the hill will have negative units of focal length. Thus the unit $s/h = -3$ corresponds to the point on the surface of the half-space surface at distance of 3 focal lengths to the left of the tip of the canyon. Similarly, points on the surface of the semi-parabolic hill are measured as positive distances along the semi-parabolic hill surface in units of focal length from the semi-parabolic hill's tip. The shape of the half-space and hill surface on which the displacements are calculated is outlined as a dotted line on the top-left graph of the figure, with the arrow indicating the corresponding direction of the incident SH wave W^i which is assumed to be coming from the left-side towards the hill (from where ${}^{s}\!/_{h} < 0$).

For the case of horizontal incidence, $\gamma = 0^\circ$ here in Fig. 6.3, the incidence wave W^i will depend only on the x-coordinate; of the form $W^i = \exp(ikx)$ will have a 1-term expansion in parabolic coordinates, from Equation (12):

$$W^{ff}\left(\eta,\xi\right) = 2D_0\left(\bar{\lambda}\eta\right)D_0\left(\lambda\xi\right) \tag{22}$$

The scattered (outside) and transmitted waves (hill region), unlike the case of the semi-parabolic canyon in Chapter II, will not be a 1-term ($n = 0$) wave, but respectively will be infinite sums (Equation (13)) for the semi-parabolic hill even for the case of horizontal incidence.

Fig. 6.4 shows that the waves on the half-space region to the left of the semi-parabolic hill have the same standing wave pattern as that or the semi-parabolic canyon in Chapter II, but to a much lesser degree. This consistency is expected. The presence of the canyon surface resulted in strong scattered waves diffracted back into the half-space surface, to be combined with the free-field waves to result in large standing wave pattern on the half-space surface (Fig. 2.2) For the case of a semi-parabolic hill, however, the free-field waves from the left hardly sees the hill surface on the right side above and so the scattered waves diffracted from the hill result in a much smaller standing wave pattern on the half-space surface (Fig. 6.4)

The displacement amplitudes on the semi-parabolic hill surface, calculated using the transmitted wave $W^{(t)}$ however, are very different from those on the semi-parabolic canyon in Chapter II. The amplitude is just a bit over 1, not close to four on the semi-parabolic canyon for horizontal incidence. This is because on the half-space surface, the incident and reflected free-field plane waves, with free-field amplitude of two, both propagates horizontally from the left and thus hardly sees the hill surface on the right side above.

Unlike the case of a semi-parabolic canyon, which acts as a semi-infinite barrier facing the free-field waves creating large diffracted and scattered waves, the semi-infinite parabolic hill is in the shadow zone of the free-filed waves, not directly facing the incidence waves, thus creating much less interference with the free-field waves compared to the semi-parabolic canyon.

Up to the dimensionless frequency of $\Omega = 10$, the surface of the hill in the vicinity of the vertex behaves like a $\nu\pi = 3\pi/2$ wedge face. This is why the amplitudes of the waves on the hill surface is close to $2/\nu = 4/3 = 1.33$ as seen on Fig. 6.4

It is also interesting to compare the displacement amplitudes around a semi-parabolic hill in Fig. 6.4 with that around a semi-circular hill in Fig. 6.2 above (which is Fig. 5 of Lee et al (2006)). It is stated in the paper of Lee et al (2006) that for this figure,

> "*… As in the cases of surface canyons and alluvial valleys, the displacement amplitudes to the left of the hill are more oscillatory than those to the right, resulting from diffraction by the hill as a surface topography. For nearly horizontal incidences (*0° and 30°*) the hill also acts as a shield for surface on the hill and to its right, shielding the waves coming from the left, resulting in a standing wave pattern. It is also noted that for nearly vertical incidences (*60° and 90°*), displacement is large and oscillatory on the hill surface. In fact, the maximum amplitudes of motions are all on the circular hill surface. These complicated patterns increase with increasing frequencies …*"

Since Fig. 6.4 plots only the displacement amplitudes around the semi-parabolic hill for horizontal incidence $\gamma = 0^\circ$, it will be compared with the top graph of Fig. 6.2, the displacement amplitudes around the semi-circular hill also for horizontal incidence $\gamma = 0^\circ$. Both graphs show that, for horizontal incidence, they exhibit a standing-wave pattern on the half-space surface to the left and in front of both the semi-circular and semi-parabolic hill.

The displacement amplitudes around the semi-parabolic and circular hills, on the other hand, are smaller than those on the left side of the half-space surface, where the incident waves come from. Beyond the left vertex in both graphs, there is much less interference.

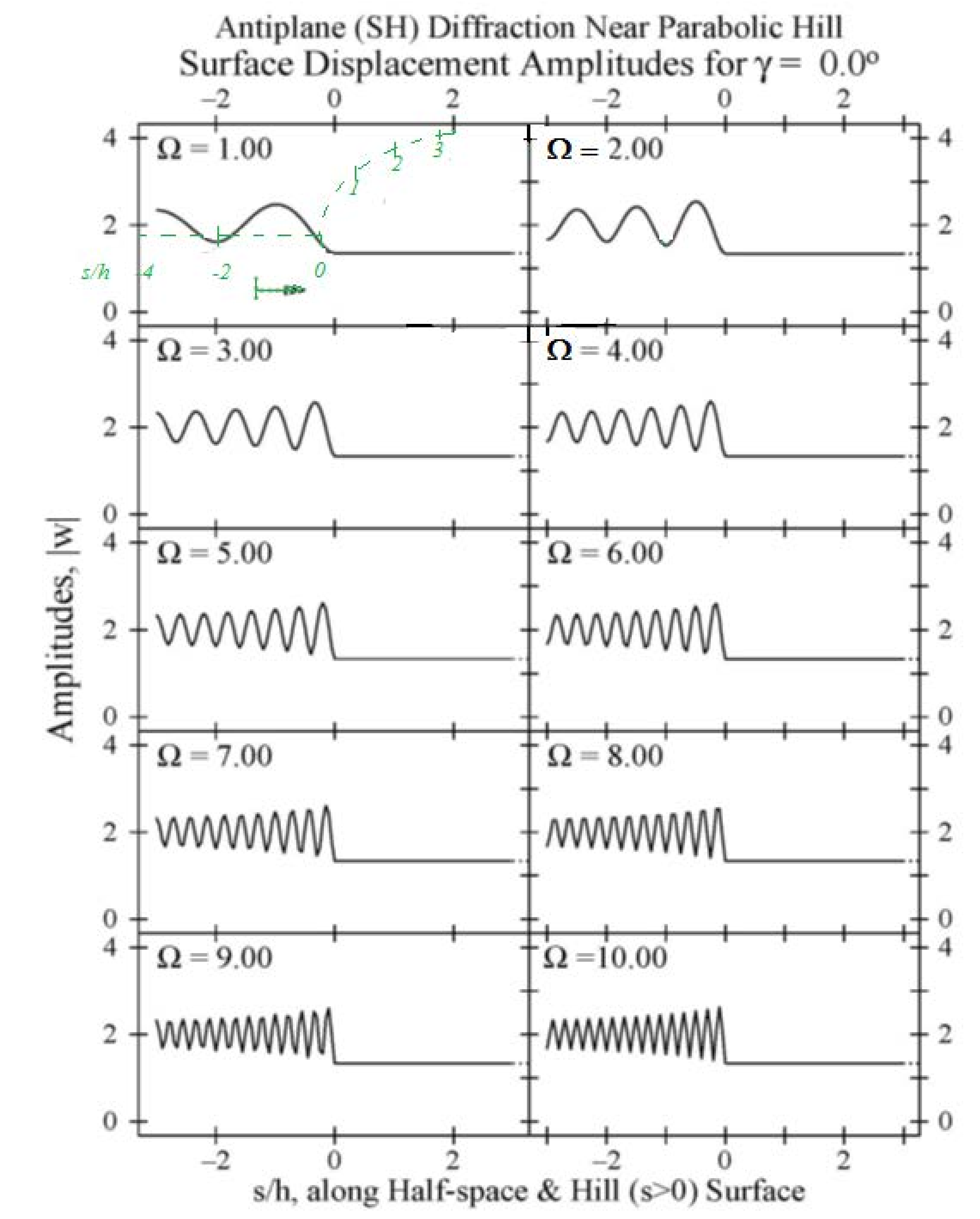

Fig. 6.4 Displacement Amplitudes for Horizontal Incidence, $\gamma = 0^{\circ}$

In this and all subsequent sections, except for Fig. 6.4 (which is 2D) above, all figures presented will now be 3D figures.

Fig. 6.5 represents the 3D displacement amplitudes $|W|$ plotted vs. the dimensionless distance s/h and the dimensionless frequency, Ω in the range $(0,10]$, for the horizontal angle of incidence of $\gamma = 0^{\circ}$.

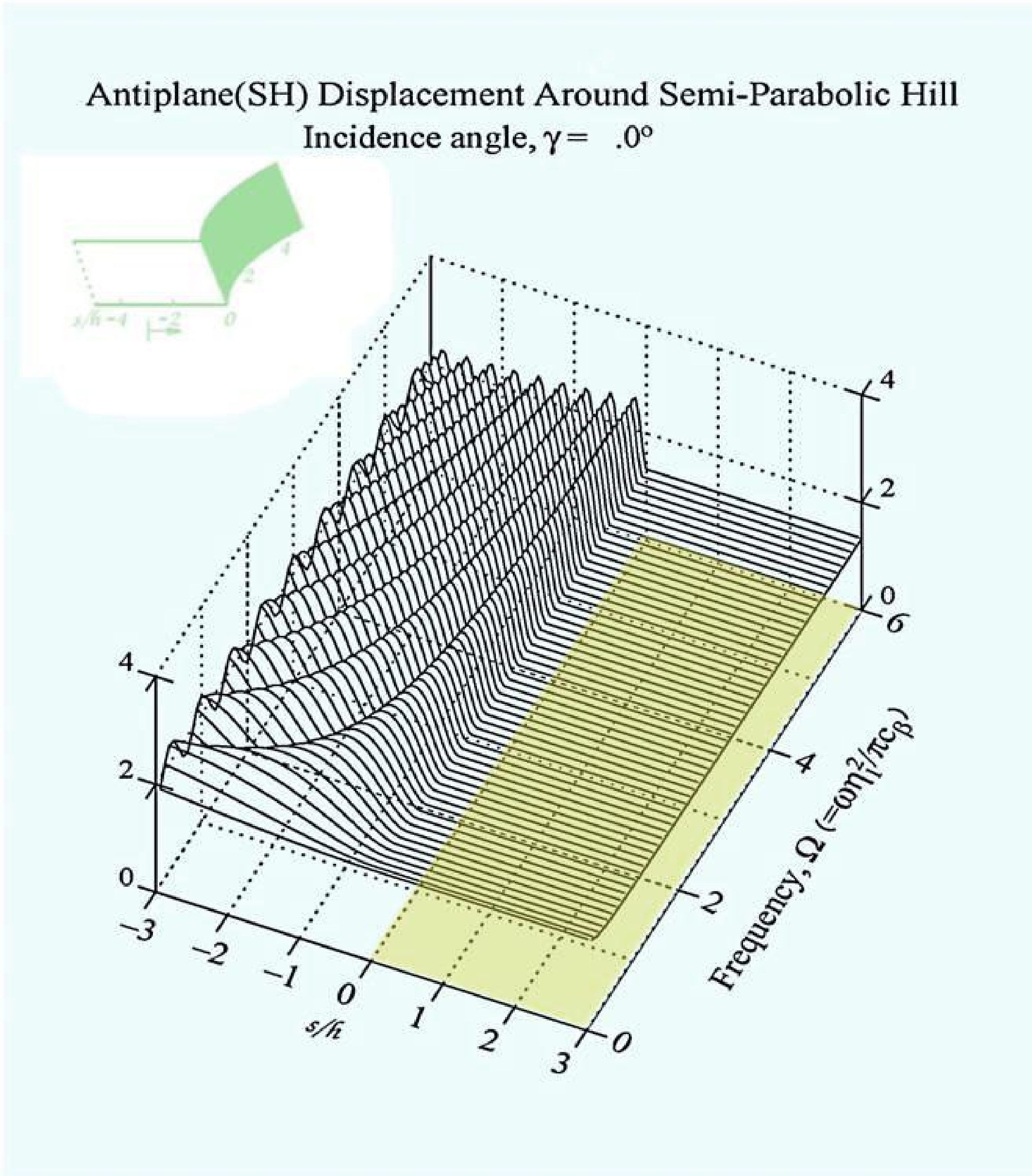

Fig. 6.5 3D Displacement Amplitudes for Horizontal Incidence, $\gamma = 0^{\circ}$

VI.5 Oblique Angles of Incidences: $\gamma = 15^\circ, 30^\circ, 45^\circ$ and 60°

Fig. 6.5 to Fig. 6.9 are the 3D plots of the displacement amplitudes on the half-space surface and around the semi-parabolic hill surface plotted vs.

1) The dimensionless distance s/h measured along the half-space and canyon surface and
2) The dimensionless frequency $\Omega = \omega\eta_0^2/\pi\beta = 2\eta_0^2/\lambda = 4h/\lambda$

respectively for incidence angles of $\gamma = 15^\circ, 30^\circ, 45^\circ$ and 60°. They are the same 3D plots of displacement amplitudes around the semi-parabolic canyon, namely respectively for the same incidence angles as in Fig. 2.7 to Fig. 2.10 in Chapter II.

The 3D plots here confirm the standing-wave patterns on the half-space surface to the left of the canyon where the incident waves come from for all angles of incidence. Unlike the case of horizontal incidence $\gamma = 0^\circ$ in Fig. 6.5, where eh constant asymptote of ~1.33 along the hill surface was observed from very low frequencies on Fig. 6.5, the displacement amplitudes along the hill surfaces are also oscillatory for oblique angles of incidence as observed.

It is again worthwhile to note the displacement amplitudes at the vertex $\left(s/h = 0 \right)$ at all frequencies for all the figures. It is observed that the amplitude of ~1.33 is achieved for all angles of incidence at very low frequency of $\Omega > 0$ and beyond. This confirms the fact that the vertex of the parabolic canyon behaves as the corner of a three-quarter space in an elastic medium. This is consistent with the observation of the displacement amplitudes at the vertex $\left(s/h = 0 \right)$ at all frequencies around the semi-parabolic canyon in Chapter II. There amplitude of 4 is achieved for all angles of incidence at very low frequency of $\Omega > 0$ and beyond. It corresponds to the fact that the vertex of the parabolic canyon behaves as the corner of a quarter spaces in an elastic medium.

Next we compare the displacement amplitudes around a semi-parabolic hill in Fig. 6.6 through 6.9 which hat around a semi-circular hill in Fig. 6.2 above (which is Fig. 5 of Lee et al (2006)). It is stated in the paper of Lee et al (2006) that, for this figure,

> *"… As in the cases of surface canyons and alluvial valleys, the displacement amplitudes to the left of the hill are more oscillatory than those to the right, resulting from diffraction by the hill as a surface topography. For nearly horizontal incidences (*0° and 30°*) the hill also acts as a shield for surface on the hill and to its right, shielding the waves coming from the left, resulting in a standing wave pattern. It is also noted that for nearly vertical incidences (*60° and 90°*), displacement is large and oscillatory on the hill surface. In fact, the maximum amplitudes of motions are all on the circular hill surface. These complicated patterns increase with increasing frequencies …"*

Here we pick just Fig. 6.7 and 6.9 plots of the displacement amplitudes around the semi-parabolic hill respectively for incidence angles of $\gamma = 30^{\circ}$ and 60°. It will be compared with the middle two graphs of Fig. 6.2, the displacement amplitudes around the semi-circular hill also for incidence angles of $\gamma = 30^{\circ}$ and 60°. Both graphs show that, for both incidences, they exhibit a standing-wave pattern on the half-space surface to the left and in front of both the semi-circular and semi-parabolic hill.

The displacement amplitudes on and around the semi-parabolic hill, on the other hand, are smaller than those on the left side of the half-space surface, where the incident waves come from. There's much less interference beyond the left vertex in both graphs. This is much different from the displacement amplitudes on the circular hill in Fig. 6.2. There it shows that the amplitudes on the circular hill are larger than those on the left side of the half-space and are much more oscillatory. This is because the semi-circular hill is a finite region. Waves from the semi-infinite half-space that entered the hill region will interfere with the refracted waves in the hill, and may even get trapped inside the hill, thus resulting in large oscillatory standing wave motions. The semi-parabolic hill region, on the other hand, unlike the semi-circular hill, is not a finite region. It is instead a semi-infinite region. The waves entering the hill from the semi-infinite half-space become refracted waves continue travelling to the right of the semi-infinite hill without being trapped. These are thus much less interference and no standing wave pattern is exhibited in the hill region. This explains the big difference in the displacement between the semi-circular and semi-parabolic hill.

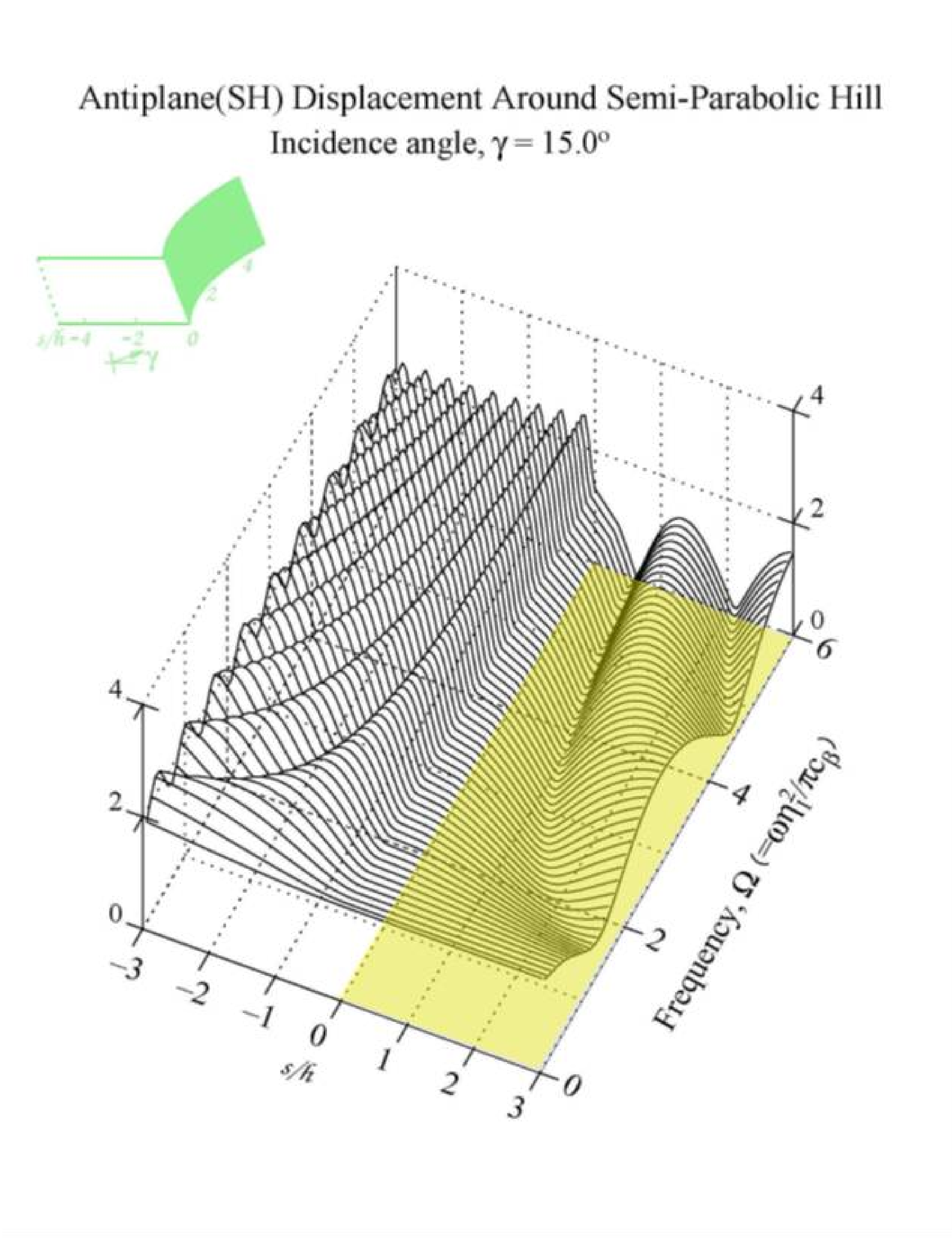

Fig. 6.6 3D Displacement Amplitudes for Oblique Incidence, $\gamma = 15^{\circ}$

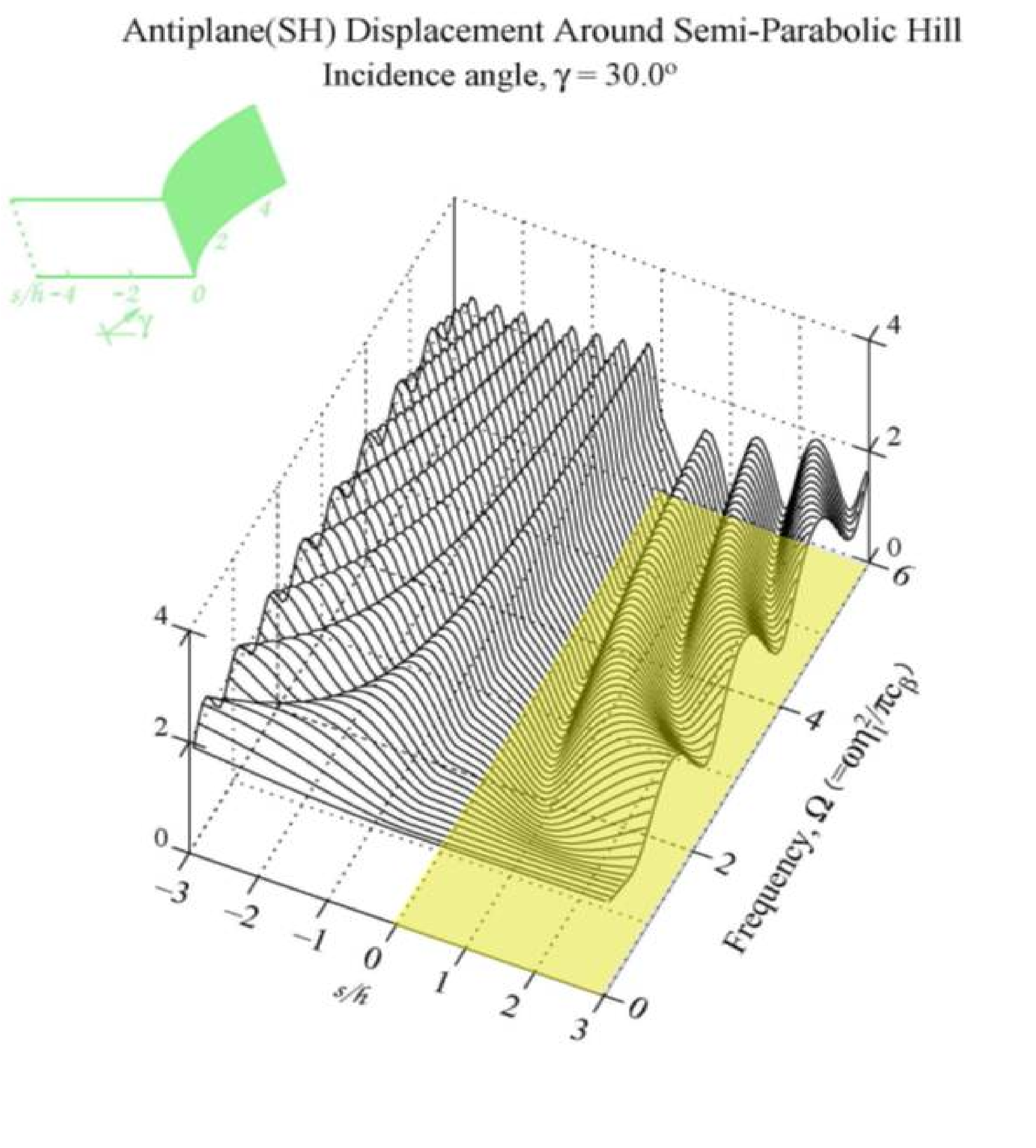

Fig. 6.7 3D Displacement Amplitudes for Oblique Incidence, $\gamma = 30^{\circ}$

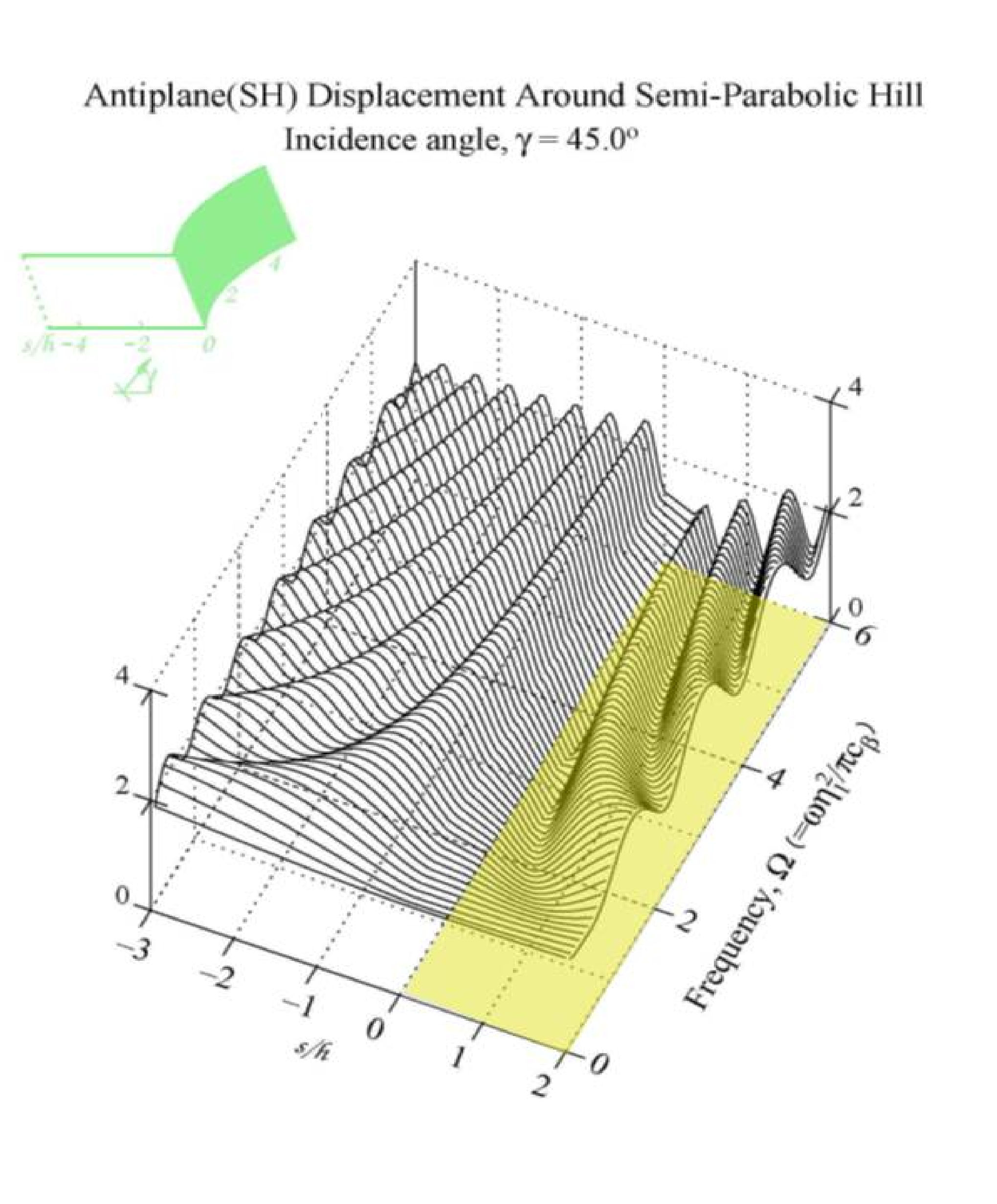

Fig. 6.8 3D Displacement Amplitudes for Oblique Incidence, $\gamma = 45^{\circ}$

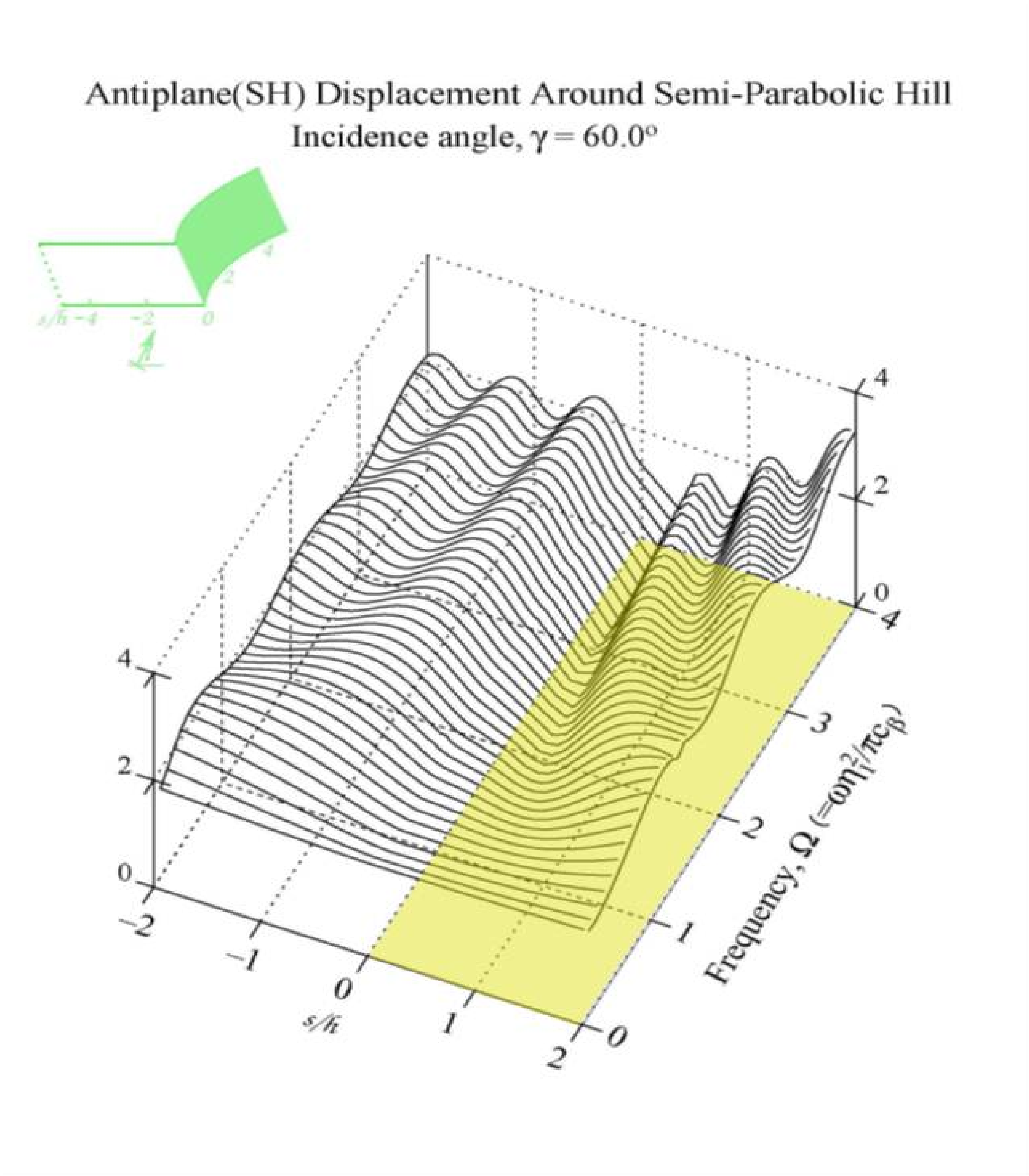

Fig. 6.9 3D Displacement Amplitudes for Oblique Incidence,

VI.6 Summary

Chapter VI extends the work of Lee el al (2006) on anti-plane diffraction around a semi-circular hill to that of a semi-parabolic hill. It is found that the displacement motions around a semi-parabolic hill are comparatively smaller than that around a semi-circular canyon. This is because the semi-circular hill in Lee et al (2006) is a finite region that creates trapped waves resulting in large amplification. The semi-parabolic hill here, on the other hand, lies in the shadow region of the incident waves, hardly seeing them.

Chapter VII. Rotation Components of Anti-Plane SH Waves around a Semi-Parabolic Hill

VII.1 Introduction

Extending the work of Lee et al (2006) for diffraction around a semi-circular hill, the computation of the displacement component around a semi-parabolic hill is completed and presented in the last chapter. The rotational and shear stress components of motions will next be derived and presented. This section is a summary of the rotation and shear stress components introduced in Chapter III, IV and V above for the diffraction of anti-plane SH waves around a semi-parabolic canyon, to be used in this Chapter for the case of semi-parabolic Hill.

Recall from Section III.2 of Chapter III, for the case of anti-plane (SH) displacement with only the z-component of motions, namely $\tilde{U} = W\hat{k} = W(x, y)\hat{k}$, the rotational vector, $\tilde{\omega}$ of motion is defined as

$$\tilde{\omega} = \begin{pmatrix} \omega_x \\ \omega_y \\ 0 \end{pmatrix} = \frac{1}{2}\begin{pmatrix} \partial W/\partial y \\ -\partial W/\partial x \\ 0 \end{pmatrix} \qquad \text{Chapter III Equation (3)}$$

and the two components of rotation are respectively the torsion and rocking motions:

1) The rotation about the vertical y-axis, the torsional motion, given by

$$\omega_y = \omega_{Tor} = -\tfrac{1}{2}\,\partial W/\partial x \qquad \text{Chapter III Equation (4a)}$$

Which when takes the form when expressed in parabolic coordinates:

$$\begin{aligned}\omega_{Tor} &= \omega_y = \tfrac{1}{2}\left(\nabla \times W\hat{k}\right)\cdot\hat{j} \\ &= -\tfrac{1}{2}\,\partial W/\partial x = -\tfrac{1}{2}\left(\frac{\partial W}{\partial \eta}\frac{\partial \eta}{\partial x} + \frac{\partial W}{\partial \xi}\frac{\partial \xi}{\partial x}\right)\end{aligned} \qquad \text{Chapter III Equation (8)}$$

and simplifies to (Chapter III.2 Equation (12)):

$$\omega_{Tor} = \left(-\tfrac{1}{2}\right)\frac{1}{\left(\xi^2+\eta^2\right)}\left(\xi\frac{\partial W}{\partial \xi} - \eta\frac{\partial W}{\partial \eta}\right) \tag{1}$$

and

2) The rotation about the horizontal x-axis, the rocking motion, given by:

$$\omega_x = \omega_{Rock} = \tfrac{1}{2}\,\partial W/\partial y \qquad \text{Chapter III Equation (4b)}$$

Which takes the form when expressed in parabolic coordinates:

$$\begin{aligned}\omega_{Rock} &= \omega_x = \tfrac{1}{2}\left(\nabla \times W\hat{k}\right)\cdot\hat{i} \\ &= \tfrac{1}{2}\,\partial W/\partial y = \tfrac{1}{2}\left(\frac{\partial W}{\partial \eta}\frac{\partial \eta}{\partial y} + \frac{\partial W}{\partial \xi}\frac{\partial \xi}{\partial y}\right)\end{aligned} \qquad \text{Chapter IV Equation (2)}$$

and simplifies to (Chapter IV.2 Equation (5))

$$\omega_{Rock} = \frac{1}{1\left(\xi^2+\eta^2\right)}\left(\xi\frac{\partial W}{\partial \eta} + \eta\frac{\partial W}{\partial \xi}\right) \tag{2}$$

note that at the half-space surface, where $y = 0$

$$\xi = 0 \qquad \text{and} \qquad \frac{\partial W}{\partial \xi} = 0 \tag{3}$$

so that the rocking motion above at the half-space surface is

$$\omega_{Rock}\Big|_{y=0} = \frac{1}{2\left(\xi^2+\eta^2\right)}\left(\xi\frac{\partial W}{\partial \eta}+\eta\frac{\partial W}{\partial \xi}\right)\Bigg|_{y=0} = 0 \tag{4}$$

which is the same case as in the rocking motions around the semi-parabolic canyon in Chapter IV, namely being zero at the half-space surface.

The equations for both torsion and rocking above will be used in the next sections to compute the rotational motions on the half-space surface to the left and on the semi-parabolic surface on the right. Refer to Fig. 6.3 for the semi-parabolic hill model. Note that the half-space, the exterior region, $\mathscr{H}$, and the parabolic hill region, the interior region $\mathscr{P}$, now uses different equations to calculate the displacements in Chapter VI and the rotations in this chapter, using Equation (13) from Section VI.3 of Chapter VI:

$$\begin{aligned} W^s(\xi,\eta) &= 2\sec{}^{\gamma}\!/_{2}\sum_{n=0}^{\infty} A_n D_{-2n-1}(\lambda\eta) D_{2n}(\lambda\xi) \\ W^t(\xi,\eta) &= 2\sec{}^{\gamma}\!/_{2}\sum_{n=0}^{\infty} B_n D_n(\bar{\lambda}\eta) D_n(\lambda\xi) \end{aligned} \qquad \text{Chapter VI Equation (13)}$$

so that the exterior half-space region $\mathscr{H}$ uses the free-field waves W^{ff} and scattered waves $W^{(s)}$ to represent the displacements and the interior hill region $\mathscr{P}$ uses the transmitted waves $W^{(t)}$ to calculate the displacements and rotations.

As in the cases of torsion and rocking respectively in Chapters III and IV, they will be normalized by the rotation amplitude of the incident waves $\left|\tilde{\omega}^i\right|$:

$$\left|\tilde{\omega}^i\right| = \left(\left|\omega_x^i\right|^2 + \left|\omega_y^i\right|^2\right)^{1/2} = k/2\left(\sin^2\gamma + \cos^2\gamma\right)^{1/2}\left|W^i\right| = k/2\left|W^i\right| = k/2 \quad \text{Chapter III Eqn (7)}$$

so that the normalized torsion and rocking amplitudes are calculated:

$$\begin{aligned}\left|\overline{\omega}_{Tor}\right| &= \left|\omega_{Tor}/\omega^i\right| = 2/k\left|\omega_{Tor}\right| = 2/k\left|\left(\omega_{Tor}^{ff} + \omega_{Tor}^{s}\right)\right| \\ &= 2/k\left|-1/2\,\partial W/\partial x\right| = 1/k\left|\partial W/\partial x\right|\end{aligned} \tag{5}$$

and

$$\begin{aligned}\left|\overline{\omega}_{Rock}\right| &= \left|\omega_{Rock}/\omega^i\right| = 2/k\left|\omega_{Rock}\right| = 2/k\left|\left(\omega_{Rock}^{ff} + \omega_{Rock}^{s}\right)\right| \\ &= 2/k\left|1/2\,\partial W/\partial y\right| = 1/k\left|\partial W/\partial y\right|\end{aligned} \tag{6}$$

Finally, the normalized resultant rotation motion, as defined in Equation (24) of Chapter V is:

$$\left|\overline{\omega}\right| = \frac{|\omega|}{\left|\omega^{i}\right|} = \frac{2}{k}|\omega| = \frac{2}{k}\left(\left|\omega_{Rock}\right|^{2} + \left|\omega_{Tor}\right|^{2}\right)^{1/2}$$
$$= \left(\left|\overline{\omega}_{x}\right|^{2} + \left|\overline{\omega}_{y}\right|^{2}\right)^{1/2} = \left(\left|\omega_{Rock}\right|^{2} + \left|\omega_{Tor}\right|^{2}\right)^{1/2} \tag{7}$$

VII.2 Normalized Torsion Amplitudes, $\left|\overline{\omega}_{Tor}\right|$

Recall from Equation (1) in the previous section:

$$\omega_{Tor} = \left(-\tfrac{1}{2}\right)\frac{1}{\left(\xi^2+\eta^2\right)}\left(\xi\frac{\partial W}{\partial \xi} - \eta\frac{\partial W}{\partial \eta}\right) \qquad \text{Equation (1) above}$$

and the displacement equation of motions at the half-space region and hill region are respectively, from Equation (12) and (13) of Chapter VI:

$$W^{ff} = W^i + W^r = \exp\left(ikx\cos\gamma\right)\sin\left(y\sin\gamma\right) \qquad \text{Chapter I Equation (6)}$$

or

$$W^{ff}\left(\eta,\xi\right) = 2\sec\tfrac{\gamma}{2}\sum_{n=0}^{\infty} a_n D_{2n}\left(\overline{\lambda}\eta\right)D_{2n}\left(\lambda\xi\right) \qquad \text{Chapter VI Equation (12)}$$

$$\begin{aligned} W^s\left(\xi,\eta\right) &= 2\sec\tfrac{\gamma}{2}\sum_{n=0}^{\infty} A_n D_{-2n-1}\left(\lambda\eta\right)D_{2n}\left(\lambda\xi\right) \\ W^t\left(\xi,\eta\right) &= 2\sec\tfrac{\gamma}{2}\sum_{n=0}^{\infty} B_n D_n\left(\overline{\lambda}\eta\right)D_n\left(\lambda\xi\right) \end{aligned} \qquad \text{Chapter VI Equation (13)}$$

With $W = W^{ff} + W^s$ being the displacement in the half-space region, and $W = W^t$ the displacement in the parabolic hill region.

At the surface of the half-space to the left of the semi-parabolic hill, where $\xi = 0\left(y=0\right)$ and $W = W^{ff} + W^s$, the torsional motion is

$$\omega_{Tor}\big|_{y=0} = \left(-\tfrac{1}{2}\right)\frac{1}{\left(\cancel{\xi}^2+\eta^2\right)}\left(\cancel{\xi}\frac{\partial W}{\partial \xi}-\eta\frac{\partial W}{\partial \eta}\right)\Bigg|_{\xi=0} = \frac{1}{2\eta}\frac{\partial W}{\partial \eta}\Bigg|_{\xi=0}$$
$$= \left(2\sec\tfrac{\gamma}{2}\right)\frac{\lambda}{2\eta}\sum_{n=0}^{\infty}\left(ia_n D'_{2n}\left(\bar{\lambda}\eta\right)+A_n D'_{-2n-1}\left(\lambda\eta\right)\right)D_{2n}\left(\lambda\xi\right)\Big|_{\xi=0} \tag{8a}$$

from which the normalized torsional motion at the half-space surface is

$$\bar{\omega}_{Tor}\big|_{y=0} = \left(\tfrac{1}{k}\right)\omega_{Tor}\big|_{y=0}$$
$$= \left(2\sec\tfrac{\gamma}{2}\right)\frac{\lambda}{2k\eta}\sum_{n=0}^{\infty}\left(ia_n D'_{2n}\left(\bar{\lambda}\eta\right)+A_n D'_{-2n-1}\left(\lambda\eta\right)\right)D_{2n}\left(\lambda\xi\right)\Big|_{\xi=0} \tag{8b}$$
$$= \left(2\sec\tfrac{\gamma}{2}\right)\frac{1}{\bar{\lambda}\eta}\sum_{n=0}^{\infty}\left(ia_n D'_{2n}\left(\bar{\lambda}\eta\right)+A_n D'_{-2n-1}\left(\lambda\eta\right)\right)D_{2n}\left(\lambda\xi\right)\Big|_{\xi=0}$$

At the surface of the semi-parabolic hill, where $\eta=\eta_1, \frac{\partial W}{\partial \eta}\Big|_{\eta=\eta_1}$, and $W=W^t$, the torsional motion is

$$\omega_{Tor}\big|_{\eta=\eta_1} = \left(-\tfrac{1}{2}\right)\frac{1}{\left(\xi^2+\eta^2\right)}\left(\xi\frac{\partial W^t}{\partial \xi}-\eta\frac{\partial W^t}{\partial \eta}\right)\Bigg|_{\eta=\eta_1} = \left(-\tfrac{1}{2}\right)\frac{1}{\left(\xi^2+\eta^2\right)}\xi\frac{\partial W^t}{\partial \xi}\Bigg|_{\eta=\eta_1}$$
$$= \left(2\sec\tfrac{\gamma}{2}\right)\frac{-\lambda\xi}{2\left(\xi^2+\eta^2\right)}\sum_{n=0}^{\infty}\left(B_n D_n\left(\bar{\lambda}\eta\right)\right)\Big|_{\eta=\eta_1} D'_n\left(\lambda\xi\right) \tag{9a}$$

From which the normalized torsional motion at the parabolic hill surface is

$$\bar{\omega}_{Tor}\big|_{\eta=\eta_1} = \left(\tfrac{1}{k}\right)\omega_{Tor}\big|_{\eta=\eta_1}$$
$$= \left(2\sec\tfrac{\gamma}{2}\right)\frac{-\lambda\xi}{2k\left(\xi^2+\eta^2\right)}\sum_{n=0}^{\infty}\left(B_n D_n\left(\bar{\lambda}\eta\right)\right)_{\eta=\eta_1} D'_n\left(\lambda\xi\right) \tag{9b}$$

Fig. 7.1 to Fig. 7.5 are 3D plots of the normalized torsional rotation amplitudes on the half-space surface and around the semi-parabolic hill surface plotted vs.

1) The dimensionless distance s/h along the half-space and hill surfaces and

2) The dimensionless frequency $\Omega = \omega\eta_0^2/\pi\beta = 2\eta_0^2/\lambda = 4h/\lambda$

respectively for the five incidence angles of $\gamma = 0^\circ, 15^\circ, 30^\circ, 45^\circ$ and 60°. They are the same 3D plots of torsional rotation amplitudes around the semi-parabolic canyon, namely respectively for the same incidence angles as in Fig. 3.3 to Fig. 3.7 in Chapter III. They are the torsional rotation amplitudes calculated at the same points on the half-space and the semi-parabolic hill surfaces. As in the last chapter, the dimensionless distance, s/h is measured in units of the focal length of the semi-parabolic hill from the tip (vertex, corner point) of the hill, where $s/h = 0$. Points on the surface of the half-space to the left of the hill will have negative units of focal length. Thus the unit $s/h = -3$ corresponds to the point on the surface of the half-space surface at distance of 3 focal lengths to the left of the tip of the canyon. Similarly, points on the surface of the semi-parabolic hill are measured as positive distances along the semi-parabolic hill surface in units of focal length from the semi-parabolic hill's tip. The shape of the half-space and hill surface on which the displacements are calculated is outlined as 3D figure on the top-right graph of the figure. There the hill surface is shaded in green, and the green arrow indicates the corresponding direction of the incident SH wave, W^i which is assumed to be coming from the left-side (from where s is negative, or $s/h < 0$ towards the hill.

Recall that in the case of displacement amplitudes for the semi-parabolic hill in the last chapter (Chapter VI) they are compared with the corresponding displacement amplitudes around a semi-parabolic canyon in Chapter II. The torsion amplitudes around the semi-parabolic hill in this section here will be compared with the torsion amplitudes around the semi-parabolic canyon in Sections III.4 and III.5 of Chapter III.

Take for example, Fig. 7.1 here for around the hill surface, with Fig. 3.3 for around the canyon surface, both 3D plots for horizontal incidence $\gamma = 0^\circ$. The torsional rotation amplitudes on both figures show that the waves on the half-space surface region to the left of the semi-parabolic hill (Fig. 7.1) have the same standing wave pattern as that of the semi-parabolic canyon (Fig. 3.3) in Chapter III but to a much lesser degree. This consistency is expected. The presence of the canyon surface resulted in strong scattered waves diffracted back into the half-space surface, to be combined with the free-field waves to result in large standing wave pattern on the half-space surface (Fig. 3.3). For the case of a semi-parabolic hill, however, the free-field waves from the left hardly sees the hill surface on the right side above, and so the scattered waves diffracted from the hill result in a much smaller standing wave pattern on the half-space surface (Fig. 7.1)

The torsion rotation amplitudes on the semi-parabolic hill surface, calculated using the transmitted wave $W^{(t)}$, however are very different from those on the semi-parabolic canyon in Chapter III. The amplitude is just a bit over 1, not close to three for torsion on the semi-parabolic canyon for horizontal incidence. This is because, on the half-space surface, the incident and reflected free-field plane waves, with free-field amplitude of two, both propagates horizontally from the left, and thus hardly sees the hill surface on the right side above.

As the angles of incidence increase from zero, with $\gamma = 15^\circ, 30^\circ, 45^\circ$ and 60° in Fig. 7.2 through 7.5, the same standing wave patterns are observed on the half-space surface to the left of the semi-parabolic hill, and the torsional rotation amplitudes on the hill surface do show a little increase in magnitude resulting from slightly more interferences of the free-filed waves on the hill region, as a result of oblique incidences.

Unlike the case of a semi-parabolic canyon, which acts as a semi-infinite barrier facing the free-field waves creating large diffracted and scattered waves, the semi-infinite parabolic hill is in the shadow zone of the free-filed waves, not directly facing the incidence waves, thus creating much less interference for the torsional rotations with the free-field rotations compared to that of the semi-parabolic canyon.

All such observations were already made for displacement amplitudes around a semi-parabolic hill in the last chapter (Chapter VI).

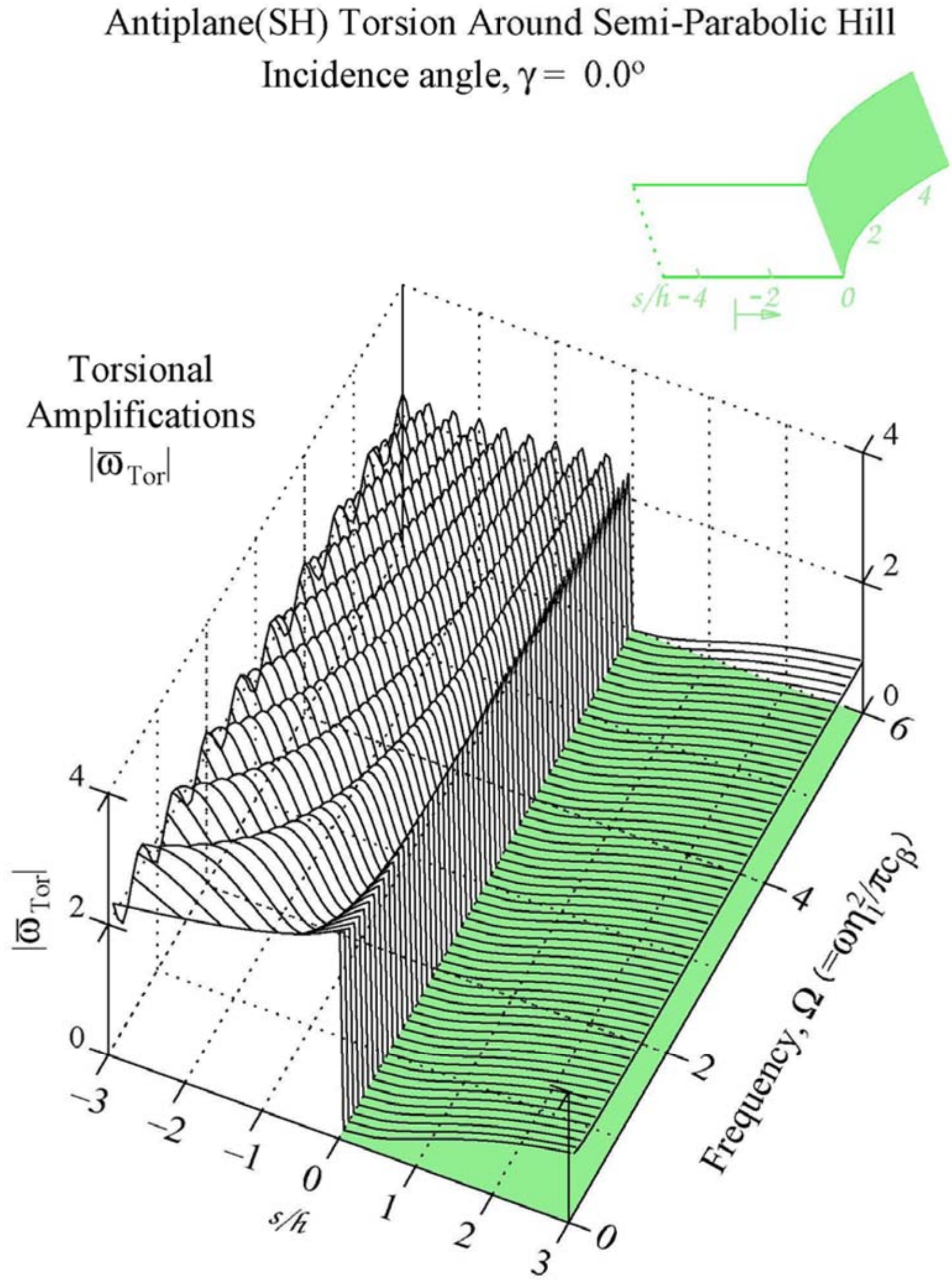

Fig. 7.1 3D Torsion Amplitudes for Horizontal Incidence, $\gamma = 0^{\circ}$

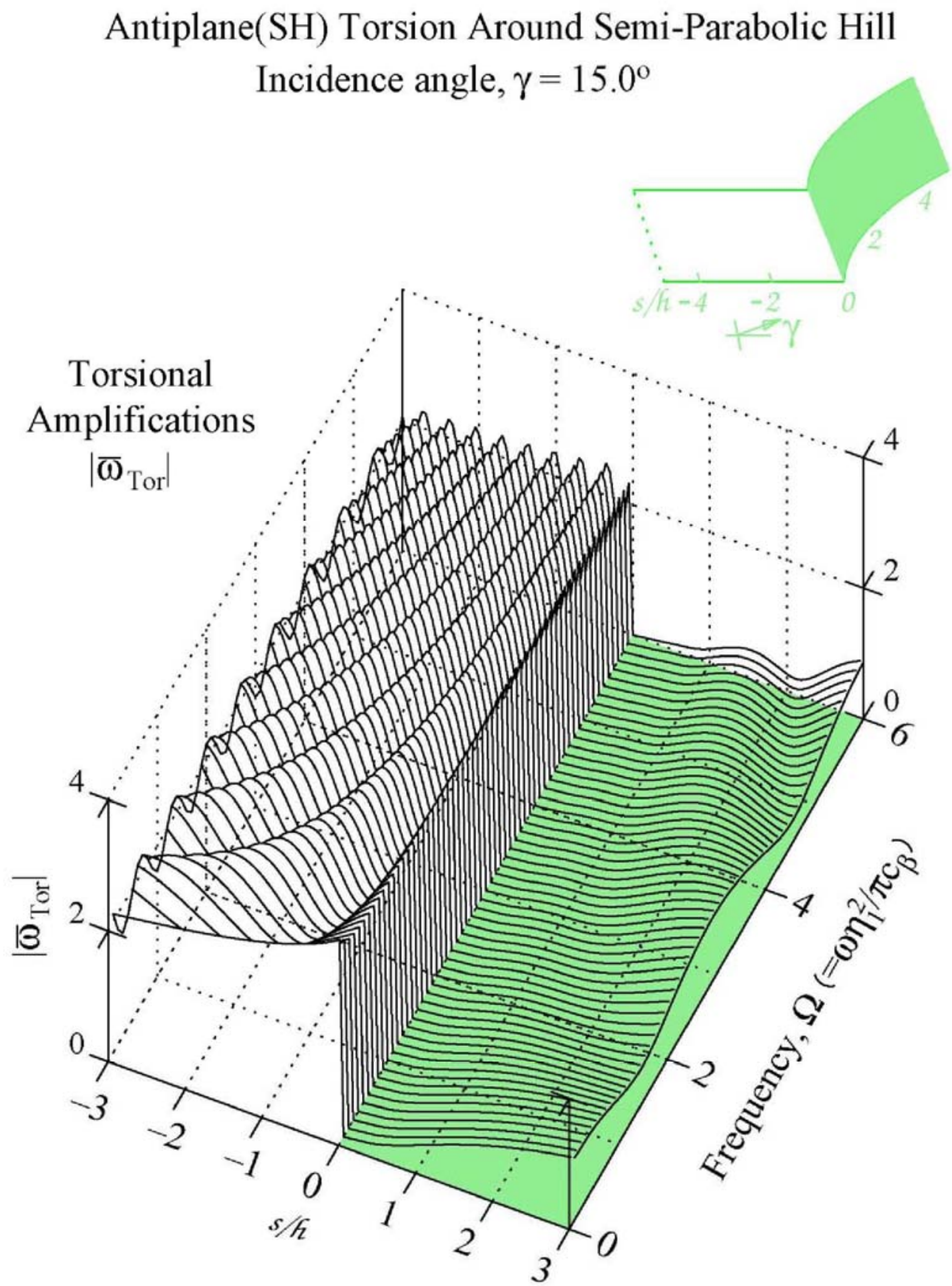

Fig. 7.2 3D Torsion Amplitudes for Oblique Incidence, $\gamma = 15^{\circ}$

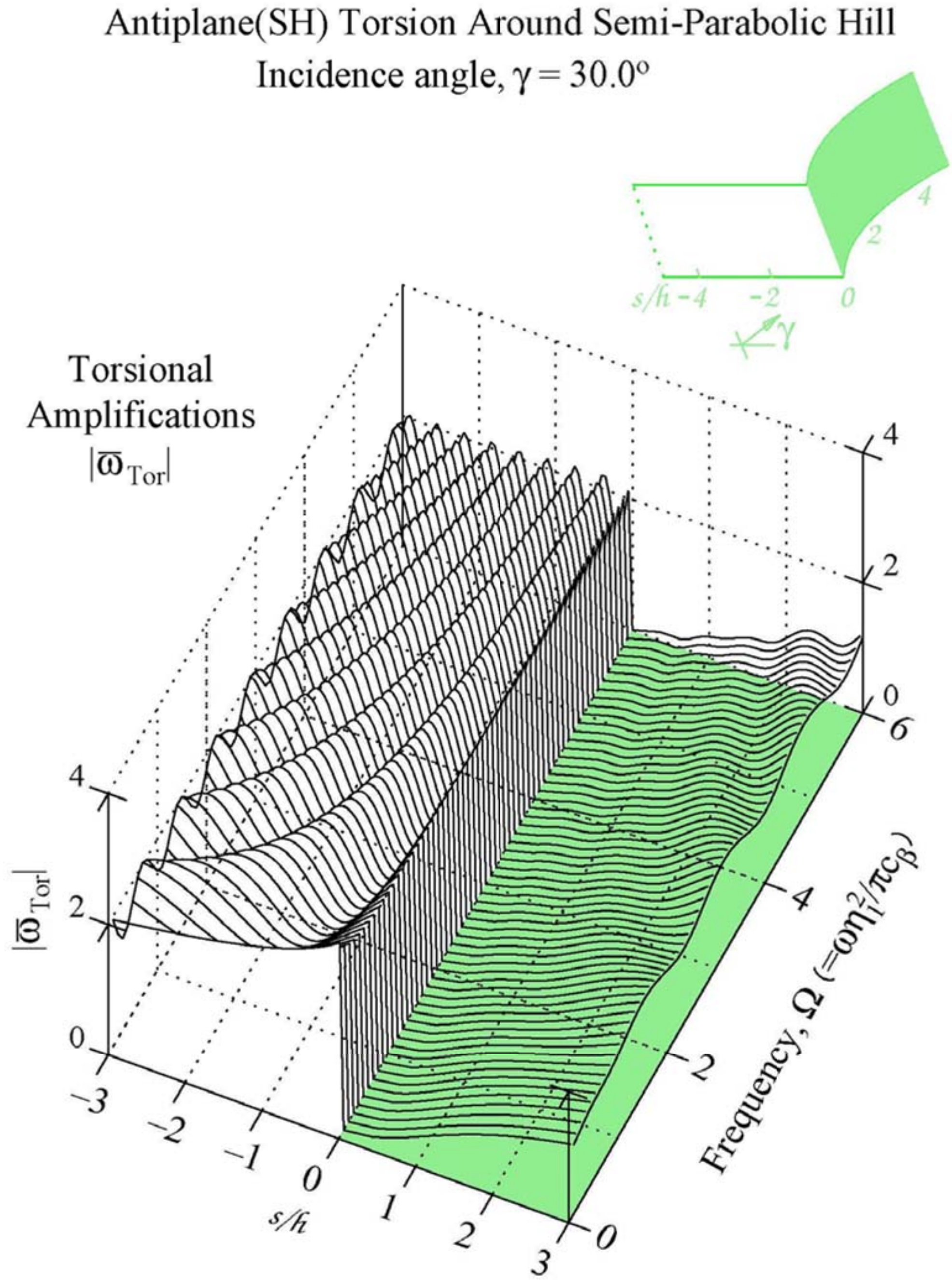

Fig. 7.3 3D Torsion Amplitudes for Oblique Incidence, $\gamma = 30^{\circ}$

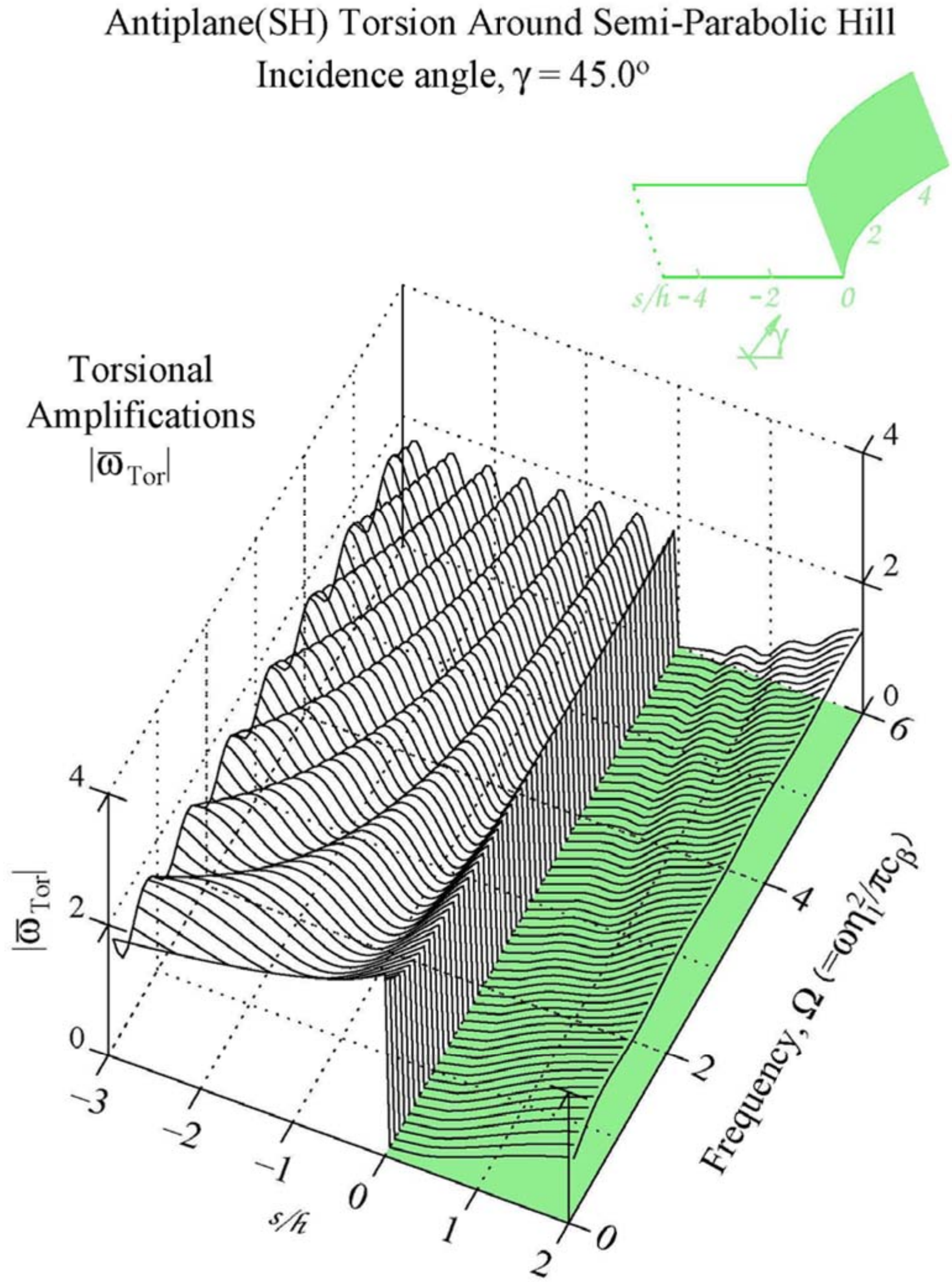

Fig. 7.4 3D Torsion Amplitudes for Oblique Incidence, $\gamma = 45^{\circ}$

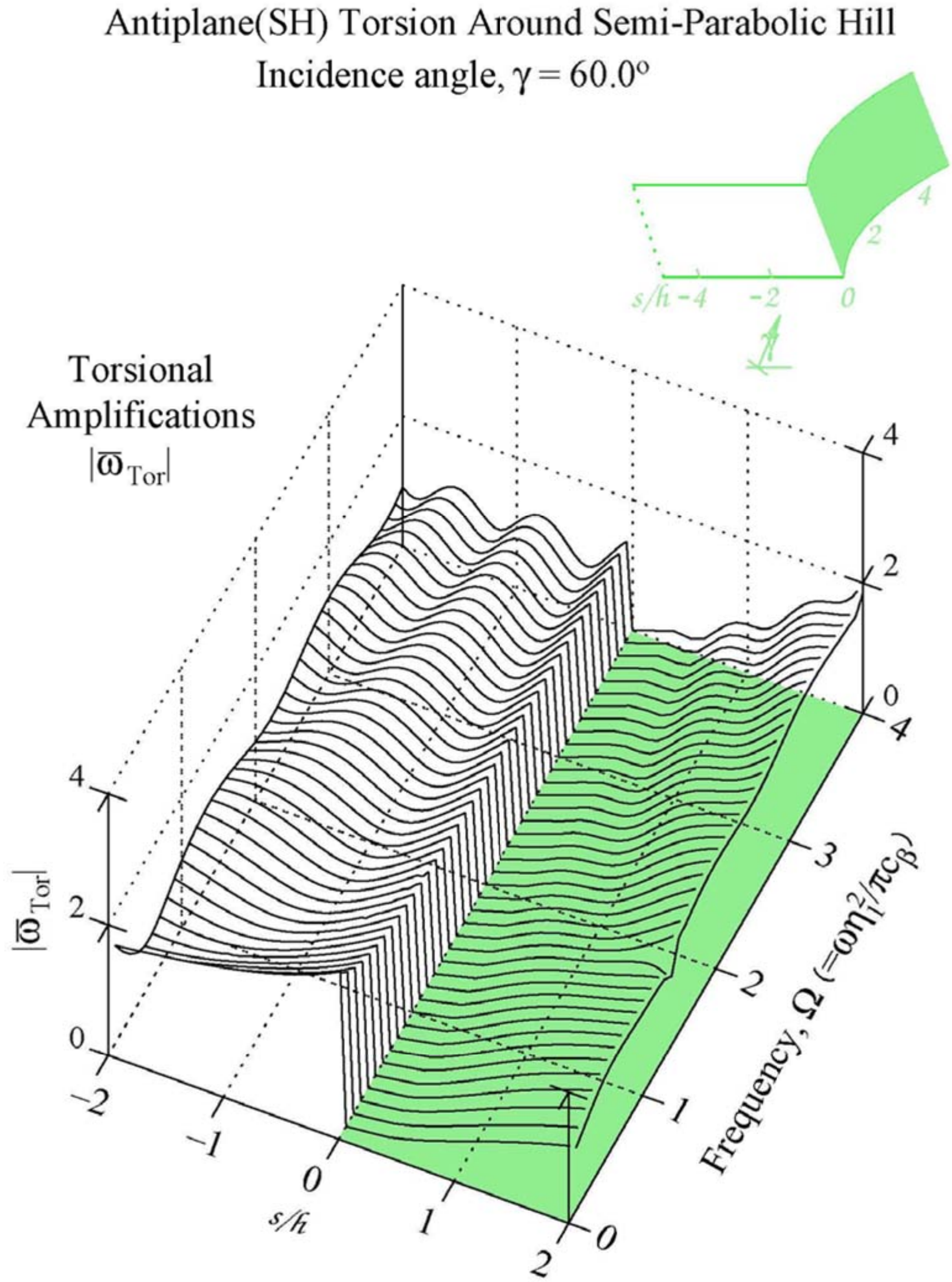

Fig. 7.5 3D Torsion Amplitudes for Oblique Incidence, $\gamma = 60^{\circ}$

VII.3 Normalized Rocking Amplitudes, $\left|\overline{\omega}_{Rock}\right|$

With the presentations of the torsional motions around the semi-parabolic hill completed in the lst section, we now turn to the cases of rocking motions. Recall from Equation (2) in the first section of the chapter above:

$$\omega_{Rock} = \frac{1}{1\left(\xi^2+\eta^2\right)}\left(\xi\frac{\partial W}{\partial \eta}+\eta\frac{\partial W}{\partial \xi}\right) \qquad \text{Equation (2) above}$$

And that the rocking motion at the half-space surface is zero:

$$\omega_{Rock}\Big|_{y=0} = \frac{1}{2\left(\cancel{\xi}^2+\eta^2\right)}\left(\cancel{\xi}\frac{\partial W}{\partial \eta}+\eta\frac{\partial W}{\partial \cancel{\xi}}\right)\Bigg|_{y=0} = 0 \qquad \text{Equation (4) above}$$

Recall that the displacement equation of motions at the hill region is, from Equation (13) of Chapter VI

$$\begin{aligned} W^s\left(\xi,\eta\right) &= 2\sec{}^{\gamma}\!\!\diagup\!_2 \sum_{n=0}^{\infty} A_n D_{-2n-1}\left(\lambda\eta\right) D_{2n}\left(\lambda\xi\right) \\ W^t\left(\xi,\eta\right) &= 2\sec{}^{\gamma}\!\!\diagup\!_2 \sum_{n=0}^{\infty} B_n D_n\left(\overline{\lambda}\eta\right) D_n\left(\lambda\xi\right) \end{aligned} \qquad \text{Chapter VI Equation (13)}$$

All the surface of the semi-parabolic hill, where $\eta=\eta_1, \left.\frac{\partial W}{\partial \eta}\right|_{\eta=\eta_1}=0$ and $W=W$ the rocking motion is

$$\begin{aligned}\omega_{Rock}\Big|_{\eta=\eta_1} &= \frac{1}{2\left(\xi^2+\eta_1^2\right)}\left(\xi\frac{\partial \cancel{W}^t}{d\eta}+\eta_1\frac{\partial W^t}{d\xi}\right)\Bigg|_{\eta=\eta_1} = \frac{\eta_1}{2\left(\xi^2+\eta_1^2\right)}\frac{\partial W^t}{d\xi}\Bigg|_{\eta=\eta_1} \\ &= \left(2\sec\frac{\gamma}{2}\right)\frac{\lambda\eta_1}{2\left(\xi^2+\eta_1^2\right)}\sum_{n=0}^{\infty}B_n D_n\left(\bar{\lambda}\eta\right)\Big|_{\eta=\eta_1} D_n^{'}\left(\lambda\xi\right)\end{aligned} \tag{11}$$

From which the normalized rocking motion takes the form:

$$\begin{aligned}\bar{\omega}_{Rock}\Big|_{\eta=\eta_1} &= \frac{1}{k}\,\omega_{Rock}\Big|_{\eta=\eta_1} \\ &= \left(2\sec\frac{\gamma}{2}\right)\frac{\lambda\eta_1}{2k\left(\xi^2+\eta_1^2\right)}\sum_{n=0}^{\infty}B_n D_n\left(\bar{\lambda}\eta\right)\Big|_{\eta=\eta_1} D_n^{'}\left(\lambda\xi\right)\end{aligned} \tag{12}$$

Fig. 7.6 to 7.10 are the rocking motions around the same semi-parabolic hill for eth same angles of incidences in this section $\gamma = 0^\circ, 15^\circ, 30^\circ, 45^\circ$ and 60°.

As in Fig. 7.1 through 7.5 for torsion amplitudes, the rocking amplitudes are calculated at points on the half-space and parabolic surfaces. The same dimensionless distance s/h is measured in units of the focal length of the parabolic canyon from the tip (vertex, corner point) of the canyon where $s/h = 0$. Refer to the description of Fig. 7.1 through 7.5 in the last section for details.

As stated in Equation (4) above, all five figures (Fig. 7.6 through 7.10) to follow have zero rocking motions at the half-space surface.

The rocking amplitudes around the semi-parabolic hill in this section here will, as with the torsion amplitudes in the previous section, again be compared with the corresponding rotation (which is rocking here) amplitudes around the semi-parabolic canyon in Sections IV.3 and IV.4 of Chapter IV, namely, Fig. 4.2 to 4.6 for rocking motions around a semi-parabolic canyon for the same angles of incidences as in this section, $\gamma = 0^\circ, 15^\circ, 30^\circ, 45^\circ$ and 60°.

As noted above, both sets of figures, Fig. 7.6 to 7.10 for semi-parabolic hill and Fig. 4.2 to 4.6 for rocking motions around a semi-parabolic canyon, have zero rocking motions at the half-space surface. Refer to Equation (2) above in this Chapter and Equation (12) in Chapter IV for details.

The rocking rotation amplitudes on the semi-parabolic hill surface, calculated using the transmitted wave $W^{(t)}$, however, are quite different from those on the semi-parabolic canyon in Chapter IV. Take the case of horizontal incidence, Fig. 7.6 here and Fig. 4.2 of Chapter IV. Starting from zero at the vertex, where $s/h = 0$ the amplitude in Fig. 7.6 here for just slightly increased to somewhere close to an amplitude of 0.5 along the hill surface, not close to two for rocking on the semi-parabolic canyon for horizontal incidence. This is because, as in the case of torsional motions, on the half-space surface, the incident and reflected free-filed plane waves, with free-field amplitude of two, both propagates horizontally from the left, and thus hardly sees the hill surface on the right side above.

As the angles of incidence increase from zero, with $\gamma = 15^{\circ}, 30^{\circ}, 45^{\circ}$ and 60° in Fig. 7.7 through 7.10, the rocking rotation amplitudes on the hill surface do show more oscillatory amplitudes, but stay low in magnitude, resulting from slightly more interferences of the free-filed waves on the hill region, as a result of oblique incidences.

For the incidence angles of $\gamma = 15^{\circ}$ and 30° (Fig. 7.7 and 7.8), the rocking amplitudes along the parabolic hill surface stays below one. For incidence angles of $\gamma = 45^{\circ}$ and 60° (Fig. 7.9 and 7.10) the rocking amplitudes along the hill do increase to above one. It is only at the incidence angle of $\gamma = 60^{\circ}$ (Fig. 7.10) that the rocking amplitudes go above and close to two at the parabolic hill surface.

Unlike the case of a semi-parabolic canyon, which acts as a semi-infinite barrier facing the free-field waves creating large diffracted and scattered waves, the semi-infinite parabolic hill is in the shadow zone of the free-field waves, not directly facing the incidence waves, thus creating much less interference for the rocking rotations with the free-field rotations compared to that of the semi-parabolic canyon.

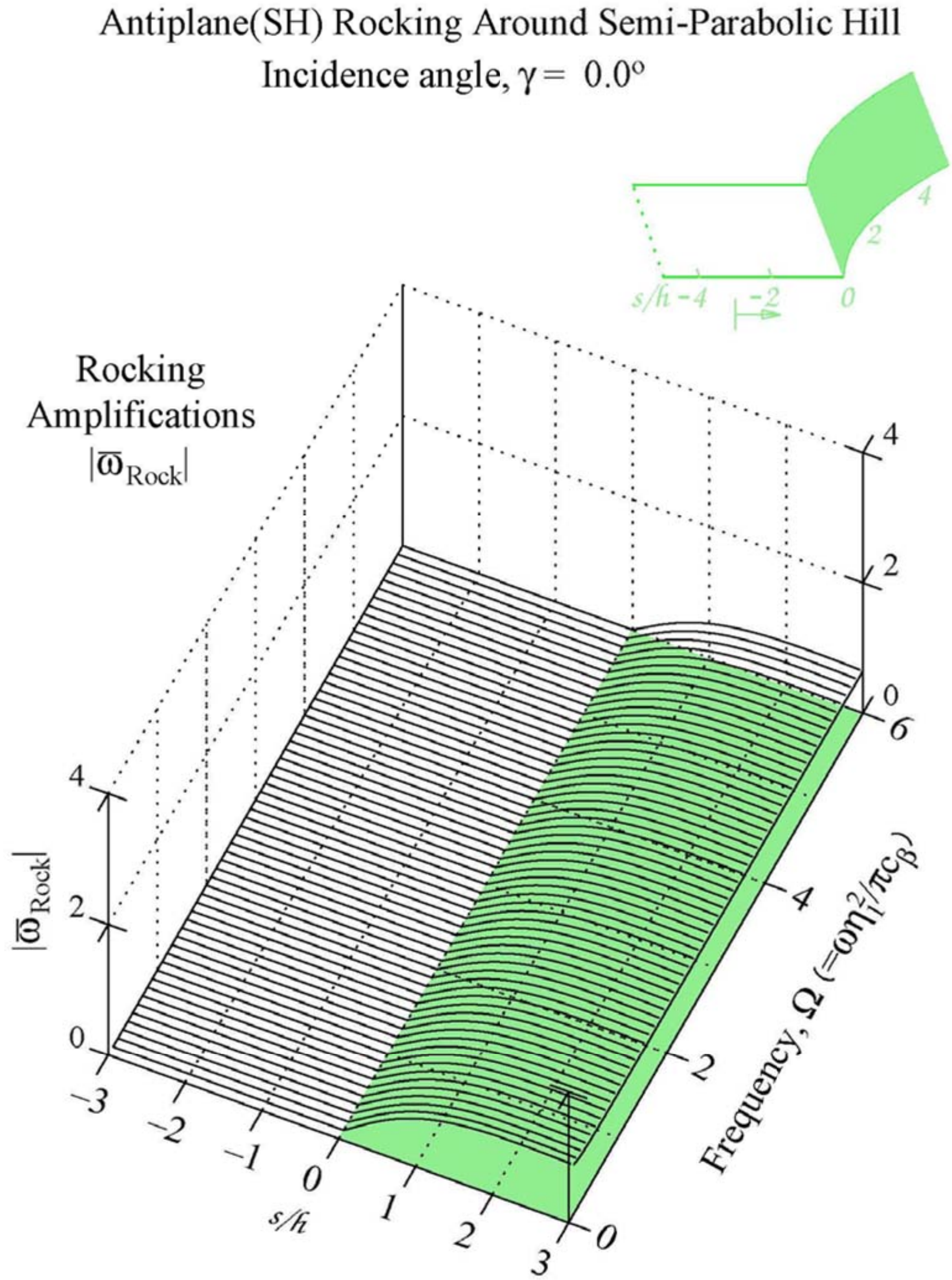

Fig. 7.6 3D Rocking Amplitudes for Horizontal Incidence, $\gamma = 0^{\circ}$

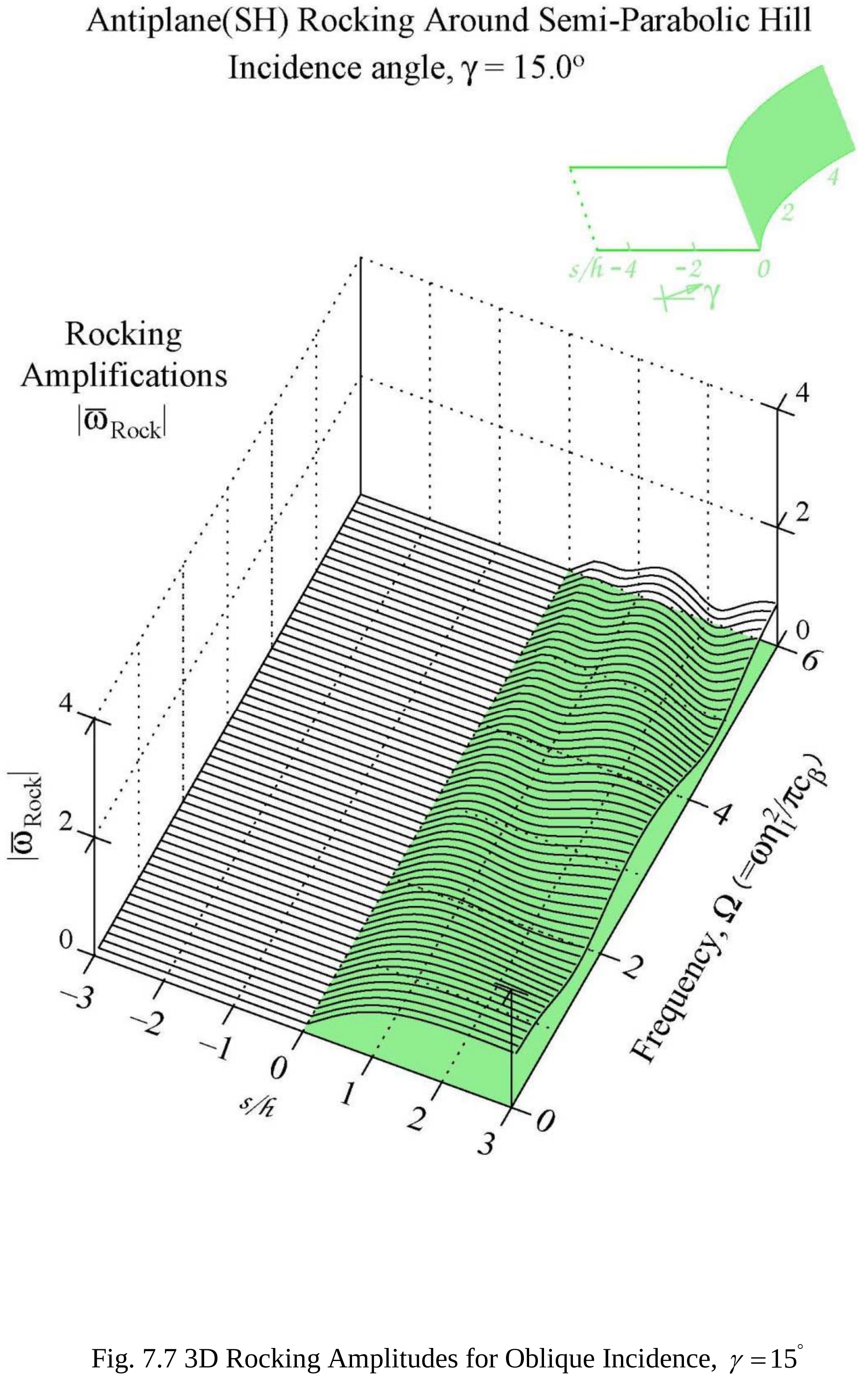

Fig. 7.7 3D Rocking Amplitudes for Oblique Incidence, $\gamma = 15^{\circ}$

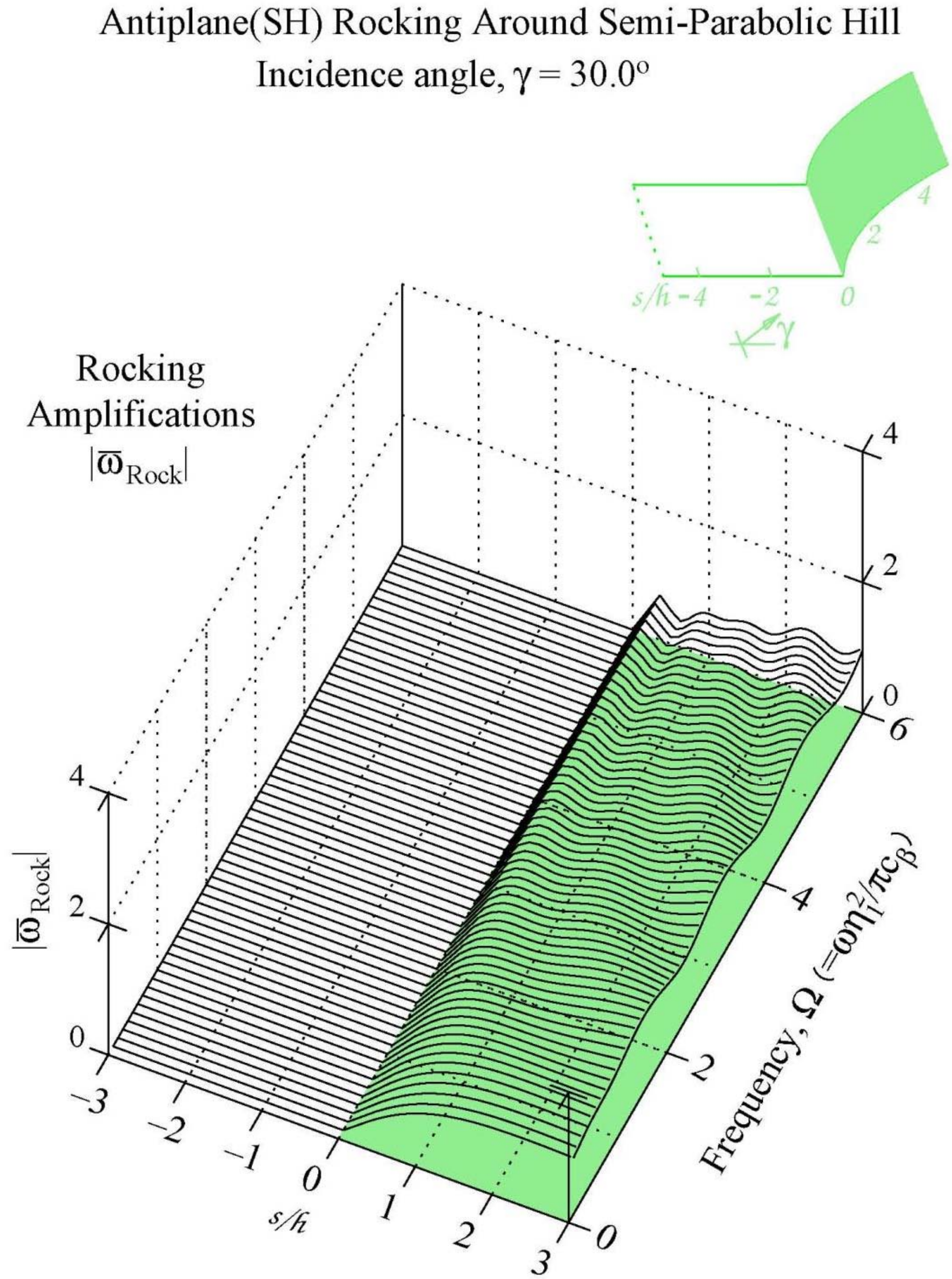

Fig. 7.8 3D Rocking Amplitudes for Oblique Incidence, $\gamma = 30^{\circ}$

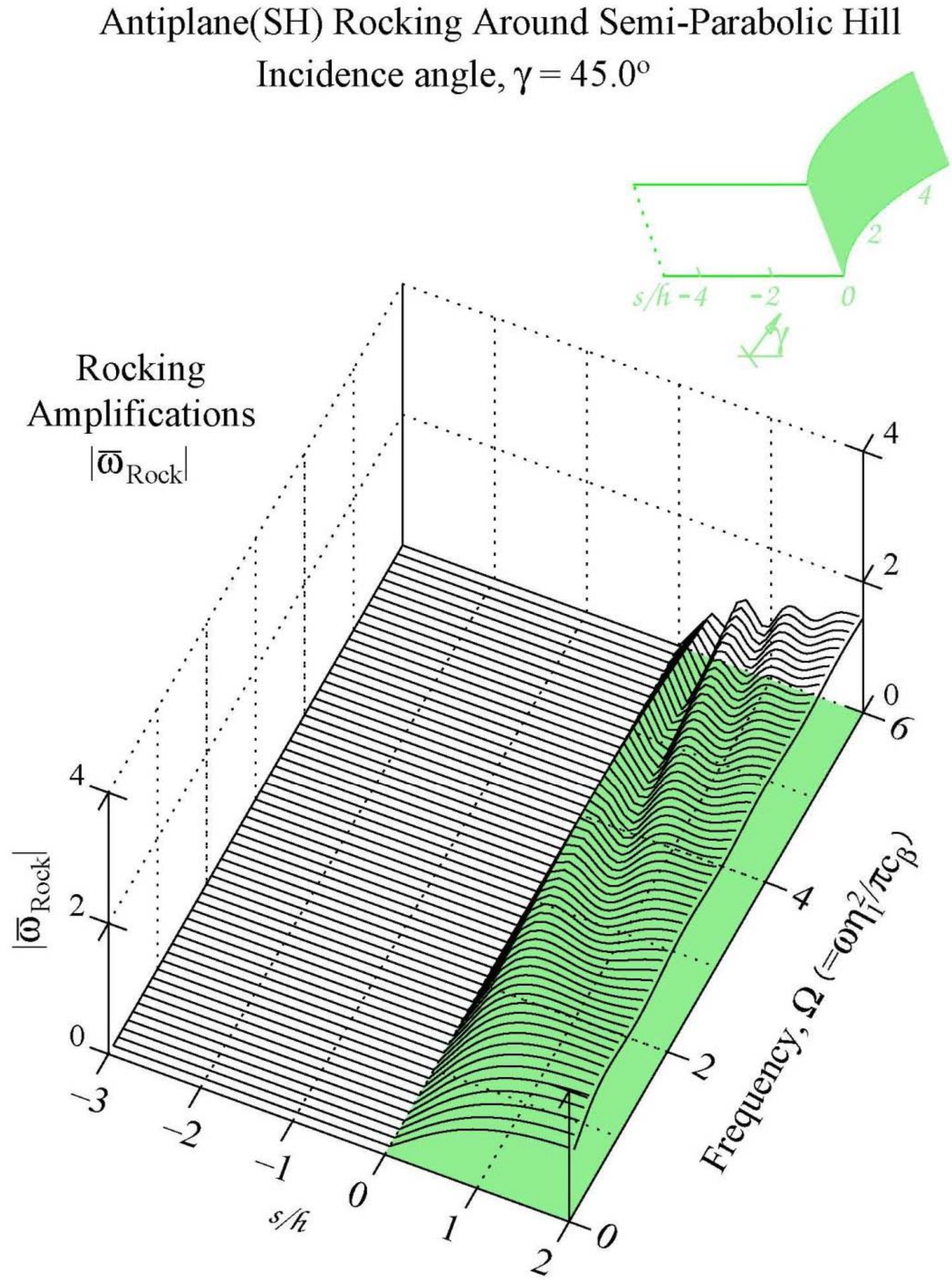

Fig. 7.9 3D Rocking Amplitudes for Oblique Incidence, $\gamma = 45^{\circ}$

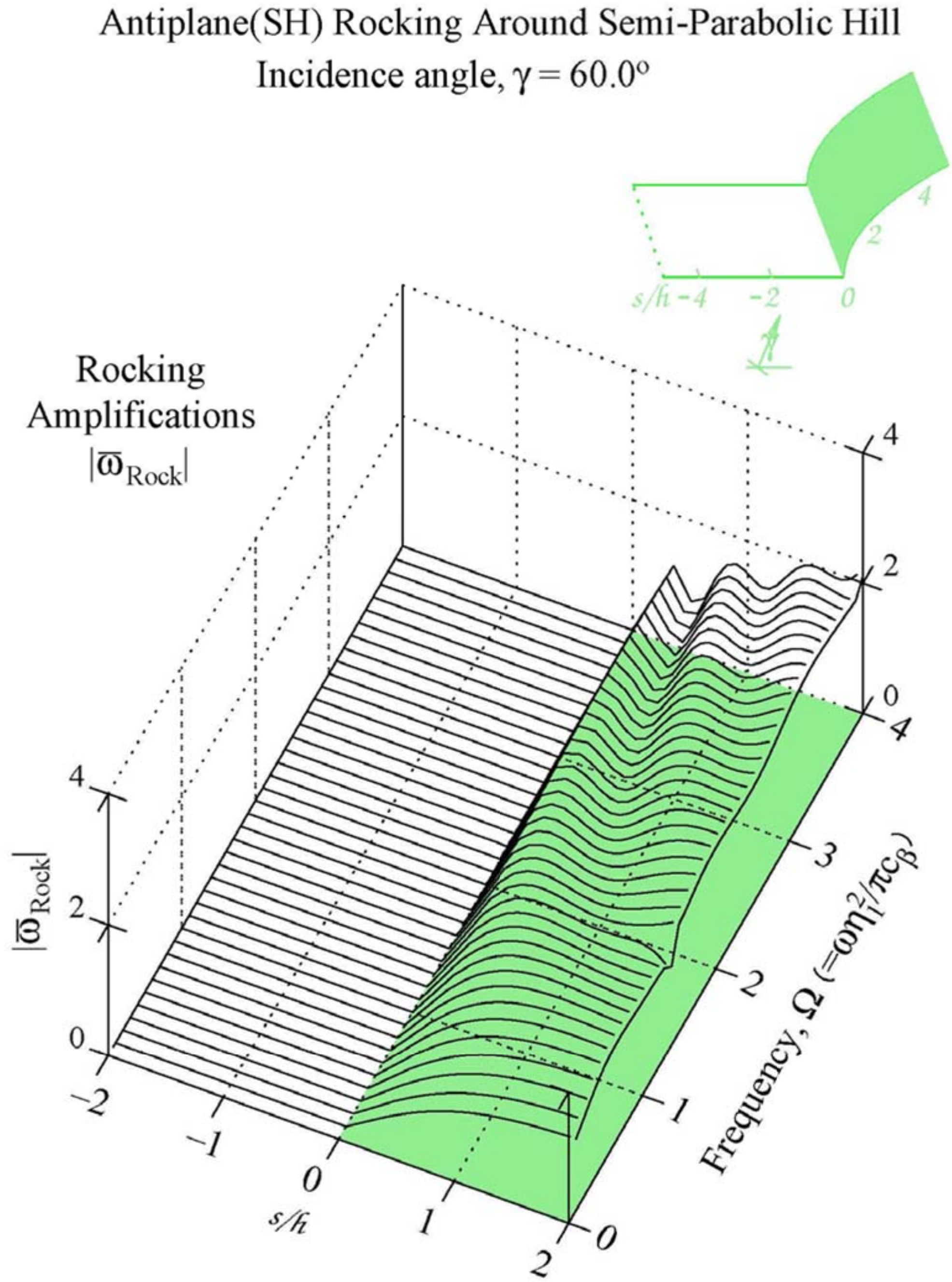

Fig. 7.10 3D Rocking Amplitudes for Oblique Incidence, $\gamma = 60^{\circ}$

VII.4 Normalized Rotation Amplitudes, $\left|\overline{\omega}\right|$

Recall from Chapter III, where the rotation components of motions are first defined:

$$\tilde{\omega} = \begin{pmatrix} \omega_x \\ \omega_y \\ 0 \end{pmatrix} = \frac{1}{2} \begin{pmatrix} \partial W / \partial y \\ -\partial W / \partial x \\ 0 \end{pmatrix} \qquad \text{Chapter III Equation (3)}$$

and for anti-plane (z-component) motion, the rotational motion is shown to have only two components, the horizontal component, which are

1) The rotation about the vertical y-axis, the torsional motion, given by

$$\omega_y = \omega_{Tor} = -\frac{1}{2} \partial W / \partial x \qquad \text{Chapter III Equation (4a)}$$

and

2) The rotation about the horizontal x-axis, the rocking motion, given by

$$\omega_x = \omega_{Rock} = \frac{1}{2} \partial W / \partial y \qquad \text{Chapter III Equation (4b)}$$

Such rotational components have been presented in the last two sections above, Sections VII.2 and VII.3.

In this section, the resultant rotation amplitudes is presented, where

$$|\omega| = \left(|\omega_x|^2 + |\omega_y|^2\right)^{1/2} = \left(|\omega_{Rock}|^2 + |\omega_{Tor}|^2\right)^{1/2} \qquad (13)$$

The resultant rotation will again be normalized with respect to that of the incident waves the rotation amplitude of the incident waves $\left|\tilde{\omega}^i\right|$:

$$\left|\tilde{\omega}^i\right| = \left(\left|\omega_x^i\right|^2 + \left|\omega_y^i\right|^2\right)^{1/2} = k/2\left(\sin^2\gamma + \cos^2\gamma\right)^{1/2}\left|W^i\right| = k/2\left|W^i\right| = k/2 \quad \text{Chapter III Equation (7)}$$

These are the same normalization factor for the torsional and rocking motions in the previous sections above, so that the normalized rotation amplitude will again be presented as:

$$\begin{aligned} \left|\overline{\omega}\right| &= |\omega| \big/ \left|\omega^i\right| = 2/k\,|\omega| = 2/k\left(\left|\omega_{Rock}\right|^2 + \left|\omega_{Tor}\right|^2\right)^{1/2} \\ &= \left(\left|\overline{\omega}_x\right|^2 + \left|\overline{\omega}_y\right|^2\right)^{1/2} = \left(\left|\overline{\omega}_{Rock}\right|^2 + \left|\overline{\omega}_{Tor}\right|^2\right)^{1/2} \end{aligned} \quad \text{Chapter IV Equation (23)}$$

Recall that the rocking motion at the surface of the half-space, $y = 0$ to the left of the semi-parabolic hill is zero:

$$\omega_{Rock}\Big|_{y=0} = \omega_{Rock}^{ff} + \omega_{Rock}^{s}\Big|_{\substack{y=0 \\ (\xi=0)}} = 0 \qquad \text{Chapter IV Equation (12)}$$

So that the normalized resultant rotation motion there at the half-space surface is

$$\left|\overline{\omega}\right|_{y=0} = \left|\overline{\omega}_{Tor}\right|_{y=0} \tag{14}$$

With no (zero) contribution from the rocking motion, the resultant rotation motion at the semi-parabolic hill surface will come from the torsional motion only.

Fig. 7.11 to Fig 7.15 are the five 3D plots of the normalized resultant rotation amplitudes again plotted vs. (as in the cases of rotational torsion and rocking):

1) The dimensionless distance s/h measured along the half-space and canyon surface and
2) The dimensionless frequency $\Omega = \omega\eta_0^2/\pi\beta = 2\eta_0^2/\lambda = 4h/\lambda$,

respectively for incidence angles $\gamma = 0^\circ, 15^\circ, 30^\circ, 45^\circ$ and 60°. As in the corresponding plots of normalized torsional and rocking rotation amplitudes, all trends of features stayed the same.

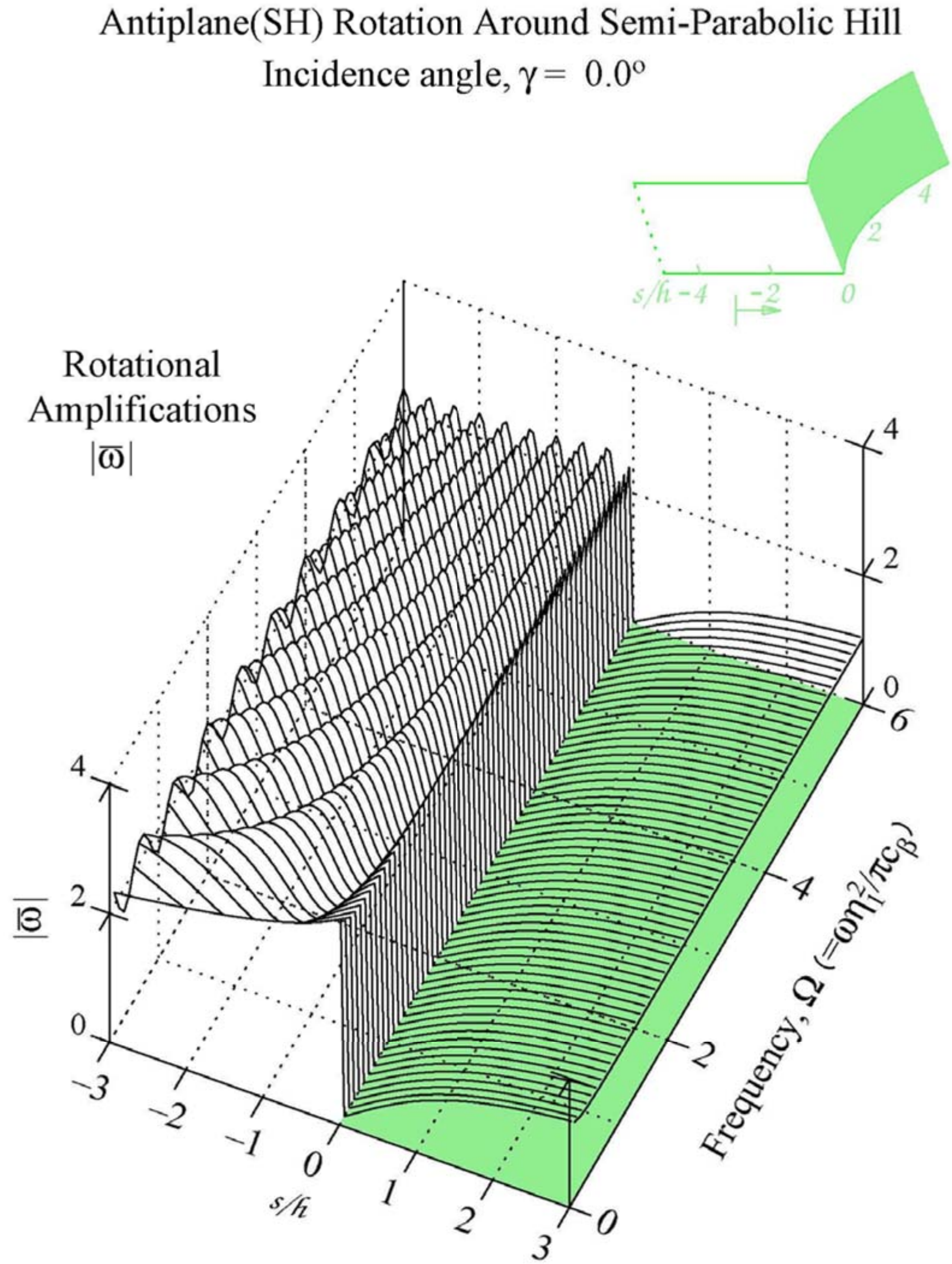

Fig. 7.11 3D Rotation Amplitudes for Horizontal Incidence, $\gamma = 0^{\circ}$

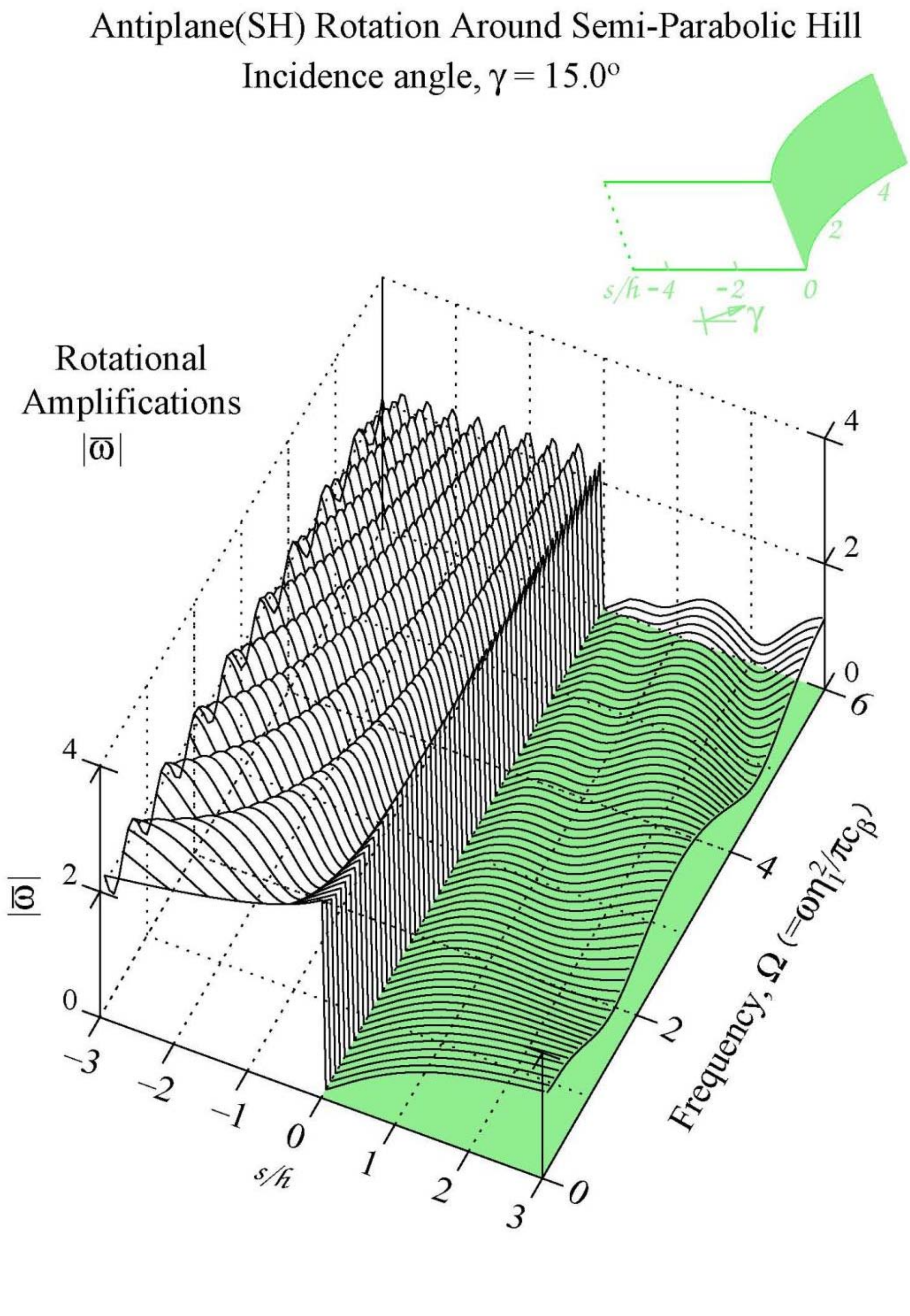

Fig. 7.12 3D Rotation Amplitudes for Oblique Incidence, $\gamma = 15^{\circ}$

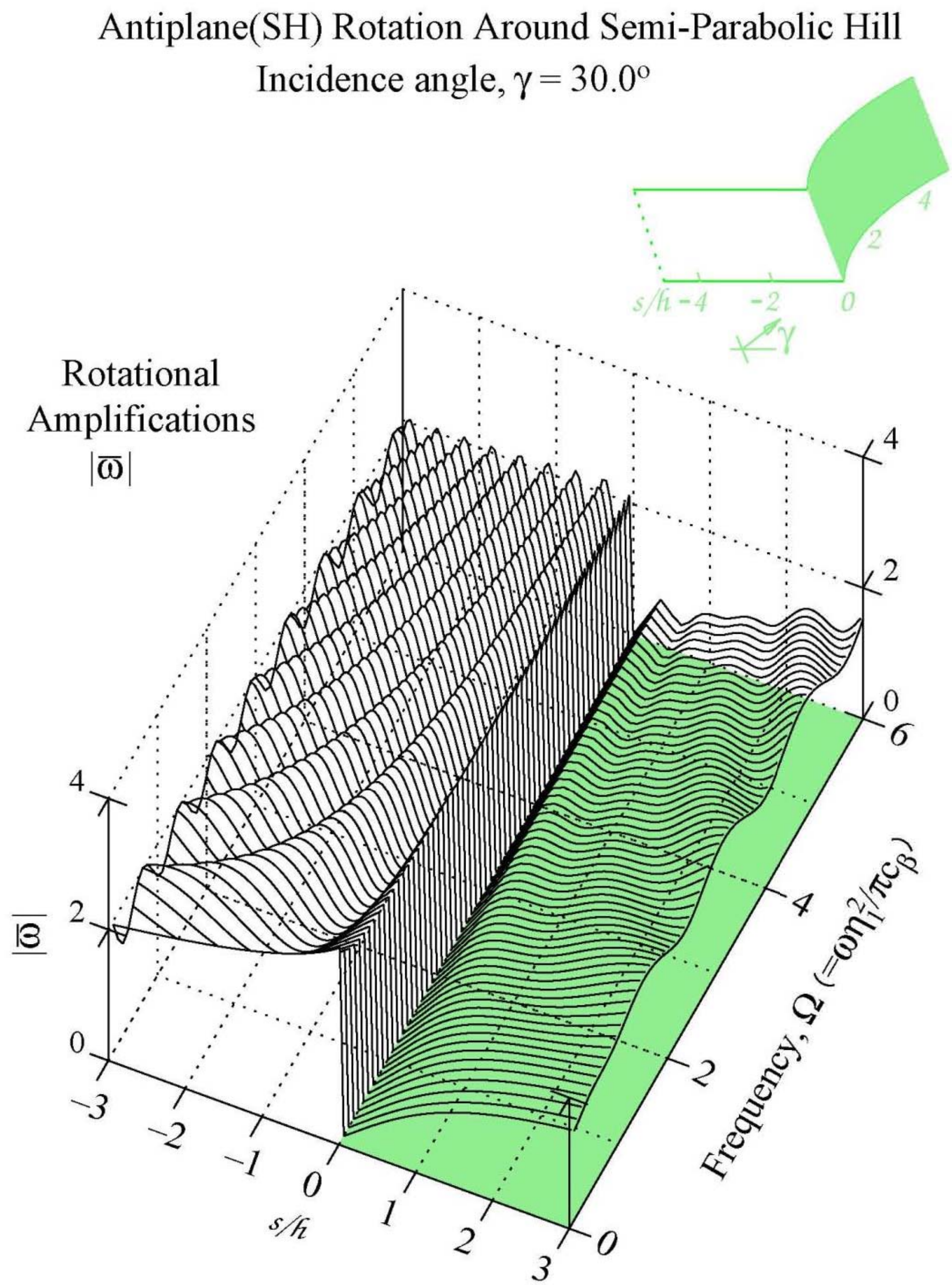

Fig. 7.13 3D Rotation Amplitudes for Oblique Incidence, $\gamma = 30^{\circ}$

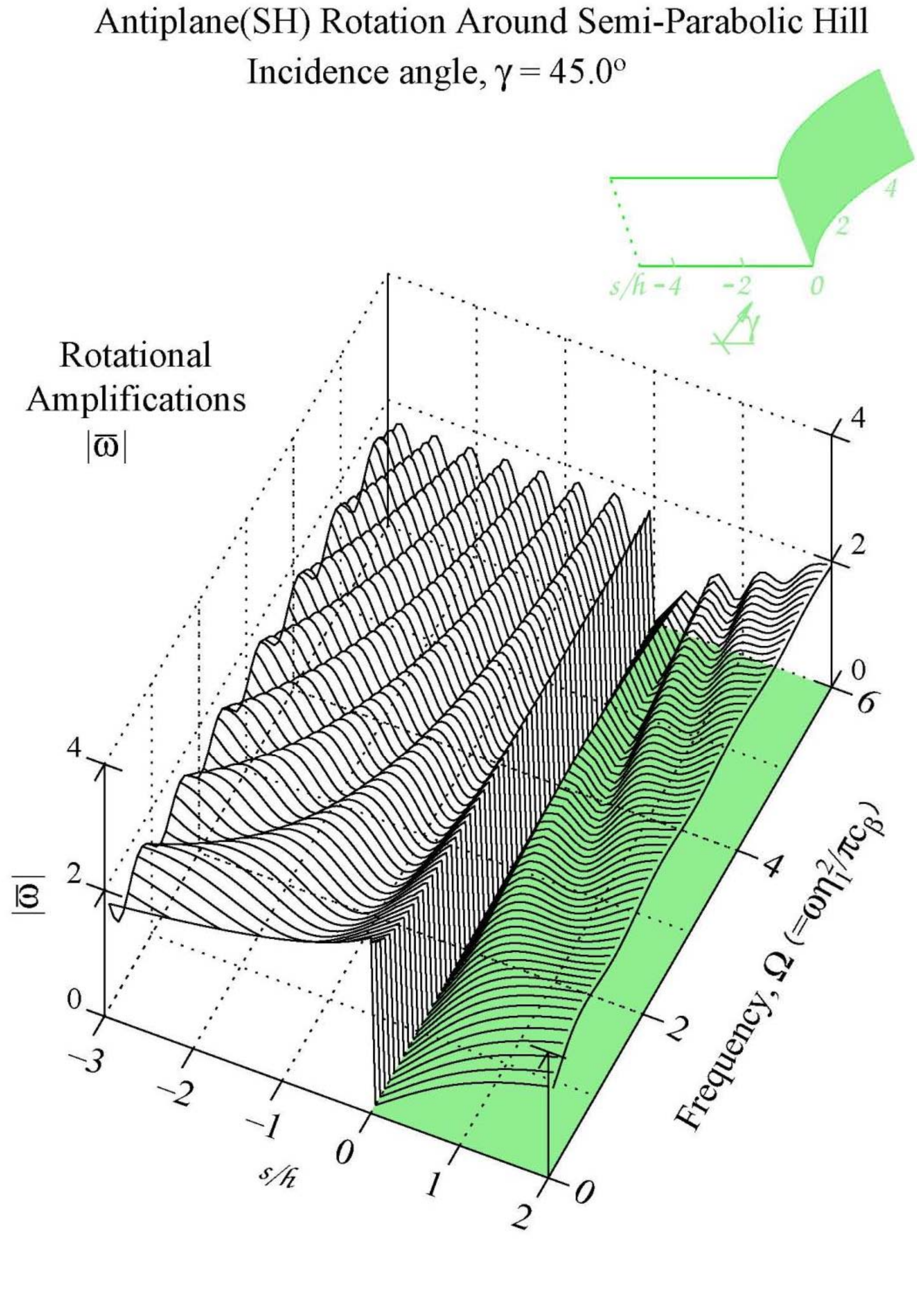

Fig. 7.14 3D Rotation Amplitudes for Oblique Incidence, $\gamma = 45^{\circ}$

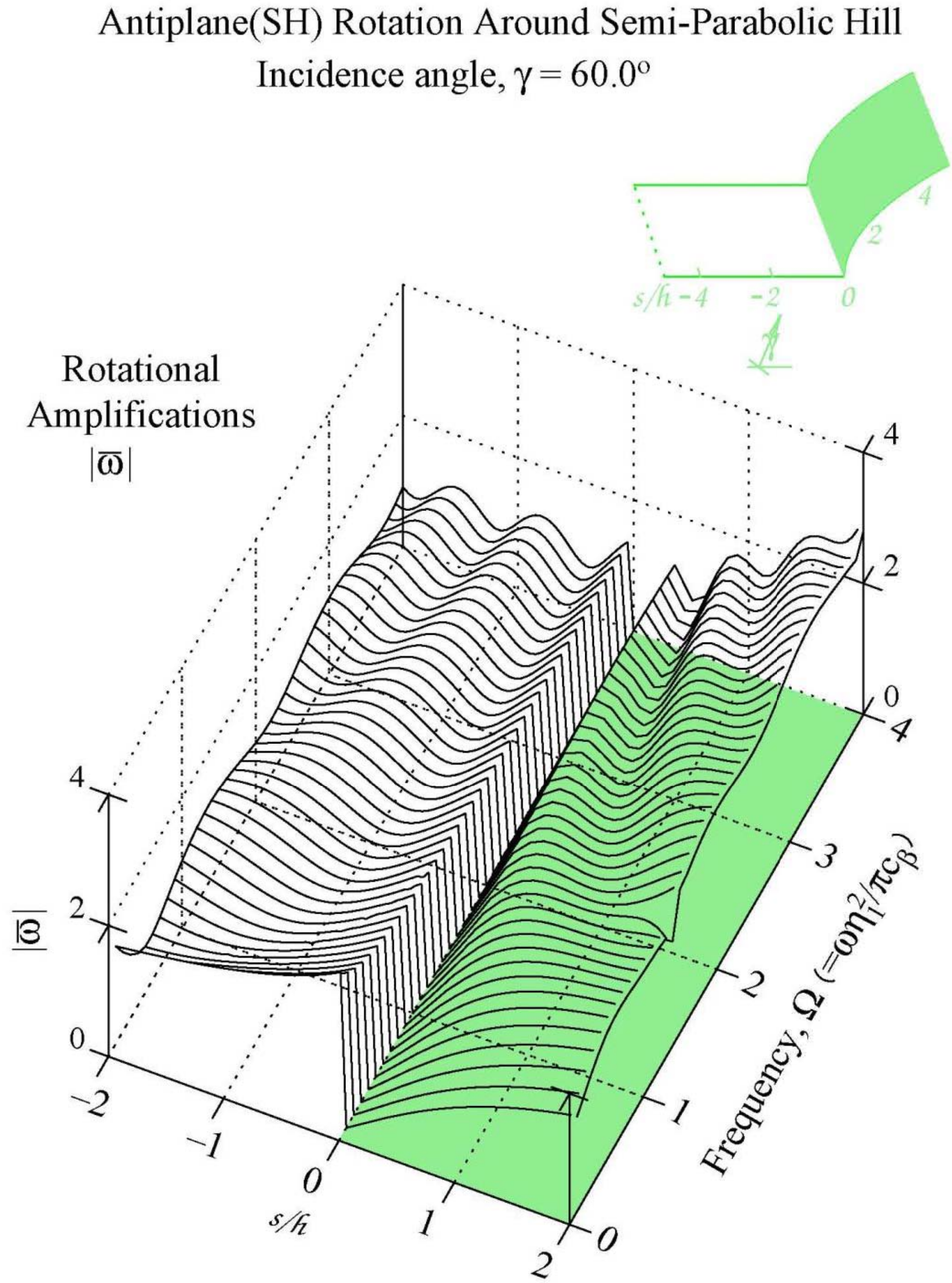

Fig. 7.15 3D Rotation Amplitudes for Oblique Incidence, $\gamma = 60^{\circ}$

VII.5 Summary

Chapter VII, as in Chapter III, extends the work of Chapter VI to compute the rotational components of motions around a semi-parabolic hill. As in the case of displacement motions, and for the same reason, it is found that the rotational motions, both torsion and rocking are comparatively smaller than the corresponding rotational motions around a semi-circular canyon.

Chapter VIII. Dynamic Shear Stress Concentration Factors of Anti-Plane SH Waves around a Semi-Parabolic Hill

VIII.1 Introduction

Recall from Section V.2 of Chapter V above, for the case of anti-plane (SH) displacement with only the z-component of motions, namely $\widetilde{U} = W\hat{k} = W(x, y)\hat{k}$, the two components of shear stresses in the x-y plane, are defined as

$$\begin{aligned} \tau_{z\eta} &= 2\mu\varepsilon_{z\eta} = \mu\frac{\partial W}{\partial \eta} \\ \tau_{z\xi} &= 2\mu\varepsilon_{z\xi} = \mu\frac{\partial W}{\partial \xi} \end{aligned} \qquad \text{Chapter V Equation (1)}$$

where $\tau_{z\eta}$ is the component of shear stress along and tangential to the lines $\xi =$ constant. Alternately, in rectangular coordinates, to be presented here for the anti-plane SH wave displacements around a semi-parabolic hill, the horizontal and vertical components of shear traction are respectively

$$\begin{aligned} \tau_{zx} &= 2\mu\varepsilon_{zx} = \mu\frac{\partial W}{\partial x} \\ \tau_{zy} &= 2\mu\varepsilon_{zy} = \mu\frac{\partial W}{\partial y} \end{aligned} \qquad (1)$$

which are the same as that calculated and presented in Chapter V for the case of semi-parabolic canyon.

The corresponding component of shear traction vector in the x-y plane is

$$\tilde{\tau}_{zt} = \begin{pmatrix} \tau_{zx} \\ \tau_{zy} \end{pmatrix} = \mu \begin{pmatrix} \partial W / \partial x \\ \partial W / \partial y \end{pmatrix} \tag{2}$$

and the shear traction (resultant) amplitude is

$$\left|\tau_{zt}\right| = \left(\left|\tau_{zx}\right|^2 + \left|\tau_{zy}\right|^2\right)^{1/2} = \mu\left(\left|\partial W / \partial x\right|^2 + \left|\partial W / \partial y\right|^2\right)^{1/2} \tag{3}$$

which is similar to what was defined in Chapter V. There, using the shear-stress components of the incident waves:

$$\tilde{\tau}^{i}_{zt} = \begin{pmatrix} \tau^{i}_{zx} \\ \tau^{i}_{zy} \end{pmatrix} = \mu \begin{pmatrix} \partial / \partial x \\ \partial / \partial y \end{pmatrix} W^{i} = \mu i k \begin{pmatrix} \cos\gamma \\ -\sin\gamma \end{pmatrix} W^{i} \qquad \text{Chapter V Equation (8)}$$

The corresponding shear stress traction amplitude is:

$$\left|\tau^{i}\right| = \left(\left|\tau^{i}_{zx}\right|^2 + \left|\tau^{i}_{zy}\right|^2\right)^{1/2} = \mu k \qquad \text{Chapter V Equation (9)}$$

And it will be used also as a normalization factor, so that the normalized shear stress amplitudes presented are shown to be identical to that used for the torsion and rocking rotation components of motions around the semi-parabolic hill in the last chapter (Chapter VII).

As pointed out in Chapter V, it can be seen from Equation (3) of Chapter VII for torsion around a semi-parabolic hill that:

$$\bar{\tau}_{zx} = \tau_{zx} \big/ \left|\tau^i\right| = 1\big/k \left(\partial W \big/ \partial x \right) = -\bar{\omega}_{Tor} \tag{4}$$

or the normalized x-component shear stress is identical to the negative of normalized torsion.

Similarly comparing Equation (1) here with Equation (4) of Chapter VII for rocking around a semi-parabolic hill that:

$$\bar{\tau}_{zy} = \tau_{zy} \big/ \left|\tau^i\right| = 1\big/k \left(\partial W \big/ \partial y \right) = -\bar{\omega}_{Rock} \tag{5}$$

or the normalized y-component shear stresses is identical to normalized rocking.

Finally, the normalized resultant shear traction is, comparing that with Equation (5) of Chapter VII for resultant rotation around a semi-parabolic hill that:

$$
\begin{aligned}
\left|\bar{\tau}_{zt}\right| &= \left[\left|\bar{\tau}_{zx}\right|^2 + \left|\bar{\tau}_{zy}\right|^2\right]^{1/2} \\
&= 1/k\left(\left|\partial W/\partial x\right|^2 + \left|\partial W/\partial x\right|^2\right)^{1/2} = \left|\bar{\omega}\right|, \text{ the resultant rotation}
\end{aligned}
\tag{6}
$$

or the normalized shear traction amplitude is identical to normalized resultant rotation amplitude.

These normalized shear stress amplitudes, $\left|\bar{\tau}_{zx}\right|, \left|\bar{\tau}_{zy}\right|$ and $\left|\bar{\tau}_{zt}\right|$ will also be referred in what follows in the rest of this chapter as dynamic shear stress concentration factors, or simply stress concentration factors. The same term was used for the normalized shear stress amplitudes around a semi-parabolic canyon in Chapter V.

Thus all previous figures of plots of torsion, rocking and rotation in Chapter VII around a semi-parabolic hill can simply be plotted and relabeled respectively as the normalized x- and y-component shear stresses amplitudes and shear traction (resultant) amplitudes around a semi-parabolic hill here and in subsequent section, without any need for new calculation.

VIII.2 Dynamic Shear Stress Concentration Factors, $\left|\bar{\tau}_{zx}\right|$

Since $$\bar{\tau}_{zx} = \tau_{zx}\Big/\left|\tau^i\right| = 1\Big/k\left(\partial W\Big/\partial x\right) = -\bar{\omega}_{Tor}$$ Equation (4) above

so as stated earlier, all derivations for expressions for torsion in Chapter VII will be used and will not be repeated here.

The normalized shear stress amplitude $\bar{\tau}_{zx}$ at the half-space and parabolic canyon surface respectively takes the form, from Chapter VII, Equation (8b):

$$\bar{\tau}_{zx}\Big|_{\substack{y=0\\(\xi=0)}}\left(=-\bar{\omega}_{Tor}\Big|_{\substack{y=0\\(\xi=0)}}\right) = -\left(2\sec\gamma\Big/2\right)\frac{1}{\bar{\lambda}\eta}\sum_{n=0}^{\infty}\left(ia_n D'_{2n}\left(\bar{\lambda}\eta\right)+A_n D'_{-2n-1}\left(\lambda\eta\right)\right)D_{2n}\left(\lambda\xi\right)\Big|_{\xi=0} \quad (7)$$

and from Chapter VII, Equation (9b):

$$\bar{\tau}_{zx}\Big|_{\eta=\eta_1}\left(=-\bar{\omega}_{Tor}\Big|_{\eta=\eta_1}\right) = \left(2\sec\gamma\Big/2\right)\frac{\lambda\xi}{2k\left(\xi^2+\eta^2\right)}\sum_{n=0}^{\infty}\left(B_n D_n\left(\bar{\lambda}\eta\right)\right)_{\eta=\eta_1} D'_n\left(\lambda\xi\right) \quad (8)$$

respectively. Its amplitude $\left|\bar{\tau}_{zx}\right|$ will also be called the stress concentration factor.

Fig. 8.1 to Fig. 8.5 are the 3D plots of the normalized stress concentration factor $\left|\bar{\tau}_{zx}\right|$ on the half-space surface and around the semi-parabolic hill surface plotted vs.

1) The dimensionless distance s/h measured along the half-space and canyon surface and

2) The dimensionless frequency $\Omega = \omega\eta_0^2/\pi\beta = 2\eta_0^2/\lambda = 4h/\lambda$,

Respectively for the five incidence angles $\gamma = 0^\circ, 15^\circ, 30^\circ, 45^\circ$ and 60°. The reader are advised to refer to Section VII.2 – Normalized Torsion Amplitudes, $\left|\overline{\omega}_{Tor}\right|$ for a detailed description of the figure since from Equation (4) above, $\overline{\tau}_{zx} = 1/k\left(\partial W/\partial x\right) = -\overline{\omega}_{Tor}$, or $\left|\overline{\tau}_{zx}\right| = \left|\overline{\omega}_{Tor}\right|$. These are identical to Fig. 7.1 to 7.5, the 3D plots of the torsional rotation amplitudes.

As in the previous chapters, the shape of the half-space and semi-parabolic hill surface model on which the displacements are calculated is outlined on the top-left graph of the figure and it is now in green color. The green arrow again indicates the corresponding direction of the incident SH wave W^t which is assumed to be coming from the left-side towards the hill.

The normalized shear stress amplitudes around the semi-parabolic hill in Fig. 8.1 through 8.5, as in the case of torsional amplitudes in Chapter VII, are consistent with the presented in Chapter VI for the corresponding displacement amplitudes, with the same range of convergence. This is no surprise, as the displacement and shear stress are respectively given by from Chapter VI, Equation (13):

$$W^t\left(\xi,\eta\right)\Big|_{\eta=\eta_1}=2\sec{}^{\gamma}\!/_{2}\sum_{n=0}^{\infty}B_nD_n\left(\bar{\lambda}\eta_1\right)D_n\left(\lambda\xi\right) \tag{9}$$

$$\bar{\tau}_{zx}\Big|_{\eta=\eta_1}\left(=-\bar{\omega}_{Tor}\Big|_{\eta=\eta_1}\right)$$
$$=\left(2\sec{}^{\gamma}\!/_{2}\right)\frac{\lambda\xi}{2k\left(\xi^2+\eta^2\right)}\sum_{n=0}^{\infty}\left(B_nD_n\left(\bar{\lambda}\eta\right)\right)_{\eta=\eta_1}D_n'\left(\lambda\xi\right)$$ Equation (8) above

so that the summation above involves the same coefficients $B_nD_n\left(\bar{\lambda}\eta\right)$ times $D_{2n}\left(\lambda\xi\right)$ for displacement and $D_{2n}'\left(\lambda\xi\right)$ for shear stress amplitudes.

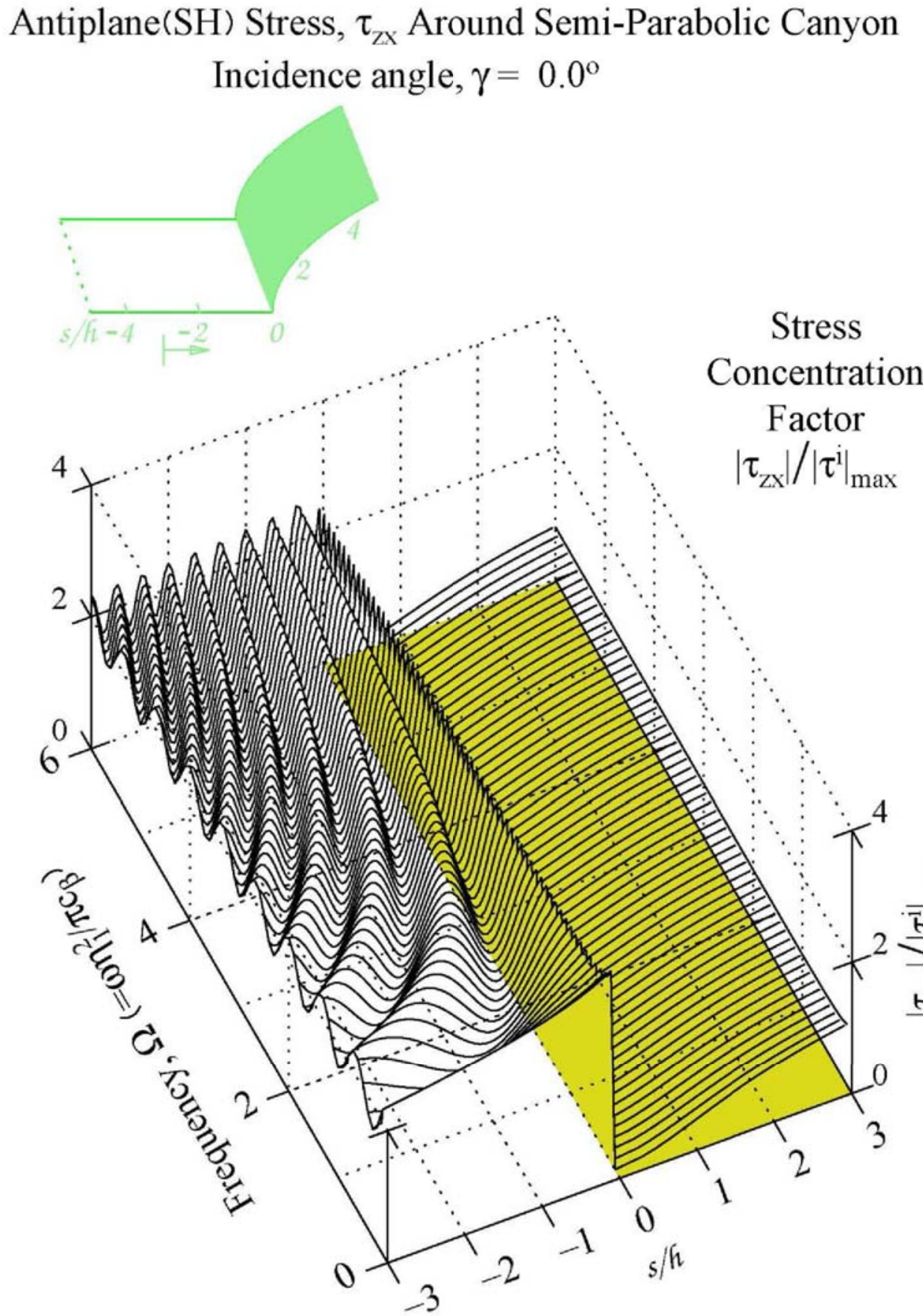

Fig. 8.1 3D Shear Stress Concentration Factor $\left|\bar{\tau}_{zx}\right|$: Horizontal Incidence, $\gamma = 0^\circ$

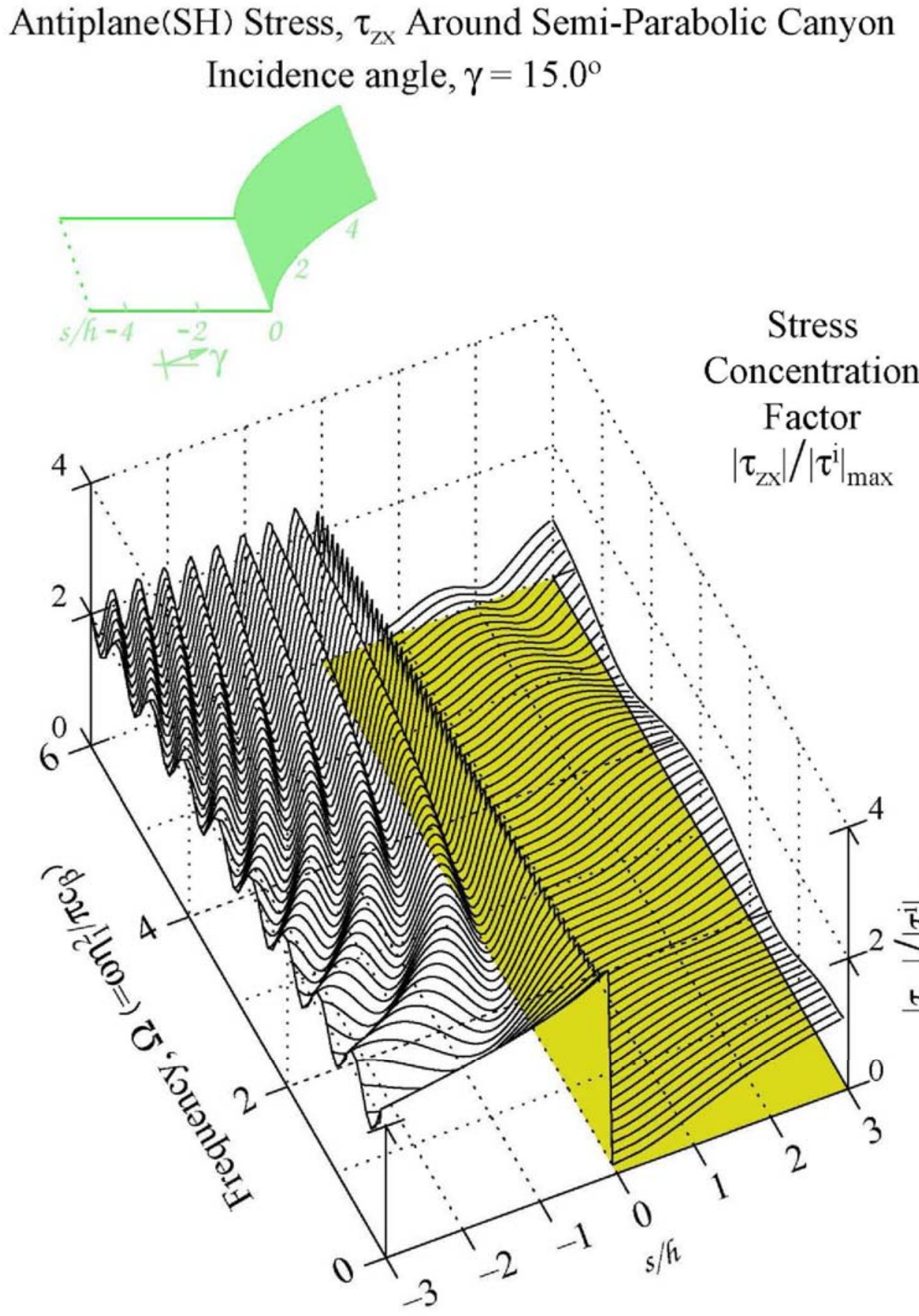

Fig. 8.2 3D Shear Stress Concentration Factor $\left|\overline{\tau}_{zx}\right|$: Oblique Incidence, $\gamma = 15^{\circ}$

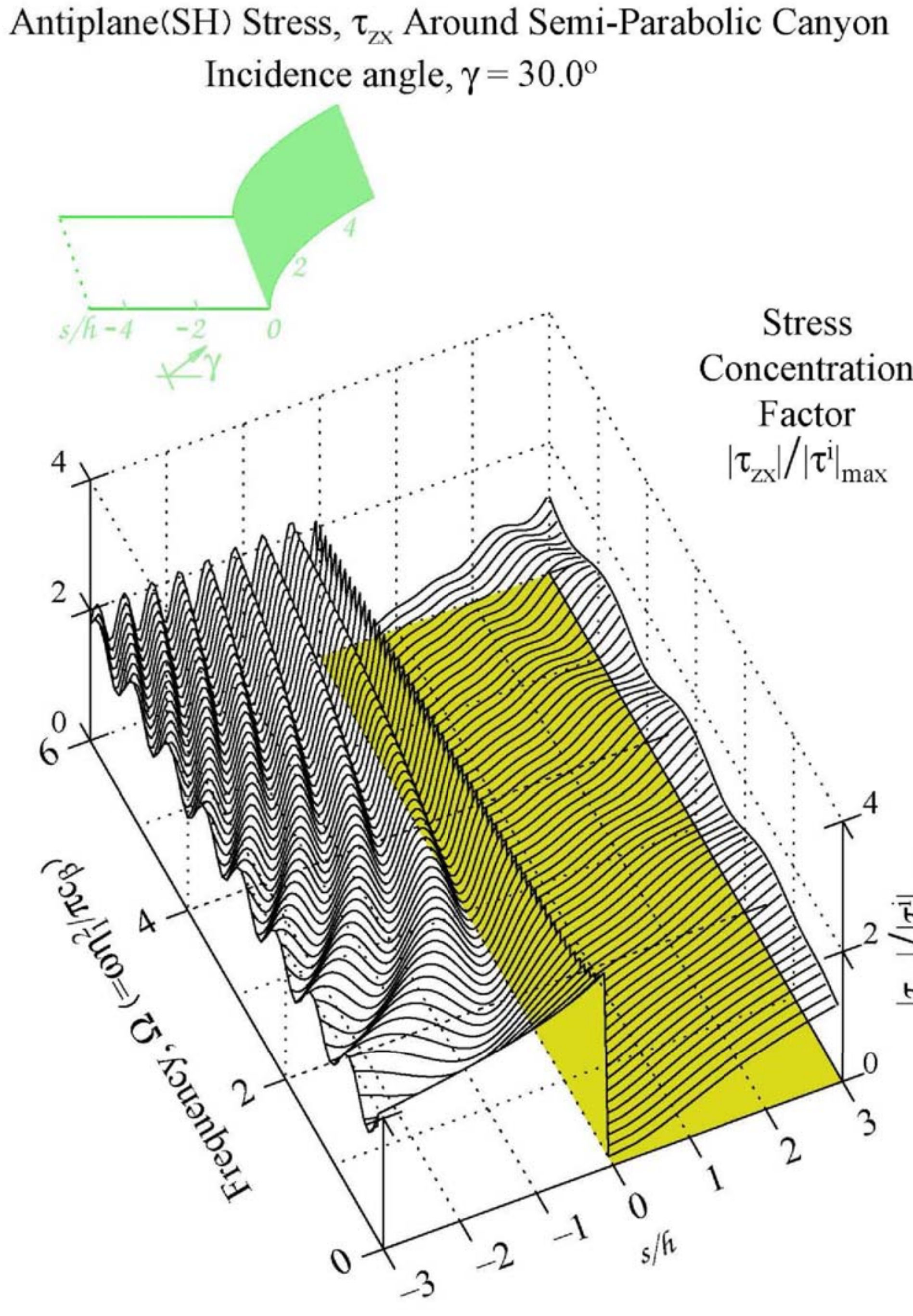

Fig. 8.3 3D Shear Stress Concentration Factor $\left|\bar{\tau}_{zx}\right|$: Oblique Incidence, $\gamma = 30^\circ$

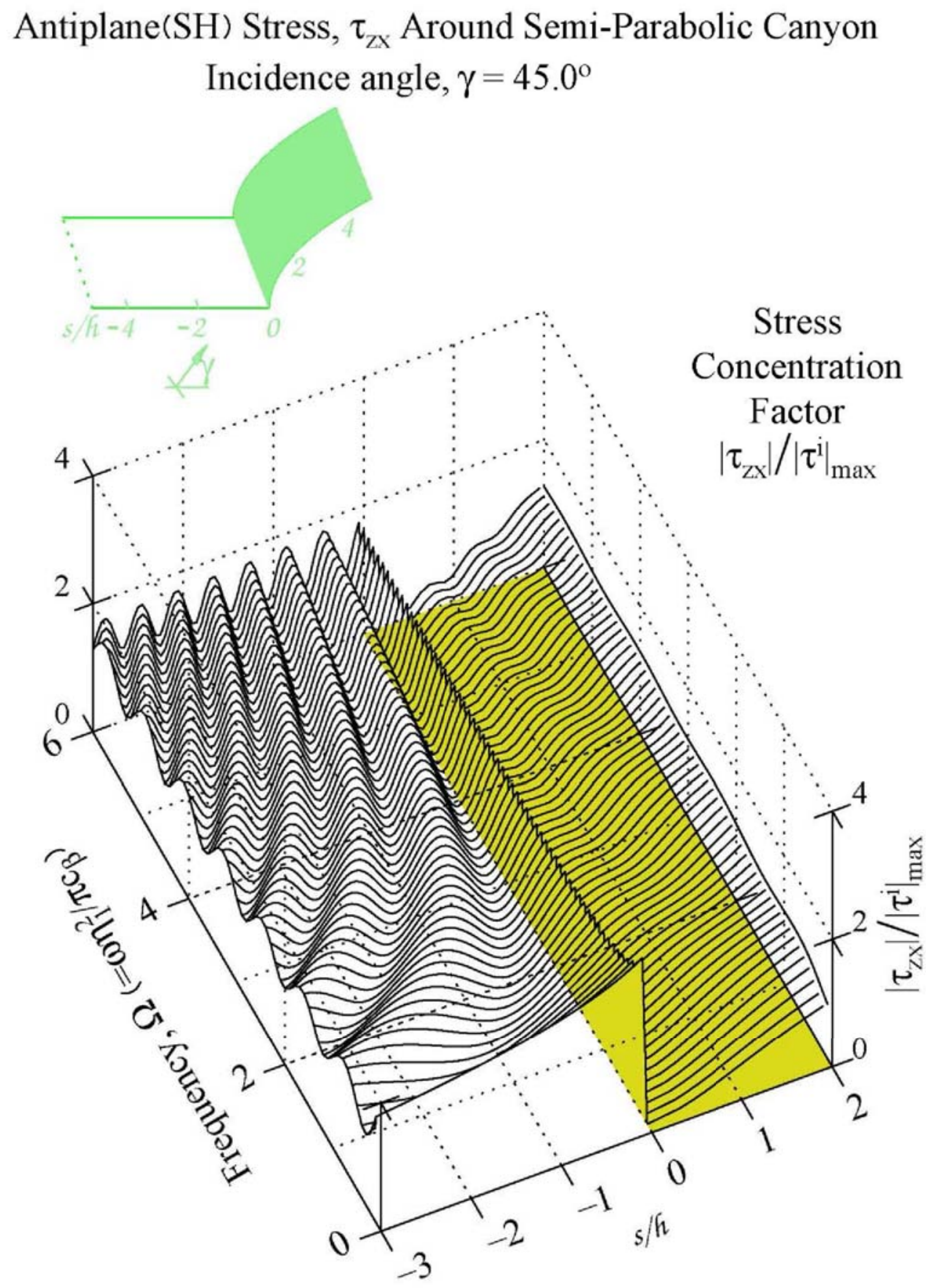

Fig. 8.4 3D Shear Stress Concentration Factor $\left|\overline{\tau}_{zx}\right|$: Oblique Incidence, $\gamma = 45^{\circ}$

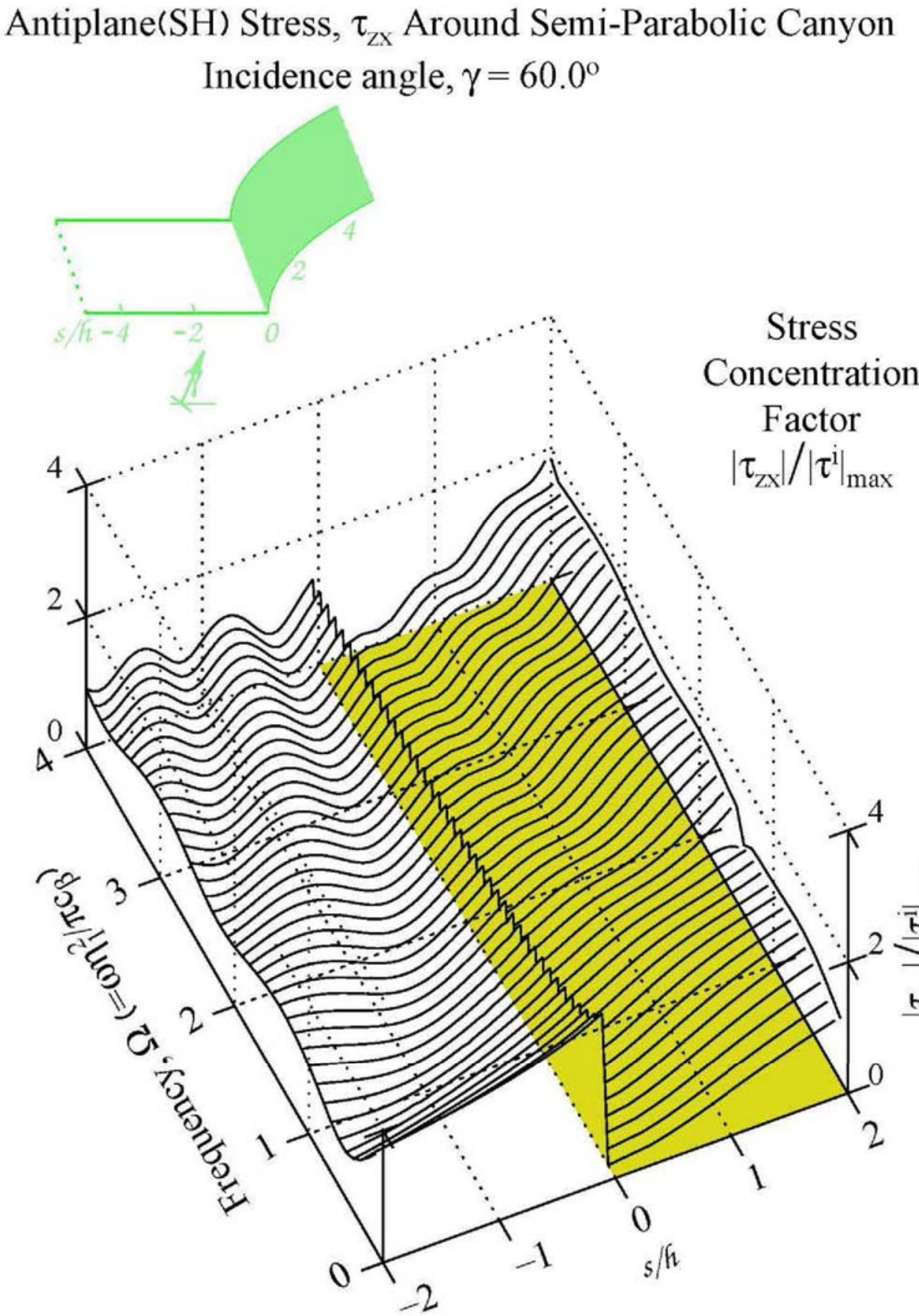

Fig. 8.5 3D Shear Stress Concentration Factor $\left|\overline{\tau}_{zx}\right|$: Oblique Incidence, $\gamma = 60^\circ$

VIII.3 Dynamic Shear Stress Concentration Factor, $\left|\bar{\tau}_{zy}\right|$

Since $\bar{\tau}_{zy} = {\tau_{zy}}\big/{\left|\tau^i\right|} = {1}\big/{k}\left({\partial W}\big/{\partial y}\right) = -\bar{\omega}_{Rock}$ Equation (5)

above so as stated earlier, all derivations for expressions for rocking rotation in Chapter VII will be used and will not be repeated here.

The normalized shear stress amplitude $\left|\bar{\tau}_{zy}\right|$ at the half-space and parabolic hill surface respectively takes the form, from Equation (4) and (12) of Chapter VII for $\bar{\omega}_{Rock}$

$$\begin{aligned} &\bar{\tau}_{zy}\Big|_{y=0}\left(=\bar{\omega}_{Rock}\Big|_{y=0}\right)=0 \\ &\bar{\tau}_{zy}\Big|_{\eta=\eta_1}=\bar{\omega}_{Rock}\Big|_{\eta=\eta_1}=\left(2\sec{\gamma}\big/{2}\right)\frac{\lambda\eta_1}{2k\left(\xi^2+\eta_1^2\right)}\sum_{n=0}^{\infty}\left(B_nD_n\left(\bar{\lambda}\eta\right)\right)_{\eta=\eta_1}D_n^{'}\left(\lambda\xi\right) \end{aligned} \tag{10}$$

Fig. 8.6 to Fig. 8.10 are the 3D plots of the normalized shear stress, $\left|\bar{\tau}_{zy}\right|$ (=rocking rotation) amplitude plotted vs.

1) The dimensionless distance ${s}\big/{h}$ measured along the half-space and canyon surface and
2) The dimensionless frequency $\Omega = {\omega\eta_0^2}\big/{\pi\beta} = {2\eta_0^2}\big/{\lambda} = {4h}\big/{\lambda}$,

respectively for incidence angles $\gamma = 0^\circ, 15^\circ, 30^\circ, 45^\circ$ and 60°. The readers are advised to refer to Section VII.3 Normalized Rocking Amplitudes $\left|\overline{\omega}_{Rock}\right|$ for a detailed description of the figures. Since from Equation (5) above $\overline{\tau}_{zy} = {}^{1}\!/_{k}\left({}^{\partial W}\!/_{\partial y}\right) = \overline{\omega}_{Rock}$. These figures are identical to Fig. 7.6 to Fig. 7.10 the 3D plots of the rocking rotation amplitudes.

The normalized shear stress amplitudes $\left|\overline{\tau}_{zy}\right|$ around a semi-parabolic hill in Fig. 8.6 through 8.10 as in the case of both the torsion and rocking amplitudes in Chapter VII, are consistent with the results presented in Chapter VI for the corresponding displacement amplitudes, and the shear stress $\left|\overline{\tau}_{zx}\right|$ in the previous section, all with the same range of convergence. This consistency is expected as the displacement, normalized share stress $\left|\overline{\tau}_{zx}\right|$ and $\left|\overline{\tau}_{zy}\right|$ are respectively given by

$$W^t(\xi,\eta)\Big|_{\eta=\eta_1} = 2\sec{}^{\gamma}\!/_{2}\sum_{n=0}^{\infty} B_n D_n\left(\overline{\lambda}\eta_1\right) D_n(\lambda\xi) \qquad \text{Equation (9) above}$$

$$\begin{aligned}&\overline{\tau}_{zx}\Big|_{\eta=\eta_1}\left(=-\overline{\omega}_{Tor}\Big|_{\eta=\eta_1}\right)\\&=\left(2\sec{}^{\gamma}\!/_{2}\right)\frac{\lambda\xi}{2k\left(\xi^2+\eta^2\right)}\sum_{n=0}^{\infty}\left(B_n D_n\left(\overline{\lambda}\eta\right)\right)_{\eta=\eta_1} D_n^{'}(\lambda\xi)\end{aligned} \qquad \text{Equation (8) above}$$

$$\bar{\tau}_{zy}\Big|_{y=0}\left(=\bar{\omega}_{Rock}\Big|_{y=0}\right)=0$$

$$\bar{\tau}_{zy}\Big|_{\eta=\eta_1}=\bar{\omega}_{Rock}\Big|_{\eta=\eta_1}$$ Equation (10) above

$$=\left(2\sec\gamma/2\right)\frac{\lambda\eta_1}{2k\left(\xi^2+\eta_1^2\right)}\sum_{n=0}^{\infty}\left(B_nD_n\left(\bar{\lambda}\eta\right)\right)_{\eta=\eta_1}D_n'\left(\lambda\xi\right)$$

so that the summation above involves the same coefficients, summation of the terms $B_nD_n\left(\bar{\lambda}\eta_1\right)$ times:

1) $D_{2n}\left(\lambda\xi\right)$ for displacement,

2) $\frac{\lambda\xi}{2k\left(\xi^2+\eta_1^2\right)}D_{2n}'\left(\lambda\xi\right)$ for shear stress $\bar{\tau}_{zx}$, and

3) $\frac{\lambda\eta_1}{2k\left(\xi^2+\eta_1^2\right)}D_{2n}'\left(\lambda\xi\right)$ for shear stress $\bar{\tau}_{zy}$.

in other words, they all have the same range of convergence at each angle of incidence as shown in Chapter VI and here.

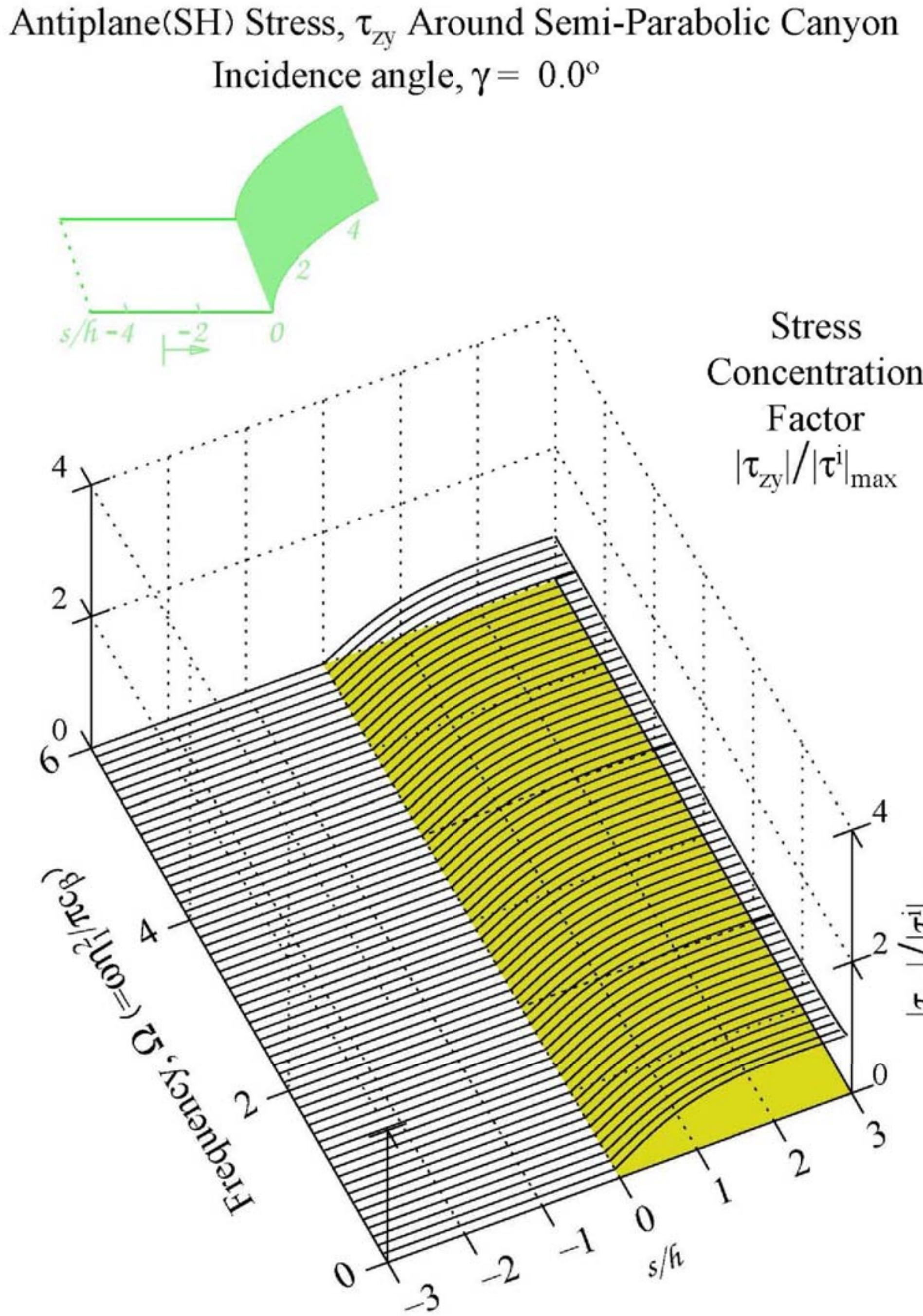

Fig. 8.6 3D Shear Stress Concentration Factor $\left|\overline{\tau}_{zy}\right|$: Horizontal Incidence, $\gamma = 0^{\circ}$

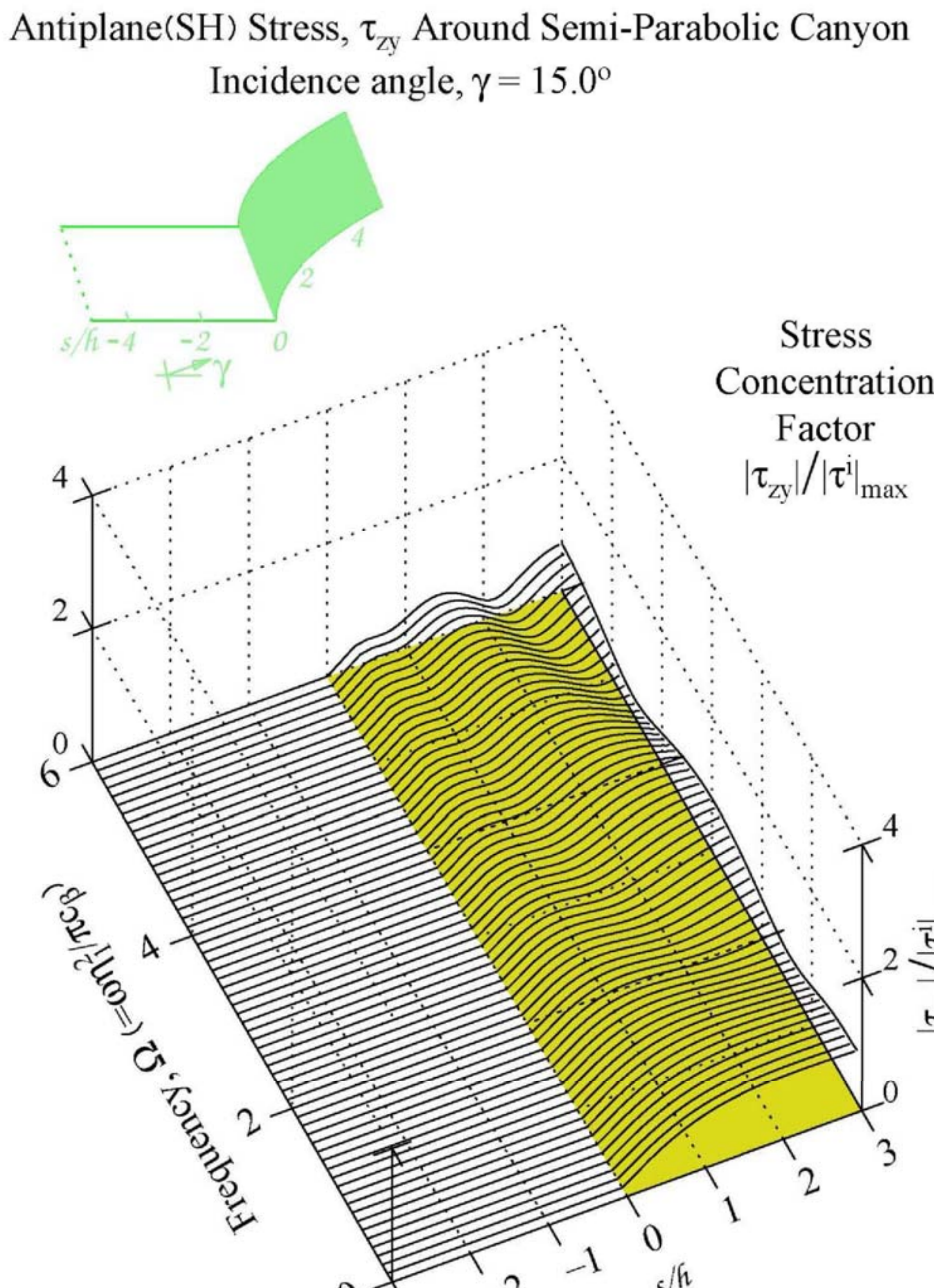

Fig. 8.7 3D Shear Stress Concentration Factor $\left|\overline{\tau}_{zy}\right|$: Oblique Incidence, $\gamma = 15^{\circ}$

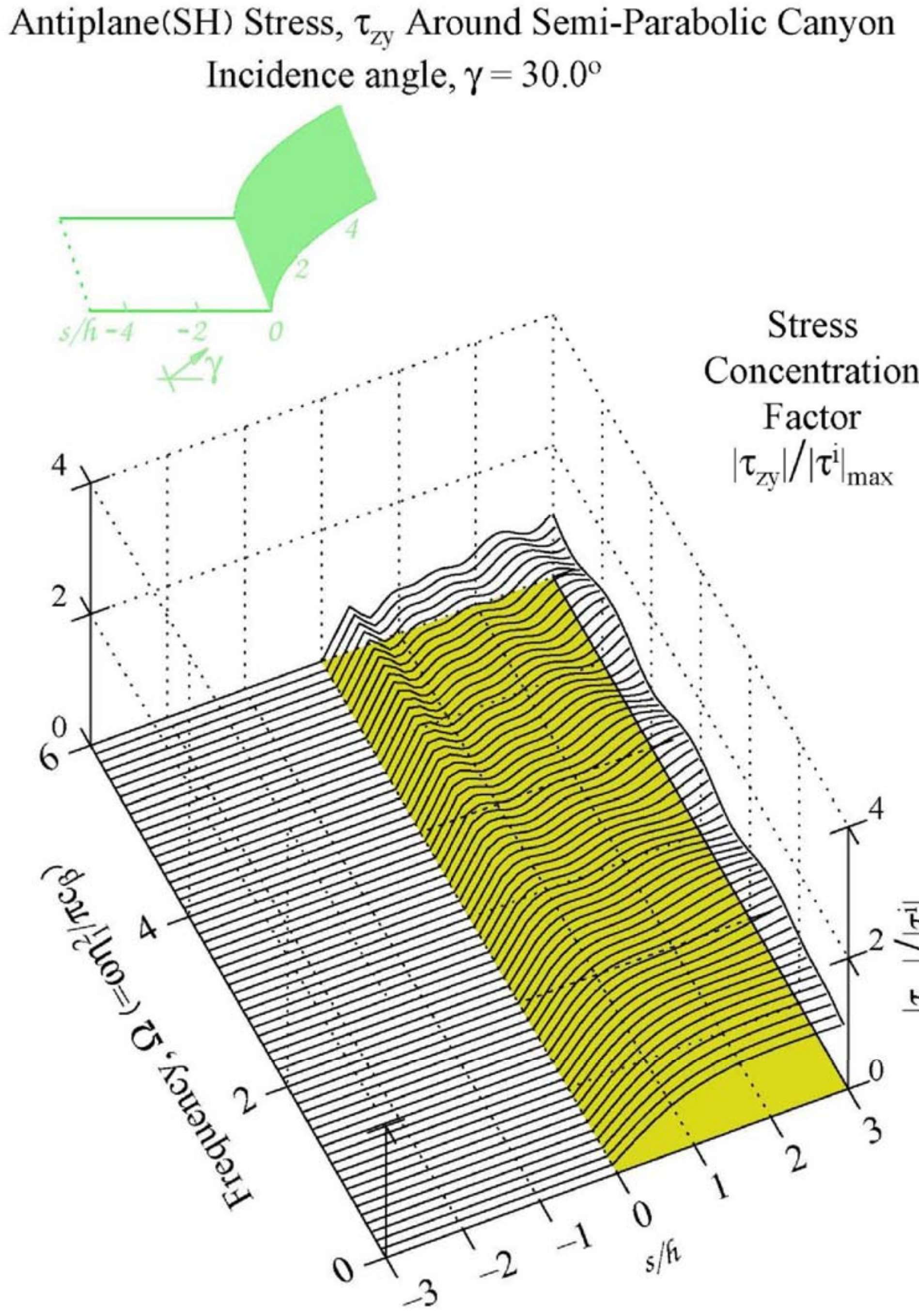

Fig. 8.8 3D Shear Stress Concentration Factor $\left|\overline{\tau}_{zy}\right|$: Oblique Incidence, $\gamma = 30^{\circ}$

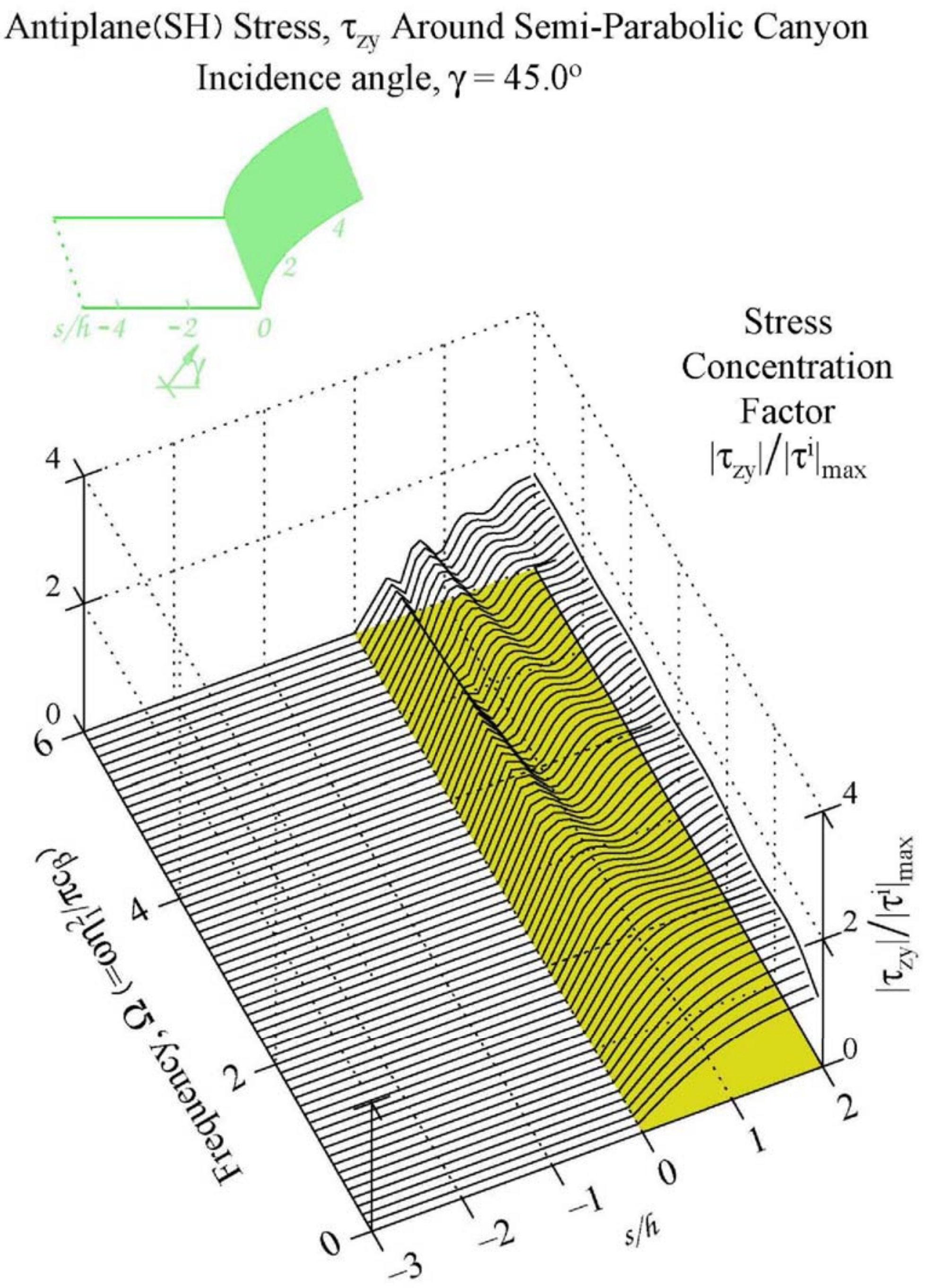

Fig. 8.9 3D Shear Stress Concentration Factor $\left|\bar{\tau}_{zy}\right|$: Oblique Incidence, $\gamma = 45^{\circ}$

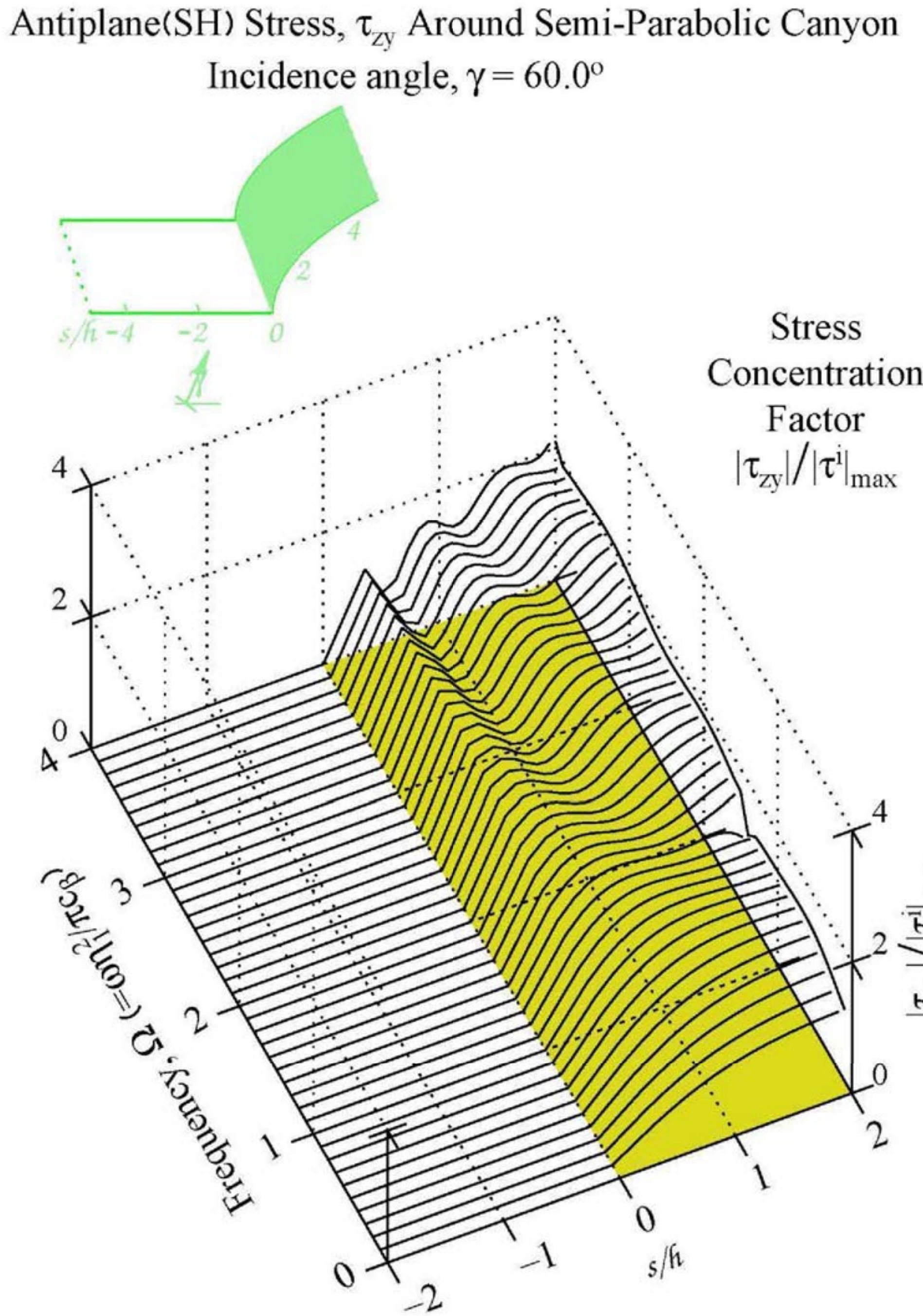

Fig. 8.10 3D Shear Stress Concentration Factor $\left|\bar{\tau}_{zy}\right|$: Oblique Incidence, $\gamma = 60^\circ$

VIII.4 Dynamic Shear Traction Concentration Factor, $\left|\bar{\tau}_{zt}\right|$

Since the resultant shear traction is

$$\left|\bar{\tau}_{zt}\right| = \left[\left|\bar{\tau}_{zx}\right|^2 + \left|\bar{\tau}_{zy}\right|^2\right]^{1/2}$$

$$= 1/k\left(\left|\partial W/\partial x\right|^2 + \left|\partial W/\partial x\right|^2\right)^{1/2} = \left|\bar{\omega}\right|, \text{ the resultant rotation} \qquad \text{Equation (6) above}$$

so as stated earlier, all derivations for expressions for resultant rotations around a semi-parabolic hill in Chapter VII will be used and will not be repeated here.

The normalized shear stress amplitude $\bar{\tau}_{zy}$ at the half-space surface takes the same form as the rocking motion

$$\bar{\tau}_{zy}\Big|_{y=0}\left(=\bar{\omega}_{Rock}\Big|_{y=0}\right) = 0 \qquad \text{Equation (10) above}$$

so that the normalized resultant traction amplitude at the half-space surface is

$$\left|\bar{\tau}_{zt}\right|_{y=0} = \left|\bar{\tau}_{zx}\right|_{y=0} \qquad (11)$$

with no (zero) contribution from the $\bar{\tau}_{zy}$ component.

At the surface of the semi-parabolic hill, the normalized $\overline{\tau}_{zx}$ and $\overline{\tau}_{zy}$ component stress are respectively

$$\left.\overline{\tau}_{zx}\right|_{\eta=\eta_1}\left(=-\left.\overline{\omega}_{Tor}\right|_{\eta=\eta_1}\right)$$

$$=\left(2\sec\gamma/2\right)\frac{\lambda\xi}{2k\left(\xi^2+\eta^2\right)}\sum_{n=0}^{\infty}\left(B_nD_n\left(\overline{\lambda}\eta\right)\right)_{\eta=\eta_1}D_n^{'}\left(\lambda\xi\right)$$ Equation (8) above

$$\left.\overline{\tau}_{zy}\right|_{\eta=\eta_1}=\left.\overline{\omega}_{Rock}\right|_{\eta=\eta_1}$$

$$=\left(2\sec\gamma/2\right)\frac{\lambda\eta_1}{2k\left(\xi^2+\eta_1^2\right)}\sum_{n=0}^{\infty}\left(B_nD_n\left(\overline{\lambda}\eta\right)\right)_{\eta=\eta_1}D_n^{'}\left(\lambda\xi\right)$$ Equation (10) above

which, from Equation (6) gives the resultant rotation amplitude as

$$\left|\overline{\tau}_{zt}\right|_{\eta=\eta_1}=\left[\left|\overline{\tau}_{zx}\right|^2+\left|\overline{\tau}_{zy}\right|^2\right]_{\eta=\eta_1}^{1/2}\left(=\left|\overline{\omega}\right|_{\eta=\eta_1}\right)$$

$$=\left(2\sec\gamma/2\right)\frac{|\lambda|\left(\xi^2+\eta_1^2\right)^{1/2}}{2k\left(\xi^2+\eta_1^2\right)}\left|\sum_{n=0}^{\infty}B_nD_n\left(\overline{\lambda}\eta\right)\right|_{\eta=\eta_1}D_n^{'}\left(\lambda\xi\right) \qquad (12)$$

or, with $\lambda=\sqrt{-2ik},|\lambda|=\sqrt{2k},|\lambda|/k = 2/\sqrt{2k} = 2/|\lambda|$

$$\left|\overline{\tau}_{zt}\right|_{\eta=\eta_1}\left(=\left|\overline{\omega}\right|_{\eta=\eta_1}\right)=\frac{4\sec\left(\gamma/2\right)}{|\lambda|\left(\xi^2+\eta_1^2\right)}\left|\sum_{n=0}^{\infty}B_nD_n\left(\overline{\lambda}\eta\right)\right|_{\eta=\eta_1}D_n^{'}\left(\lambda\xi\right) \qquad (13)$$

Fig. 8.11 to 8.15 are the 3D plots of the normalized shear traction amplitudes around a semi-parabolic hill plotted vs.

1) The dimensionless distance s/h measured along the half-space and canyon surface and

2) The dimensionless frequency $\Omega = \omega\eta_0^2/\pi\beta = 2\eta_0^2/\lambda = 4h/\lambda$,

respectively for incidence angles $\gamma = 0^\circ, 15^\circ, 30^\circ, 45^\circ$ and 60°. As in the corresponding plots of normalized shear stress amplitudes of $\bar{\tau}_{zx}$ and $\bar{\tau}_{zy}$, all trends of features stayed the same.

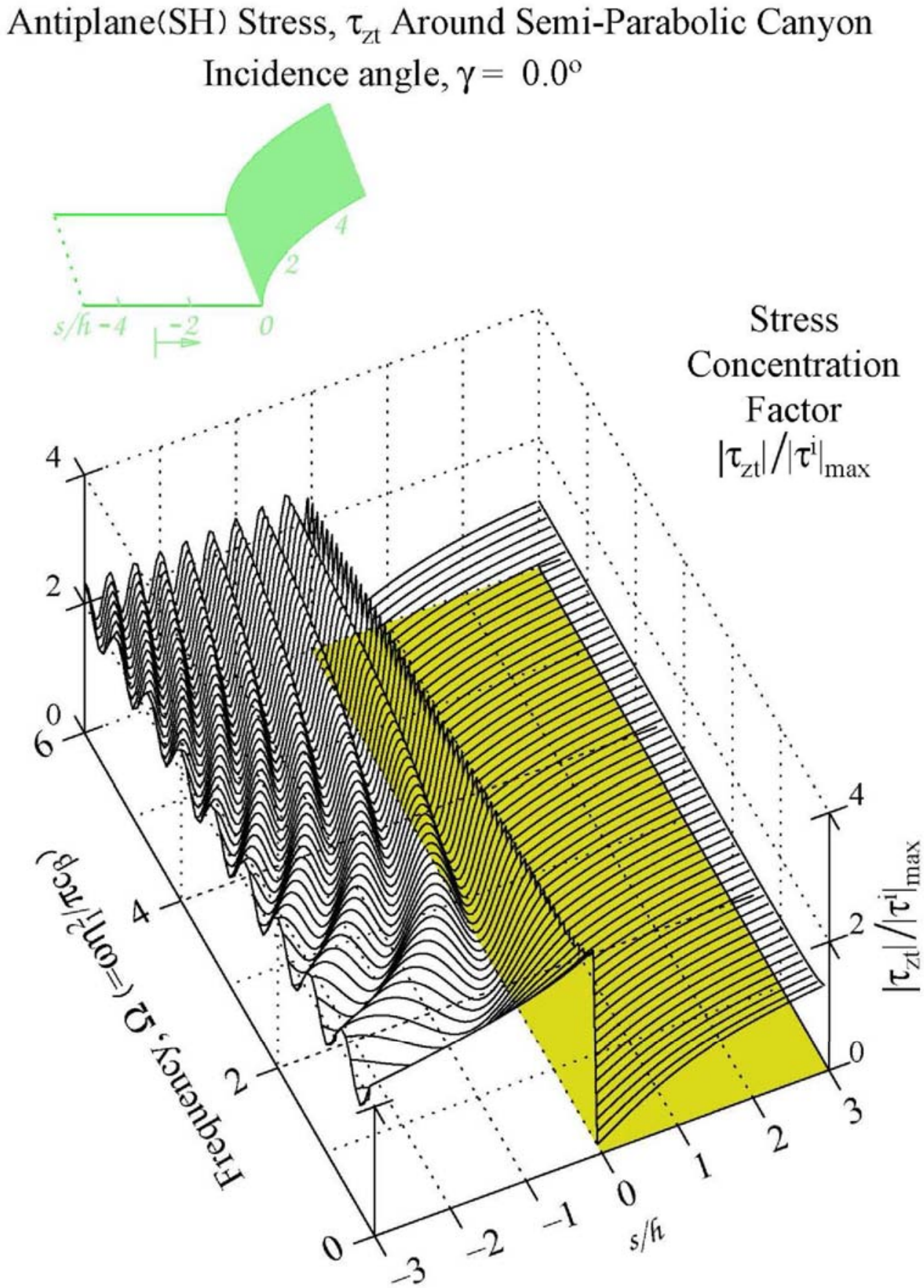

Fig. 8.11 3D Shear Traction Concentration Factors $\left|\overline{\tau}_{zt}\right|$: Horizontal Incidence, $\gamma = 0^{\circ}$

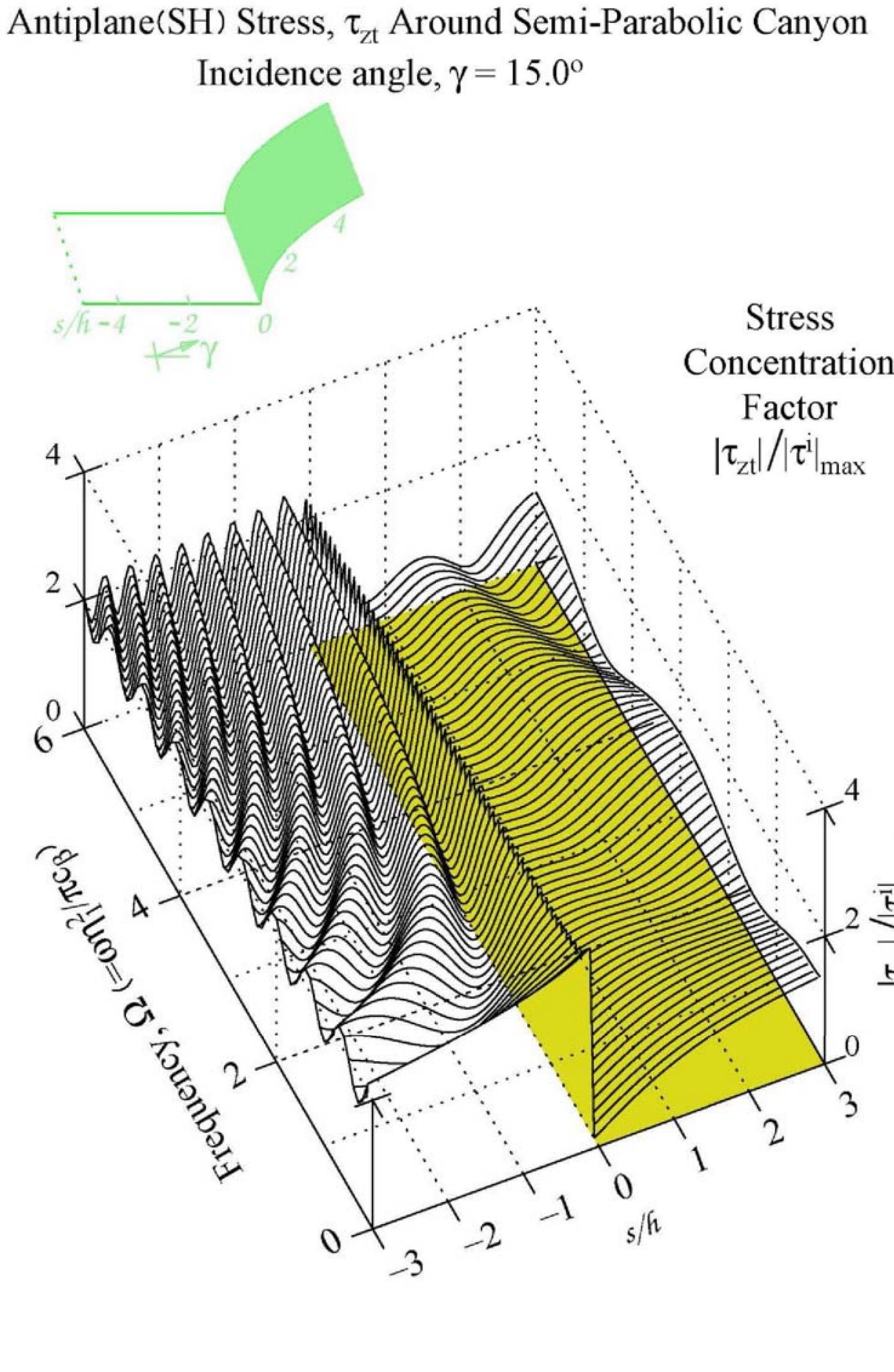

Fig. 8.12 3D Shear Traction Concentration Factors $\left|\overline{\tau}_{zt}\right|$: Oblique Incidence, $\gamma = 15^{\circ}$

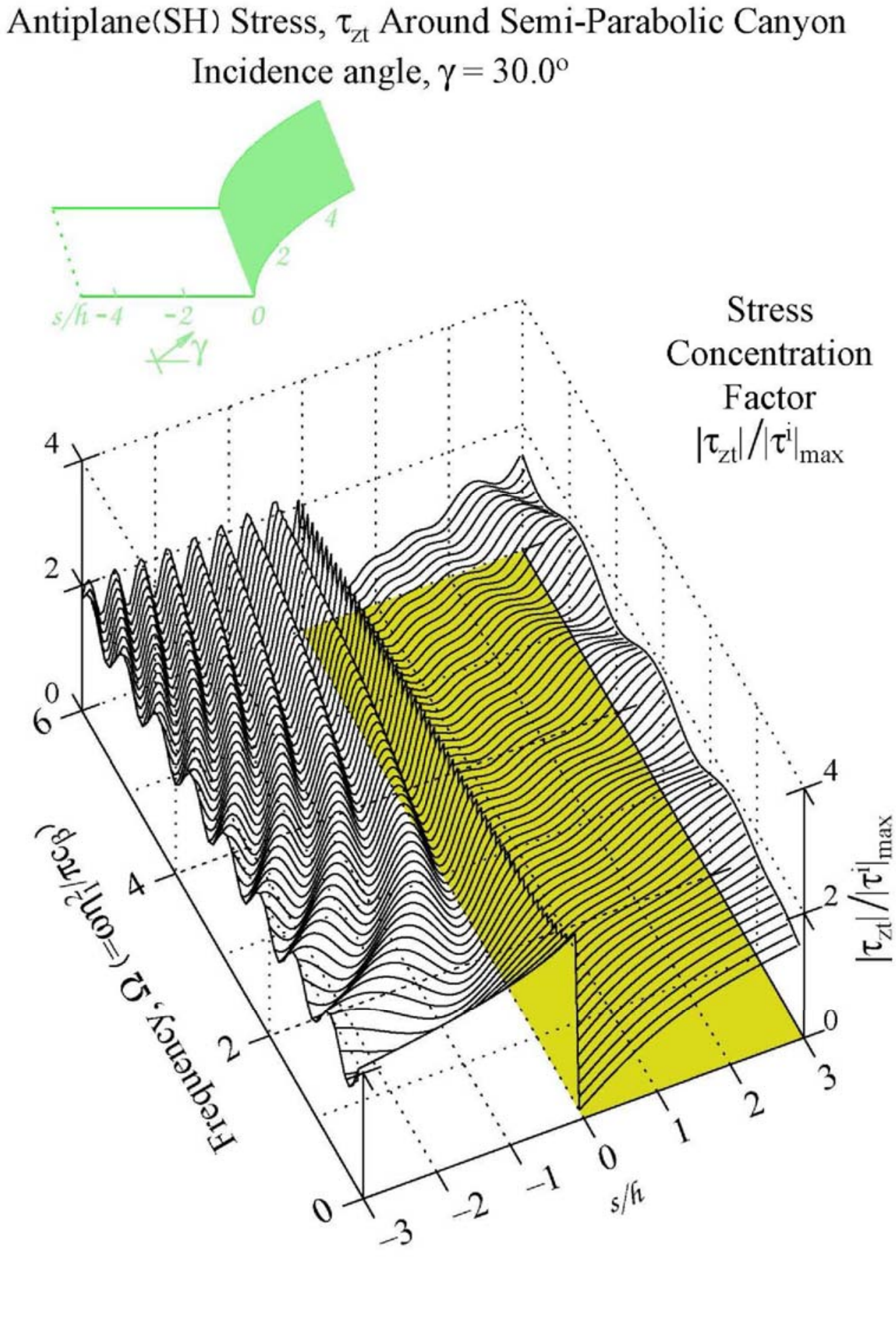

Fig. 8.13 3D Shear Traction Concentration Factors $\left|\overline{\tau}_{zt}\right|$: Oblique Incidence, $\gamma = 30^{\circ}$

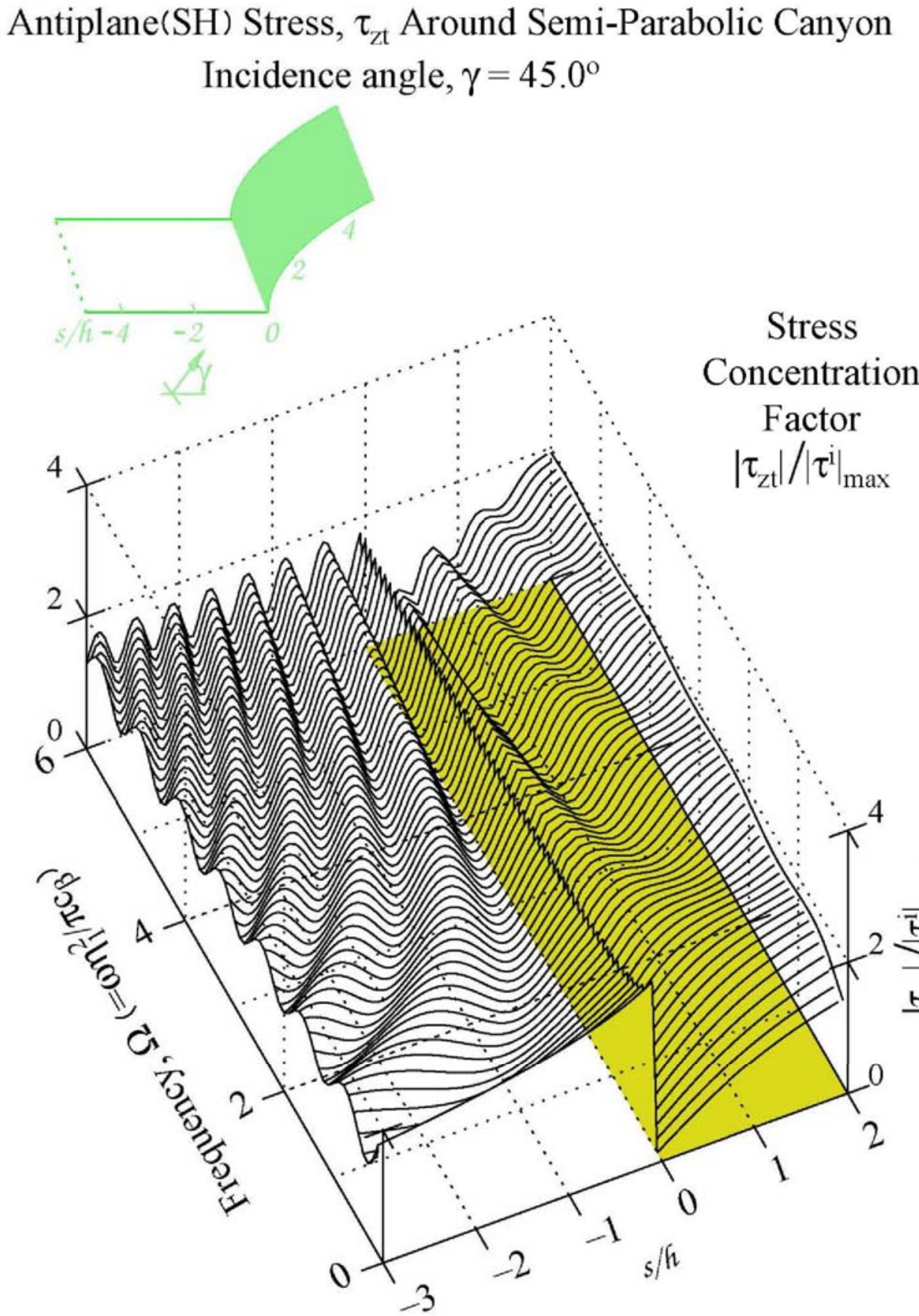

Fig. 8.14 3D Shear Traction Concentration Factors $\left|\bar{\tau}_{zt}\right|$: Oblique Incidence, $\gamma = 45^{\circ}$

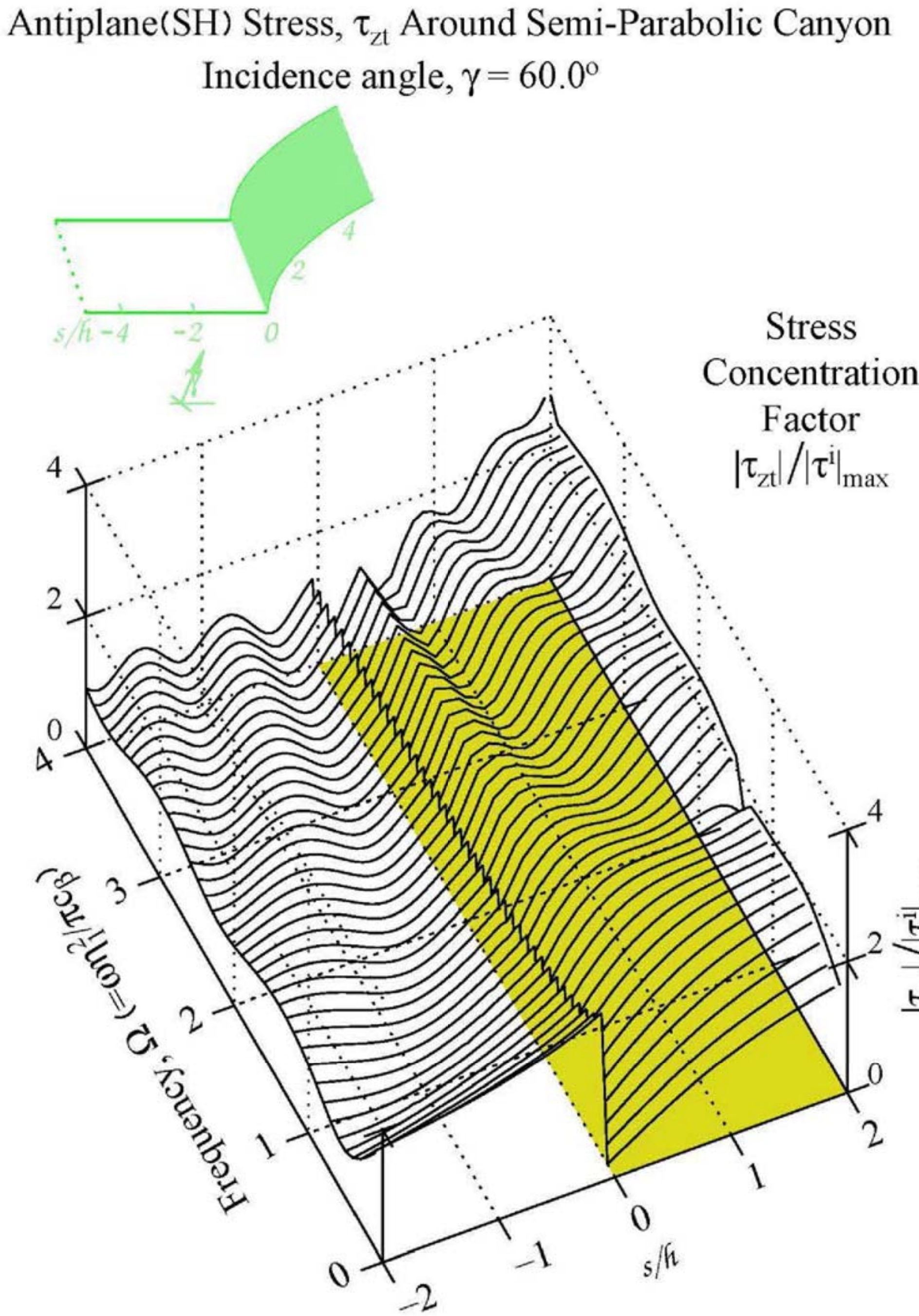

Fig. 8.15 3D Shear Traction Concentration Factors $\left|\bar{\tau}_{zt}\right|$: Oblique Incidence, $\gamma = 60^{\circ}$

VIII. 5 Comparison Graphs for Anti-Plane Stress with Incidence Angles $\gamma = 0^{\circ}, 15^{\circ}, 30^{\circ}, 45^{\circ}$ and 60°

In order to gain a better understanding for the importance of the amplified displacement created due to the anti-plane stress in cocking, rotation and stress concentration factor, a comparison graph has been put together in Fig. 8.16 to 8.20 with incident angles $\gamma = 0^{\circ}, 15^{\circ}, 30^{\circ}, 45^{\circ}$ and 60°. The shape of the half-space and hill surface model on which the displacements are calculated are outlined on the top-left graph of the figure and is in green color. The green arrow is the direction of the incident SH wave, W^i which is assumed to be coming from the left-side towards the hill. These figures show the displacement amplitudes due to rocking (top), rotation (middle) and the combination resultant force for both rocking and rotation (bottom).

In normal engineering design practice, rocking, rotation and stress concentration factor are not being considered in design force as engineers' make assumptions as the effects are small enough to be ignored or effects would cancel out in process. Engineers normally review the impact of each factor separately. This is even more so for the hill topography as shown in the following graphs. However, by putting the figures side by side, we can see the impact in displacement of each reaction, especially with the combination resultant force. Displacement is comparatively small for both rocking and rotation especially when location is far away from bottom of the hill, however, in reality, rocking and rotation comes in a package which is in form of the combination resultant force and the graph clearly show how the large impact these forces create in displacement.

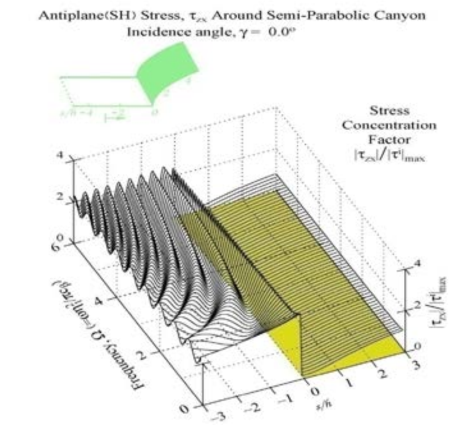

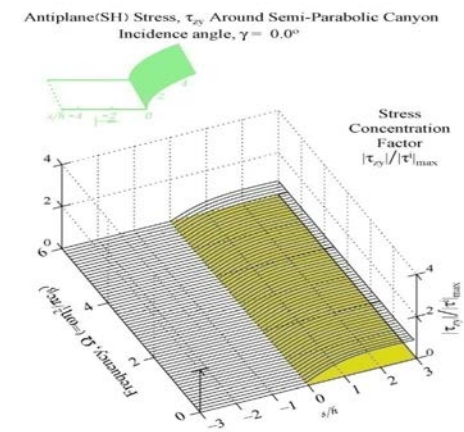

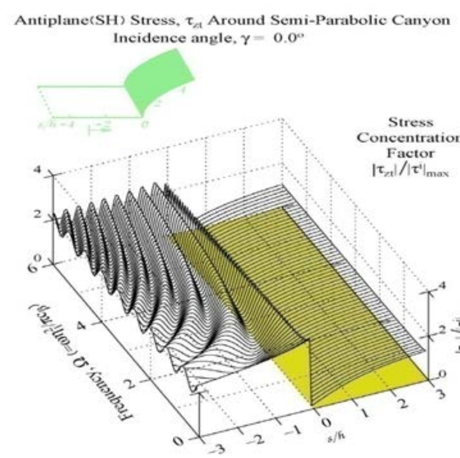

Fig. 8.16 3D Shear Stress Amplitudes, $|\tau_{zx}|,|\tau_{zy}|$ and $|\tau_{zt}|$ Comparison for Horizontal Incidence Angle, $\gamma = 0^\circ$

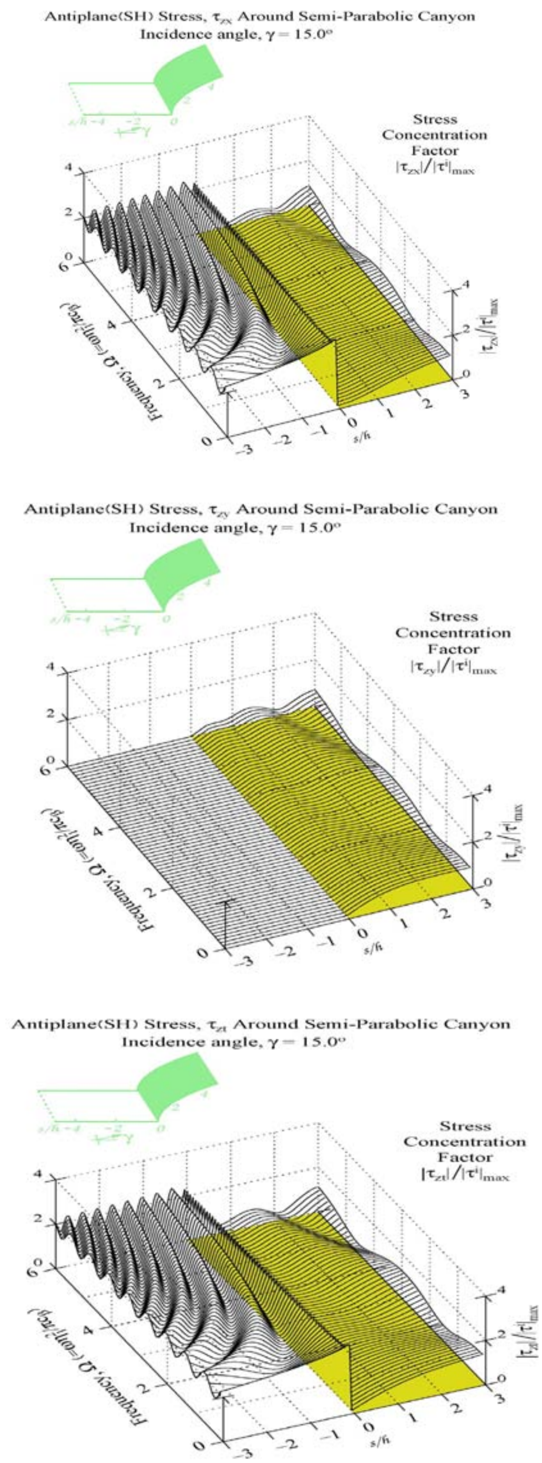

Fig. 8.17 3D Shear Stress Amplitudes, $|\tau_{zx}|, |\tau_{zy}|$ and $|\tau_{zt}|$ Comparison for Oblique Incidence Angle, $\gamma = 15^{\circ}$

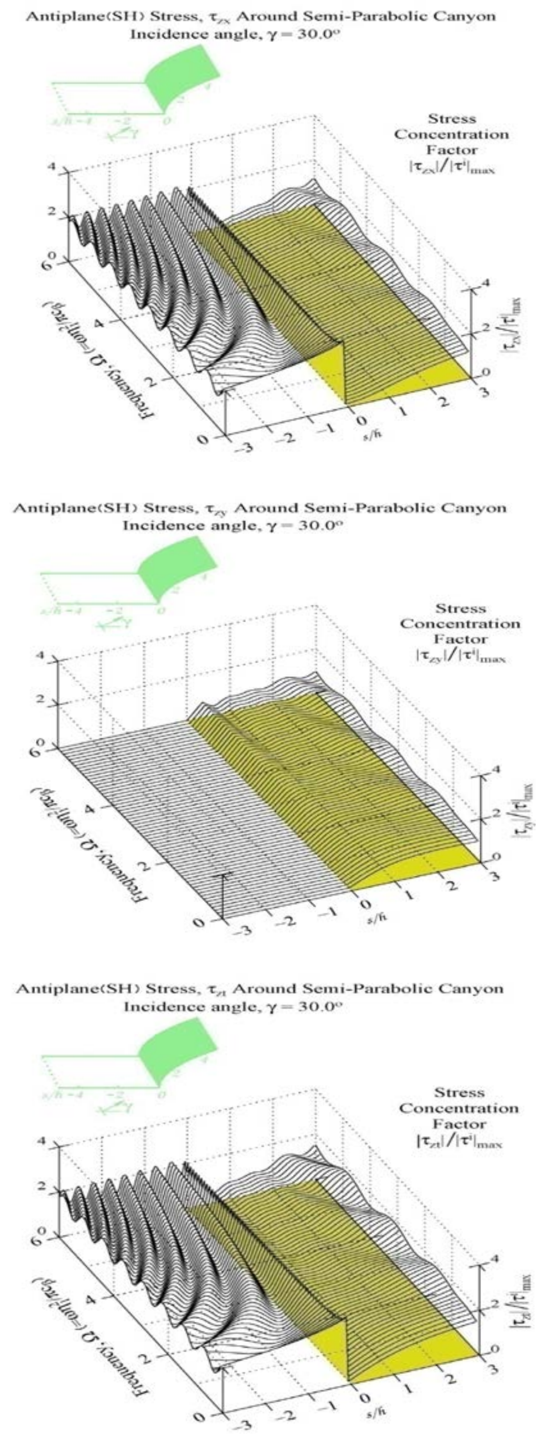

Fig. 8.18 3D Shear Stress Amplitudes, $|\tau_{zx}|, |\tau_{zy}|$ and $|\tau_{zt}|$ Comparison for Oblique Incidence Angle, $\gamma = 30^{\circ}$

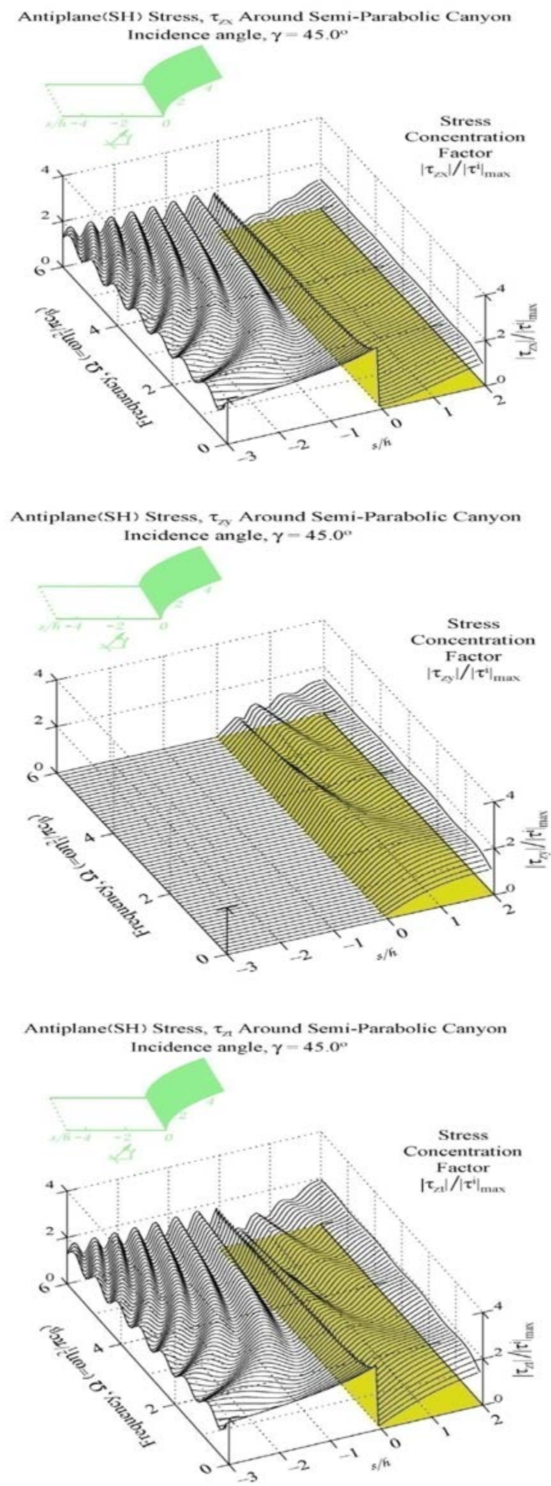

Fig. 8.19 3D Shear Stress Amplitudes, $|\tau_{zx}|, |\tau_{zy}|$ and $|\tau_{zt}|$Comparison for Oblique Incidence Angle, $\gamma = 45^{\circ}$

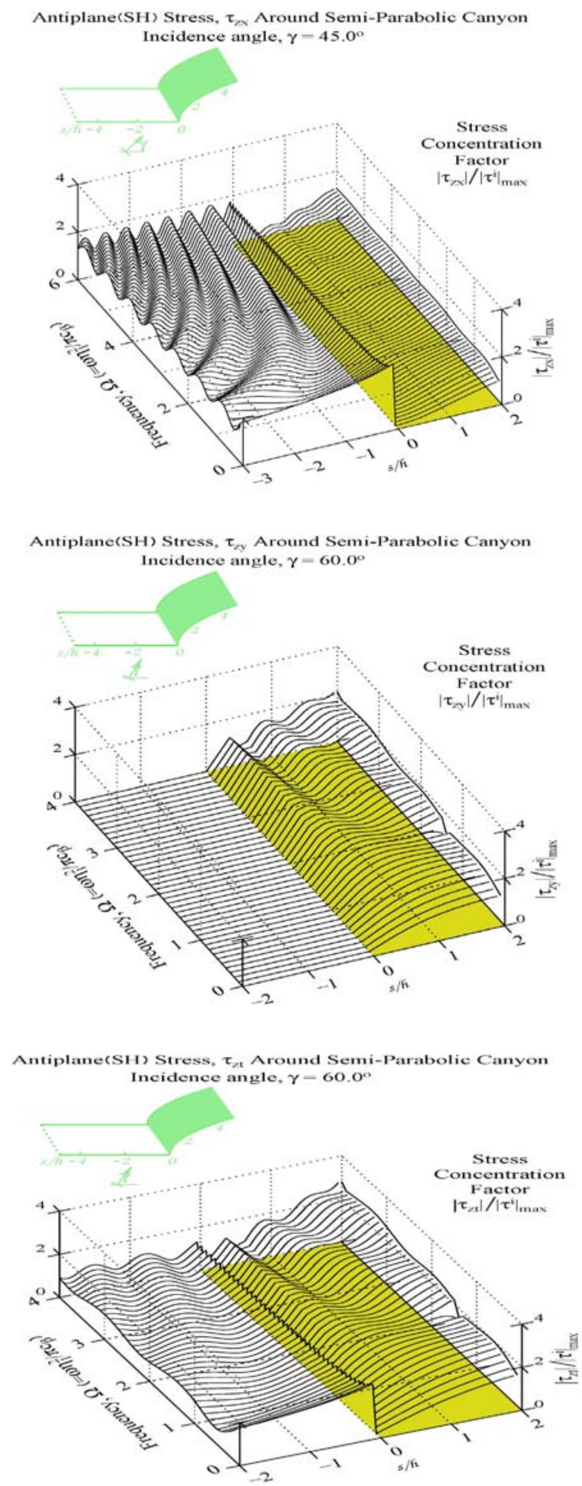

Fig. 8.20 3D Shear Stress Amplitudes, $|\tau_{zx}|, |\tau_{zy}|$ and $|\tau_{zt}|$ Comparison for Oblique Incidence Angle, $\gamma = 60^{\circ}$

VIII.5 Summary

Finally, Chapter VIII calculates the stress concentration factors around the semi-parabolic hill, whose amplitudes are again shown to be identical to the corresponding rotation motions. Thus the stress concentration factors are again smaller than those present around the semi-parabolic canyon.

Chapter IX. Summary, Conclusions and Future Work

IX.1 Summary and Conclusions

This is summary and conclusions that can be drawn from each of the above chapters. As stated in Section I.4 – Objective of Chapter I – Introduction, the thesis is divided into two parts. The first part, Chapters I to V studied the anti-plane displacements, rotations and stress concentration factors around a semi-parabolic canyon. The second part, Chapters VI to VIII studied the anti-plane displacements, rotations and stress concentration factors around a semi-parabolic hill.

In Chapter I, it was found that much of the research work on the diffraction of elastic waves by surface and subsurface topographies were conducted on finite topographies, and hardly any work existed for semi-infinite topographies. This thesis extends the work on finite topographies to a case of semi-infinite topographies, a semi-parabolic canyon and a semi-parabolic hill.

In Chapter II, the work of Lee (1990) on the anti-plane (SH) wave diffraction around a semi-parabolic canyon in an elastic half-space was extended to higher frequencies, with frequencies to be presented here as high as five times that pressed by Lee (1990). This is made possible by the simplification of the terms of the wave functions with the use of the Wronskian relations. In the frequency range and incidence angles presented, amplification as high as four is observed along the canyon surface.

Chapter III extends the work of Chapter II to compute the rotational components of motions. For anti-plane SH wave motions, it is shown that two components of motions are present: the torsional and rocking motions. Chapter III studies the torsional component of rotation. As in the translational motions, the use of the Wronskian relations again allow the torsional motions to be computed up to the dimensionless frequency of $\Omega = 10$. Torsional motions as high as 4 are observed in front of the semi-parabolic canyon.

The rocking component of rotations are derived and studied in Chapter IV. It showed that the rocking motion is zero at the half-space surface, and the corresponding rocking motions on the semi-parabolic canyon surface are smaller than the corresponding torsional motions. Finally the resultant rotational motions combining torsion and rocking is presented. It shows that the resultant rotational motions are large both on the half-space and canyon surfaces.

Chapter V studies the stress concentration factors present in the model. For anti-plane SH wave motions, it is shown that two components of shear stresses are present: the τ_{zx} and τ_{zy} stresses, both being on the x-y plane. It was shown that the τ_{zx} and τ_{zy} stresses are identical respectively to the normalized torsion and rocking components of rotations, and thus the resultant traction stress concentration factors (= resultant rotational motions) are large both on the half-space and canyon surfaces. As in the rotational motions, the shear traction concentration factors are large both on the half-space and canyon surfaces.

This completes the first part of the thesis dealing with semi-parabolic canyon. The second part, Chapter VI to Chapter VIII deals with the semi-parabolic hill.

Chapter VI extends the work of Lee et al (2006) on anti-plane diffraction around a semi-circular hill to that of a semi-parabolic hill. It is found that the displacement motions around a semi-parabolic hill are comparatively smaller than that around a semi-circular canyon. This is because the semi-circular hill in Lee et al (2006) is a finite region that creates trapped waves resulting in large amplification. The semi-parabolic hill here, on the other hand, lies in the shadow region of the incident waves, hardly seeing them.

Chapter VII, as in Chapter III, extends the work of Chapter VI to compute the rotational components of motions around a semi-parabolic hill. As in the case of displacement motions, and for the same reason, it is found that the rotational motions, torsion and rocking, are comparatively smaller than the corresponding rotational motions around a semi-circular canyon.

Finally, Chapter VIII calculates the stress concentration factors around the semi-parabolic hill, whose amplitudes are again shown to be identical to the corresponding rotational motions. Thus the stress concentration factors are again smaller than those present around the semi-parabolic canyon.

IX.2 Future Work

The work presented here on semi-parabolic canyon and hill is for the diffraction of anti-plane SH waves. It will be more complete if future work includes the scattering and diffraction around the semi-parabolic canyon and hill of elastic waves that are in plane waves, namely longitudinal P-, shear SV- and Rayleigh surface waves. The difference between in-plane elastic P, SV and Rayleigh surface waves mentioned here and the anti-plane elastic SH waves in the previous chapters will be that of mode conversion. The cases of anti-plane elastic SH waves are that of stand-alone cases without mode conversion. With the input incident waves being SH waves studied here, all reflected, scattered, diffracted and transmitted output waves will all be SH wave, with no mode conversion, as seen in the previous chapters. With the input incident waves being just one of P, SV or Rayleigh surface waves, all reflected, scattered, diffracted and transmitted output waves, will have both P- and SV- waves present, the case of mode conversion. This makes the boundary-valued problem much more complicated, as the stress and displacement boundary conditions now involve both P- and SV-waves, whose wave functions in general together are not orthogonal.

Take, for example, the case of incident in-plane P-waves onto a semi-parabolic canyon. Fig. 9.1 is a model for one such possible future study. The excitation consists of the incident wave P-potentials with angle of incidence γ_α (with respect to the horizontal x-axis):

$$
\begin{aligned}
\varphi^{(i)} &= \exp\left[ik_\alpha\left(x\cos\gamma_\alpha - y\sin\gamma_\varepsilon\right)\right] \\
&= \sum_{m=0}^{\infty} a_m^{(i)} D_m\left(\overline{\lambda}_\alpha \eta\right) D_m\left(\lambda_\alpha \xi\right) \\
\psi^{(i)} &= 0
\end{aligned}
\tag{1}
$$

In the presence of the half-space surface (y=0) and the absence of the semi-parabolic canyon, the incident plane P-waves are reflected as plane P – and SV – waves, whose potentials are given by, with γ_β the angle of reflection of the plane SV-waves:

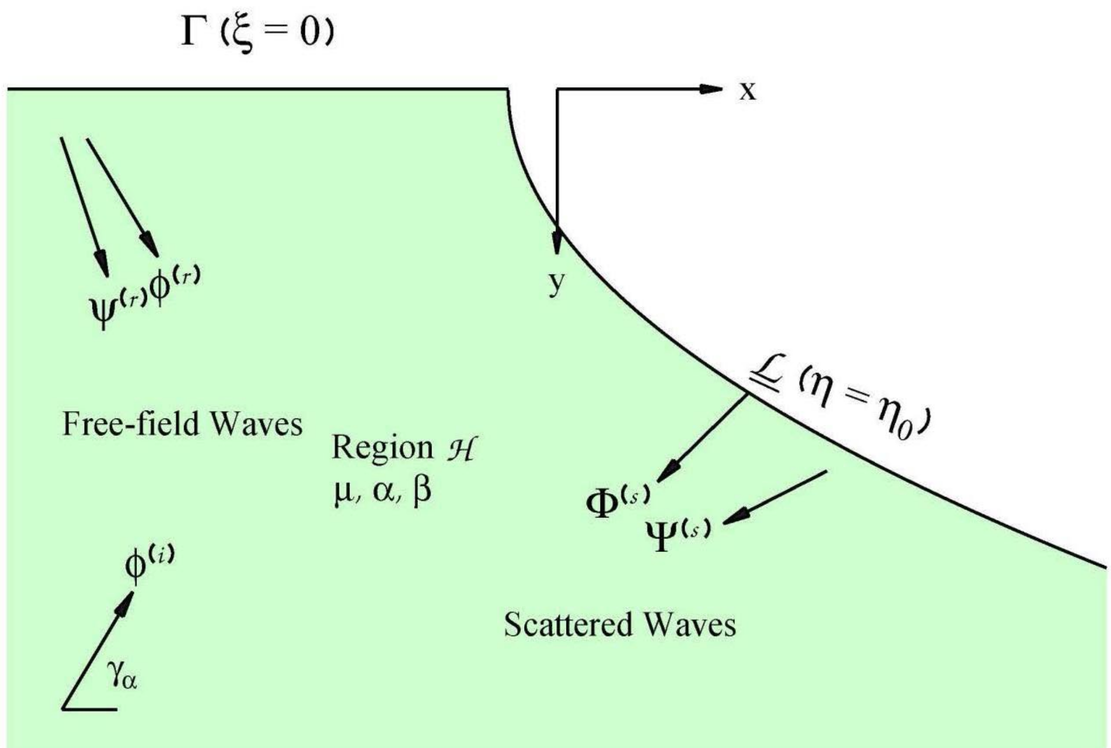

Fig. 9.1 A Semi-Parabolic Canyon in an Elastic Half-Space

$$
\begin{aligned}
\text{P:}\quad \varphi^{(r)} &= K_1 \exp\left[ik_\alpha\left(x\cos\gamma_\alpha + y\sin\gamma_\alpha\right)\right] \\
&= K_1 \exp\left[ik_\alpha\left(x\sin\theta_\alpha + y\cos\theta_\alpha\right)\right] \\
\text{SV:}\quad \psi^{(r)} &= K_2 \exp\left[ik_\beta\left(x\cos\gamma_\beta + y\sin\gamma_\beta\right)\right] \\
&= K_2 \exp\left[ik_\beta\left(x\sin\theta_\beta + y\cos\theta_\beta\right)\right]
\end{aligned}
\tag{2}
$$

where $\theta_\alpha\left(=\pi/2-\gamma_\alpha\right)$ and $\theta_\beta\left(=\pi/2-\gamma_\beta\right)$ are respectively the angles of reflection of the plane P- and SV-waves with respect to the vertical y-axis, and K_1 K_2 reflection coefficients given by

$$
\begin{aligned}
K_1 &= \frac{\sin 2\theta_\alpha \sin 2\theta_\beta - K^2\cos 2\theta_\beta}{\sin 2\theta_\alpha \sin 2\theta_\beta + K^2\cos 2\theta_\beta} \\
K_2 &= \frac{2\sin 2\theta_\alpha c\,\mathrm{os}\, 2\theta_\beta}{\sin 2\theta_\alpha \sin 2\theta_\beta + K^2\cos 2\theta_\beta}
\end{aligned}
\tag{3}
$$

The reflected potentials can also be expanded in terms of the Weber parabolic wave functions:

$$
\begin{aligned}
\text{P:}\quad \varphi^{(r)} &= K_1 \exp\left[ik_\alpha\left(x\cos\gamma_\alpha + y\sin\gamma_\alpha\right)\right] = \sum_{m=0}^{\infty} a_m^{(r)} D_m\left(\overline{\lambda}_\alpha\eta\right) D_m\left(\lambda_\alpha\xi\right) \\
\text{SV:}\quad \psi^{(r)} &= K_2 \exp\left[ik_\beta\left(x\cos\gamma_\beta + y\sin\gamma_\beta\right)\right] = \sum_{m=0}^{\infty} b_m^{(r)} D_m\left(\overline{\lambda}_\beta\eta\right) D_m\left(\lambda_\beta\xi\right)
\end{aligned}
\tag{4}
$$

Where the incident and reflection coefficients are given by

$$
\begin{aligned}
a_m^{(i)} &= \sec\frac{\gamma_\alpha}{2}\frac{(-i)^m}{m!}\tan^m\frac{\gamma_\alpha}{2} \\
a_m^{(r)} &= K_1\sec\frac{\gamma_\alpha}{2}\frac{i^m}{m!}\tan^m\frac{\gamma_\alpha}{2} \\
b_m^{(r)} &= K_2\sec\frac{\gamma_\beta}{2}\frac{i^m}{m!}\tan^m\frac{\gamma_\beta}{2}
\end{aligned}
\tag{5}
$$

Together, the incident and reflected plane P- and SV- wave potentials form the free-field input waves for the diffraction boundary-valued problem:

$$
\begin{aligned}
\text{P:}\quad \varphi^{ff} &= \varphi^{(i)} + \varphi^{(r)} \\
&= \exp\left[ik_\alpha\left(x\cos\gamma_\alpha - y\sin\gamma_\alpha\right)\right] + K_1\exp\left[ik_\alpha\left(x\cos\gamma_\alpha - y\sin\gamma_\alpha\right)\right] \\
&= \sum_{m=0}^{\infty} a_m D_m\left(\overline{\lambda}_\alpha\eta\right) D_m\left(\lambda_\alpha\xi\right) \\
\text{SV:}\quad \psi^{ff} &= \cancel{\psi^{(i)}} + \psi^{(r)} = K_2\exp\left[ik_\beta\left(x\cos\gamma_\beta + y\sin\gamma_\beta\right)\right] \\
&= \sum_{m=0}^{\infty} b_m D_m\left(\overline{\lambda}_\beta\eta\right) D_m\left(\lambda_\beta\xi\right)
\end{aligned}
\tag{6}
$$

with $a_m = a_m^{(i)} + a_m^{(r)}$ and $\mathrm{b}_m = b_m^{(r)}$ for $m = 0,1,2...$ in Equation (6)

The presence of the semi-parabolic surface $\eta = \eta_0$ will result in scattered P- and SV-wave potentials, given by, as outgoing, scattered waves:

$$
\begin{aligned}
\varphi^{(s)} &= \sum_{m=0}^{\infty} A_m D_{-m-1}\left(\lambda_\alpha\eta\right) D_m\left(\lambda_\alpha\xi\right) \\
\psi^{(s)} &= \sum_{m=0}^{\infty} B_m D_{-m-1}\left(\lambda_\beta\eta\right) D_m\left(\lambda_\beta\xi\right)
\end{aligned}
\tag{7}
$$

Together with the free-filed waves $\varphi^{(ff)}$ and $\psi^{(ff)}$, they must satisfy the stress-free boundary conditions at the surface of the canyon and that of the half-space.

$$
\begin{aligned}
\text{At } \eta = \eta_0 \qquad & \sigma_{\eta\eta} = \sigma_{\eta\eta}^{(ff)} + \sigma_{\eta\eta}^{(s)} = 0, \\
& \sigma_{\eta\xi} = \sigma_{\eta\xi}^{(ff)} + \sigma_{\eta\xi}^{(s)} = 0, \\
\text{and at } \xi\text{=0:}\quad & \sigma_{\xi\xi} = \cancel{\sigma_{\xi\xi}^{(ff)}} + \sigma_{\xi\xi}^{(s)} = \sigma_{\xi\xi}^{(s)} = 0, \\
& \sigma_{\xi\eta} = \cancel{\sigma_{\xi\eta}^{(ff)}} + \sigma_{\xi\eta}^{(s)} = \sigma_{\xi\eta}^{(s)} = 0, \\
\text{as } \sigma_{\xi\xi}^{(ff)} = \sigma_{\xi\eta}^{(ff)} = 0 \qquad & \text{at } \xi\text{=0}
\end{aligned}
\tag{8}
$$

This is well-defined boundary-valued problem, but, because of the mode conversion involving both P- and SV-waves, which are non-orthogonal, is a very difficult, challenging problem to solve.

References

Chapter I

1. **Abramowitz, M. and Stegan, I.A.** *Handbook of Mathematical Functions***,** Dover Publication, Inc., New York. **1972**

2. **Cao, H. & Lee, V. W.** Scattering of Plane SH Waves by Circular Cylindrical Canyons with Variable Depth-to-Width Ratio, *European J. Earthquake Eng., III(2):29-37,* **Dec, 1989**

3. **Cao, H. & Lee, V.W.** Scattering and Diffraction of Plane P Waves by Circular Cylindrical Canyons with Variable Depth-to-Width Ratio, *Int. J. Soil Dynamics & Earthquake Eng., 9(3):141-150,* **May, 90**

4. **Epstein** (1914) *Diffraction from a Plane Screen. P. S. Epstein* Beugung an einem ebenen Schirm Dissertation, Munich, **1944**

5. **Lamb** (1914) On Sommerfeld's diffraction problem, and on reflection by a parabolic mirror, Proc. London Math. Soc., 4, 190. **1907**

6. **Lee, V.W.** In Deformations Near Circular Underground Cavity Subjected to Incident Plane SH Waves, *Symposium of Applications of Computer Methods in Engineering,* Aug 23-26, P. 951-961, *University of Southern California, Los Angles, USA.,* **1977**

7. **Lee, V.W.** On the Scattering of Plane SH Waves by a Semi-Parabolic Cylindrical Canyon in an Elastic Half-Space, *Geophysical J., 100:79-86,* **Feb, 1990**

8. **Lee, V.W. & Cao, H.** Diffraction of SV Waves by Circular Cylindrical Canyons of Various Depths, *J. Eng. Mech., A.S.C.E., 115(9):2035-2056,* **Sep., 1989**

9. **Lee, V.W. & Trifunac, M.D.** Response of Tunnels to Incident SH Waves, *J. Eng. Mech., A.S.C.E., 105:643-659,* **Aug., 1979**

10. **Lee, V. W. & Wu, X. Y.** Application of the Weighted Residual Method to Diffraction by 2-D Canyons of Arbitrary Shape, I: Incident SH Waves, *Int. J. Soil Dynamics & Earthquake Eng., 13(5):355-364,* **Oct, 1994a**

11. **Lee, V. W. & Wu, X. Y.** Application of the Weighted Residual Method to Diffraction by 2-D Canyons of Arbitrary Shape, II: Incident P, SV & Rayleigh Waves, *Int. J. Soil Dynamics & Earthquake Eng., 13(5):365-373,* **Oct, 1994b**

12. **Lee, V.W., Chen, S. & Hsu, L.R.** Anti-plane Diffraction from Canyon Above a Subsurface Unlined Tunnel, *J. Eng. Mech., A.S.C.E., 125(6):668-675,* **June 1999**

13. **Liang, J.W., Zhang, Y., Gu, X. & Lee, V.W.** Surface Motion of Circular-Arc Layered Alluvial Valley for Incident Plane SH Waves, *Chinese J. Geotechnical Engineering, 22(4):396-401*, **Jul, 2000**

14. **Liang, J.W., Yan, L. & Lee, V.W. (2001a)** Scattering of Plane P Waves Around Circular-Arc Layered Alluvial Valleys: Analytical Solution, *ACTA Seismologica Sinica 14(2):176-195,* **Mar., 2001** *(Chinese Translation: Seismologic Sinica 23(2), P. 167-184)*

15. **Liang, J.W., Yan, L. & Lee, V.W. (2001b)** Effect of a Covering Layer in a Circular-Arc Canyon on Incident Plane SV Waves, *ACTA Seismologica Sinica 14(6):660-675, 16 Pages, 9Refs.,* **Nov. 2001**

16. **Liang, J.W., Yan, L. & Lee, V.W. (2002)** Scattering of Incident Plane P Waves by a Circular – Arc Canyon with a Covering Layer, *ACTA Mechanica Solida Sinica, 23(4)*, **Dec. 2002**

17. **Liang, J.W., Yan, L. & Lee, V.W. (2003a)** Diffraction of Plane SV Waves by a Circular-Arc Layered Alluvial Valley: Analytical Solution, *Mechanica Solida Sinica, 24(2):235-243,* **2003**

18. **Liang, J.W., Yan, L. & Lee, V.W. (2003b)** Dynamic Response of Circular-Arc and Sedimentary Valley Site Under Incident SV Waves, *China Civil Engineering Journal, 236(12), 74-82,* **2003**

19. **Liang, J.W., Zhang, Y., Gu, X. & Lee, V.W. (2003a)** Scattering of Plane Elastic SH Waves by Circular-Arc Layered Canyon, *Journal of Engineering Vibrations, 16(2):158-165*, **June 2003**

20. **Liang, J.W., Zhang, H. & Lee, V.W. (2003b)** A series Solution for Surface Motion Amplification due to Underground Twin Tunnels: Incident SV Waves, *Int. J. Earthquake Eng. & Eng. Vibration, 2(2):289-298,* **Dec. 2003**

21. **Liang, J.W., Zhang, H. & Lee, V.W. (2004a)** A Series Solution for Surface Motion Amplification due to Underground Group Cavities: Incident P Waves, *ACTA Seismologica Sinica 17(3):296-307,* **May 2004**

22. **Liang, J.W., Luo, H. & Lee, V.W. (2004b)** Scattering of Plane SH Waves by a Circular-Arc Hill with a Circular Tunnel, *ACTA Seismologica Sinica 17(5):549-563*, **Sep. 2004**

23. **Liang, J.W., Zhang, H. & Lee, V.W. (2004c)** An Analytical Solution for Dynamic Stress Concentration of Underground Twin Cavities due to Incident SV Waves, *Journal of 5Vibration Engineering 17(2):132-140,* **Jun, 2004**

24. **Liang, J.W., Zhang, H. & Lee, V.W. (2004d)** An Analytical Solution for Dynamic Stress Concentration of Underground Cavities under incident P Waves, *Journal of Geotechnical Engineering 26(6):815-819*, **Nov. 2004**

25. **Liang, J.W., Ji, X.D. & Lee, V. W. (2005a)** Effects of an underground Lined Tunnel on Ground Motion (I): Series Solutions, *J. Rock and Soil Mechanics, Academia Sinica, 26(4): 520-524,* **Apr. 2005**

26. **Liang, J.W., Ji, X.D., & Lee, V.W. (2005b)** Effects of an underground Lined Tunnel on Ground Motion (II): Numerical Results, *J. Rock and Soil Mechanics, Academia Sinica, 26(5):687-692*, **May. 2005**

27. **Moeen-Vaziri & Trifunac, M.D. (1985)** Scattering of Plane SH-Waves by Cylindrical Canals of Arbitrary Shapes, *Int. J. Soil Dynamics and Earthquake Engineering, 4(1):18-23,* **1985**

28. **Morse, P. M. & Feshbach, H**. *Method of Theoretical Physics*. McGraw-Hill. **1953**

29. **Mow, C.C. and Pao, Y.H.** The diffraction of elastic waves and dynamic stress concentrations, a report prepared for United States Air Force Project Rand. **1971**

30. **Sabina & Willis** Surface of SH Waves by Rough Half-Space of Arbitrary Slope, *Geophysical Journal of the Royal Astronomical Society, 42:685-703* **1975**

31. **Sánchez-Sesma, F.J. & Rosenblueth, E.,** Ground Motion at Canyons of Arbitrary Shape under Incident SH Waves, *Earthquake Engineering. Structural. Dyn., 7: 441–450.* **1979**

32. **Sommerfeld, A.** Mathematische theorie der diffraction, *Math. Ann.,* B47, S17, **1896**

33. **Thau, S.A.** Diffraction of Elastic Waves by a Parabolic Cylinder and Dynamic Stress Concentration, *Ph.D. Thesis, Cornell University, Ithaca, New York*, **1966**

34. **Thau, S.A. & Pao, Y.H.** Diffraction of Horizontal Shear Waves by a Parabolic Cylinder and Dynamic Stress Concentrations, *J. Appl. Mech.*, 33, 785-792, **1966**

35. **Thau, S.A. & Pao, Y.H. (1967a)** Stress-intensification near a Semi-infinite Rigid Smooth Strip due to Diffraction of Elastic Waves, *J. Appl. Mech.*, 34, 119-126, **1967**

36. **Thau, S.A. & Pao, Y.H. (1967b)** Wave Function Expansion and Perturbation Methods for the Diffraction of Elastic Waves, *J. Appl. Mech.*, 34, 915-921, **1967**

37. **Todorovska, M.I. & Lee, V.W. (1991a)** Surface Motion of Shallow Circular Alluvial Valleys for Incident Plane SH Waves – Analytical Solution, *Int. J. Soil Dynamics & Earthquake Eng.*, 10(4), 192-200, **May, 1991**

38. **Todorovska, M.I. & Lee, V.W (1991b)** A Note on Scattering of Rayleigh Waves by Shallow Circular Canyons: Analytical Approach, *ISET J. Earthquake Technology*, 28(2, 1-16, **Jun, 1991**

39. **Trifunac, M.D.** A Note on Scattering of Plane SH Waves by a Semi-Cylindrical Canyon, Int. *J. of Earthquake Engineering and Struct. Dynamics*, **1**, 267-281, **1973**

40. **Wong, H.L. & Jennings, P.C.** Effect of Canyon Topographies on Strong Ground Motions, *Bull. Seismo. Soc. Am.*, 65, 1239-1257, **1975**

41. **Wong, H.L. & Trifunac, M.D.** Scattering of Plane SH-Waves by a Semi-Elliptical Canyon, *Intl. J. of Earthquake Engineering and Struct. Dynamics*, **3**, 157-169, **1974**

Chapter II:

1. **Cao, H. & Lee, V. W.** Scattering of Plane SH Waves by Circular Cylindrical Canyons with Variable Depth-to-Width Ratio, *European J. Eathquake Eng., III(2), 29-37,* **Dec, 1989**

2. **Cao, H. & Lee, V. W.** Scattering and Diffraction of Plane P Waves by Circular Cylindrical Canyons with Variable Depth-to-Width Ratio, *Int. J. Soil Dynamics & Eathquake Eng., 9(3), 141-150,* **May 1990**

3. **Lee, V.W.** On the Scattering of Plane SH Waves by a Semi-Parabolic Parabolic Cylindrical Canyon in an Elastic Half-Space, *Geophysical J., 100, 79-86,* **Feb., 1990**

4. **Lee, V.W. & Cao, H.** Diffraction of SV Waves by Circular Cylindrical Canyons of Various Depths, *J. Eng. Mech., A.S.C.E., 115(9), 2035-2056,* **Sep. 1989**

5. **Todorovska, M.I. & Lee, V.W.** A Note on Response of Shallow Circular Valleys to Rayleigh Waves: Analytical Approach, *Earthquake Eng. & Eng. Vibration, 10(1), 21-34,* **Mar, 1990**

6. **Todorovska, M.I. & Lee, V.W. (1991a)** Surface Motion of Shallow Circular Alluvial Valleys for Incident Plane SH Waves – Analytical Solution, *Int. J. Soil Dynamics & Earthquake Eng., 10(4), 192-200,* **May, 1991a**

7. **Todorovska, M.I & Lee, V.W. (1991b)** A note on Scattering of Rayleigh Waves by Shallow Circular Canyons: Analytical Approach, *ISET J. Earthquake Technology, 28(2), 1-16,* **Jun, 1991b**

8. **Trifunac, M.D.**, Surface Motion of a Semi-Cylindrical Alluvial Valley for Incident Plane SH Waves, *Bull. Seism. Soc. Amer*., **61**, 1755-1770, pp. 15, **1971**

9. **Trifunac, M.D.,** Interaction of a Shear Wall with the Soil for Incident Plane SH Waves, *Bull. Seism. Soc. Amer., **62**, 63-83*, **1972**

10. **Trifunac, M.D.** A Note on Scattering of Plane SH Waves by a Semi-Cylindrical Canyon, Int. *J. of Earthquake Engineering and Structural. Dynamics,* **1**, 267-281, pp. 14, **1973**

11. **Wong, H.L. and Trifunac, M.D. (1974a)** Scattering of Plane SH Waves by a Semi-Elliptical Canyon, *Intl. J. of Earthquake Engineering and Structural. Dynamics, **3**, 157-169,* **1974a**

12. **Wong, H.L. and Trifunac, M.D. (1974b)** Surface Motion of a Semi-Elliptical Alluvial Valley for Incident Plane SH Waves, *Bull. Seism. Soc. Amer., **64**, 1389-1408,* **1974b**

13. **Wong H.L. and Trifunac, M. D. (1974c)** Interaction of a Shear Wall with the Soil for Incident Plane SH Waves: Elliptical Rigid Foundation, *Bull. Seism. Soc. Amer., **64**, 1825-1842,* **1974c**

14. **Zhang, S. & Jin, J.** Computation of Special Function *John Wiley & Sons, New York,* **1996**

Chapter III:

1. **Aviles, J. & Suarez, M.** Natural and Accidental Torsion in One-Story Structures on Elastic Foundation under Non-Vertically Incident SH Waves, *Earthquake Engineering & Struct. Dynamics, Vol. 35 Issue 7, 829-850* **Jun 2006**

2. **Ibsen, L.B., Liingaard, M. & Anderson, L.** Dynamic Stiffness of Suction Caissons – Torsion, Sliding and Rocking, *DCE Technical Report No. 8, Division of Water & Soil, Department of Civil Engineering, Aalborg, Univ. Sohnaardsholmsvej 57, DK-9000 Aalborg, Denmark,* **Dec 2006**

3. **Lee, V.W. & Liang, J.W.** Rotational Components of Strong-Moti0n Earthquakes, *presented at the 14th World Conference on Earthquake Engineering held at Beijing, China on* **Oct 12-17, 2008**

4. **Lee, V.W. & Trifunac, M.D.** Torsional Accelerograms, *Int. J. soil Dynamics & Earthquake Eng., 4(3), 132-139* **Aug 1985**

5. **Lee, W.H.K.** A Glossary for Rotational Seismology, *Bull. Seismol. Soc. Am.* **99***No. 2B, 1082-1090*

6. **Lee, W.H.L., Celebi, M., Todorovska, M.I. & Igel, H. (2009a)** Introduction to the Special Issue on Rotational Seismology and Engineering Applications, *Bulletin of the Seismological Society of America, V. 99, No. 2B, 945-957* **May 2009**

7. **Lee, W.H.K., Huang, Bor-Shouh, Langston, C.A., Lin, C.J., Liu, C.C., Shin, T.C., Teng, T.L. & Wu, C.F. (2009b)** Review: Progress in Rotational Ground-Motion Observations from Explosions and Local Earthquakes in Taiwan, *Bulletin of the Seismological Society of America, V. 99, 958-967* **May 2009**

8. **Lee, W.H.K., Igel, H. & Trifunac, M.D.** Recent Advances in Rotational Seismology, *Seismological Research Letters, V. 80, No. 3, 479-490* **May/Jun 2009**

9. **Luco, J.E.** Torsional Response of Structures for SH Waves: The Case of Hemispherical Foundation, *Bull. Seism. Soc. Amer.* 66, *109-123,* **1943**

10. **Oldham, R. D.**, Report of the great earthquake of 12th June, 1897, *Mem. Geol. Surv. India*, pp. 379. **1899** (Reprinted by Geol. Surv. of India, Calcutta 1981.)

11. **Ryan, K.L.** Estimating the Seismic Response of Base-Isolated Buildings including Torsion, Rocking, and Axial-Load Effects *Ph. D Dissertation, University of California, Berkeley, 248 Pages; Publication 3183859***, 2004**

12. **Schreiber, K.U., Velikoseltsev, A., Carr, A.J. & Framco-Anaya, R.** The Application of Fiber Optic Gyroscopes for the Measurement of Rotations in Structural Engineering, *Bull. Of the Seismological Society of America, V..99 No. 2B, 1207-1214,* **May 2009**

13. **Trifunac, M.D.** Effects of Torsional and Rocking Excitations on the Response of Structures, *CH39 in the book Earthquake Source Asymmetry, Structural Media and Rotation Effects, Edited by R. Teisseyre, M. Takeo and E. Majewski, Springer, Heidelberg, Germany, 569-582,* **2006**

14. **Wong, H.L. & Trifunac, M.D.** Synthesizing Realistic Strong Motion Accelerograms, *Department of Civil Engineering. CE78-07, University of Southern California, Los Angeles*, **1978**

Chapter IV:

1. **Godinho, L., P. Amado Mendes & Tadeu, A.** Numerical Simulation of Ground Rotations along 2D Topographical Profiles under the Incidence of Elastic Plane Waves, *Bulletin of the Seismological Society of America, V. 99, No. 2B 1147-1161,* **May 2009**

2. **Hu, X.Q., Cai, Y.Q., Ding, G.Y. & Wang, J.** Rocking Vibrations of a Rigid Embedded Foundation in a Poroelastic Half-Space, *International Journal for Numerical and Analytical Methods in Geomechanics V. 34, Issue 13 1409-1430,* **Sep. 2010**

3. **Hung, H.H., Chang, K.C., Liu, K.Y. & Ho, T.H.** An Experimental Study on Rocking Response of Bridge Spread Foundations, *The 14th World Conference on Earthquake Engineering,* **Oct 12-17, 2008** *Beijing, China*

4. **Lee, V.W. & Trifunac, M.D.** Torsional Accelerograms, *Int. J. Soil Dynamics & Earthquake Engineering, 4(3), 132-139***, Aug. 1985**

5. **Lee, V.W. & Trifunac, M.D.** Rocking Strong Earthquake Accelerations, *Int. J. Soil Dynamics & Earthquake Eng., 6(2), 75-89,* **Apr. 1987**

6. **Lee, W.H.L., Celebi, M., Todorovska, M.I. & Igel, H. (2009a)** Introduction to the Special Issue on Rotational Seismology and Engineering Applications, *Bulletin of the Seismological Society of America, V. 99, No. 2B, 945-957* **May 2009**

7. **Luco, J.E. & Wong, H.L.** Response of Structures to Non-Vertically Incident Seismic Waves, *Bull. of Seismology Society of America, 72, 275-302,* **1982**

Chapter V:

1. **Cheng, G.C., Loree, H.M., Kamm, R.D., Fishbein, M. C. & Lee, R. T.**, Distribution of Circumferential Stress in Ruptured and Stable Atherosclerotic

Lesions. A Structural Analysis with Histopathological Correlation. *Circulation, 87, pp. 1179–1187*. **1993**

2. **Huajian Gao, Baohua Ji, Ingomar L. Jäger, Eduard Arzt, and Peter Fratzl** Materials Become Insensitive to Flaws at Nanoscale: Lessons from Nature PNAS May 13, **2003** *V. 100 No. 10 5597-5600.*

3. **Knopoff, G.F.** Scattering of Impulsive Elastic Waves by a Rigid Cylinder, *Journal Acoust. Soc. Am 31:1169-1175,* **1959**

4. **L Van Miegroet & Pierre Duysinx** Stress Concentration Minimization of 2D Filets Using X-FEM and Level Set Description *Structural and Multidisciplinary Optimization V.* 33, Numbers 4-5, 425-438, **2007**

5. **Nishimura & Jimbo** A Dynamic Problem of Stress Concentration – Stresses in the Vicinity of a Spherical Matter Included in an Elastic Solid Under Dynamic Force, *University of Tokyo, Japan, 24, 101,* **1955**

6. **Packard, C.E. & Schuh, C.A.** Initiation of Shear Bands Near a Stress Concentration in Metallic Glass *Acta Materialia, 55(17), 5948-5958,* **Oct 2007**

7. **Pao, Y.H. & Mow, C.C.** The Diffraction of Elastic Waves and Dynamics Stress Concentrations *Crane, Russack and Company Inc. New York***, 1973**

8. **Peterson, R.E.** Stress Concentration Design Factors, *John Wiley and Sons, New York,* **1953**

9. **Pilkey, Walter D.** Peterson's Stress Concentration Factors, *John Wiley and Sons, Inc., Published online* **Dec. 18th, 2007**

10. **Rooke, D.P. & Cartwright, D.J.** Compendium of Stress Intensity Factors, *H. M. S. O. Publisher, London,* **1976**

11. **Shigley, J., Mischke, C. & Budynas, R.** Mechancial Engineering Design *McGraw Hill Series in Mechanical Engineering, 7th Edition, New York,* **1989**

12. **Takeuchi, H.** Diffration of Elastic Waves by an Elastic Sphere, *Geophysical Notes, 3(19)* **1950**

13. **Timoshenko, S. & Dietz, W.** Stress Concentration Produced by Holes and Fillets, *Trans. ASME 47:pp199* **1925**

14. **Timoshenko, S.** Stress Concentration and Fatigue Failure, *Proc. Inst. Mech. Engineering 157 pp163,* **1947**

15. **Walker, K.** The Effect of Stress Ratio During Crack Propagation and Fatigue for 2024-T3 and 7075-T6 Aluminum *Effects of Environment and Complex Load History on Fatigue Life, ASTM STP 462. American Society for Testing & Materials 1-14* **1970**

16. **White, R. M.** Elastic Wave Scattering of a Cylindrical Discontinuity in a Solid, *J. Acoust. Society America, 30, pp771* **1958**

17. **Whitney, J.M.** Stress Fracture Criteria for Laminated Composites Containing Stress Concentration. *Journal of Composite Materials, vol. 8 no. 3 253-265* **July 1974**

18. **Wang, Qizhi & Wong, Xiaoli** Expression of Stress Concentration Factors for an Eccentric Circular Hole in a Tension Orthotropic Finite-Width Strip *[J];Acta Materiae Compositae Sinica;2003-06* **2003**

19. **Ying, C. F. and R. Truell**, Scattering of a Plane Longitudinal Wave by a Spherical Obstacle in an Isotropically Elastic Solid. *J. Appl. Phys.*, **27**, 1086–1097, **1956**

20. **Young, W.C. & Budynas, R.G.** Roark's Formulas for Stress and Strain *McGraw-Hills Companies Inc. New York, 7th Edition,* **2002**

Chapter VI:

1. **Abramowitz, M. and I. A. Stegan,** *Handbook of Mathematical Functions,* Dover Publication, Inc., New York. **1972**
2. **Erdélyi, A., Magnus, W., Oberhettinger, F. & Tricomi, F.G.** Higher Transcendental Functions, Vol. I *McGraw-Hill, New York* **1953**

3. **Hinders, M.K. & Yaghjian, A.D.** Dual-series Solution to Scattering from a Semicircular Channel in a Ground Plane. *Microwave and Guided Wave Letters*, IEEE Volume1, Issue: 9, 239-242, **1991**

4. **Park, S.K., Johnston, M.J.S., Morgan, F.D. & Morrison, H.F.** Electromagnetic Precursors to Earthquakes in the ULF Band: A Review of Observations and Mechanisms *Reviews of Geophysics, 31, 2/***May, 1993** *117-132*

5. **Lee, V.W.** On Deformations Near Circular Underground Cavity Subjected to Incident Plane SH Waves, *Symposium of Applications of Computer Methods in Engineering,* **Aug 23-26,** *951-961, University of Southern California, Los Angeles, U.S.A.,* **1977**

6. **Lee, V.W. & Trifunac, M.D.** Response of Tunnels to Incident SH Waves, *J. Engineering Mech., A.S.C.E., 105, 643-659* **Aug. 1979**

7. **Lee, V.W & Cao, H.** Diffraction of SV Waves by Circular Cylindrical Canyons of Various Depths, *J. Eng. Mech., A.S.C.E., 115(9), 2035-2056,* **Sep. 1989**

8. **Lee, V.W. & Karl, J. (1993a)** Diffraction of SV Waves by Underground, Circular, Cylindrical Cavities, *Int. J. Soil Dynamics & Earthquake Eng., 11(8), 1992, 445-456* **Jun, 1993**

9. **Lee, V.W. & Karl, J. (1993b)** Diffraction of Elastic Plane P Waves by Circular Underground Unlined Tunnels, *European J. Earthquake Eng., Val (1),29-36* **Aug. 1993**

10. **Lee, V.W. & Wu, X.Y. (1994a)** Application of the Weighted Residual Method to Diffraction by 2D Canyons of Arbitrary Shape, I: Incident SH Waves, *Int. J. Soil Dynamics & Earthquake Eng., 13(5), 1994, 355-364,* **Oct. 1994**

11. **Lee, V.W. & Wu, X.Y. (1994b)** Application of the Weighted Residual Method to Diffraction by 2D Canyons of Arbitrary Shape, II: Incident P, SV & Rayleigh Waves, *Int. J. Soil Dynamics & Earthquake Eng., 13(5), 1994, 365-373,* **Oct. 1994**

12. **Lee, V.W., Luo, H. & Liang, J.H.** Diffraction of Anti-Plane SH Waves by a Semi-Circular Cylindrical Hill with an Inside Semi-Circular Concentric Tunnel, *Int. J. Earthquake Eng. & Eng. Vibration, 3(2) 249-262,* **Dec. 2004**

13. **Lee, V.W., Luo, H. & Liang, J.H.** Scattering of Plane SH Waves by a Circular-Arc Hill with a Circular Tunnel, *ACTA Seismologica Sinica 17(5) 549-563,* **Sep. 2004**

14. **Lee, V. W., Luo, H. & Liang, J. H.** Anti-Plane Diffraction Around a Semi-Circular Hill Re-derived: Accurate Closed-Form Analytic Solution, *J. Eng. Mech., A.S.C.E., 132(10), 1106-1114,* Oct. 2006

15. **Pao, Y.H. and Mow, C.C.**, *The Diffraction of Elastic Waves and Dynamic Stress Concentrations*. Crane and Russak, New York. **1973**

16. **Trifunac, M. D.**, Surface Motion of a Semi-Cylindrical Alluvial Valley for Incident Plane SH Waves, *Bull.. Seism. Soc. Amer*., **61**, 1755-1770, pp. 15, **1971**

17. **Trifunac, M. D.** A Note on Scattering of Plane SH Waves by a Semi-Cylindrical Canyon, Int. *J. of Earthquake Engineering and Struct. Dynamics*, **1**, 267-281, pp. 14, **1973**

18. **Yuan, Xiaoming & Men, Fu-Lu** Scattering of Plane SH Waves by a Semi-Cylindrical Hill, *Earthquake Engineering & Structural Dynamics Volume 21, Issue 12, pages 1091–1098,* **1992**

19. **Yuan, Xiaoming & Liao, Zhen-Peng** Surface Motion of a Cylindrical Hill of Circular—Arc Cross-Section for Incident Plane SH Waves, *Soil Dynamics and Earthquake Engineering Volume 15, Issue 3, 189–199,* **April 1996**

Chapter VII:

1. **Lee, V. W., Luo, H. & Liang J.W.** Anti-Plane Diffraction Around a Semi-Circular Hill Re-derived: Accurate Closed-Form Analytic Solution, *J. Eng. Mech., A.S.C.E., 132(10), 1106-1114,* **Oct. 2006**

Chapter VIII:

1. **Lee, V. W., Luo, H. & Liang J.W.** Anti-Plane Diffraction Around a Semi-Circular Hill Re-derived: Accurate Closed-Form Analytic Solution, *J. Eng. Mech., A.S.C.E., 132(10), 1106-1114,* **Oct. 2006**